advanced diffusion measures from reduced dmri acquisitions

selected papers

Santiago Aja-Fernández
Antonio Tristán-Vega

M I P
MEDICAL IMAGING PRESS

M I P
MEDICAL IMAGING PRESS

Advanced Diffusion Measures from Reduced dMRI Acquisitions

Selected Papers

Santiago Aja Fernández & Antonio Tristán-Vega

with

Tomasz Pieciak, Rodrigo de Luis-García and Guillem París

Edited by Santiago Aja-Fernández

Brain Imaging Valladolid (BIVa)
Laboratorio de Procesado de Imagen (LPI)
Universidad de Valladolid
Spain

Advanced Diffusion Measures from Reduced dMRI Acquisitions. Selected Papers
May 15, 2023
MIP: Medical Imaging Press

Universidad de Valladolid
Laboratorio de Procesado de Imagen (LPI)
ETS Ingenieros de Telecomunicación
Paseo de Belén, 47011 Valladolid (Spain)
Contact: sanaja@tel.uva.es

Introduction

Diffusion magnetic resonance imaging (dMRI) has gained much interest from the neuroimaging community over the last two decades, due to its ability to analyze in vivo structures within the white matter of the brain. These techniques are used by many prestigious international centers and have been the basis of major international projects in the last decades with millions of Euros of funding, such as the Human Brain Project (EU) or the NIH Human Connectome Project (USA). The current trend in dMRI analysis is the calculation of increasingly advanced metrics focused on subtle aspects of the diffusion and brain microstructure.

However, for the calculation of these advanced measures, the acquisition requirements may get higher and higher:

1. Increasingly powerful MRI scanners, such as the Siemens 3T MAGNETOM Prisma (with a gradient power of 80mT/m), Siemens 3T Connectome (with a gradient power of 300mT/m) or commercial scanners up to 7T.

2. Denser q-space sampling: higher number of shells (b-values) and higher number of samples per shell.

In the first case, there is a clear economic limitation: not all centers can afford such expensive dedicated equipment. For the second requirement, an increase in the number of samples at each acquisition leads to longer acquisition times. Thus, these techniques are not totally compatible with clinical and research acquisitions that can be performed in standard medical or research centers. In the standard case:

1. Acquisitions must be performed within a preset time, for the patient's convenience and to take advantage of the scanners. Typically, studies are performed in addition to clinical acquisitions, so a patient cannot spend 2 hours inside the machine. For studies with a larger number of patients, this would simply imply times that cannot be afforded by the public health system.

2. The scanners available for research in most centers are those that are also used clinically. Many national centers already have 3T scanners (as opposed to the large number of 1.5T scanners still in use). However, there are no national centers with advanced scanners specialized for diffusion.

These limitations could make it impossible for most national research and clinical centers to carry out state-of-the-art brain research using advanced diffusion metrics.

To alleviate this problem, the authors have been working for years on advanced measures that provide similar clinical information to existing ones but using commercial scanners and a limited number of samples. Several techniques have been proposed, based on different models.

Methods are based on the reduction of the number of degrees of freedom of the estimation problem by introducing prior assumptions and thus reducing the minimum number of data needed for estimation. The main methods are:

1. **Apparent Measures Using Reduced Acquisitions (AMURA)**. The method allows the direct estimation of diffusion measures such as RTOP, RTAP and PA, avoiding the calculation of the EAP while reducing the number of necessary samples and the computational cost. It assumes a behavior of the diffusion process that is roughly independent from the b-value. This assumption, common in high angular resolution diffusion imaging (HARDI) acquisitions, allows the calculation of these metrics from single-shell acquisitions, typical in clinical routine. Since the assumed model only holds within a limited range around the b-value considered, the derived measures must be considered as apparent values at a given b-value, dependent on the selected shell. However, despite this dependence with the b-value, the apparent metrics calculated with AMURA have shown a good correlation with the same metrics calculated using standard multi-shell approaches.

2. **Micro-Structure-adaptive convolution kernels and dual Fourier domains Integral Transforms (MiSFIT)**. This technique calculates the EAP and then the metrics can be derived. As opposed to the related approaches in the state of the art, MiSFIT is not based on fitting the EAP in some functions basis, which makes it time efficient at the same time it relaxes the low-frequency constraints imposed by the maximum b-value acquired. Instead, it is based on convolution kernels and dual Fourier domains Integral Transforms. Due to the low-rank signal representation, with at most 3 parameters to estimate, it could provide a full representation of the EAP and all the scalar moments with just 2 shells (for the simplified representation) or 3 shells if free water is also estimated. At the same time, the decoupled optimization in a low rank non-linear problem for the radial behavior and a model-free, linear problem for the orientation makes MiSFIT extremely time-efficient, beating the computation times of other methods by two orders of magnitude.

3. **Hybrid Diffusion Imaging (HyDI) - Diffusion Spectrum Imaging (DSI)**. It is aimed at non-parametrically describing the EAP through a set of particular values sampled at the nodes of a regular 3-D Cartesian lattice. As opposed to the direct approach originally proposed by Wu and colleagues, where the dual space of the EAP w.r.t. the Fourier transform is interpolated to get a Cartesian lattice and then the FFT is computed to retrieve the EAP, we directly relate the sparse multi-shell samples in the dual space to the Cartesian lattice of the EAP without interpolation. This is solved by means of a constrained Quadratic Problem. This formalism allows to compute non-negative EAP samples, as well as analytical estimates of common diffusion markers like the return-to-origin, return-to-plane, or return-to-axis probabilities, all of them in a time-efficient framework. Orientation Distribution Functions (ODFs), and even Positive-Definite ODFs, can also be computed in a combined numerical-analytical fashion, and represented in the basis of Spherical Harmonics.

In what follows, you can find, properly sorted, the main works we have published about this topics:

1. Single Shell Acquisitions: AMURA

a) AMURA: Micro-structure diffusion scalar measures from reduced MRI acquisitions. Original paper. We develop the method to estimate RTOP, RTAP and RTPP.

b) Apparent Propagator Anisotropy from Single-Shell Diffusion MRI Acquisitions. We extend AMURA to calculate novel anisotropy metrics.

c) Moment-based representation of the diffusion inside the brain from reduced DMRI acquisitions: generalized AMURA. Generalized formulation of AMURA and new metrics.

d) Viability of AMURA biomarkers from single-shell diffusion MRI in Clinical Studies

2. Multishell Acquisitions

a) Efficient and accurate EAP imaging from multi-shell dMRI with Micro-Structure adaptive convolution kernels and dual Fourier Integral Transforms (MiSFIT).

b) Efficient Estimation of Propagator Anisotropy and Non-Gaussianity in multishell diffusion MRI with MiSFIT. Extension of the method to calculate NG and PA.

c) HYDI-DSI revisited: constrained non-parametric EAP imaging without q-space re-gridding. New non parametric method.

3. Practical Extensions

a) Anisotropy Measure from Three Diffusion-Encoding Gradient Directions. Using AMURA anisotropy metrics to calculate Anisotropy from just 3 gradient directions.

b) Accurate free-water estimation in white matter from fast diffusion MRI acquisitions using the spherical means technique. Modification of MiSFIT to estimate water with just two acquired shells.

Contents

Part I

Single Shell Acquisitions: AMURA

1

AMURA: Micro-structure diffusion scalar measures from reduced MRI acquisitions

Santiago Aja-Fernández[1], Rodrigo de Luis-García[1], Maryam Afzali[3], Malwina Molendowska[3], Tomasz Pieciak[2], Antonio Tristán-Vega[1]

[1] *Laboratorio de Procesado de Imagen (LPI), Universidad de Valladolid, Spain*
[2] *AGH University of Science and Technology, Krakow, Poland*
[3] *Cardiff University Brain Research Imaging Center (CUBRIC), University of Cardiff, UK*

Abstract: In diffusion MRI, the Ensemble Average diffusion Propagator (EAP) provides relevant micro-structural information and meaningful descriptive maps of the white matter previously obscured by traditional techniques like Diffusion Tensor Imaging (DTI). The direct estimation of the EAP, however, requires a dense sampling of the Cartesian q-space involving a huge amount of samples (diffusion gradients) for proper reconstruction. A collection of more efficient techniques have been proposed in the last decade based on parametric representations of the EAP, but they still imply acquiring a large number of diffusion gradients with different b-values (shells). Paradoxically, this has come together with an effort to find scalar measures gathering all the q-space micro-structural information probed in one single index or set of indices. Among them, the return-to-origin (RTOP), return-to-plane (RTPP), and return-to-axis (RTAP) probabilities have rapidly gained popularity. In this work, we propose the so-called "Apparent Measures Using Reduced Acquisitions" (AMURA) aimed at computing scalar indices that can mimic the sensitivity of state of the art EAP-based measures to micro-structural changes. AMURA drastically reduces both the number of samples needed and the computational complexity of the estimation of diffusion properties by assuming the diffusion anisotropy is roughly independent from the radial direction. This simplification allows us to compute closed-form expressions from single-shell information, so that AMURA remains compatible with standard acquisition protocols commonly used even in clinical practice. Additionally, the analytical form of AMURA-based measures, as opposed to the iterative, non-linear reconstruction ubiquitous to full EAP techniques, turns the newly introduced *apparent* RTOP, RTPP, and RTAP both robust and efficient to compute.

Originally published as: *Santiago Aja-Fernández, Rodrigo de Luis-García, Maryam Afzali, Malwina Molendowska, Tomasz Pieciak, Antonio Tristán-Vega, Micro-structure diffusion scalar measures from reduced MRI acquisitions, PloS one, 15-3, e0229526. 2020*

1.1 Introduction

Under the name of Diffusion Magnetic Resonance Imaging (DMRI) we gather a set of diverse MRI imaging techniques with the ability of extracting *in vivo* relevant information regarding the random, anisotropic diffusion of water molecules that underlay the structured nature of different living tissues. It has attracted an extraordinary interest among the scientific community over recent years due to the relationships found between a number of neurological and neurosurgical pathologies and alterations in the white matter as revealed by an increasing number of DMRI studies [1.1, 1.2, 1.3].

The most relevant feature of DMRI is its ability to measure directional variance, i.e. anisotropy. In the beginning of the 2000s, diffusion tensor MRI [1.4, DT-MRI] gained huge popularity in white matter studies, not only among technical researchers but also among clinical partners, to the point that even nowadays most of the research studies involving DMRI focus on the diffusion tensor (DT). By using a simple Gaussian regressor, the anisotropy of the tissues is actually probed by acquiring as few as 20 to 60 images, which is acceptable in clinical practice. DT-MRI brought to light one of the most common problems in DMRI techniques: in order to carry out clinical studies, the information given by the selected diffusion analysis method must be translated into some scalar measures that describe different features of the diffusion within every voxel. That way, measures like the Fractional Anisotropy (FA), the Axial and Radial Diffusivity (AD, RD) or the Mean Diffusivity (MD) were defined [1.5]. Even at the early stages of DT-MRI, it was clear that the Gaussian assumption had important limitations. It provided a useful tool allowing clinical studies, but the underlying diffusion processes were not accurately described because of the over-simplified fitting, so that more evolved techniques with more degrees-of-freedom naturally arose, such as High Angular Resolution Diffusion Imaging [1.6, 1.7, 1.8, HARDI] or Diffusion Kurtosis Imaging [1.9, DKI]. It seems obvious that more degrees-of-freedom require more diffusion images to be acquired, but the requirement of an accurate angular resolution also implies the need for a finer angular contrast, which translates in the need for stronger gradients to probe diffusion, i.e., higher b-values [1.10].

The trend over the last decade has consisted in acquiring a large number of diffusion-weighted images distributed over several shells together with moderate-to-high b-values to estimate more advanced diffusion descriptors, such as the Ensemble Average diffusion Propagator [1.11, 1.12, EAP]. This leads to a completely model-free, non parametric approach for diffusion that can accurately describe most of the relevant phenomena associated to diffusion.

The most straightforward way of estimating the EAP is Diffusion Spectrum Imaging [1.11, DSI], that relies on the dense sampling of the q-space for discrete Fourier transformation. Hence, it requires a huge number of images to avoid aliasing artifacts and attain a decent accuracy, which makes it not so appealing in practice. As a consequence, alternative techniques aim to parametrically reconstruct the EAP from reduced samplings of the q-space, most of them related to the recent advances in compressed sensing and sparse reconstruction [1.13, 1.14]. In practice, some multi-shell reconstruction techniques may be used to compute the EAP, typically as a superposition of the integrals analytically computed for each basis function. Some of the most prominent methods are *Hybrid Diffusion Imaging* [1.15, HYDI], the *multiple q-shell diffusion propagator imaging* [1.16, 1.17, mq-DPI], the *Bessel Fourier Orientation Reconstruction* [1.18, BFOR], the *directional radial basis functions* [1.19,

RBFs], or the *Simple Harmonic Oscillator Based Reconstruction and Estimation* [1.20, SHORE]. More recently, the *Mean Apparent Propagator MRI* [1.12, MAP-MRI] and its improved version, the so-called *Laplacian-regularized MAP-MRI* [1.21, MAPL], have gained interest among the community due to the compelling results demonstrated in several clinical trials [1.22].

There is no doubt the EAP provides rich and valuable anatomical information about the diffusion process, though such amount of information may result overwhelming and difficult to integrate within clinical studies. This pitfall is usually circumvented by computing some sort of radial averaging of the EAP to obtain scalar measures directly related to the characteristics of diffusion. These measures act as biomarkers candidates aimed at describing diffusivity, anisotropy, intra-cellular vs. extra-cellular water movement, etcetera. Some prominent examples in this sense are the probability of zero displacement (or return-to-origin probability, RTOP), the mean-squared displacement (MSD), the q-space inverse variance (QIV), or the return-to-plane and return-to-axis probabilities (RTPP, RTAP) [1.23, 1.24, 1.19].

Although the use of these measures is not generalized among the clinical community, there is a growing interest in the exploration of their potential clinical applicability. To date, the relevance of scalar descriptors of the brain micro-structure has been proved on both *ex vivo* [1.25, 1.12, 1.26] and *in vivo* studies of healthy and diseased subjects [1.27, 1.23, 1.22, 1.28, 1.29, 1.30]. In particular, RTOP has also demonstrated to be a better indicator for cellularity and diffusion restrictions than the DTI-related mean diffusivity (MD) [1.22] and, together with MSD, a proper measure for the assessment of myelination [1.31]. These results were later confirmed by [1.29], where the authors reinforced the hypothesis on RTOP to have greater sensitivity to reflect cellularity and restricted diffusion.

The obvious drawback of this methodology is the need of acquiring very large data sets with many q-space samples in different shells (some of them with very large b-values, which implies an additional problem due to noise, eddy currents, non-linear effects, etcetera). Even when sophisticated non-linear techniques based on compressed sensing are used, the number of gradient images to be acquired vastly exceeds that needed for single-shell protocols like DT-MRI or HARDI. This is clearly a practical limitation: a large number of samples goes together with longer scanning times, subject movement, and patient discomfort that make them unfit for clinical practice and for many clinical studies. Besides, some methods require b-values that not every commercial MRI device is prepared to acquire.

The present paper delves into the question if scalar measures such as RTOP, RTPP, or RTAP are intrinsically tied up to the computation of the whole, model-free EAP. More precisely, we hypothesize that a constrained model for radial diffusion may reveal valuable information using simpler acquisition protocols, so that a set of *apparent* scalar measures probed at one single shell will exhibit a sensitivity to micro-structural changes comparable to *non-apparent* measures computed from the full EAP. The rationale behind this is that state of the art EAP techniques probe (instead of modeling) the actual radial behavior of the diffusion signal just to subsequently collapse it in a radial integral (average), so that the extra information provided by multi-shell acquisitions is indeed marginalized. In other words, we intend to substitute the whole average for all b-values with an *apparent* value at a single b-value.

To test our hypothesis, we have first reformulated RTOP, RTPP, and RTAP for a single-shell acquisition based on different diffusion models, yielding to closed form expressions and numerical implementations that are both robust and fast to compute. These *apparent*

measures at one shell are compared with their state of the art counterparts based on the whole EAP in a set of experiments with real data sets. The figure of merit in such comparison is the ability to discern voxels with different anisotropy configurations, i.e., the sensitivity to micro-structural changes.

1.2 Background

1.2.1 The Diffusion signal

The EAP, $P(\mathbf{R})$, is the three dimensional Probability Density Function (PDF) of the water molecules inside a voxel moving an effective distance $\mathbf{R}$ in an effective time τ. It is related to the normalized magnitude image provided by the MRI scanner, $E(\mathbf{q})$, by the Fourier transform [1.32]:

$$P(\mathbf{R}) = \int_{\mathbb{R}^3} E(\mathbf{q}) e^{-2\pi j \mathbf{q}\cdot\mathbf{R}} d\mathbf{q} = \mathcal{F}\left\{|E(\mathbf{q})|\right\}(\mathbf{R}). \tag{1.1}$$

The inference of exact information on the $\mathbf{R}$–space would require the sampling of the whole $\mathbf{q}$–space to use the Fourier relationship between both spaces.

In order to obtain a closed-form analytical solution from a reduced number of acquired images, a model for the diffusion behavior must be adopted. The most common techniques rely on the assumption of a Gaussian diffusion profile and a steady state regime of the diffusion process that yields to the well-known Diffusion Tensor (DT) approach. Alternatively, a more general expression for $E(\mathbf{q})$ can be used [1.8]:

$$E(\mathbf{q}) = \exp\left(-4\pi^2 \tau q_0^2 D(\mathbf{q})\right) = \exp\left(-b \cdot D(\mathbf{q})\right), \tag{1.2}$$

where the positive function $D(\mathbf{q}) = D(q_0, \theta, \phi) > 0$ is the Apparent Diffusion Coefficient (ADC), $b = 4\pi^2\tau\|\mathbf{q}\|^2$ is the so-called b-value and $q_0 = \|\mathbf{q}\|$, and θ, ϕ are the angular coordinates in the spherical system. According to [1.33], in the mammalian brain, this mono-exponential model is predominant for values of b up to $2,000\text{s/mm}^2$ and it can be extended to higher values (up to $3,000\text{s/mm}^2$) if appropriate multi-compartment models of diffusion are used.

1.2.2 Advanced diffusion scalar measures

Although the EAP provides the global information about the diffusion in every voxel of the brain, that information must be properly translated to be used in clinical trials or to study the features of particular tissues. Regardless of the method used to estimate the EAP, it must provide a set of metrics to inspect the changes of complex brain micro-structures, e.g., multiple compartments or restricted diffusion. Some of the most relevant measures usually derived from the EAP are:

1. **Return-to-origin probability (RTOP):** also known as *probability of zero displacement*, it is related to the probability density of water molecules that minimally diffuse within the diffusion time τ. It is known to provide relevant information about the white

matter structure [1.34, 1.23, 1.24], and has demonstrated to be a better indicator for cellularity and diffusion restrictions than the DTI-related mean diffusivity (MD) [1.22]. It is defined as the value of $P(\mathbf{R})$ at the origin, related to the volume of the signal $E(\mathbf{q})$:

$$\text{RTOP} = P(\mathbf{0}) = \int_{\mathbb{R}^3} E(\mathbf{q}) d\mathbf{q}. \tag{1.3}$$

2. **Return-to-plane probability (RTPP)**, defined as:

$$\text{RTPP} = \int_{\mathbb{R}^2} P(\mathbf{R}_\perp) d\mathbf{R}_\perp = \int_{\mathbb{R}} E(q_{||}) dq_{||}, \tag{1.4}$$

where $q_{||}$ denotes the direction of maximal diffusion. It is known to be a good indicator of restrictive barriers in the axial orientation, and it is related to the mean pore length [1.12].

3. **Return-to-axis probability (RTAP)**, defined as:

$$\text{RTAP} = \int_{\mathbb{R}} P(R_{||}) dR_{||} = \int_{\mathbb{R}^2} E(\mathbf{q}_\perp) d\mathbf{q}_\perp, \tag{1.5}$$

where $\mathbf{q}_\perp$ is the set of directions perpendicular to $\mathbf{q}_{||}$ (the one with maximal diffusion). It is also a directional scalar index and an indicator of restrictive barriers in the radial orientation. According to [1.12], RTPP and RTAP values can be seen as the *decomposition* of the RTOP values into two components, parallel and perpendicular to the maximum diffusion.

Remarkably, each one of these measures is computed in the $\mathbf{q}$-space as an integral in either $\mathbb{R}$, $\mathbb{R}^2$, or $\mathbb{R}^3$, which in the spherical coordinates system translates to an integral over the radial coordinate $q \equiv \|\mathbf{q}\|$ that averages the measured signal $E(\mathbf{q})$ over all shells.

1.3 Methods

1.3.1 Diffusion measures from single shell acquisitions

The estimation of a given magnitude is always a trade-off between the available data and the complexity of the model. In this case, we consider a single shell acquisition compatible with HARDI: moderated-to-high b-value (ranging from $2,000\text{s/mm}^2$ to $3,000\text{s/mm}^2$) and moderated-to-large number of gradients. Since the amount of data is reduced, we are forced to assume a restricted diffusion model consistent with single-shell acquisitions: the ADC will be roughly independent from the radial direction within the range of b-values probed, so that $D(\mathbf{q}) = D(\theta, \phi)$. This way Eq. (1.2) becomes:

$$E(\mathbf{q}) = E(q_0, \theta, \phi) = \exp\left(-4\pi^2 \tau q_0^2 \, D(\theta, \phi)\right). \tag{1.6}$$

With this model, the radial integral in q that defines all the previously introduced measures can be analytically computed without the need to actually sample q itself. The corresponding formulations can be simplified accordingly:

1. **RTOP:** By using the simplification in Eq. (1.6), we can write Eq. (1.3) in spherical coordinates and integrate with respect to the radial component q_0:

$$\begin{aligned} \text{RTOP} &= \int_0^{\infty}\int_0^{2\pi}\int_0^{\pi} \exp(-4\pi^2\tau q_0^2 \cdot D(\theta,\phi)) q_0^2 \sin\theta \; d\phi \; d\theta \; dq_0 \\ &= \frac{1}{4}\frac{\sqrt{\pi}}{(4\pi^2\tau)^{3/2}} \int_S \frac{1}{D(\theta,\phi)^{3/2}} dS, \end{aligned} \tag{1.7}$$

   where $\int_S$ denotes the integral in the surface of a sphere S of radius one. This way, the integration in the whole $\mathbf{q}$-space in Eq. (1.3) reduces to the integration on the surface of a single shell.

2. **RTPP:** The diffusion signal $D(\mathbf{q})$ in the maximum diffusion direction is given by $D(r_0)$, with $r_0 = q_{||}$. Since that direction does not depend on q_0, we can integrate with respect to the radial component:

$$\begin{aligned} \text{RTPP} &= \int_{-\infty}^{\infty} \exp(-4\pi^2\tau q_0^2 D(r_0)) dq_0 \\ &= \sqrt{\frac{\pi}{(4\pi^2\tau)}}\sqrt{\frac{1}{D(r_0)}}. \end{aligned} \tag{1.8}$$

3. **RTAP:** Let θ' be the angle that parameterizes the equator normal to the maximum diffusion direction and $D(\theta')$ the diffusion signal at that equator. Once more, $D(\theta')$ does not depend on the radial component and the integral can be solved:

$$\begin{aligned} \text{RTAP} &= \int_0^{\infty}\int_0^{2\pi} \exp(-4\pi^2\tau q_0^2 D(\theta')) \; q_0 \; d\theta' \; dq_0 \\ &= \frac{1}{2\cdot 4\pi^2\tau} \int_0^{2\pi} \frac{1}{D(\theta')} d\theta'. \end{aligned} \tag{1.9}$$

   The original integral reduces to the line integral of a function in a plane perpendicular to the maximum diffusion direction.

Although the mono-exponential assumption in Eq. (1.6) may seem restrictive, it has been successfully adopted before for single-shell, HARDI models to accurately describe several predominant diffusion directions within the imaged voxel [1.35, 1.36, 1.8, 1.7]. Moreover, it allows to get rid of the dense sampling required by the original formulations of RTOP, RTPP, and RTAP, as long as the volumetric integrals over the whole q-space are replaced by surface integrals over one single shell.

On the other hand, the mono-exponential model will roughly hold only within a limited range around the measured b-value, but diffusion features will diverge for very different b-values. For this reason, the measures derived this way must be seen as *apparent* values at a given b-value, related to the original ones but dependent on the selected shell. In what follows, they will be referred to as **Apparent Measures Using Reduced Acquisitions (AMURA)**.

1.3.2 Numerical Implementation

We propose a robust numerical implementation of the integrals that define the *apparent* RTOP and RTAP, as well as the formula for the *apparent* RTPP, based on Spherical Harmonics (SH) expansions:

1. **RTOP:** the integral of a signal $H(\theta,\phi)$ over the surface of the unit sphere S relates to the 0–th order coefficient (DC component) of its SH series expansion, $C_{0,0}\{H(\theta,\phi)\}$:

$$C_{0,0}\{H(\theta,\phi)\} = \frac{1}{\sqrt{4\pi}}\int_S H(\theta,\phi)dS, \tag{1.10}$$

   so that the RTOP becomes:

$$\text{RTOP} \quad = \quad \frac{1}{(4\pi)^2\tau^{3/2}}\, C_{0,0}\left\{(D(\theta,\phi))^{-3/2}\right\}. \tag{1.11}$$

2. **RTPP:** The value of RTPP previously defined in Eq. (1.8) depends on $D(r_0)$, the ADC evaluated at the direction of maximum diffusion. In order to avoid the variability that a maximum operator may introduce, we calculate the index over a regularized version of $D(\theta,\phi)$. Let us call $D_{\text{SH}}(\theta,\phi)$ a version of the original diffusion signal regularized using SH. Then, we can write the RTPP as

$$\text{RTPP} \quad = \quad \frac{1}{\sqrt{4\pi\tau}}\frac{1}{\sqrt{D_{\text{SH}}(\mathbf{r}_0)}}, \tag{1.12}$$

   where $\mathbf{r}_0$ denotes the maximum diffusion direction.

3. **RTAP:** The value of $\int_0^{2\pi} D(\theta')^{-1}d\theta'$ is the line integral of $D(\theta')^{-1}$ along an equator perpendicular to the direction of maximum diffusion $\mathbf{r}_0$, i.e., the Funk-Radon Transform (FRT) of $D(\theta')^{-1}$ evaluated at $\mathbf{r}_0$, $\mathcal{G}\{D\}(\mathbf{r}_0)$ [1.37]:

$$\text{RTAP} = \frac{1}{2\cdot 4\pi^2\tau}\mathcal{G}\left\{\frac{1}{D(\theta')}\right\}(\mathbf{r}_0) = 2\Psi(\mathbf{r}_0), \tag{1.13}$$

   where $\Psi(\mathbf{r})$ is the pQ-Balls whose definition and SH-based numerical implementation are addressed in [1.38, 1.39].

An overview of AMURA, together with the specific numerical implementation of each *apparent* measure, is presented in Table 1.1.

1.4 Experiments and results

1.4.1 Setting-up of the experiments

As explained above, AMURA measures rely on the expansion of spherical functions at a given shell in the basis of SH, for which the implementation described in [1.40] is used: even SH orders up to 6 are fitted with a Laplace-Beltrami penalty $\lambda = 0.006$. RTAP is computed from

Measure	Definition	Numerical Implementation
RTOP	$= \frac{1}{4}\frac{\sqrt{\pi}}{(4\pi^2\tau)^{3/2}}\int_S \frac{1}{D(\theta,\phi)^{3/2}}dS$	$= \frac{1}{(4\pi)^2\tau^{3/2}} C_{0,0}\left\{(D(\theta,\phi))^{-3/2}\right\}$
RTPP	$= \frac{1}{\sqrt{4\pi\tau}}\frac{1}{\sqrt{D(\mathbf{r}_0)}}$	$= \frac{1}{\sqrt{4\pi\tau}}\frac{1}{\sqrt{D_{\text{SH}}(\mathbf{r}_0)}}$
RTAP	$= \frac{1}{2\cdot 4\pi^2\tau}\int_0^{2\pi}\frac{1}{D(\theta')}d\theta'$	$= 2\Psi(\mathbf{r}_0)$, see [1.39]

Tab. 1.1.: Survey of the q-space measures gathered by AMURA, along with their specific numerical implementations.

pQ-Balls with this same design for SH expansions [1.39]. For the sake of repeatability, *in vivo* data have been chosen exclusively from publicly available databases:

1. From the Human Connectome Project (HCP)[1], five volumes were chosen: MGH 1007, MGH 1010, MGH 1016, MGH 1018 and MGH 1019, acquired in a Siemens 3T Connectome scanner with 4 different shells at b $= \{1,000,\ 3,000,\ 5,000,\ 10,000\}$ s/mm^2, with $\{64, 64, 128, 256\}$ gradient directions each, in-plane resolution 1.5 mm^2, and slice thickness 1.5 mm. Acquisition parameters are TE=57 ms and TR=8800 ms. The acquisition included 40 different baselines that were averaged to improve their SNR[2].

2. From the Public Parkinson's Disease database (PPD)[3], 53 subjects from a cross-sectional Parkinson's Disease (PD) study comprising 27 patients together with 26 age, sex, and education-matched control subjects. Data were acquired on a 3T head-only MR scanner (Magnetom Allegra, Siemens Medical Solutions, Erlangen, Germany) operated with an 8-channel head coil. Diffusion-weighted (DW) images were acquired with a twice-refocused, spin-echo sequence with EPI readout at two distinct b-values b $= \{1,000,\ 2,500\}$ s/mm^2, and along 120 evenly spaced encoding gradients. For the purposes of motion correction, 22 unweighted (b = 0) volumes, interleaved with the DW images, were acquired. Acquisition parameters are TR=6800 ms, TE=91 ms, and FOV=211 mm^2, no parallel imaging and 6/8 partial Fourier were used. More information can be found in [1.42].

[1] Data obtained from the Human Connectome Project (HCP) database (`https://ida.loni.usc.edu/login.jsp`). The HCP project (Principal Investigators: Bruce Rosen, M.D., Ph.D., Martinos Center at Massachusetts General Hospital; Arthur W. Toga, Ph.D., University of Southern California, Van J. Weeden, MD, Martinos Center at Massachusetts General Hospital) is supported by the National Institute of Dental and Craniofacial Research (NIDCR), the National Institute of Mental Health (NIMH) and the National Institute of Neurological Disorders and Stroke (NINDS). HCP is the result of efforts of co-investigators from the University of Southern California, Martinos Center for Biomedical Imaging at Massachusetts General Hospital (MGH), Washington University, and the University of Minnesota.

[2] The SNR of each of the individual baselines is high enough to make a Gaussian approximation feasible with a small error. Under this approximation we can assure that the average operator provides an unbiased output image [1.41].

[3] Acquired at the Cyclotron Research Centre, University of Liège. Available: `https://www.nitrc.org/frs/?group_id=835`.

Volume	Slice numbers	Volume	Slice numbers
MGH 1007	42, 52, 65	MGH 1018	31, 41, 51
MGH 1010	46, 54, 60	MGH 1019	40, 50, 64
MGH 1016	42, 55, 68		

Tab. 1.2.: Selected slices from each diffusion volume from the HCP.

1.4.2 Consistency of *apparent*, single-shell measures

Since AMURA are intended to reveal similar micro-structural changes as multi-shell EAP estimators, each one of the *apparent* RTOP, RTPP, and RTAP are expected to correlate well with their multi-shell counterparts, meaning the anatomical information they assess is closely related. To check this point, AMURA is compared against three state of the art EAP estimation techniques not requiring dense samplings of the q-space: RBFs with constrained ℓ_2 regularization as described in [1.19], MAP-MRI with anisotropic basis and radial order 6 [1.12], and MAPL with anisotropic basis, radial order 8, and regularization weighting $\lambda = 0.2$ [1.21].

In order to attain an affordable complexity for this experiment, the study is restricted to three different axial slices for each selected volume as depicted in Table 1.2.

For each volume and slice, the three measures are calculated with RBFs, MAP-MRI, and MAPL using either 3 shells (b $= \{1,000,\ 3,000,\ 5,000\}$ s/mm^2), or 2 shells (b $= \{1,000,\ 3,000\}$ s/mm^2). AMURA are calculated using one single shell at either b $= 3,000$s/mm^2 or b $= 5,000$s/mm^2. This sum up 8 different calculations of each of RTOP, RTPP and RTAP for each volume and slice as illustrated in Fig. 1.1, where those voxels with FA bellow 0.2 have been masked.

A simple visual inspection suggests that indeed all the 8 different computations of RTOP, RTPP, and RTAP provide congruent information about the anatomies imaged. This qualitative evidence is confirmed in Table 1.3, where the correlation coefficients ρ between each pair of measures are computed. In precise terms, let $\{r_i\}_{i=1}^N$ be the values of the measure defined at each row of Table 1.3, and $\{c_i\}_{i=1}^N$ the values of the measure defined at each column; the set $i = 1 \dots N$ gathers all those voxels with FA above 0.2. Then:

$$\rho_{rc} = \frac{\sum_{i=1}^{N} (r_i - \bar{r})\,(c_i - \bar{c})}{(N-1)\sigma_r\ \sigma_c}, \text{ for: } \bar{x} = \frac{1}{N}\sum_{i=1}^{N} x_i \text{ and } \sigma_x = \frac{1}{N-1}\sum_{i=1}^{N} (x_i - \bar{x})^2 . \qquad (1.14)$$

Results for RTOP show a strong correlation, in some cases over 90%, between the measure estimated with AMURA and the calculation given by the other techniques, particularly those based on MAP. It is worth noticing that AMURA-RTOP correlates better with MAP-RTOP than RBF-RTOP does, even when RBF is computed from 3 shells (left column) and AMURA is using as few as 64 gradients (b $= 3,000$s/mm^2) or 128 gradients (b $= 5,000$s/mm^2) in one single shell.

For RTPP, though the absolute correlations between each pair of computations are clearly weaker than for RTOP, AMURA still exhibits a higher consistency towards MAP-based

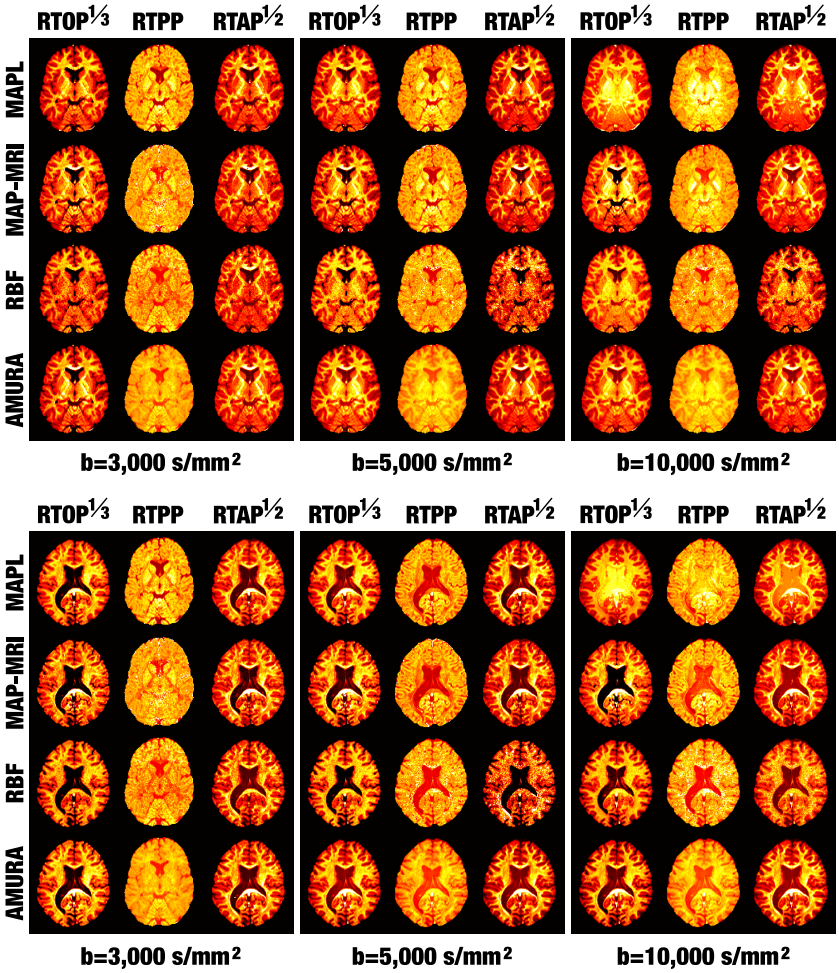

Fig. 1.1.: Visual assessment of the consistency of AMURA. (Top) Slice 42 of the MGH1016 volume from HCP; (Bottom) Slice 51 of the MGH1018. AMURA is calculated with one single shell at the specified b-value. MAPL, MAP-MRI and RBF are calculated using either 2 or 3 shells at the maximum b-value specified. For the sake of visual comparison, RTOP and RTAP have been gamma-corrected as specified.

measures than RBF does. At the sight of Fig. 1.1, the noisier nature of RTPP could probably explain the net decrease in the correlations. Interestingly, the computation of RTPP with 2 shells seems more consistent between multi-shell techniques than it is with 3 shells. For example, the correlation between RBF-RTPP and MAPL-RTPP falls as low as 10%.

Since RTAP provides *cleaner* maps than RTPP (see Fig. 1.1), the discussion becomes similar to the case of RTOP: the overall correlations between the different computations are much higher in this case, with AMURA correlating up to 90% with MAPL and MAP-MRI. Once again, RBF-RTAP seems less consistent with MAP-like-RTAP than AMURA-RTAP.

Summarizing, AMURA provide information that closely resembles that computed with multi-shell methods. Moreover, AMURA are more consistent with MAP-like measures than other multi-shell methods like RBF. This might suggest that the deviations introduced by the election of different basis functions and different numerical schemes in each multi-shell

		3 shells			2 shells		
		RBF	**MAPL**	**MAP-MRI**	**RBF**	**MAPL**	**MAP-MRI**
RTOP	**AMURA** 3k	0.7636	0.8616	**0.9202**	0.8051	**0.9047**	**0.9027**
	AMURA 5k	0.7629	**0.9538**	**0.9151**	0.7264	0.8950	0.8278
	RBF	–	0.7320	0.6408	–	0.7746	0.7136
	MAPL	–	–	0.8356	–	–	0.7334
RTPP	**AMURA** 3k	0.2565	**0.7035**	0.6811	0.6464	**0.7497**	0.6423
	AMURA 5k	0.2295	0.6077	0.4530	0.3155	0.3884	0.2415
	RBF	–	0.1041	0.1139	–	0.7089	0.6096
	MAPL	–	–	**0.9416**	–	–	**0.8678**
RTAP	**AMURA** 3k	0.4918	0.8800	**0.9305**	0.7846	0.8955	**0.9341**
	AMURA 5k	0.5145	0.9382	**0.9406**	0.8009	0.8993	**0.9049**
	RBF	–	0.4740	0.4706	–	0.7739	0.8170
	MAPL	–	–	0.8885	–	–	0.8451

Tab. 1.3.: Correlation coefficients between the different methods to estimate RTOP, RTPP and RTAP. The higher the better. AMURA are computed from one single shell at either $b = 3,000 s/mm^2$ (3k) or $b = 5,000 s/mm^2$ (5k). Multi-shell methods are always compared between them with the same number of shells (2 or 3).

method could indeed surpass the error AMURA introduce as a consequence of modeling (instead of sampling) the radial behavior of $E(\mathbf{q})$.

1.4.3 Sensitivity of *apparent* single-shell measures to tissue properties

Though AMURA provide anatomical maps that closely resemble those yielded by multi-shell methods (see Fig. 1.1), it is not necessarily implied that they have the same capabilities to distinguish analogous tissue properties. Such capabilities are first put to the test by means of a classification problem where two classes are defined depending on the values of either RTOP, RTPP, or RTAP computed from MAPL with 4 shells, see Fig. 1.2. This way, MAPL becomes a bronze standard given its high consistency with both MAP-MRI and AMURA (it shows also the strongest correlations with RBF, see Table 1.3), and assuming it probes actual micro-structural information. The problem design is as follows:

1. Once the background of the image is removed, the histogram of either RTOP, RTPP, or RTAP is computed from the bronze standard (MAPL). A threshold is selected in the valley right after the main lobe for each MAPL-measure (for RTOP: $2 \cdot 10^6 mm^{-3}$; for RTPP: $90 mm^{-1}$; for RTAP: $1.5 \cdot 10^4 mm^{-2}$). Classes 1 and 2 are defined as either below or above this threshold, see Fig. 1.2(A).

2. From each of the other methods (MAP-MRI, RBF, AMURA, and MAPL itself with less that 4 shells), RTOP, RTPP, and RTAP are computed and used as discriminant features of each voxel.

3. In case a given method were actually providing the exact same micro-structural information as the bronze standard, such features should suffice to mimic the exact same classification designed in Fig. 1.2(A). Otherwise, both false positives (class 1

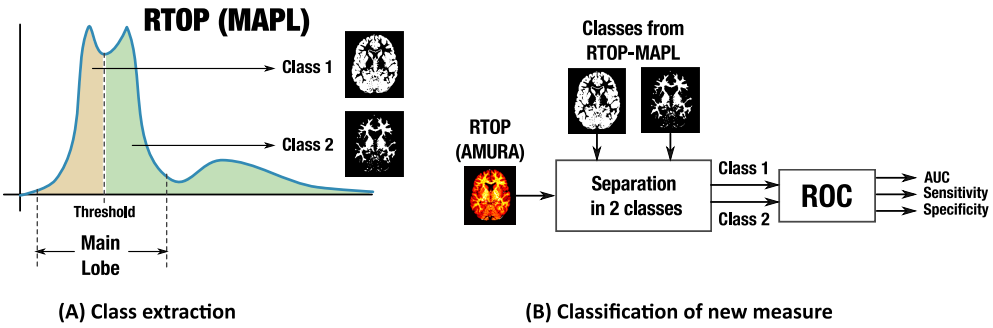

Fig. 1.2.: Conceptual description of the problem designed to test the sensitivity of AMURA to micro-structural changes. (A) The pixels in the image are split into 2 classes by thresholding the corresponding MAPL measure (RTOP in the example). (B) Each one of the methods to be tested: MAPL, MAP-MRI, RBF, or AMURA (AMURA in the example) is used to compute this same measure, and a ROC curve is calculated with the classes defined in (A) as the target.

voxels tagged as class 2) and false negatives (class 2 voxels tagged as class 1) will appear that reflect discrepancies in the information measured.

4. Such discrepancies are quantified by means of a Receiver Operating Characteristics (ROC) curve: for a given measure, corresponding values are computed using each method; these values are further classified using a *moving* threshold ranging from the minimum computed value to its maximum. This way, each value of the *moving* threshold defines a classification that is compared to the bronze standard in step 1 in search for false positives and false negatives. The ROC curve is the graphic relating these two rates as the threshold moves. Finally, three standard Figures of Merit (FoM) related to the ROC are reported: the area under the curve (AUC), the sensitivity at the optimum threshold, and the specificity at the optimum threshold, see Fig. 1.2(B).

The results are gathered, respectively, in Table 1.4 (RTOP), Table 1.5 (RTPP), and Table 1.6 (RTAP). In all cases, the closer to 1 is the better. While AMURA are computed from one shell, the other methods use either 2 shells (at maximum b $= 3,000$s/mm^2), 3 shells (at maximum b $= 5,000$s/mm^2) or 4 shells (at maximum b $= 10,000$s/mm^2).

As can be seen, AMURA scores high FoMs in all cases, even above those obtained with MAP-MRI (which is a non-improved version of MAPL itself). For example, the *apparent* value of AMURA-RTOP at any shell scores higher than any of the computations from MAP-MRI regardless on the number of shells it uses (Table 1.4). Indeed, this same comment holds true for the other two measures, with the exception of the specificity of RTPP with MAP-MRI at 4 shells (Table 1.5) and the specificity of RTAP with MAP-MRI at 4 shells (Table 1.6). In the same way as in Table 1.3, the measures computed with RBF tend to deviate from those based on MAP even if the number of shells increases. Finally, it is worth noticing that the *apparent* values obtained with AMURA at either b $= 3,000$s/mm^2 or b $= 5,000$s/mm^2 score pretty close to MAPL when the outermost shell at b $= 10,000$s/mm^2 is suppressed from the bronze standard.

Summarizing, not only AMURA strongly correlate with measures derived from multi-shell techniques, but they seem to distinguish tissue properties as well as the other methods do.

		MAPL	AMURA	RBF	MAP-MRI
AUC	b=3000	0.8796	0.8285	0.6887	0.6839
	b=5000	**0.9343**	**0.9205**	0.7251	0.7035
	b=10000	**1.0000**	**0.9771**	0.7762	0.7219
		MAPL	**AMURA**	**RBF**	**MAP-MRI**
Sensitivity	b=3000	0.8114	0.7527	0.6108	0.6123
	b=5000	**0.8802**	**0.8520**	0.6480	0.6378
	b=10000	**1.0000**	**0.9213**	0.7318	0.6402
		MAPL	**AMURA**	**RBF**	**MAP-MRI**
Specificity	b=3000	**0.9114**	0.8367	0.7915	0.8109
	b=5000	**0.9454**	**0.9334**	0.8480	0.8285
	b=10000	**1.0000**	**0.9623**	**0.9359**	0.8788

Tab. 1.4.: ROC FoMs for RTOP (the closer to 1, the better). MAPL with 4 shells at a maximum $b = 10,000 s/mm^2$ is the bronze standard.

		MAPL	AMURA	RBF	MAP-MRI
AUC	b=3000	0.7884	0.6900	0.5736	0.5550
	b=5000	**0.8647**	0.7657	0.4632	0.6038
	b=10000	**1.0000**	**0.8261**	0.4735	0.6488
		MAPL	**AMURA**	**RBF**	**MAP-MRI**
Sensitivity	b=3000	0.6761	0.5803	0.5008	0.5000
	b=5000	**0.7516**	0.6332	0.4807	0.5295
	b=10000	**1.0000**	**0.7077**	0.4828	0.5677
		MAPL	**AMURA**	**RBF**	**MAP-MRI**
Specificity	b=3000	**0.7828**	0.7162	0.7260	0.6608
	b=5000	**0.8440**	0.7469	0.5171	0.7442
	b=10000	**1.0000**	**0.7713**	0.5440	**0.8284**

Tab. 1.5.: ROC FoMs for RTPP (the closer to 1, the better). MAPL with 4 shells at a maximum $b = 10,000 s/mm^2$ is the bronze standard.

Interestingly, the micro-structural properties described by multi-shell techniques do not seem to *converge* even if the q-space sampling is improved.

1.4.4 Potential of *apparent* single-shell measures in clinical setups

The previous experiment relies on an artificial classification of voxels depending on MAPL as a bronze standard. To further test the capabilities of AMURA to probe tissue properties, we have devised an additional experiment involving the clinical data in the PPD database. Though PD is known to affect the substantia nigra or the gray matter more than the *standard* white matter tracts commonly studied in group-wise analyses based on DMRI, significant differences have also been reported in several white matter regions such as the corpus callosum, the corticospinal tract, or the fornix [1.43]. Accordingly, we have focused on commonly-studied white matter tracts that are segmented for each volume in the PDD

		MAPL	AMURA	RBF	MAP-MRI
AUC	b=3000	**0.9218**	**0.8959**	0.7338	0.7592
	b=5000	**0.9537**	**0.9446**	0.6543	0.7717
	b=10000	**1.0000**	**0.9755**	0.7456	0.7993
		MAPL	**AMURA**	**RBF**	**MAP-MRI**
Sensitivity	b=3000	0.8516	0.8204	0.6309	0.6844
	b=5000	**0.8864**	**0.8808**	0.5911	0.6997
	b=10000	**1.0000**	**0.9223**	0.6900	0.7430
		MAPL	**AMURA**	**RBF**	**MAP-MRI**
Specificity	b=3000	**0.9232**	0.8848	0.8266	0.8473
	b=5000	**0.9480**	**0.9152**	0.6665	0.8612
	b=10000	**1.0000**	**0.9482**	0.7728	**0.9205**

Tab. 1.6.: ROC FoMs for RTAP (the closer to 1, the better). MAPL with 4 shells at a maximum $b = 10,000 s/mm^2$ is the bronze standard.

database based on the ENIGMA-DTI template[4] [1.44] and the JHU WM atlas [1.45] as follows:

1. The FA is calculated as a reference value using MRTRIX[5] for $b = 1,000 s/mm^2$. Its value is registered against the ENIGMA-DTI FA template using deformable image registration based on the local cross-correlation between the images [1.46].

2. The JHU WM atlas classifies 48 disjointed white matter regions in the image space of the ENIGMA-DTI template. Their segmentations are back-projected onto the image space of each subject in the PDD database using the output deformation field of the registration. Working on the original image space avoids interpolation artifacts as well as side effects induced by the higher resolution of the ENIGMA-DTI template as compared to the PDD subjects.

3. The ENIGMA-DTI template comprises segmentations of both the whole white matter tracts and their FA skeletons. Back-projection is repeated for both segmentations, hence both a full segmentation of each tract and its pseudo-skeleton (central core) is available in the original image space (see Fig 1.3).

4. Outliers are removed from the segmentations by eliminating those voxels with abnormal values (i.e. values outside the range $[0, 1]$) of the FA and "Westin's scalars", C_p, C_l, C_s [1.5].

Each segmented tract is characterized by one single scalar measure: for AMURA, the *apparent* RTOP, RTPP, and RTAP at $b = 2,500 s/mm^2$ are averaged over each pseudo-skeleton. As in the previous section, their MAPL counterparts (using the 2 available shells) are targeted to as the state of the art. Additionally, a tensor model-driven version of the indices (at $b = 2,500 s/mm^2$) is tested as a sort of end of scale (see Appendix for the implementation details). Finally, the raw FA is also included in the analysis since it is the standard index to test in group studies [1.43].

[4]ENIGMA project web page: `http://enigma.ini.usc.edu/`. Template data and processing protocols for DTI: `https://www.nitrc.org/projects/enigma_dti`.
[5]Available at: `http://www.mrtrix.org`.

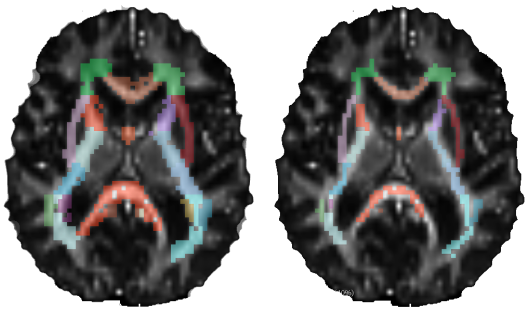

Fig. 1.3.: Registration-based segmentation of WM tracts of a control subject in the PDD database. (Left) Whole tracts. (Right) Pseudo-skeletons.

	Tensor	Tensor			MAPL		
	FA	RTOP	RTPP	RTAP	RTOP	RTPP	RTAP
GCC	0.087	0.357	0.028	0.174	0.557	0.021	0.322
BCC	0.055	0.165	0.749	0.130	0.334	0.420	0.172
SCC	0.014	0.135	0.036	0.030	0.164	0.015	0.069

	AMURA		
	RTOP	RTPP	RTAP
GCC	0.334	0.011	0.214
BCC	0.193	0.470	0.137
SCC	0.272	0.003	0.144

Tab. 1.7.: Two-sample t-tests for each measure and at each section of the corpus callosum (the lower the better). The p-values represent the probability that the measure has identical means for both controls and patients. Differences with statistical significance above 99% (resp. 95%) are highlighted in green (resp. amber).

Among the 48 tracts in the JHU WM, we have found statistically relevant differences mainly at the corpus callosum, which is in agreement with the related literature [1.43]. Table 1.7 shows the results for two-sample, pooled variance t-tests over Gaussian-corrected data between controls and patients for each of the measures considered and at each of the three sections of the corpus callosum segmented in the JHU WM (genu –GCC–, body –BCC–, and splenium –SCC–).

RTPP-related measures result in discriminant markers for this particular problem at the genu and the splenium of the corpus callosum. Remarkably, the raw FA is only able to find differences at the splenium, meanwhile RTAP and RTOP are unable to plot significant differences in a consistent way. To further understand why RTPP consistently finds significant differences, and how this is related to the information it measures, its actual distribution (PDF) inside the pseudo-skeleton of each segment (GCC, BCC, SCC) is estimated by using Parzen windowing in Fig. 1.4.

AMURA-RTPP is able to consistently distinguish between two different populations within each region of the corpus callosum. Meanwhile these two groups are also discriminated at the genu by the other approaches, this is not the case at the body and, above all, at the splenium, where even the MAPL-RTPP fails to find the valley between the two populations. Specifically,

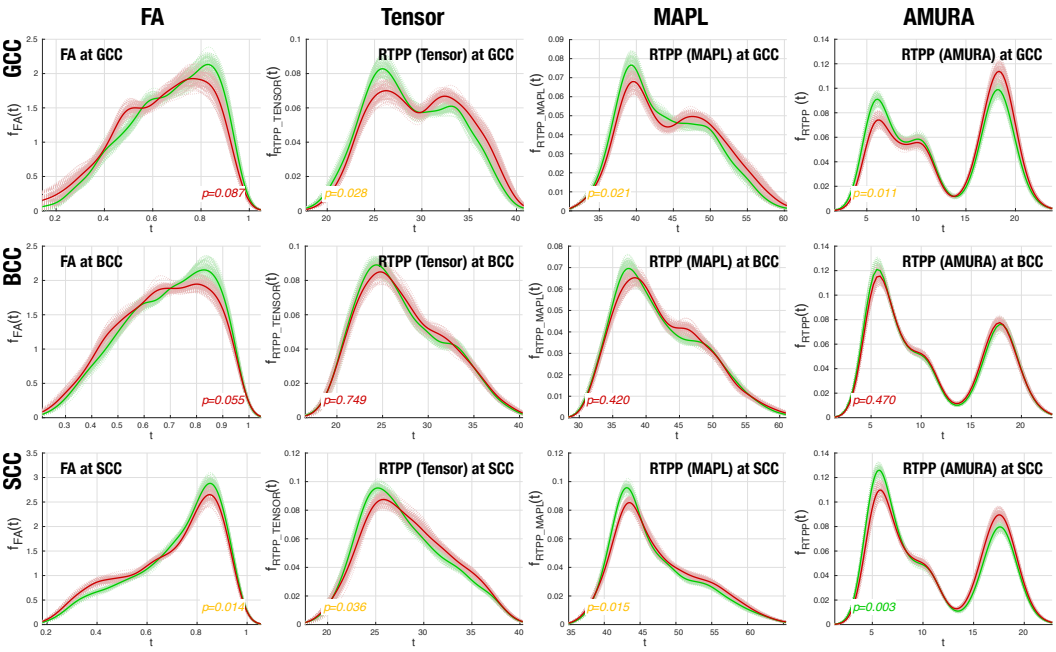

Fig. 1.4.: PDFs of RTPP computed from either the tensor model, MAPL, or AMURA (plus the FA) and within each of GCC, BCC, or SCC. (Red) Patients; (Green) Controls. (Dashed line) Bootstrap PDF from 100 iterations with 15 subjects each; (Solid line) Global PDF for all controls/patients. The p-values are referred to the t-tests reported in Table 1.7.

statistically significant differences between controls and patients appear wherever there is a change in the relative distribution of voxels between the two populations, i.e., at both the genu and the splenium. This provided, and anytime the separation between the two populations can be easily identified at AMURA-RTPP $= 27\text{mm}^{-1}$, the segmentation of the corpus callosum depending on its *apparent* RTPP is straightforward by thresholding. Such processing has been applied to each subject in the database (both controls and patients), and the resulting segmentations have been projected onto the image space of the ENIGMA template to compute the average segmentation shown in Fig. 1.5.

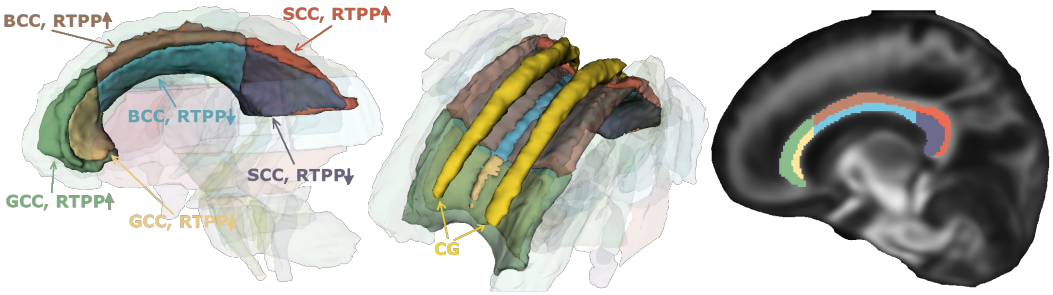

Fig. 1.5.: Average segmentation of the corpus callosum in the space of the ENIGMA template by AMURA-RTPP thresholding at 27 mm^{-1}. The cingulum (CG) is also rendered in the 3D view for reference purposes. A sagittal slice of the average FA of the PDD is also shown for reference.

The two populations identified by AMURA-RTPP correspond to a clean segmentation of the corpus callosum distinguishing between its lowermost (closer to the cerebrospinal fluid)

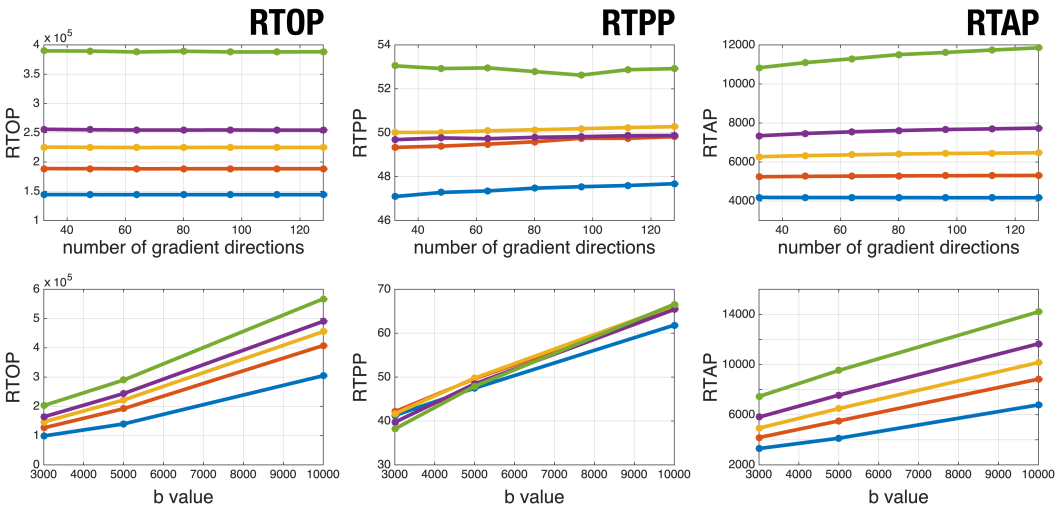

Fig. 1.6.: *Apparent* values of AMURA as a function of the number of acquired gradients (top) or the b-value (bottom) for subject MGH 1016. Each line correspond to a cluster of FA values computed from 5-fold fuzzy c-means. AMURA as a function of the number of gradients (top) are depicted at b $= 5,000$s/mm^2.

and its uppermost (closer to the cingulum) sections, so that we can reasonably argue that AMURA-RTPP is actually able to discern micro-structural properties that remain hidden with DT-related measures (see Fig. 1.4).

1.4.5 Variability of *apparent* measures depending on the acquisition parameters

Since AMURA provide *apparent* measures at a given shell, the question of how much these measures depend on the actual shell measured naturally arises. As long as AMURA have been designed for *reduced* acquisition protocols, it also makes sense to check their sensitivity to the number of diffusion samples taken at a given shell. To put this to the test, a set of experiments have been designed using volume MGH 1016: the variability with the b-value is probed by subsequently computing AMURA with each of the available shells at either b $= 3,000$s/mm^2, b $= 5,000$s/mm^2, or b $= 10,000$s/mm^2. For the variability with the number of diffusion gradients, we start with the 128 samples at b $= 5,000$s/mm^2 and uniformly subsample this set to obtain either 32, 48, 64, 80, 96, 112, or 128 diffusion directions subsets[6]. To plot such a huge amount of information, only those voxels of MGH 1016 with FA above 0.2 are included, and they are further clustered depending on their FA using fuzzy c-means. This results in 5 classes with centroids $C_L = \{0.24, 0.36, 0.51, 0.66, 0.86\}$, for which the median of each AMURA measure is used as a representative, see Fig. 1.6. AMURA seem extremely robust to the number of acquired gradients even in the case of very heavy subsamplings. This is as expected, since Fig. 1.6 shows mean values but not variances. On the contrary, all three measures show a clear dependency with the b-value since the assumption that

[6] A "uniform" subsampling of n gradients among the original 128 is here defined as those n directions that minimize the overall electrostatic repulsion energy amongst all $\binom{128}{n}$ combinations. The optimization is carried out using heuristic rules.

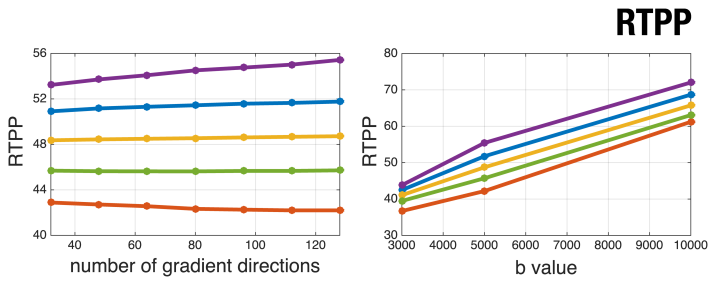

Fig. 1.7.: AMURA-RTPP as a function of the number of acquired gradients (left) or the b-value (right) for subject MGH 1016. Each line correspond to a cluster of RTPP values computed from 5-fold fuzzy c-means. AMURA-RTPP as a function of the number of gradients (left) is depicted at b $= 5,000$s/mm^2.

$D(\theta, \phi)$ is roughly constant holds only within a limited range of b-values. In any case, the monotonical behavior of each cluster is preserved for both RTOP and RTAP, i.e. an increasing value of the FA comes along with an increasing value of RTOP and RTAP for all shells. Since both RTOP and RTAP resemble anisotropy maps, see Fig. 1.1, this is as expected. This is not necessarily the case for RTPP, whose graphics for each cluster cross each other as the b-value varies. If the experiment is repeated for RTPP using a clustering of its own (i.e., by running fuzzy c-means over RTPP itself at b $= 5,000$s/mm^2, yielding five centroids $C_L = \{20.72, 22.80, 24.35, 25.92, 27.83\}$), a perfect monotonical behavior is of course obtained as shown in Fig. 1.7.

A similar test may be run over the multi-shell techniques. In this case we are interested in checking the variability of the measures depending on the number of shells used (either 2, 3, or 4). The same five volumes and 3 slices in Table 1.2 are used, and the fuzzy c-means clustering above described is repeated yielding centroids $C_L = \{0.24, 0.33, 0.45, 0.58, 0.76\}$. Fig. 1.8 demonstrates that indeed multi-shell measures do depend on the sampling scheme (number of shells).

Specifically, including the fourth shell at b $= 10,000$s/mm^2 heavily alters the measured RTOP, RTPP, and RTAP in all cases. Note that, while the monotonical behavior of RTOP and RTAP holds for MAP-like estimators, this is not always the case for RBF (which, in the light of this experiment, seems particularly unstable). As it was pointed out in the previous paragraph, RTPP is not necessarily expected to monotonically increase with the FA in any case.

1.4.6 Computational issues and execution times

AMURA relies on SH expansions computed as linear, regularized LS problems. On the contrary, multi-shell methods depend on heavily non-linear, sparsity-driven, possibly constrained optimization problems. The linear nature of LS usually yields to well-behaved, stable solutions, meanwhile non-linear optimization usually arises numerical issues.

Besides, the computational load of LS is noticeably more modest (it reduces to invert one single matrix for the whole volume or even the whole cohort), to the point that AMURA can be several orders of magnitude faster than multi-shell techniques. This is illustrated

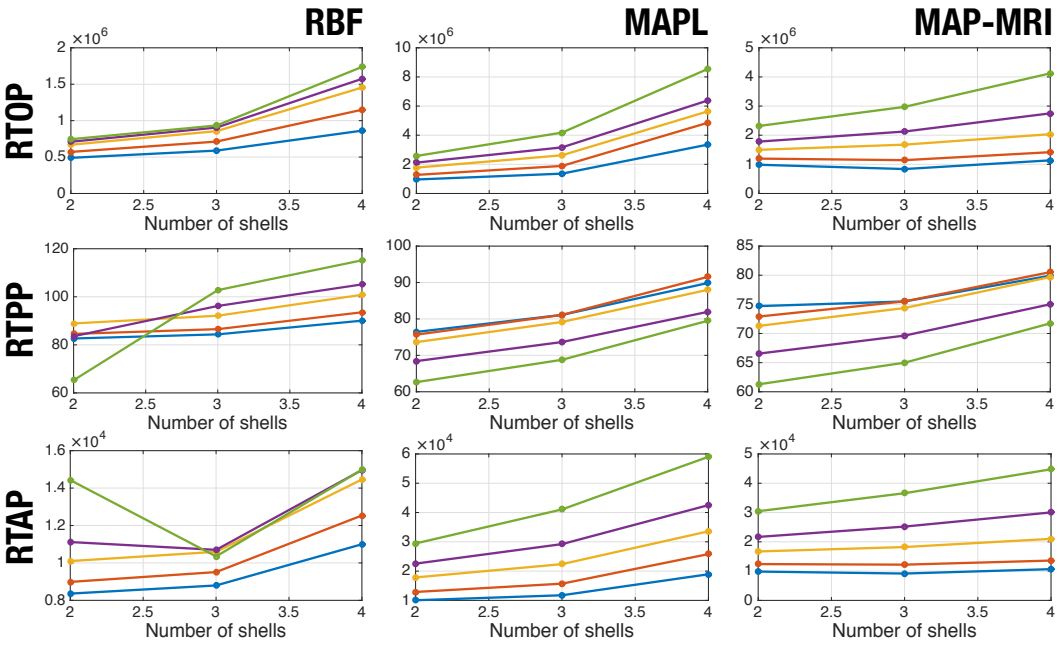

Fig. 1.8.: Measured values with multi-shell techniques as a function of the number of shells acquired. Each line correspond to a cluster from 5-fold fuzzy c-means.

Execution times			
Method	**Two shells**	**Three shells**	**Four shells**
RBFs	118h 10min	332h 40min	577h 12min
MAP-MRI	13h 43min	13h 46min	16h 20min
MAPL	2h 11min	2h 14min	2h 22min
AMURA	**6min 41s**	**7min 17s**	**8min 28s**

Tab. 1.8.: Estimated execution times for the calculation of the measures with different methods. One single volume (HCP MGH 1016) is processed.

here through volume MGH 1016 from the HCP. The measures of interest are computed on a quad-core Intel(R) Core(TM) i7-6700K 4.00GHz processor under Debian GNU/Linux 8.6 SO. The available code for RBFs[7] was run under MATLAB 2013b (The MathWorks, Inc., Natick, MA) and the DIPY 0.13.0 library[8] under Python 3.6.4 (scipy 1.0.0) was used for MAP-MRI and MAPL. AMURA is implemented in MATLAB without multi-threading to report the results in Table 1.8.

Though raw execution times are an ambiguous performance index (they can be dramatically improved, for example, via GPU acceleration), they give a reasonable idea of the complexity of each method. Note the reported times for most of the methods make them unfeasible to be used on practical studies. In the case of RBF, they range from 5 to 24 days per volume, something that goes beyond the capability of clinical groups. Even in the best of the cases, MAPL is 17 times slower than AMURA. In all the cases, most of the time is spent in calculating the EAP. In MAPL, for instance, only 0.6% of the calculation time corresponds

[7] `https://github.com/LipengNing/RBF-Propagator`.
[8] `http://nipy.org/dipy`.

to the measures, while the remaining 99.4% is spent in estimating the EAP. In the case of AMURA, 50% of the execution time corresponds to RTAP, since the estimation of the ODF is the most expensive operation, followed by RTPP, which takes 40% of the time. RTOP is the fastest measure, since it takes only 16s, 29s, and 54s for the different shells.

1.5 Discussion and conclusions

AMURA are not intend to approximate the exact same numeric parameters as multi-shell methods compute. On the contrary, their aim is inferring micro-structural information related to, and with comparable discrimination power as, that revealed by MAP-MRI, MAPL, or RBF. Fig. 1.1 and Table 1.3 evidence the anatomical consistency of AMURA, both visually and numerically. Tables 1.4, 1.5, and 1.6 confirm they are able to discriminate tissue properties in a similar way as multi-shell methods do.

With regard to the first issue, i.e. anatomical consistency, EAP-based measures explicitly account for the radial behavior of the diffusion signal, which is actually sampled. With AMURA, the radial behavior is not sampled but modeled as a mono-exponential decay. The hypothesis leading to the computation of the whole EAP should be, therefore, that the study of the whole EAP provides more specific/sensitive measures, i.e., there is certain anatomical information encoded in the radial behavior of the EAP that would remain hidden with AMURA. However, Table 1.3 highlights this is not always the case: different EAP-methods bring in less consistent results among them than some of them exhibit with AMURA for analogous measures (RTOP, RTPP, or RTAP). Paradoxically, the similarity between RBF and MAP-like methods even worsens as new shells with higher b-values are introduced.

As a first attempt to explain this behavior, we may recall that the measures computed are merely scalars, i.e., the complex information gathered in the whole 3-D domain of the EAP is somehow collapsed to one single number: the RTOP, for instance, is the value of the EAP at a single point (zero), which corresponds to the integration of the diffusion signal in the whole q-space, in a way that most of the information is lost in the average.

However, the averaging process behind the scalar measures does not explain why the corresponding outputs obtained from the different EAP-based methods do not converge to analogous values, or why the model-constrained AMURA measures seem to mimic MAPL values better than model-free, EAP-based MAP-MRI and RBF in Table 1.3. Moreover, as the number of shells and the number of samples per shell increase, MAPL, MAP-MRI, and RBF would be expected to converge to exactly the same values, since all of them estimate the same mathematical entity (the EAP) and all of them use the same mathematical description of the related measures (RTOP, RTPP, and RTAP). The experiments here reported show this is not always the case and, surprisingly, MAP-MRI and RBF tend to diverge from MAPL more than AMURA does.

Obviously, the mono-exponential model introduces a non-negligible error in the estimated measures. But the estimation of the EAP is by no means free of certain issues that compromise its accuracy: first, the EAP is usually represented as a superposition of functions selected from a basis or frame where the EAP is assumed to be sparse, which is only a rough approximation; second, the estimation is usually grounded on non-linear, iterative

procedures, whose numerical stability is not always guaranteed and whose actual convergence is often conditioned by computational time restrictions; third, EAP estimation requires probing very strong diffusion gradients that drastically worsen the SNR, which may have an uncertain impact depending on the optimization method to be used; fourth, an additional side effect of the use of strong diffusion gradients is that the linear Fourier transform relation between the EAP and the diffusion signal, which is the keystone of all EAP-based methods, may no longer hold with accuracy due to non-linearity, diffraction, and/or non-negligible diffusion during the application of pulsed gradients in a time δ (see Fig. 1.8, where including the fourth shell in the estimation heavily increases all measures for MAPL; this might suggest the Fourier model has been compromised at this point).

The combination of these four factors (and possibly others) may affect each EAP-based method in very different ways, and they could even represent a larger error than that introduced by the mono-exponential model. This could possibly explain the discrepancies between the measures computed with any of the three EAP-based methods, especially the higher deviations of RBF when 3 shells (instead of 2) are used in Table 1.3. Of course, AMURA does not get rid of this issue. But, once again, the goal of AMURA is not estimating the exact same values as EAP-based methods: a shifted (level/contrast changed) version of a given measure will have exactly the same discriminant power as its former version, and therefore it will be equally valuable. Going back to Fig. 1.8, EAP-based measures do not always respect this principle: RBF, for example, assigns very different, non-consistent relative values of RTAP among anatomies with similar FA depending on the number of shells used. Since RTAP is somehow related to the anisotropy (to the FA), this is by no means the expected behavior. MAP-like estimators, as well as AMURA, get rid of this artifact for RTAP but not for RTPP. However, since RTPP is not as closely related to the anisotropy as RTAP, and as long as AMURA-RTPP is still consistent with MAP-RTPP, this seems acceptable.

All in all, the *apparent* nature of AMURA makes corresponding measures heavily dependent on the measured shell (see Fig. 1.6), but a similar variability is also found in multi-shell methods (Fig. 1.8).

Once the consistency of AMURA has been thoroughly discussed, the big deal is their power to resolve micro-structural features beyond the capabilities of conventional DT-MRI. Tables 1.4, 1.5, and 1.6 suggest that AMURA might be as good as the other multi-shell techniques to distinguish different populations based on tissue properties. Going back to the previous discussion, the lack of consistency between the raw values of RTOP, RTPP, and RTAP computed with different multi-shell methods translates in similar discrepancies in the classification of white matter voxels. If AMURA correlated with MAPL stronger than the other multi-shell techniques did, they indeed provide better overlapped classifications too. Remarkably, AMURA finds two populations that more closely resemble those found by MAPL than MAP-MRI does, even when MAPL and MAP-MRI share a good number of common features. This remains true for all *apparent* measures at all available b-values. Hence, if we admit that EAP imaging provides measures that actually relate to micro-structural properties [1.12, 1.22, 1.29, 1.31], corresponding AMURA indexes should be assumed to probe actual tissue information as well. Once again, this claim can be justified only under the hypothesis that the radial integration to compute scalar measures blurs out a major part of the radial information within the q-space.

The experiment in Fig. 1.4 supports this claim, at least for RTPP: while tensor-derived measures are not able to distinguish different populations within the corpus callosum,

AMURA-RTPP finds two distinct regions that can be easily identified in Fig 1.5. In other words, AMURA-RTPP is measuring a micro-structural information that is not revealed with standard DT-MRI. Paying attention to Fig. 1.5, the two populations distinguished by AMURA-RTPP become evident: in the outermost region, the corpus callosum is interleaved with the cingulum, so that restricted diffusion prevails, the maximum diffusivity decreases, and the RTPP increases (lobes at the right of the valley in Fig. 1.4, rightmost column). In the innermost part, on the contrary, the corpus callosum is closer to the CSF and non-restricted diffusion takes a more relevant role: the maximum diffusivity increases and, as a consequence, the RTPP decreases (lobes at the left of the valley in Fig. 1.4). At the sight of Fig. 1.4, MAPL seems to find only subtle differences between these two populations, *performing worse* than AMURA. Nonetheless, the PDD database comprises only 2 shells, and hence it is not particularly well suited for this technique.

In any case, RTPP yields statistically significant differences between controls and patients at both the GCC and the SCC in all cases, see Table 1.7 (though the AMURA-RTPP yields a higher significance). This is not the case for RTOP and RTAP. It is important to stress here that the aim of the experiment is not demonstrating the clinical usefulness of AMURA in the particular case of PD, but testing its capability to describe micro-structural features. In other words, the fact that RTOP and RTAP are not able to find significant differences between controls and PD patients only means that the micro-structural properties they describe do not seem to be altered by this particular pathology and/or in this particular data set.

One further step in the present study would be the validation of AMURA as clinical biomarker candidates for diverse pathologies. Though Table 1.7 somehow points in this direction, this aspect must be thoroughly tested. In this sense, one major advantage of AMURA is its compatibility with nowadays standard acquisition protocols, so that they can be computed over already existing data sets such as the PDD database. Indeed, in case several shells with different b-values are available in one such database (as it is the case with PDD), AMURA can be trivially extended to fit the mono-exponential model to the entire data set and obtain more robust markers. On the contrary, multi-shell methods like MAPL need *ad-hoc* new acquisitions to attain satisfactory results, which complicates their clinical validation.

Moreover, since AMURA avoids the estimation of the actual EAP, the computation of its related measures may be done in a fast and robust way, i.e., without imposing a computational burden to the standard protocols: some of the experiments in the present paper report an acceleration about three orders of magnitude (10^3) compared to EAP-based measures, see Table 1.8. A whole volume can be processed in 6 to 8 minutes, so that a clinical study with 200 different subjects could be finished in 26 hours. The same cohort would take 4808 days (RBF), 135 days (MAP-MRI), or 19 days (MAPL), which obviously limits the applicability of these methods. The computational simplicity of AMURA, however, does not only imply faster execution times, but also more robust estimations due to its closed-form. As opposed, EAP-based techniques usually estimate the whole EAP from multi-shell samplings based on iterative procedures, which, as discussed above, lead to high discrepancies in the output measures.

On the other side of the coin, the major drawback behind AMURA is the explicit assumption of a specific radial behavior for the diffusion, which cannot fit the whole q-space. As a consequence, the selection of a particular b-value may change the anatomical measures that have been consequently dubbed *apparent*. However, as we have shown, this dependence on the b-value can also be found in other state of the art methods (see Fig 1.8), whose

outputs vary with the number of shells used for the estimation of the EAP. This implies the results of clinical trials could be compared against each other only if the same b-value is preserved across the studies. This is by no means something new to diffusion imaging: it is well-known that a change in the acquisition parameters (number of gradients, b-value, resolution, scanner vendor, etcetera) seriously affects scalar measures like the FA or the MD [1.47, 1.48].

Acknowledgments

This work was supported by Ministerio de Ciencia e Innovación of Spain with research grants RTI2018-094569-B-I00 and PRX18/00253 (Estancias de profesores e investigadores senior en centros extranjeros). Maryam Afzali is supported by a Wellcome Trust grant (096646/Z/11/Z). Tomasz Pieciak acknowledges National Science Centre (Poland) for funding resource (2015/19/N/ST7/01204)

The authors acknowledge Lipeng Ning, Carl-Fredrik Westin and Yogesh Rathi from Brigham and Women's Hospital, Harvard Medical School for sharing the source code of directional RBFs and their outstanding assistance. The authors thank the contributors of DIPY project (http://nipy.org/dipy/) for providing the MAP-MRI basis implementation.

Data collection and sharing for this project was provided by (1) the *Human Connectome Project* (HCP; Principal Investigators: Bruce Rosen, M.D., Ph.D., Arthur W. Toga, Ph.D., Van J. Weeden, MD). HCP funding was provided by the National Institute of Dental and Craniofacial Research (NIDCR), the National Institute of Mental Health (NIMH), and the National Institute of Neurological Disorders and Stroke (NINDS). HCP data are disseminated by the Laboratory of Neuro Imaging at the University of Southern California; (2) the *High-quality diffusion-weighted imaging of Parkinson's disease* data base, Cyclotron Research Centre, University of Liège.

Appendices

1.A Calculation of the structural measures using the diffusion tensor

If a Gaussian diffusion propagator is assumed, $P(\mathbf{R})$ is a mixture of independent and (nearly) identically distributed bounded cylinder statistics and, by virtue of the central limit theorem, their superposition is Gaussian distributed. The measured signal in the q–space is the (inverse) Fourier transform of the PDF and it can be expressed as:

$$E(\mathbf{q}) = \mathcal{F}^{-1}\left\{P(\mathbf{R})\right\}(\mathbf{q}) = \exp\left(-4\pi^2\tau\mathbf{q}^T\mathcal{D}\mathbf{q}\right), \tag{1.15}$$

which represents the well-known Stejskal–Tanner equation [1.49]. The diffusion tensor $\mathcal{D}$ is the anisotropic covariance matrix of the Gaussian PDF $P(\mathbf{R})$, and therefore it is a symmetric,

positive–definite matrix with positive eigenvalues and orthonormal eigenvectors. If we use this model to estimate the measures, we obtain:

$$\begin{aligned} \text{RTOP} &= \frac{1}{\sqrt{(4\pi\tau)^3}} \cdot (\lambda_1 \cdot \lambda_2 \cdot \lambda_3)^{-1/2} \\ &= \text{RTPP} \cdot \text{RTAP}; \qquad (1.16) \\ \text{RTPP} &= \frac{1}{\sqrt{4\pi\tau}} \cdot (\lambda_1)^{-1/2}; \qquad (1.17) \\ \text{RTAP} &= \frac{1}{\sqrt{(4\pi\tau)^2}} \cdot (\lambda_2 \cdot \lambda_3)^{-1/2}, \qquad (1.18) \end{aligned}$$

where $\lambda_1 \geq \lambda_2 \geq \lambda_3$ are the three real, non-negative eigenvalues of $\mathcal{D}$.

Bibliography

[1.1] Rovaris M, Filippi M. Diffusion tensor MRI in multiple sclerosis. J Neuroimaging. 2007;17(s1):27S–30S.

[1.2] Bester M, Jensen J, Babb J, Tabesh A, Miles L, Herbert J, et al. Non-Gaussian diffusion MRI of gray matter is associated with cognitive impairment in multiple sclerosis. Multiple Sclerosis Journal. 2015;21(7):935–944.

[1.3] Pasternak O, Westin CF, Dahlben B, Bouix S, Kubicki M. The extent of diffusion MRI markers of neuroinflammation and white matter deterioration in chronic schizophrenia. Schizophrenia research. 2015;161(1):113–118.

[1.4] Basser P, Pierpaoli C. Microstructural features measured using diffusion tensor imaging. J Magn Reson B. 1996;111(3):209–219.

[1.5] Westin CF, Maier SE, Mamata H, Nabavi A, Jolesz FA, Kikinis R. Processing and visualization for diffusion tensor MRI. Medical image analysis. 2002;6(2):93–108.

[1.6] Tuch DS, Reese TG, Wiegell MR, Wedeen VJ. Diffusion MRI of complex neural architecture. Neuron. 2003;40:885–895.

[1.7] Tristán-Vega A, Westin CF, Aja-Fernández S. Estimation of fiber orientation probability density functions in high angular resolution diffusion imaging. NeuroImage. 2009;47(2):638–650.

[1.8] Özarslan E, Sepherd TM, Vemuri BC, Blackband SJ, Mareci TH. Resolution of complex tissue microarchitecture using the Diffusion Orientation Transform (DOT). NeuroImage. 2006;31:1086–1103.

[1.9] Jensen JH, Helpern JA, Ramani A, Lu H, Kaczynski K. Diffusional kurtosis imaging: The quantification of non-gaussian water diffusion by means of magnetic resonance imaging. Magn Reson Med. 2005;53(6):1432–1440.

[1.10] LeBihan D. Molecular diffusion nuclear magnetic resonance imaging. Magn Reson Quaterly. 1991;7(1):1–30.

[1.11] Wedeen VJ, Hagmann P, Tseng WYI, Reese TG, Weisskoff RM. Mapping complex tissue architecture with diffusion spectrum magnetic resonance imaging. Magnetic resonance in medicine. 2005;54(6):1377–1386.

[1.12] Özarslan E, Koay CG, Shepherd TM, Komlosh ME, İrfanoğlu MO, Pierpaoli C, et al. Mean apparent propagator (MAP) MRI: a novel diffusion imaging method for mapping tissue microstructure. NeuroImage. 2013;78:16–32.

[1.13] Landman BA, Bogovic JA, Wan H, ElShahaby FEZ, Bazin PL, Prince JL. Resolution of crossing fibers with constrained compressed sensing using diffusion tensor MRI. NeuroImage. 2012;59(3):2175–2186.

[1.14] Merlet S, Deriche R. Compressed sensing for accelerated EAP recovery in diffusion MRI. In: MICCAI; 2010. p. Page–14.

[1.15] Wu YC, Alexander AL. Hybrid diffusion imaging. NeuroImage. 2007;36(3):617–629.

[1.16] Descoteaux M, Deriche R, Le Bihan D, Mangin JF, Poupon C. Diffusion propagator imaging: using Laplace's equation and multiple shell acquisitions to reconstruct the diffusion propagator. In: International Conference on Information Processing in Medical Imaging. Springer; 2009. p. 1–13.

[1.17] Descoteaux M, Deriche R, Le Bihan D, Mangin JF, Poupon C. Multiple q-shell diffusion propagator imaging. Medical image analysis. 2011;15(4):603–621.

[1.18] Hosseinbor AP, Chung MK, Wu YC, Alexander AL. Bessel fourier orientation reconstruction (BFOR): An analytical diffusion propagator reconstruction for hybrid diffusion imaging and computation of q-space indices. NeuroImage. 2013;64:650–670.

[1.19] Ning L, Westin CF, Rathi Y. Estimating diffusion propagator and its moments using directional radial basis functions. IEEE Trans Med Imag. 2015;34(10):2058–2078.

[1.20] Özarslan E, Koay C, Basser P. Simple harmonic oscillator based estimation and reconstruction for one-dimensional q-space MR. In: Proc. Intl. Soc. Mag. Reson. Med. vol. 16; 2008. p. 35.

[1.21] Fick RH, Wassermann D, Caruyer E, Deriche R. MAPL: Tissue microstructure estimation using Laplacian-regularized MAP-MRI and its application to HCP data. NeuroImage. 2016;134:365–385.

[1.22] Avram AV, Sarlls JE, Barnett AS, Özarslan E, Thomas C, Irfanoglu MO, et al. Clinical feasibility of using mean apparent propagator (MAP) MRI to characterize brain tissue microstructure. NeuroImage. 2016;127:422–434.

[1.23] Hosseinbor AP, Chung MK, Wu YC, Fleming JO, Field AS, Alexander AL. Extracting Quantitative Measures from EAP: A Small Clinical Study Using BFOR. In: Med Image Comput Comput Assist Interv. vol. 7511. Springer; 2012. p. 280–287.

[1.24] Wu YC, Field AS, Alexander AL. Computation of Diffusion Function Measures in q-Space Using Magnetic Resonance Hybrid Diffusion Imaging. IEEE transactions on medical imaging. 2008;27(6):858–865.

[1.25] Daianu M, Jacobs RE, Weitz TM, Town TC, Thompson PM. Multi-shell hybrid diffusion imaging (HYDI) at 7 Tesla in TgF344-AD transgenic alzheimer rats. PloS one. 2015;10(12):e0145205.

[1.26] Fick RH, Daianu M, Pizzolato M, Wassermann D, Jacobs RE, Thompson PM, et al. Comparison of biomarkers in transgenic alzheimer rats using multi-shell diffusion MRI. In: International Conference on Medical Image Computing and Computer-Assisted Intervention. Springer; 2016. p. 187–199.

[1.27] Brusini L, Obertino S, Zucchelli M, Galazzo IB, Krueger G, Granziera C, et al. Assessment of Mean Apparent Propagator-Based Indices as Biomarkers of Axonal Remodeling after Stroke. In: Medical Image Computing and Computer-Assisted Intervention – MICCAI 2015. Springer International Publishing; 2015. p. 199–206.

[1.28] Brusini L, Obertino S, Galazzo IB, Zucchelli M, Krueger G, Granziera C, et al. Ensemble average propagator-based detection of microstructural alterations after stroke. International journal of computer assisted radiology and surgery. 2016;11(9):1585–1597.

[1.29] Boscolo Galazzo I, Brusini L, Obertino S, Zucchelli M, Granziera C, Menegaz G. On the Viability of Diffusion MRI-Based Microstructural Biomarkers in Ischemic Stroke. Frontiers in neuroscience. 2018;12:92.

[1.30] Zucchelli M, Brusini L, Méndez CA, Daducci A, Granziera C, Menegaz G. What lies beneath? Diffusion EAP-based study of brain tissue microstructure. Medical image analysis. 2016;32:145–156.

[1.31] Alimi A, Petiet A, Santin M, Philippe AC, Lehéericy S. Towards the assessment of myelination using time-dependent diffusion MRI indices. In: ISMRM 2018 - International Society for Magnetic Resonance in Medicine; 2018. p. 1–4.

[1.32] Callaghan P, Eccles C, Xia Y. NMR microscopy of dynamic displacements: k-space and q-space imaging. Journal of Physics E: Scientific Instruments. 1988;21(8):820.

[1.33] Basser PJ. Relationships between diffusion tensor and q-space MRI. Magnetic Resonance in Medicine. 2002;47(2):392–397.

[1.34] Assaf Y, Mayk A, Cohen Y. Displacement imaging of spinal cord using q-space diffusion-weighted MRI. Magn Reson Med. 2000;44(5):713–722.

[1.35] Descoteaux M, Angelino E, Fitzgibbons S, Deriche R. Apparent Diffusion Profile estimation from High Angular Resolution Diffusion Images: estimation and applications. Magn Reson Med. 2006;56(2):395–410.

[1.36] Frank LR. Characterization of anisotropy in high angular resolution diffusion-weighted MRI. Magn Reson Med. 2002;47(6):1083–1099.

[1.37] Tuch DS. Q–Ball Imaging. Magn Reson Med. 2004;52:1358–1372.

[1.38] Canales-Rodríguez EJ, Melie-García L, Iturria-Medina Y. Mathematical description of q-space in spherical coordinates: exact q-ball imaging. Magn Reson Med. 2009;61(6):1350–1367.

[1.39] Tristan-Vega A, Westin CF, Aja-Fernandez S. A new methodology for the estimation of fiber populations in the white matter of the brain with the Funk–Radon transform. Neuroimage. 2010;49(2):1301–1315.

[1.40] Descoteaux M, Angelino E, Fitzgibbons S, Deriche R. Regularized, Fast, and Robust Analytical Q-Ball Imaging. Magn Reson Med. 2007;58:497–510.

[1.41] Aja-Fernández S, Vegas-Sánchez-Ferrero G. Statistical Analysis of Noise in MRI. Springer; 2016.

[1.42] Ziegler E, Rouillard M, André E, Coolen T, Stender J, Balteau E, et al. Mapping track density changes in nigrostriatal and extranigral pathways in Parkinson's disease. Neuroimage. 2014;99:498–508.

[1.43] Atkinson-Clement C, Pinto S, Eusebio A, Coulon O. Diffusion tensor imaging in Parkinson's disease: Review and meta-analysis. Neuroimage: Clinical. 2017;16:98–110.

[1.44] Jahanshad N, Kochunov PV, Sprooten E, Mandl RC, Nichols TE, Almasy L, et al. Multi-site genetic analysis of diffusion images and voxelwise heritability analysis: A pilot project of the ENIGMA-DTI working group. NeuroImage. 2013;81:455 – 469.

[1.45] Mori S, Wakana S, Van Zijl PC, Nagae-Poetscher L. MRI atlas of human white matter. Elsevier; 2005.

[1.46] Tristan-Vega A, Vegas-Sanchez-Ferrero G, Aja-Fernandez S. Local similarity measures for demons-like registration algorithms. In: 2008 5th IEEE International Symposium on Biomedical Imaging: From Nano to Macro; 2008. p. 1087–1090.

[1.47] Aja-Fernández S, Pieciak T, Tristán-Vega A, Vegas-Sánchez-Ferrero G, Molina V, de Luis-García R. Scalar diffusion-MRI measures invariant to acquisition parameters: a first step towards imaging biomarkers. Magn Reson Imag. 2018;.

[1.48] Barrio-Arranz G, de Luis-García R, Tristán-Vega A, Martín-Fernández M, Aja-Fernández S. Impact of MR acquisition parameters on DTI scalar indexes: a tractography based approach. PloS one. 2015;10(10):e0137905.

[1.49] Stejskal EO, Tanner JE. Spin Diffusion Measurements: Spin Echoes in the Presence of a Time-Dependent Field Gradient. J Chem Phys. 1965;42:288–292.

2

Apparent Propagator Anisotropy from Single-Shell Diffusion MRI Acquisitions

Santiago Aja-Fernández[1], Antonio Tristán-Vega[1] and Derek K. Jones[2]

1 *Laboratorio de Procesado de Imagen (LPI), ETSI Telecomunicación, Universidad de Valladolid, Spain*
2 *Cardiff University Brain Research Imaging Centre (CUBRIC), School of Psychology, Cardiff University, UK*

Abstract:
Purpose: The Apparent Propagator Anisotropy (APA) is a new diffusion MRI metric that, while drawing on the benefits of the Ensemble Averaged Propagator Anisotropy (PA) compared to the Fractional Anisotropy (FA), can be estimated from single-shell data.
Theory and Methods: Computation of the full PA requires acquisition of large data sets with many diffusion directions and different b-values, and results in extremely long processing times. This has hindered adoption of the PA by the community, despite evidence that it provides meaningful information beyond the FA. Calculation of the complete propagator can be avoided under the hypothesis that a similar sensitivity/specificity may be achieved from *apparent* measurements at a given shell. Assuming that diffusion anisotropy is non-dependent on the b-value, a closed-form expression using information from one single shell (i.e. b-value) is reported.
Results: Publicly available databases with healthy and diseased subjects are used to compare the APA against other anisotropy measures. The structural information provided by the APA correlates with that provided by the PA for healthy subjects, while it also reveals statistically relevant differences in white matter regions for two pathologies, with a higher reliability than the FA. Additionally, APA has a computational complexity similar to the FA, with processing-times several orders of magnitude below the PA.
Conclusions: The APA can extract more relevant white matter information than the FA, without any additional demands on data acquisition. This makes APA an attractive option for adoption into existing diffusion MRI analysis pipelines.

Originally published as: *S Aja-Fernández, A Tristán-Vega, DK Jones, Apparent propagator anisotropy from single-shell diffusion MRI acquisitions, Magnetic resonance in medicine 85 (5), 2869-2881, 2021*

2.1 Introduction

The term Diffusion Magnetic Resonance Imaging (dMRI) refers to a set of diverse imaging techniques that, when applied to brain studies, provide useful information about the microscopic organization and connectivity of the white matter. One relevant feature of dMRI is its ability to measure orientational variance in the different tissues, i.e. anisotropy.

Nowadays, the most common way to estimate the anisotropy is via the diffusion tensor (DT) [2.1]. Diffusion tensor MRI (DT-MRI) brought to light one of the common issues of dMRI techniques: in order to carry out clinical studies, the information given by the selected diffusion analysis method must be translated into some scalar measures that describe different features of diffusion within every voxel. That way, metrics like the Fractional Anisotropy (FA) were defined with the DT as a starting point [2.1]. Despite the strong limitations that the underlying Gaussian assumption imposes, the FA is still widely used in clinical studies involving dMRI.

In practice, the diffusion mechanisms cannot be fully described by DT-MRI because of the oversimplified Gaussian fitting. Accordingly, techniques with more degrees-of-freedom naturally arose, such as Diffusion Kurtosis Imaging (DKI) [2.2] or methods based on High Angular Resolution Diffusion Imaging (HARDI) [2.3, 2.4]. The trend over the last decade has been to acquire a large number of diffusion-weighted images distributed over several shells (i.e. with several gradient strengths) and with moderate-to-high b-values to estimate more advanced diffusion descriptors, such as the Ensemble Average diffusion Propagator (EAP) [2.5]. The estimation relies on model-free, non parametric approaches that can accurately describe most of the relevant diffusion phenomena.

The most straightforward strategy to estimate the EAP is to sample the Cartesian q-space densely enabling Diffusion Spectrum Imaging (DSI) [2.6], which requires a vast number of acquisitions. Alternatively, several methods were proposed grounded on sparse samplings of the q-space, being the most prominent: Hybrid Diffusion Imaging (HYDI) [2.7, 2.8], multiple q-shell Diffusion Propagator Imaging (mq-DPI) [2.9, 2.10], Bessel Fourier Orientation Reconstruction (BFOR) [2.11], the directional Radial Basis Functions (RBFs) [2.12], the Mean Apparent Propagator MRI (MAP-MRI) [2.5, 2.13], or the Laplacian-regularized MAP-MRI (MAPL) [2.14].

Regardless of the method selected for estimating the EAP, the typical end-user condenses the information provided by the whole EAP into a set of scalar metrics such as: the probability of zero displacement (or return-to-origin probability, RTOP), the q-space inverse variance, the return-to-plane (RTPP) and return-to-axis probabilities (RTAP) [2.8, 2.15, 2.12], or the Propagator Anisotropy (PA) [2.5]. In this work we will focus on the latter.

The PA can be seen as an alternative anisotropy measure able to discern changes that remain hidden for the FA. It reveals microstructural information of interest in the white matter. For example, a recent study in transgenic rats suggests that the PA may be a valid biomarker for Alzheimer's disease [2.16]. The same study also shows that the PA could be an important marker in longitudinal studies, indicating a possible dependency with age. [2.13] showed that the PA shows higher tissue contrast than the FA in white matter. Finally, [2.17] detected the main limitation of the PA: the bottleneck of studies with EAP-derived measures is the amount of data needed for the calculation. This issue, together with the long processing times needed for EAP imaging, has slowed down a widespread adoption of propagator-based anisotropy measures by the clinical community and motivated the current work.

This same pitfall has been recently addressed by [2.18] for the computation of other EAP imaging-related markers (namely: RTOP, RTPP, and RTAP). The so-called "Apparent Measures Using Reduced Acquisitions" (AMURA) can mimic the sensitivity of EAP-based measures to microstructural changes when a reduced amount of data distributed in a few shells (even one) is available. AMURA assumes a prior model for the behavior of the radial

q-space instead of trying to numerically describe it, yielding closed-form expressions that can be computed easily even from single-shell acquisitions.

The present paper extends AMURA to the estimation of the PA. To that end, the same constrained model for radial diffusion used by [2.18] is adopted here, i.e., the diffusion anisotropy is assumed to be independent of the actual b-value of the measured shells. We use this simplification to derive alternative closed-forms for the inner products that define the original PA that can be computed even from single-shell acquisitions. At the same time, the so-called Apparent Propagator Anisotropy (APA), together with other closely related measures we derive from it, may reveal analogous tissue anisotropy features as the original PA and other anisotropy measures. The use of a constrained model, instead of regularizing a heavily under-determined problem, makes the APA more robust for certain brain structures than the PA itself, as we illustrate over an extensive set of experiments performed on data acquired with a 'clinical' type acquisition.

2.2 Theory

2.2.1 The Diffusion Signal

The EAP, $P(\mathbf{R})$, is the Probability Density Function of the water molecules inside a voxel moving an effective distance $\mathbf{R}$ in a time Δ. It is related to the normalized magnitude signal provided by the MRI scanner, $E(\mathbf{q})$, by the Fourier transform $\mathcal{F}\{.\}$ [2.19]:

$$P(\mathbf{R}) = \int_{\mathbb{R}^3} E(\mathbf{q}) e^{-2\pi j \mathbf{q}\cdot\mathbf{R}} d\mathbf{q} = \mathcal{F}\left\{|E(\mathbf{q})|\right\}(\mathbf{R}). \tag{2.1}$$

The inference of exact information on the $\mathbf{R}$–space would require the sampling of the whole $\mathbf{q}$–space to exploit the Fourier relationship between both spaces.

In order to obtain a closed-form analytical representation from a reduced number of acquired images, a model of the diffusion behavior must be adopted. The most common techniques rely on the assumption of a Gaussian diffusion profile and a steady state regime of the diffusion process leading to DT representation [2.20]. Alternatively, a more general expression for $E(\mathbf{q})$ can be used [2.21]:

$$E(\mathbf{q}) = \exp\left(-4\pi^2 \tau q_0^2 D(\mathbf{q})\right) = \exp\left(-b \cdot D(\mathbf{q})\right) \tag{2.2}$$

where the positive function $D(\mathbf{q}) = D(q_0, \theta, \phi)$ is the Apparent Diffusion Coefficient (ADC), $b = 4\pi^2\tau\|\mathbf{q}\|^2$ is the so-called b-value, $q_0 = \|\mathbf{q}\|$ and θ, ϕ are the angular coordinates in the spherical system. The effective diffusion time τ is defined as $\tau = \Delta - \delta/3$, where the diffusion time Δ is usually corrected with the pulse duration δ.

The mono-exponential assumption is ubiquitous to many HARDI techniques, and it implies the anisotropy of the diffusion signal is roughly independent of the b-value. The accuracy of such an assumption depends on the range of b-values considered: according to [2.21] this mono-exponential signal representation is predominant in the mammalian brain for b-values up to 2000 s/mm^2. Beyond this value, in the range 2000 to 10000 s/mm^2, it has been proven that the deviation of the actual signal from mono-exponentials embeds

meaningful information about the diffusion process [2.5]. However, the relevance of this extra information might be at stake due to the limitations inherent to commonly used samplings (with maximum b-values ranging 3,000 to 5,000 s/mm^2), which are able to capture only the low-frequency spectrum.

2.2.2 Propagator Anisotropy and Inner Product

In [2.5], the authors propose a measure called the Propagator Anisotropy (PA) that quantifies how the propagator diverges from the isotropic one. The PA is defined as a function of the sine of the angle between two propagators as:

$$\text{PA} = \gamma\left(\sin\left(\angle[P(\mathbf{R}), P_I(\mathbf{R})]\right), \epsilon\right), \tag{2.3}$$

where $P(\mathbf{R})$ is the actual propagator and $P_I(\mathbf{R})$ its equivalent isotropic propagator. The function $\gamma\left(., \epsilon\right)$ is a contrast enhancement to better distribute the output values in the range $[0, 1]$. For the sake of simplicity, hereon, we will use θ_{P,P_I} to denote the angle.

In order to calculate this metric, we need to define the inner product between two propagators. Let $P_1(\mathbf{R})$ and $P_2(\mathbf{R})$ be two different propagators. If we consider them as two different signals defined over a common signal space $\mathcal{S}$, we can define an inner product as [2.5, 2.22]:

$$\langle P_1(\mathbf{R}), P_2(\mathbf{R})\rangle = \int_{\mathbb{R}^3} P_1(\mathbf{R}) P_2^*(\mathbf{R}) d\mathbf{R}. \tag{2.4}$$

where $P_2^*(\mathbf{R})$ is the conjugate of $P_2(\mathbf{R})$. According to Parseval's Theorem [2.22], since variables $\mathbf{R}$ and $\mathbf{q}$ are related via the Fourier Transform, there is an equivalence of this product in the $\mathbf{q}$-space. Considering that the magnitude-reconstructed diffusion-weighted MR signal $E(\mathbf{q})$ is always real and symmetric, $E^*(\mathbf{q}) = E(\mathbf{q})$ and $E(\mathbf{q}) = E(-\mathbf{q})$, we can write:

$$\langle P_1(\mathbf{R}), P_2(\mathbf{R})\rangle = \int_{\mathbb{R}^3} E_1(\mathbf{q}) E_2(\mathbf{q}) d\mathbf{q}, \tag{2.5}$$

where $E_1(\mathbf{q}) = \mathcal{F}^{-1}\left\{P_1(\mathbf{R})\right\}(\mathbf{q})$ and $E_2(\mathbf{q}) = \mathcal{F}^{-1}\left\{P_2(\mathbf{R})\right\}(\mathbf{q})$. The norm of a signal is defined as:

$$||P_1(\mathbf{R})|| = \langle P_1(\mathbf{R}), P_1(\mathbf{R})\rangle^{1/2} = \left(\int_{\mathbb{R}^3} |E_1(\mathbf{q})|^2 d\mathbf{q}\right)^{1/2}. \tag{2.6}$$

The *similarity* between two signals is given by the cosine of the angle between them, defined as:

$$\cos\theta_{P_1,P_2} = \frac{\langle P_1(\mathbf{R}), P_2(\mathbf{R})\rangle}{||P_1(\mathbf{R})|| \cdot ||P_2(\mathbf{R})||}. \tag{2.7}$$

The sine is calculated from Eq. (2.7) as:

$$\sin\theta_{P_1,P_2} = \sqrt{1 - \cos^2\theta_{P_1,P_2}}. \tag{2.8}$$

This result can be extrapolated for the EAP, $P(\mathbf{R})$, and its isotropic equivalent, $P_I(\mathbf{R})$, to define the PA as in Eq. (2.3).

2.3 Methods

2.3.1 Apparent Propagator Anisotropy

The calculation of the PA demands the full estimation of the EAP which requires an extensive data acquisition. In contrast, AMURA permits the use single-shell data at the expense of constraining the radial behavior so that the diffusivity $D(\mathbf{q})$ does not depend on the radial direction (i.e., independent of the magnitude of the q-vector): $D(\mathbf{q}) = D(\mathbf{u})$, where $\|\mathbf{u}\| = 1$ and $\mathbf{q} = q\mathbf{u}$ [2.18]. Then, Eq. (2.2) becomes:

$$E(\mathbf{q}) = E(q, \mathbf{u}) = \exp\left(-4\pi^2\tau q^2\ D(\mathbf{u})\right). \tag{2.9}$$

Note that, although $D(\mathbf{q})$ is independent of q, the signal attenuation, $E(\mathbf{q})$, still has q-dependence. This assumption, although restrictive, is used to define certain diffusion representations in HARDI [2.23, 2.4], where only one data-shell (i.e., b-value) is usually acquired.

In what follows, we explicitly calculate the inner product that defines the PA by using the simplification in Eq. (2.9), yielding an anisotropy metric related to the PA for a specific shell.

First, we define an isotropic signal equivalent to the mono-exponential model, $E_I(\mathbf{q})$. Pursuing an analogous formulation to that in AMURA [2.18], we propose an alternative formulation, leading to a linear computation:

$$E_I(\mathbf{q}) \triangleq \exp\left(-4\pi^2\tau q^2\ D_{\text{AV}}\right), \tag{2.10}$$

for:

$$D_{\text{AV}} = \frac{1}{4\pi}\int_S D(\mathbf{u})d\mathbf{u}. \tag{2.11}$$

The integration on the surface of the sphere from a limited number of samples is performed by fitting corresponding signals in the basis of Spherical Harmonics (SH), whose 0-th order coefficient is defined as:

$$C_{0,0}\left\{H(\mathbf{u})\right\} = \frac{1}{\sqrt{4\pi}}\int_S H(\mathbf{u})d\mathbf{u}. \tag{2.12}$$

Therefore, D_{AV} can be calculated as:

$$D_{\text{AV}} = \frac{1}{\sqrt{4\pi}}C_{0,0}\left\{D(\mathbf{u})\right\},\ \text{so that}\ E_I(\mathbf{q}) = \exp\left(-2\pi^{3/2}\tau q^2\ C_{0,0}\left\{D(\mathbf{u})\right\}\right). \tag{2.13}$$

Second, we calculate the norm of $P(\mathbf{R})$ and $P_I(\mathbf{R})$ under the considered assumption:

$$\begin{aligned} ||P(\mathbf{R})||^2 &= \int_{\mathbb{R}^3} \exp\left(-4\pi^2\tau q^2\ 2\ D(\mathbf{u})\right) d\mathbf{q} \\ &= \int_0^\infty \int_S \exp\left(-4\pi^2\tau q^2\ 2\ D(\mathbf{u})\right) q^2 d\mathbf{u}\ dq \\ &= C_p \int_S \frac{1}{(2\cdot D(\mathbf{u}))^{3/2}} d\mathbf{u} \qquad (2.14) \\ &= C_p \cdot \sqrt{\frac{\pi}{2}} \cdot C_{0,0} \left\{ D(\mathbf{u})^{-3/2} \right\}, \qquad (2.15) \end{aligned}$$

where C_p is a constant. Following the same reasoning, the norm of the isotropic equivalent is:

$$\begin{aligned} ||P_I(\mathbf{R})||^2 &= \int_{\mathbb{R}^3} \exp\left(-4\pi^2\tau q^2\ 2\ D_{\text{AV}}\right) d\mathbf{q} \\ &= C_p\sqrt{2}\pi \cdot D_{\text{AV}}^{-3/2}. \qquad (2.16) \end{aligned}$$

Third, we calculate the inner product of both signals using the single shell assumption:

$$\begin{aligned} \langle P(\mathbf{R}), P_I(\mathbf{R})\rangle &= \int_{\mathbb{R}^3} \exp\left(-4\pi^2\tau q^2\ \ (D(\mathbf{u}) + D_{\text{AV}})\right) d\mathbf{q} \\ &= C_p \int_S \frac{1}{(D(\mathbf{u}) + D_{\text{AV}})^{3/2}} dS \qquad (2.17) \\ &= C_p \cdot \sqrt{4\pi} \cdot C_{0,0} \left\{ (D(\mathbf{u}) + D_{\text{AV}})^{-3/2} \right\}. \qquad (2.18) \end{aligned}$$

Next, we calculate the cosine and sine of the angle between both signals:

$$\begin{aligned} \cos^2\theta_{P,P_I} &= \frac{\langle P(\mathbf{R}), P_I(\mathbf{R})\rangle^2}{||P(\mathbf{R})||^2 \cdot ||P_I(\mathbf{R})||^2} \\ &= \frac{4}{\sqrt{\pi}} \frac{\left[C_{0,0}\left\{(D(\mathbf{u}) + D_{\text{AV}})^{-3/2}\right\}\right]^2}{C_{0,0}\left\{\cdot D(\mathbf{u})^{-3/2}\right\} \cdot D_{\text{AV}}^{-3/2}}; \qquad (2.19) \\ \sin\theta_{P,P_I} &= \sqrt{1 - \cos^2\theta_{P,P_I}}. \qquad (2.20) \end{aligned}$$

From here, we can define the anisotropy measure prior to the non-linear transformation as:

$$\text{APA}_0 = \sin\theta_{P,P_I}. \qquad (2.21)$$

Finally, the PA is calculated using the Gamma transformation proposed by [2.5]:

$$\gamma(t,\epsilon) = \frac{t^{3\epsilon}}{1 - 3t^{\epsilon} + 3t^{2\epsilon}}. \qquad (2.22)$$

This way, the Apparent Propagator Anisotropy (APA) at a given b-value is calculated as:

$$\text{APA} = \gamma\left(\sin\theta_{P,P_I}, \epsilon\right). \qquad (2.23)$$

Measure	Formula	Practical implementation
APA	$\gamma\left(\mathrm{APA}_0, \epsilon\right)$	$\gamma\left(\mathrm{APA}_0, \epsilon\right)$
APA_0	$\sqrt{1-\frac{\left[\int_S (D(\mathbf{u})+D_{\mathrm{AV}})^{-3/2} d\mathbf{u}\right]^2}{\sqrt{2}\pi D_{\mathrm{AV}}^{-3/2} \int_S (2D(\mathbf{u}))^{-3/2} d\mathbf{u}}}$	$\sqrt{1-\frac{4}{\sqrt{\pi}}\frac{\left[C_{0,0}\left\{(D(\mathbf{u})+D_{\mathrm{AV}})^{-3/2}\right\}\right]^2}{C_{0,0}\left\{D(\mathbf{u})^{-3/2}\right\}\cdot D_{\mathrm{AV}}^{-3/2}}}$
D_{AV}	$\frac{1}{4\pi}\int_S D(\mathbf{u}) d\mathbf{u}$	$\frac{1}{\sqrt{4\pi}} C_{0,0}\left\{D(\mathbf{u})\right\}$
DiA	$\sqrt{\frac{4\pi\cdot\int_S D^2(\mathbf{u}) d\mathbf{u} - \left[\int_S D(\mathbf{u}) d\mathbf{u}\right]^2}{4\pi\cdot\int_S D^2(\mathbf{u}) d\mathbf{u}}}$	$\sqrt{1-\frac{\frac{1}{\sqrt{4\pi}}\cdot C_{0,0}^2\{D(\mathbf{u})\}}{C_{0,0}\{D^2(\mathbf{u})\}}}$

Tab. 2.1.: Summary of the proposed anisotropic diffusion metrics.

2.3.2 Alternative form of the APA

The need for a contrast enhancement of the raw values of the PA through the gamma correction in Eq. (2.23) was already recognized by [2.5]. Generalizing this idea, we can apply a contrast enhancement to the attenuation signal itself before the PA is actually computed. Since $E(\mathbf{q})$ is bounded in the range $(0,1)$, the negative logarithm of $E(\mathbf{q})$, i.e. $D(\mathbf{q})$, is an appropriate transformation in this sense. Hence, we can reformulate:

$$\langle D_1(\mathbf{q}), D_2(\mathbf{q})\rangle = \int_S D_1(\mathbf{u}) D_2(\mathbf{u}) d\mathbf{u}; \tag{2.24}$$

$$||D(\mathbf{q})||^2 = \int_S D^2(\mathbf{u}) d\mathbf{u}, \tag{2.25}$$

and the Diffusion Anisotropy (DiA) is defined straightforwardly as:

$$\begin{aligned} \mathrm{DiA} &= \sin\theta_{D,D_{\mathrm{AV}}} \\ &= \sqrt{1-\frac{\left[D_{\mathrm{AV}}\cdot\int_S D(\mathbf{u}) d\mathbf{u}\right]^2}{4\pi\cdot D_{\mathrm{AV}}^2\cdot\int_S D^2(\mathbf{u}) d\mathbf{u}}} \\ &= \left(\frac{C_{0,0}\{D^2(\mathbf{u})\} - \frac{1}{\sqrt{4\pi}}\cdot C_{0,0}^2\{D(\mathbf{u})\}}{C_{0,0}\{D^2(\mathbf{u})\}}\right)^{1/2}, \end{aligned} \tag{2.26}$$

so that the term D_{AV} no longer appears. The DiA can be seen as a generalization of the Coefficient of Variation of the Diffusion (CVD) defined in [2.24] as a robust alternative for the FA. According to [2.25], the DiA is also an alternative definition to the Generalized Anisotropy proposed by [2.26]. Note that the derived DiA also resembles to the Generalized Fractional Anisotropy (GFA) defined in [2.27].

An overview of all the proposed diffusion anisotropy metrics, together with their specific numerical implementations, is presented in Table 2.1.

2.3.3 Public data sets used for the experiments

In order to test the proposed measures for a wide range of acquisition protocols and MR hardware configurations, four different data sets were used:

- **Human Connectome Project (HCP)**[1]: specifically volumes MGH1007, acquired on a Siemens 3T Connectom scanner with 4 different shells at $b = [1000, 3000, 5000, 10000]$ s/mm^2, with [64, 64, 128, 256] gradient directions each, in-plane resolution 1.5 mm and slice thickness was 1.5 mm.
- **Public Parkinson's disease database (PPD)**: publicly available database[2] acquired in the Cyclotron Research Centre, University of Liège. It consists of 53 subjects in a cross-sectional Parkinson's disease (PD) study: 27 PD patients and 26 age, sex, and education-matched control subjects. Data were acquired on a 3T head-only MR scanner (Magnetom Allegra, Siemens Medical Solutions, Erlangen, Germany) operated with an 8-channel head coil. DWIs were acquired with a twice-refocused spin-echo sequence with EPI readout at two shells $b = [1000, 2500, 5000, 10000]$ s/mm^2 along 120 encoding gradients. Acquisition parameters are TR=6800 ms, TE=91 ms, and FOV=211 mm^2, voxel size 2.4×2.4×2.4 mm, no parallel imaging and 6/8 partial Fourier were used. More information can be found in [2.28].
- **ADNI database (ADNI)**: multi-shell data from 55 subjects were obtained from the Alzheimer's Disease Neuroimaging Initiative (ADNI) database [3]. From the whole database we have focused on those subjects scanned with more than one shell (ADNI 3 advanced protocol). The data used consist of 38 cognitively normal elderly controls (CN; mean age: 71.4±6.4 yrs, 15M/23F) and 17 with mild cognitive impairment (MCI; mean age: 71.6±8.6 yrs, 10M/7F). Data were acquired on 3T Siemens Advanced Prisma scanners (at 9 different acquisition sites). DW images were acquired at three distinct b-values $b = [500, 1000, 2000, 10000]$ s/mm^2 with different encoding gradients for each shell: 6 (b=500 s/mm^2), 48 (b=1000 s/mm^2), 60 (b=2000 s/mm^2) and 12 unweighted (b = 0) volumes. Acquisition parameters are TR=3300 ms, TE=71, 116×116 matrix, 81 slices, voxel size 2×2×2 mm, whole scanned volume 232×232×160 mm. All raw DWI were corrected for motion, eddy-current and echo-planar imaging (EPI) induced susceptibility artifacts and B1 field inhomogeneity.
- **Multi-shell data acquired at CUBRIC (CBR)**[4]: 14 healthy volunteers scanned on a 3T Siemens Prisma scanner (80 mT/m) with a pulsed-gradient spin-echo (PGSE) sequence.

[1] Data obtained from the Human Connectome Project (HCP) database (`ida.loni.usc.edu/login.jsp`). The HCP project (Principal Investigators: Bruce Rosen, M.D., Ph.D., Martinos Center at Massachusetts General Hospital; Arthur W. Toga, Ph.D., University of Southern California, Van J. Weeden, MD, Martinos Center at Massachusetts General Hospital) is supported by the National Institute of Dental and Craniofacial Research (NIDCR), the National Institute of Mental Health (NIMH) and the National Institute of Neurological Disorders and Stroke (NINDS). HCP is the result of efforts of co-investigators from the University of Southern California, Martinos Center for Biomedical Imaging at Massachusetts General Hospital (MGH), Washington University, and the University of Minnesota.

[2] `www.nitrc.org/frs/?group_id=835`.

[3] Data used in preparation of this article were obtained from ADNI database (`adni.loni.isc.edu`). As such, the investigators within the ADNI contributed to the design and implementation of ADNI and/or provided data but did not participate in analysis or writing of this report. A complete listing of ADNI investigators can be found at: `http://adni.loni.usc.edu/wp-content/uploads/how_to_apply/ADNI_Acknowledgement_List.pdf`. The ADNI was launched in 2003 as a public-private partnership, led by Principal Investigator Michael W. Weiner, MD. The primary goal of ADNI has been to test whether serial MRI, PET, other biological markers, and clinical and neuropsychological assessment can be combined to measure the progression of MCI and early Alzheimer's Disease (AD).

[4] `www.cardiff.ac.uk/cardiff-university-brain-research-imaging-centre/research/projects/cross-scanner-and-cross-protocol-diffusion-MRI-data-harmonisation`

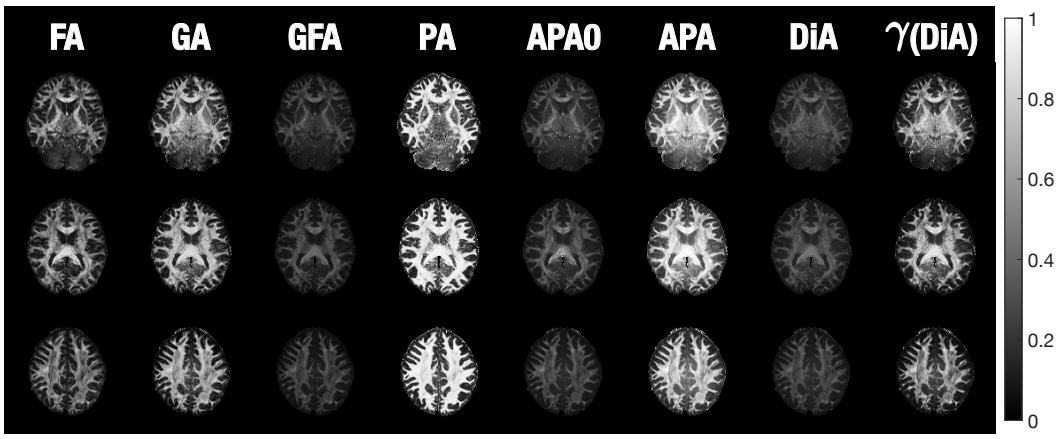

Fig. 2.1.: Visual comparison of the diffusion anisotropy metrics using slices 42, 52 and 65 of the MGH1007 volume from HCP. FA is calculated using b=1000 s/mm^2, GA, GFA, APA0, APA, and DiA using b=3000 s/mm^2, and PA using 4 shells (1000, 3000, 5000 and 10000 s/mm^2). γ(DiA) is the gamma-corrected version of DiA, constructed for visualization purposes.

Three shells were acquired at $b = [1200, 3000, 5000]$ s/mm^2 with 60 directions per value. The resolution is 1.5$\times$ 1.5$\times$1.5 mm. Other acquisition parameters are: TE=80 ms, TR=4500ms, $\Delta/\delta = 38.3/19.5$ ms, parallel imaging acquisition (GRAPPA2) with sum of squares combination and 32 channels.

2.4 Results

2.4.1 Visual Assessment

A preliminary visual assessment of the different metrics was performed using 3 slices (42, 52, 65) from the HCP volume MGH1007. The proposed measures (APA$_0$, APA, and DiA) were calculated using a single shell at b=3000 s/mm^2. For the sake of comparison, we have also calculated the FA at b=1000 s/mm^2, the GA and GFA (calculated using FSL) at b=3000 s/mm^2, and the PA using all the available information (4 shells). Results are shown in Fig. 2.1. A gamma-corrected version of DiA is also presented to enhance the contrast. It is calculated using the transformation in Eq. (2.22) over Eq. (2.26). As expected, all the metrics highlight the anisotropy of the white matter, meanwhile they suppress the signal from the (approximately) isotropic gray matter. isotropic gray matter. APA$_0$ and DiA are not uniformly distributed over the range $[0, 1]$, an effect also present in the GFA, which is palliated by the APA. Comparing the new measures with the original PA, the latter seems over-saturated towards 1, in a way that most of the white matter looks homogeneous. Conversely, the APA exhibits wider dynamic range across the white matter, making it possible to distinguish different anatomical features.

Moreover, Fig. 2.2 suggests that the APA exhibits a good noise behavior across the entire cerebrum, even in those areas with low anisotropy such as the CSF (which has low APA) and areas of intermediate anisotropy, such as thalamus and head of caudate. This is in stark contrast to the PA computed using MAP-MRI, where there is elevated anisotropy in the

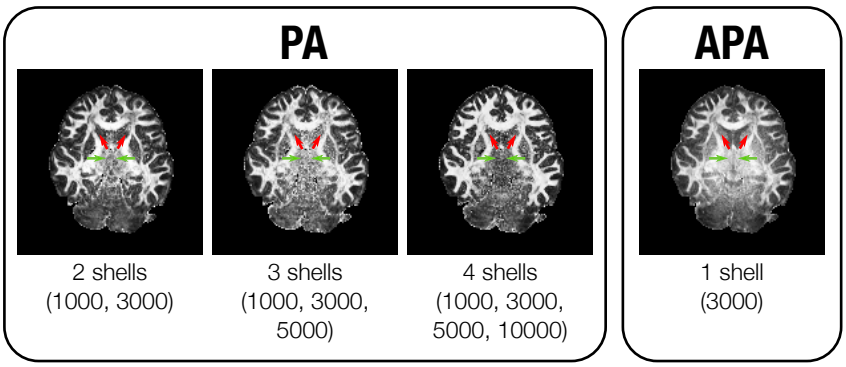

Fig. 2.2.: Visual comparison of PA to APA using slice 42 of the MGH1007 volume from HCP. APA is calculated using one single shell (b=3000 s/mm^2), and PA using 2 (1000 and 3000 s/mm^2), 3 (1000, 3000 and 5000 s/mm^2) and 4 shells (1000, 3000, 5000 and 10000 s/mm^2). There are marked differences between APA and PA in the basal ganglia, including the head of caudate (red arrows) and thalamus (green arrows),

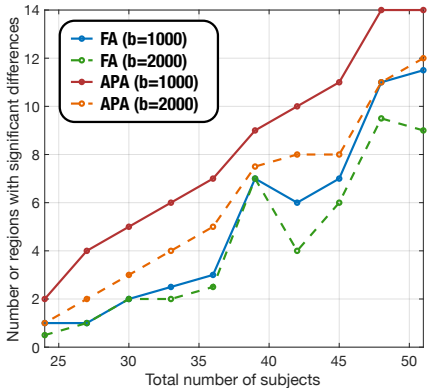

Fig. 2.3.: Number of regions with significant differences ($p < 0.05$) for different number of samples. FA is compared to APA for the ADNI database to find differences between control and MCI subjects. Only those regions with more than 2500 voxels are considered.

ventricles, and the poor contrast-to-noise ratio in the basal ganglia occludes corresponding structures.

2.4.2 Validation with Clinical Data

The next set of experiments aims at quantitatively evaluating the potential of the new metrics for the clinical analysis of real data provided in public databases. The assessment is based on the ability to find significant differences between two different cases: (1) mild cognitive impairment (MCI), using the ADNI database, and (2) Parkinson disease (PD), using the PPD database. We have selected these two cases as they are illustrative of very different clinical studies: according to the literature, significant differences in diffusion anisotropy can be easily found between MCI and controls in a large number of brain regions [2.29, 2.30]. In contrast, although patient-control anisotropy differences have been reported in white matter

Number of subjects	51	48	45	42	39	36	33	30	27	24
2-sided	11	17	16	13	15	13	10	11	12	7
APA-not(FA)	10	15	15	14	15	15	11	11	12	9
FA-not(APA)	1	2	1	0	1	0	0	0	0	0

Tab. 2.2.: Results of the McNemar's test on the ADNI data: comparison of areas detected by APA and FA ($p < 0.01$).

regions for PD [2.31], such differences are harder to find using standard dMRI analysis. This way, the the ability of the new measures to detect pathology are evaluated under two different difficulty levels.

For all the experiments, the FA was calculated as a reference value using MRTRIX [2.32][5] from the data collected at b=1000 s/mm^2. The FA maps of all the volumes were warped to a common template using the standard TBSS pipeline [2.33]. The same transformation was applied to all the metrics considered for the experiment.

Let us focus first on the **MCI experiment**. The FA was compared to the APA using two different shells for both measures (b=1000 and b=2000 s/mm^2) in order to check the capability of the latter to discriminate differences between MCI and healthy controls. To that end, a region of interest (ROI) analysis was carried out: 48 different ROI were identified on the subjects using the JHU WM atlas [2.34]. For the sake of robustness, only those 22 ROIs containing more than 2500 voxels were considered for the experiment. The average value of the FA and the APA inside each ROI was calculated using the 2% and 98% percentiles. Then we carried out a two-sample, pooled variance t-test between controls and patients for each of the measures considered and at each of the 22 ROIs. To observe the dependence of the measures with the number of subjects, the t-test was repeated in sub-samples of the original set. Starting with 55 subjects (38 CN and 17 MCI), the number of subjects per group was progressively reduced in 3 subjects (2 CN and 1 MCI) for each iteration, until no regions with significant differences were found. For each iteration, 200 repetitions were performed, each of them generating a random sub-sample of subjects for which the inference was carried out. This inference plots differences between the two groups in a certain number of white matter regions with significance $p < 0.05$ (uncorrected). The median value of regions with significant differences across the 200 repetitions was considered as the figure of merit for each iteration.

Results are shown in Fig. 2.3. As expected, the number of regions showing significant group differences decreased together with the number of subjects in each group. However, for any given sample size, the APA consistently finds a larger number of regions with significant patient-control differences than the other metrics. Moreover, the APA is able to obtain similar results as the FA with a smaller sample size. This feature makes the APA a robust alternative to the FA even with data sets collected for DT-MRI-based analysis, i.e. single-shell data with b≈1000 s/mm^2. In this experiment, it is precisely at b=1000 s/mm^2 where the best discrimination results were obtained for the APA compared to the FA.

Complementarily, in order to test the sensitivity of APA compared to FA, we have conducted a McNemar's statistical test with the results provided by bootstrapping for FA and APA with $b = 1000$s/mm^2, for each subsample set and the 200 repetitions. This type of test is usually

[5] `mrtrix.org`

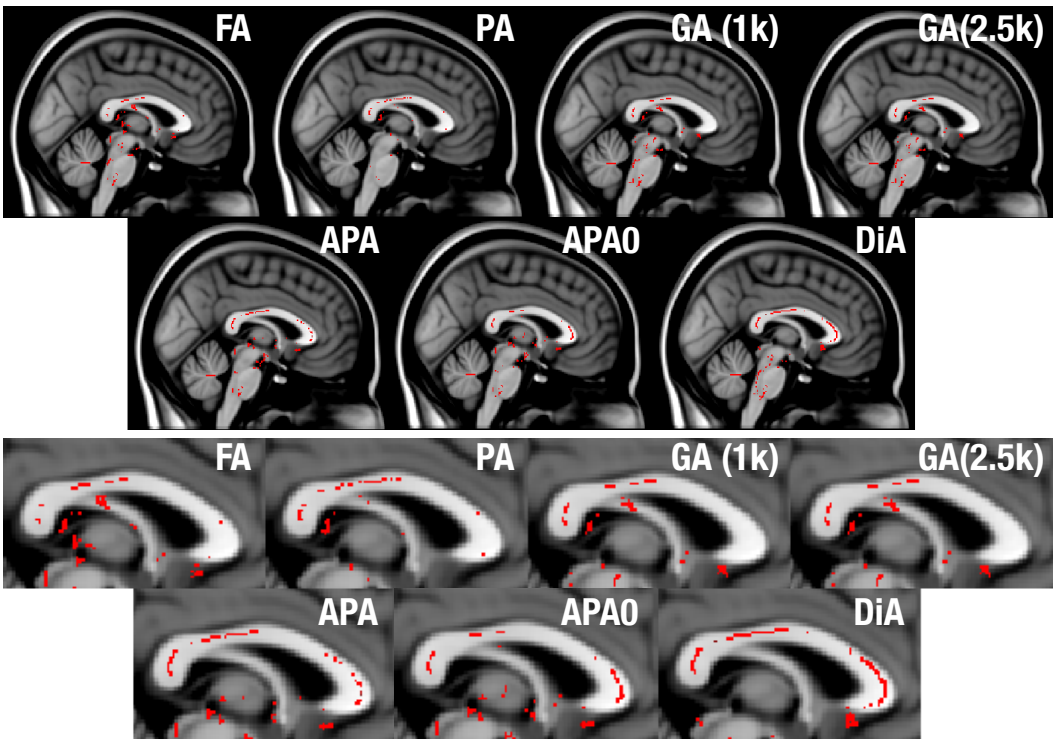

Fig. 2.4.: Significant differences found by statistical test for the Parkinson database, using a voxel-wise analysis over the FA skeleton for the different considered metrics (sagittal view). In red, those points where the considered metric decreases in the PD with respect to the controls with statistical significance above 99% (p< 0.01).

employed to assess sensitivity and specificity of two different tests on the same sample. To that end, we have tested the null hypothesis that APA and FA detect differences in the same regions, and three alternative hypotheses: (1) APA detects more regions than FA (APA-not(FA)); (2) FA detects more regions than APA (FA-not(APA)); and (3) FA and APA detect different number of regions (2-sided). Results can be seen in Table 2.2 where we show the number of regions with $p < 0.01$ for each subsample. Note that, according to the results, APA is able to detect differences in regions not detected by the FA (high values in the row APA-not(FA)), while most of the findings reported by FA are in areas also reported by APA (low values in the row FA-not(APA)).

Next, we test the utility of the new measures using the **PPD database**. Though PD is known to affect the substantia nigra or the gray matter more than the white matter, significant differences have also been reported in several white matter regions such as the corpus callosum (CC), the corticospinal tract and the fornix [2.31]. The aim of this experiment was to test the ability of the proposed measures to detect differences in the white matter. Two different analysis were considered:

1. A voxelwise cross-subject analysis using the FA skeleton with the `randomise` tool from the FSL toolbox (which performs a non-parametric permutation inference over the data) with 500 realizations. Those voxels with $p < 0.01$ (without TFCE) are highlighted in Fig. 2.4. Voxels colored red denote where the considered metric decreases in the PD with respect to the controls.

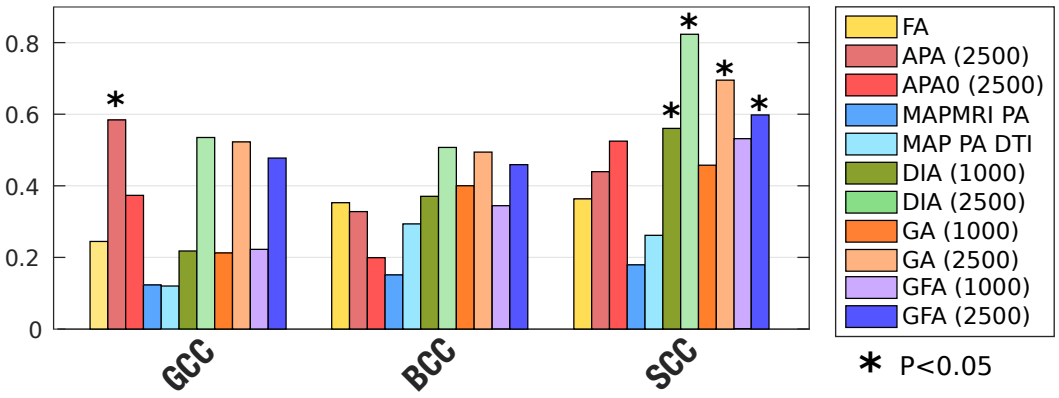

Fig. 2.5.: Absolute value of effect sizes (Absolute Cohen's d) for associations between PD and controls in the Parkinson data base for different metrics and, where appropriate, different b-shells.

2. A ROI oriented analysis: the three regions of the CC (genu –GCC–, body –BCC–, and splenium –SCC–) were identified on the subjects using the JHU WM atlas [2.34]. The average values of the different measures inside each ROI were calculated using the 2% and 98% percentiles. First, effect sizes were estimated using the Cohen's d. Results are depicted in Fig 2.5. Then we carried out a two-sample, pooled variance t-test between controls and patients for each of the measures considered and at each of the three sections of the CC segmented in the JHU WM. Table 2.3 shows the results.

We have focused on the CC since this is the region where previous studies have reported group differences between PD and healthy controls. If we focus on this area in a sagittal plane in Fig. 2.4, the FA and the GA only find some isolated voxels with statistically significant differences. The PA finds some extra voxels, but cannot show its true potential due to the small b-values considered. In contrast, the proposed measures show more differences across the whole CC. All of them, especially the DiA, find differences in the Genu of the CC (GCC). The slightly better performance of the DiA compared to the PA in this experiment supports the logarithmic contrast enhancement in the attenuation signal despite the uneven distribution of DiA values over the range $[0, 1]$ seen in Fig. 2.1.

In the ROI analysis, it is precisely at the SCC where all the measures show the greatest values of Cohen's d, see Fig. 2.5. Once again, DiA shows larger effect sizes, although the GA and GFA (with b=2500 s/mm^2) are also able to find significant differences in this ROI, see Table 2.3. However, note that the DiA shows a statistical significance above 99%. If we focus on the GCC ROI, only the APA is able to find differences. In contrast, the PA calculated with MAP-MRI and the DTI version (proposed in [2.5]) both show very low effect sizes and are unable to detect significant differences in any part of the CC.

Finally, it is important to stress here that the aim of the experiments carried out in this section was not to demonstrate the clinical usefulness of APA in the particular case of MCI and PD, but rather to test its ability to detect differences in the white matter on real datasets. The fact that a particular measure finds significant patient-control differences indicates that the diffusion properties it describes is altered by this particular pathology and/or in this particular data set.

	B val	GCC	BCC	SCC
FA	1000	0.378	0.205	0.192
MAPMRI-PA	all	0.656	0.585	0.517
MAP-PA-DTI	all	0.664	0.290	0.345
GA	1000	0.443	0.151	0.102
	2500	0.063	0.078	0.015
GFA	1000	0.428	0.211	0.059
	2500	0.095	0.102	0.034
APA	1000	0.555	0.296	0.310
	2500	0.038	0.238	0.116
APA_0	1000	0.309	0.676	0.436
	2500	0.180	0.472	0.062
DIA	1000	0.431	0.183	0.047
	2500	0.057	0.071	0.004

Tab. 2.3.: Two-sample, pooled variance, t-tests for each measure and at each section of the corpus callosum: GCC (genu), BCC (body), and SCC (splenium). The p-values represent the probability that the averaged values (using the values between the 2% and 98% percentiles) of each region of the corresponding tract have identical means for both controls and patients. Differences with statistical significance above 99% are highlighted in green, and those with significance over 95% are highlighted in amber.

2.4.3 Sensitivity analysis to acquisition parameters

Next, we tested the dependency of APA on the b-value and the number of diffusion samples taken in a given shell. To that end, we used 5 whole volumes from the CBR data. Each volume was divided in 6 different regions according to their diffusion features. The APA was first calculated and those voxels with APA< 0.1 removed. The remaining voxels were clustered in 6 different groups using k-means (at b=3000 s/mm^2). Each voxel in the white matter was assigned to one cluster using its PA value and the minimum distance. The following test was carried out: first, the variability with the b-value was probed by computing the different anisotropy measures with each of the available shells at b=1200 s/mm^2, b=3000 s/mm^2, or b=5000 s/mm^2. For the variability with the number of diffusion sampling directions, we began with the 60 samples at b=3000 s/mm^2 and uniformly downsampled this set to obtain either 25, 32, 40 and 48 diffusion directions subsets[6]. All the proposed anisotropic diffusion measures were computed for each considered case, and the median value inside each of the six clusters is depicted in Fig. 2.6.

Note that all the measures show a dependence on the b-value: the smallest values tend to increase monotonically with the b-value, whereas the higher values tend to show a monotonic decrease. However, and this is the key point, the separation between clusters remains the same for different b values. This means that the differences in the anisotropy detected by these measures can be detected when using different shells. All the measures show a extremely robust behavior to the variation in the number of sampling directions even in the case of very heavy downsampling.

[6] A "uniform" downsampling of n gradients among the original 60 is here defined as those n directions that minimize the overall electrostatic repulsion energy among all $\binom{60}{n}$ combinations. The optimization is carried out using heuristic rules.

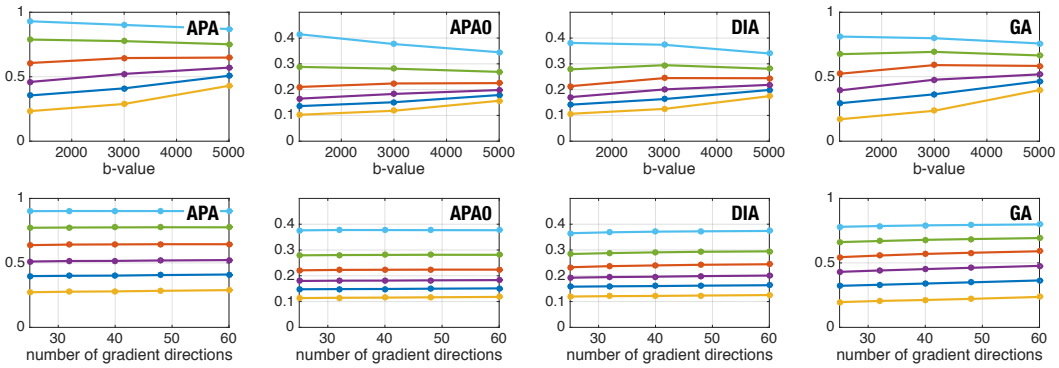

Fig. 2.6.: Evolution of the proposed measures with the b-value (top) and the angular resolution (bottom), using data from a 3T Prisma scanner. The volume has been clustered in 6 different sets (for PA at b=3000 s/mm^2) and the median of each set is shown. Centroids of the data $C_L = \{0.27, 0.41, 0.52, 0.65, 0.78, 0.91\}$.

2.4.4 Execution Times

The long processing times associated with the estimation of EAP-based measures is one of the issues that has hindered a widespread clinical adoption of the PA. In comparison, the linear nature of SH needed to estimate the APA results in a significant reduction of the calculation time, that can be several orders of magnitude faster than whole EAP-based techniques.

To test this extreme, a volume from the PPD was used here to compute APA and PA measures on a quad-core Intel(R) Core(TM) i7-4770K 3.50GHz processor under Ubuntu Linux 16.04 SO. PA was calculated using the two available shells with MAP-MRI using the DIPY library under Python 3.6.4 (scipy 1.0.0)[7]. APA was implemented using one single shell in MATLAB R2013b without multi-threading. The calculation of APA took **3.17**s, while MAP-MRI-PA 2h 53min for the same volume. Though raw execution times are an ambiguous performance index (they can be dramatically improved, for example, via GPU acceleration), they give a reasonable idea of the relative complexity of each method. The calculation of the APA for the whole volume is almost instantaneous, which makes it feasible for practical studies.

2.5 Discussion

The intention of the new anisotropy measure proposed here, APA, is not to exactly replicate a measure like the PA but, using a similar philosophy, to infer anatomical information with comparable discrimination power as the PA estimated using EAP-based methods (mainly, MAP-MRI). The original PA calculated from the EAP explicitly accounts for the radial behavior of the diffusion signal, which also needs to be sampled extensively. For the APA calculation, the radial behavior is not sampled but modeled as a mono-exponential decay.

One might anticipate that the computation of the whole EAP would provide a more specific and sensitive measure than the APA, since the anisotropy information encoded in the radial

[7]The PA calculation is not available in the public distribution of DIPY. The current implementation has been kindly provided by Dr. Fick.

direction is otherwise neglected in the APA. This would be the case for a dense sampling of the q-space, or at least for a truly sparse one. However, actual samplings comprise a structured, regular grid of gradient directions describing a reduced number of shells (b-values). This way, the measured radial information does not suffice to describe the behavior of the attenuation signal in detail, so that a strong regularization of the prior model is required, leading to a heavily low-pass filtered estimation of the true EAP. As we report in the results with clinical data (see the PPD experiment), this issue may cause the original PA to lack the expected discriminant power, or even to have less discriminant power than conventional DT-MRI.

Moreover, Fig. 2.2 suggests that the lack of a proper radial description of the diffusion signal, and the consequent over-regularization of the problem, may cause EAP estimators like MAP-MRI to completely blur out white matter regions such as the thalamus or the caudate, which are more clearly defined by the APA.

The experiments carried out in this paper confirm that the proposed measures show a discriminant power that is superior to traditional DT-MRI markers and, in some occasions, even over the PA. We are aware that the finding of more significant differences between groups does not directly imply that one method is better than other. However, under the assumption that the group differences represented here are true positives (which is endorsed by the related literature), the proposed APA may be reasonably attributed a higher sensitivity.

The main advantage of the proposed measures, when compared to the PA, is that they can be calculated from a reduced set of measures leading to a significant reduction in data acquisition time. Initially they are intended for data collected with one shell (b-value), but the methodology can be easily extrapolated to more than one. In addition, the experiments with different gradient directions carried out over the CBR data set have shown a robustness to differences in the number of gradient directions, which will allow a further reduction in the amount of requisite data, making it compatible with contemporary acquisition protocols widely deployed in studies, with as few as 64 gradient directions. It is a common practice to acquire two shells (b=[1000, 3000] s/mm^2, for instance) to estimate classical DT-MRI parameters, like the FA and MD, but also advanced models (DKI, HARDI, CHARMED, etcetera). The APA (or the DiA) proposed here can also be calculated with no additional effort and without changing the acquisition protocol.

Moreover, since the computation of the APA avoids the estimation of the actual EAP, it can be done in a fast and robust way, i.e., without imposing a computational burden to the standard protocols. A whole volume can be processed in a matter of seconds while the processing of the original PA usually takes hundreds of minutes, which obviously limits its applicability.

On the other hand, the major drawback of the APA is the explicit assumption of a specific radial behavior for the diffusion, which cannot characterize the whole q-space. As a consequence, the selection of the b-value may impact the absolute values of the measures and difficult multi-centre studies. However, we have shown that the relative anatomical differences between different regions are preserved regardless of the absolute changes in APA values: as long as the same b-value is preserved across each study, the results of different clinical trials in terms of increased/decreased anisotropy should be broadly compared. This is by no means something new to diffusion imaging: it is well-known that a change in the

acquisition parameters (number of gradients, b-value, resolution, scanner vendor, etcetera) seriously affects scalar measures like the FA or the MD [2.24, 2.35].

2.6 Conclusions

The newly introduced APA (or, alternatively, the DiA) can be easily integrated into the processing pipeline of currently existing single-shell dMRI protocols and databases to unveil anatomical details that remain hidden in traditional-FA-based studies. Its simplicity (it is mainly based on linear fitting of Spherical Harmonics coefficients) prevents the need for cumbersome parameter tuning procedures via cross-validation or trial and error, so that the same setting-up will suit virtually any acquisition protocol out-of-the-box, regardless of the number of acquired gradients and/or b-values.

In the case of multi-shell protocols, and whenever the accuracy in the computation of the full PA gets compromised by the lack of a detailed sampling of the whole q-space, the proposed measures are a robust and useful alternative.

Software

The full implementation of AMURA, including the APA and the DiA as described here, may be downloaded for Matlab© and Octave, together with use-case examples and test data, from: `http://www.lpi.tel.uva.es/AMURA`.

Acknowledgments

This work was supported by Ministerio de Ciencia e Innovación of Spain with research grants RTI2018-094569-B-I00 and PRX18/00253 (Estancias de profesores e investigadores senior en centros extranjeros). DKJ is supported by a Wellcome Trust Investigator Award (096646/Z/11/Z) and a Wellcome Trust Strategic Award (104943/Z/14/Z)

The authors thank Álvaro Planchuelo for discussion and his insight about the statistical analysis of the clinical data. The authors also thank the contributors of DIPY project (`http://nipy.org/dipy/`) for providing the MAP-MRI basis implementation and specially to Rutger Fick for his implementation for PA calculation and interesting discussion about MAP-MRI model.

Data collection and sharing for this project was provided by (1) the *Human Connectome Project* (HCP; Principal Investigators: Bruce Rosen, M.D., Ph.D., Arthur W. Toga, Ph.D., Van J. Weeden, MD). HCP funding was provided by the National Institute of Dental and Craniofacial Research (NIDCR), the National Institute of Mental Health (NIMH), and the National Institute of Neurological Disorders and Stroke (NINDS). HCP data are disseminated by the Laboratory of Neuro Imaging at the University of Southern California; (2) the *High-quality diffusion-weighted imaging of Parkinson's disease* data base, Cyclotron Research Centre, University of Liège; (3) Cardiff University Brain Research Imaging Centre, provided

by Chantal Tax. The data were acquired at the UK National Facility for In Vivo MR Imaging of Human Tissue Microstructure funded by the EPSRC (grant EP/M029778/1), and The Wolfson Foundation. (4) Data collection and sharing for this project was also funded by the Alzheimer's Disease Neuroimaging Initiative (ADNI) (National Institutes of Health Grant U01 AG024904) and DOD ADNI (Department of Defense award number W81XWH-12-2-0012). ADNI is funded by the National Institute on Aging, the National Institute of Biomedical Imaging and Bioengineering, and through generous contributions from the following: AbbVie, Alzheimer's Association; Alzheimer's Drug Discovery Foundation; Araclon Biotech; BioClinica, Inc.; Biogen; Bristol-Myers Squibb Company; CereSpir, Inc.; Cogstate; Eisai Inc.; Elan Pharmaceuticals, Inc.; Eli Lilly and Company; EuroImmun; F. Hoffmann-La Roche Ltd and its affiliated company Genentech, Inc.; Fujirebio; GE Healthcare; IXICO Ltd.; Janssen Alzheimer Immunotherapy Research & Development, LLC.; Johnson & Johnson Pharmaceutical Research & Development LLC.; Lumosity; Lundbeck; Merck & Co., Inc.; Meso Scale Diagnostics, LLC.; NeuroRx Research; Neurotrack Technologies; Novartis Pharmaceuticals Corporation; Pfizer Inc.; Piramal Imaging; Servier; Takeda Pharmaceutical Company; and Transition Therapeutics. The Canadian Institutes of Health Research is providing funds to support ADNI clinical sites in Canada. Private sector contributions are facilitated by the Foundation for the National Institutes of Health (`www.fnih.org`). The grantee organization is the Northern California Institute for Research and Education, and the study is coordinated by the Alzheimer's Therapeutic Research Institute at the University of Southern California. ADNI data are disseminated by the Laboratory for Neuro Imaging at the University of Southern California.

Conflict of interest

The authors declare that there is no conflict of interest.

Appendices

2.A Isotropic Ensamble Average Propagator

In the main document, section 3.1, we explicitly calculate the inner product that defines the PA by using the simplification in eq. (9), yielding an anisotropy metric related to the PA for a specific shell, namely the APA. After [2.5], this metric requires the definition of an isotropic signal equivalent to the mono-exponential model. The rationale behind [2.5] is that the EAP can be averaged over the directional coordinates to obtain the closest isotropic signal to the original one. By using

$$P(\mathbf{R}) = \int_{\mathbb{R}^3} E(\mathbf{q}) e^{-2\pi j \mathbf{q}\cdot\mathbf{R}} d\mathbf{q} = \mathcal{F}\left\{|E(\mathbf{q})|\right\}(\mathbf{R}), \tag{2.27}$$

we have:

$$P_I(\mathbf{R}) \triangleq \frac{1}{4\pi}\int_S P(\mathbf{R}) d\mathbf{r} = \frac{1}{4\pi}\int_S \left(\int_{\mathbb{R}^3} E(\mathbf{q}) e^{-2\pi j \mathbf{q}\cdot\mathbf{R}} d\mathbf{q}\right) d\mathbf{r}, \tag{2.28}$$

where $\|\mathbf{r}\| = 1$ and $\mathbf{R} = R\mathbf{r}$. The inner integral in $\mathbb{R}^3$ is usually computed in spherical coordinates, so that $d\mathbf{q} = q^2 d\mathbf{u}\, dq$ and a straightforward manipulation yields:

$$\begin{aligned} P_I(\mathbf{R}) &= \frac{1}{4\pi}\int_0^\infty\!\!\int_S q^2 E(\mathbf{q}) \left(\int_S e^{-2\pi j \mathbf{q}\cdot\mathbf{R}} d\mathbf{r}\right) d\mathbf{u}\, dq = \frac{1}{2}\int_0^\infty\!\!\int_S q^2 E(\mathbf{q}) \frac{J_{1/2}(2\pi qR)}{\sqrt{qR}} d\mathbf{u}\, dq \\ &= \frac{1}{2\sqrt{R}}\int_0^\infty q^{3/2} J_{1/2}(2\pi qR) \left(\int_S E(\mathbf{q}) d\mathbf{u}\right) d\mathbf{q}, \end{aligned} \tag{2.29}$$

where $J_{1/2}$ stands for Bessel's function of the first kind with index $1/2$. The meaning of eq. (2.29) is that the isotropic EAP defined as the directional average of the original EAP becomes the Bessel transform of the isotropic diffusion signal defined as the directional average of the original diffusion signal. In other words, the isotropic equivalent to the EAP corresponds to a diffusion signal that is indeed computed in the same manner:

$$P_I(\mathbf{R}) = \frac{1}{4\pi}\int_S P(\mathbf{R}) d\mathbf{r} \quad \longleftrightarrow \quad E_I(\mathbf{q}) = \frac{1}{4\pi}\int_S E(\mathbf{u}) d\mathbf{u}. \tag{2.30}$$

By assuming a mono-exponential model of $E(\mathbf{q})$ itself, we can compute:

- The (squared) ℓ_2 norm of $E(\mathbf{q})$:

$$\begin{aligned} \|E\|^2 &= \int_0^\infty\!\!\int_S q^2 \left|\exp\left(-4\pi^2\tau q^2 D(\mathbf{u})\right)\right|^2 d\mathbf{u}\, dq = \int_S\!\!\int_0^\infty q^2 \exp\left(-8\pi^2\tau q^2 D(\mathbf{u})\right) dq\, d\mathbf{u} \\ &= \int_S \frac{\sqrt{\pi}}{4\left(8\pi^2\tau D(\mathbf{u})\right)^{3/2}} d\mathbf{u}. \end{aligned} \tag{2.31}$$

- The (squared) ℓ_2 norm of $E_I(\mathbf{q})$:

$$\begin{aligned} \|E_I\|^2 &= \int_0^\infty\!\!\int_S q^2 \left|\frac{1}{4\pi}\int_S \exp\left(-4\pi^2\tau q^2 D(\mathbf{v})\right) d\mathbf{v}\right|^2 d\mathbf{u}\, dq \\ &= 4\pi\int_0^\infty q^2 \left|\frac{1}{4\pi}\int_S \exp\left(-4\pi^2\tau q^2 D(\mathbf{v})\right) d\mathbf{v}\right|^2 dq \\ &= \frac{1}{4\pi}\int_0^\infty q^2 \left(\int_S \exp\left(-4\pi^2\tau q^2 D(\mathbf{u})\right) d\mathbf{u}\right)\left(\int_S \exp\left(-4\pi^2\tau q^2 D(\mathbf{v})\right) d\mathbf{v}\right) dq \\ &= \frac{1}{4\pi}\int_S\!\!\int_S \left(\int_0^\infty q^2 \exp\left(-4\pi^2\tau q^2 \left(D(\mathbf{u}) + D(\mathbf{v})\right)\right)\right) d\mathbf{u}\, d\mathbf{v} \\ &= \frac{1}{4\pi}\int_S\!\!\int_S \frac{\sqrt{\pi}}{4\left(4\pi^2\tau\left(D(\mathbf{u}) + D(\mathbf{v})\right)\right)^{3/2}} d\mathbf{u}\, d\mathbf{v}. \end{aligned} \tag{2.32}$$

- The inner product between $E(\mathbf{q})$ and $E_I(\mathbf{q})$:

$$\begin{aligned} \langle E, E_I\rangle &= \int_0^\infty\!\!\int_S q^2 \left[\exp\left(-4\pi^2\tau q^2 D(\mathbf{u})\right)\left(\frac{1}{4\pi}\int_S \exp\left(-4\pi^2\tau q^2 D(\mathbf{v})\right) d\mathbf{v}\right)\right] d\mathbf{u}\, dq \\ &= \frac{1}{4\pi}\int_S\!\!\int_S \left(\int_0^\infty q^2 \exp\left(-4\pi^2\tau q^2\left(D(\mathbf{u}) + D(\mathbf{v})\right)\right)\right) d\mathbf{u}\, d\mathbf{v} \\ &= \frac{1}{4\pi}\int_S\!\!\int_S \frac{\sqrt{\pi}}{4\left(4\pi^2\tau\left(D(\mathbf{u}) + D(\mathbf{v})\right)\right)^{3/2}} d\mathbf{u}\, d\mathbf{v} = \|E_I\|^2. \end{aligned} \tag{2.33}$$

- The cosine between both two signals, which implicitly defines the PA:

$$\cos^2\left(\angle[E,E_I]\right)=\cos^2\theta_{E,E_I}=\frac{\int_S\int_S\left(D(\mathbf{u})+D(\mathbf{v})\right)^{-3/2}d\mathbf{u}\,d\mathbf{v}}{4\pi\int_S\left(2D(\mathbf{u})\right)^{-3/2}d\mathbf{u}}. \tag{2.34}$$

Using this complete approach, we achieve a a closed form of the APA that involves the computation of a quadratic form on the measured values at each voxel. Pursuing an analogous formulation to that in AMURA [2.18], in the main document we propose an alternative formulation leading to a linear computation with negligible deviations from the model. To that end, instead of using eq. (2.30) for the isotropic equivalent, we use the following expression instead::

$$E_I(\mathbf{q})\stackrel{\Delta}{=}\exp\left(-4\pi^2\tau q^2\ D_{\text{AV}}\right), \tag{2.35}$$

with

$$D_{\text{AV}}=\frac{1}{4\pi}\int_S D(\mathbf{u})d\mathbf{u}. \tag{2.36}$$

2.B Practical implementations

Note that the computation of $\|E_I\|^2=\langle E,E_I\rangle$ in eq. (2.30) requires evaluating a double surface integral in the orientation variables $\mathbf{u}$ and $\mathbf{v}$. In a practical implementation, such integrals are computed based on spherical harmonics expansions. In precise terms, let $\{\mathbf{u}_n\}_{n=1}^N$ be the set of the N acquired gradients within the measured shell; let $\{Y_j(\mathbf{u})\}_{j=1}^M$ be the set of the M first (low order) spherical harmonics (typically $M<N$). The coefficients $\{c_j\}_{j=1}^M$ of a given orientation function, $S(\mathbf{u})$, in this basis will be fitted as a Laplacian-regularized least squares problem:

$$\mathbf{S}\simeq\mathbf{BC}\Rightarrow\mathbf{C}=\left(\mathbf{B}^T\mathbf{B}+\lambda\mathbf{L}^2\right)^{-1}\mathbf{B}^T\mathbf{S}, \tag{2.37}$$

where the $M\times 1$ vector $\mathbf{C}$ stacks the coefficients c_j; the $N\times 1$ vector $\mathbf{S}$ stacks the measurements of the orientation function, $S(\mathbf{u}_n)$; the $N\times M$ matrix $\mathbf{B}$ stacks the values of the basis functions, $\mathbf{B}_{n,j}=Y_j(\mathbf{u}_n)$; λ is the Laplace-Beltrami regularization parameter so that the $M\times M$ matrix $\mathbf{L}$ contains the eigenvalues of spherical harmonics for the Laplacian (we fix it to constant value of 0.006 in all cases). Since the $0-$th order spherical harmonic encodes the DC component of the signal, the integral of the orientation function over the unit sphere reduces to a scaled version of its c_0 coefficient. For example, eq. (2.31) can be estimated as:

$$\|E\|^2=\frac{\sqrt{\pi}}{4\left(8\pi^2\tau\right)^{3/2}}\sqrt{4\pi}\,\mathbf{s}\bar{\mathbf{D}}, \tag{2.38}$$

where $\mathbf{s}$ stands for the first row of $\left(\mathbf{B}^T\mathbf{B}+\lambda\mathbf{L}^2\right)^{-1}\mathbf{B}^T$ and the $N\times 1$ vector $\bar{\mathbf{D}}$ stacks the N values of $D(\mathbf{u}_n)^{-3/2}$. In order to compute eqs. (2.32) and (2.33), we arrange a $N\times N$ matrix $\bar{\bar{\mathbf{D}}}$ whose entries are $\bar{\bar{\mathbf{D}}}_{n_1,n_2}=\left(D(\mathbf{u}_{n_1})+D(\mathbf{u}_{n_2})\right)^{-3/2}$. Then:

$$\|E_I\|^2=\langle E,E_I\rangle=\frac{\sqrt{\pi}}{16\pi\left(4\pi^2\tau\right)^{3/2}}\,4\pi\,\mathbf{s}\bar{\bar{\mathbf{D}}}\mathbf{s}^T, \tag{2.39}$$

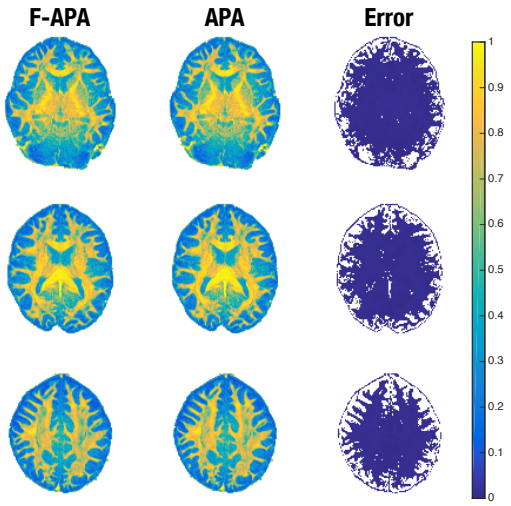

Fig. 2.7.: Visual comparison of the APA calculated with the two approaches, full (F-APA) and simplified (APA), together with the absolute error. Slices 42, 52 and 65 of MGH1007 volume from the HCP are used. Both measures have been calculated using using b=3000 s/mm^2.

where the left product with $\mathbf{s}$ stands for the outermost integral in eq. (2.32) in the variable $\mathbf{v}$ for each constant $\mathbf{u}$ (each column $\mathbf{u}_{n_2}$), meanwhile the right product with $\mathbf{s}^T$ stands for the innermost integral in eq. (2.32) in the variable $\mathbf{u}$ for each constant $\mathbf{v}$ (each row $\mathbf{u}_{n_1}$). This way, the computational complexity of computing simple surface integrals remains linear with the number of sampled gradients, $\mathcal{O}(N)$, while the complexity of double surface integrals becomes $\mathcal{O}(N^2)$.

2.C Comparison of both APA implementations

In order to compare the results given by the simplified APA implementation proposed in the main document to the complete implementation described in this supplementary material, an experiment is carried out. For the sake of comparison, we will denote full-APA (F-APA) to the complete implementation derived from eq. (2.34), and simply APA to the fast approach used along the paper, derived from eq. (2.35). For a visual comparison we use three slices from the HCP volume MGH1007 using a single shell for b=3000 s/mm^2. We consider the absolute error as the quality measure:

$$\text{Error}(\mathbf{x}) = |\text{APA}(\mathbf{x}) - \text{F-APA}(\mathbf{x})|.$$

A mask is used in order to limit the measurement of the error to the white matter area. Both measures are bounded in the interval [0,1] and so will be the error. A visual comparison for slices (42, 52, 65) is shown in Fig. 2.7. The average error for the white matter is calculated for the whole volume at b=3000 s/mm^2 and b=5000 s/mm^2 and it can be found in Table 2.4. Note that the average error is smaller than 1% for both shells, which implies that both measures are practically the same and both provide very similar results. In addition, from the visual comparison in Fig. 2.7, we can also conclude that the error is uniformly distributed in the white matter, which, from a practical view point, it can be seen as a very small bias in

the measure. Some of the experiments with real data from the main document were also redone for F-APA with no noticeable differences from those with APA.

Shell (s/mm^2)	3000	5000
Average error	0.0083	0.0083

Tab. 2.4.: Average absolute error between F-APA and APA for the whole MGH1007 volume. Two different shells are considered.

Although both methods provide similar results, in this work we have opted for APA, for a matter of simplicity. As previously stated, the computational complexity of computing simple surface integrals is $\mathcal{O}(N)$, while the complexity of double surface integrals becomes $\mathcal{O}(N^2)$. Since APA is only based on simple integrals, similar results can be obtained in reduced computation time. In order to test it on real data, we measure the execution times of computing the metrics over the MGH1007 volume previously described. The experiment is run on a quad-core Intel(R) Core(TM) i7-4770K 3.50GHz processor under Ubuntu Linux 16.04 So using one single shell in MATLAB R2013b without multi-threading. The results are reported in Table 2.5. As a consequence of the simplicity on the implementation of APA, it shows execution times 200 faster than F-APA.

Thus, since the implementation error is so small and the gain in execution time is so high, we have opted to use the fast implementation thorough the whole paper.

Shell (s/mm^2)	3000	5000
APA	6.05 s	12.24 s
F-APA	1152 s	2738.75s

Tab. 2.5.: Estimated execution time for the calculation of APA and F-APA for the MGH1007 volume.

Bibliography

[2.1] P. Basser, C. Pierpaoli, Microstructural features measured using diffusion tensor imaging, J Magn Reson B 111 (3) (1996) 209–219.

[2.2] B. Hansen, S. N. Jespersen, Kurtosis fractional anisotropy, its contrast and estimation by proxy, Scientific reports 6 (2016) 23999.

[2.3] D. S. Tuch, T. G. Reese, M. R. Wiegell, V. J. Wedeen, Diffusion MRI of complex neural architecture, Neuron 40 (2003) 885–895.

[2.4] E. Özarslan, T. M. Sepherd, B. C. Vemuri, S. J. Blackband, T. H. Mareci, Resolution of complex tissue microarchitecture using the Diffusion Orientation Transform (DOT), NeuroImage 31 (2006) 1086–1103.

[2.5] E. Özarslan, C. G. Koay, T. M. Shepherd, M. E. Komlosh, M. O. Irfanoğlu, C. Pierpaoli, P. J. Basser, Mean apparent propagator (MAP) MRI: a novel diffusion imaging method for mapping tissue microstructure, NeuroImage 78 (2013) 16–32.

[2.6] V. J. Wedeen, P. Hagmann, W.-Y. I. Tseng, T. G. Reese, R. M. Weisskoff, Mapping complex tissue architecture with diffusion spectrum magnetic resonance imaging, Magnetic resonance in medicine 54 (6) (2005) 1377–1386.

[2.7] Y.-C. Wu, A. L. Alexander, Hybrid diffusion imaging, NeuroImage 36 (3) (2007) 617–629.

[2.8] Y.-C. Wu, A. S. Field, A. L. Alexander, Computation of diffusion function measures in q-space using magnetic resonance hybrid diffusion imaging, IEEE transactions on medical imaging 27 (6) (2008) 858–865.

[2.9] M. Descoteaux, R. Deriche, D. Le Bihan, J.-F. Mangin, C. Poupon, Diffusion propagator imaging: using Laplace's equation and multiple shell acquisitions to reconstruct the diffusion propagator, in: International Conference on Information Processing in Medical Imaging, Springer, 2009, pp. 1–13.

[2.10] M. Descoteaux, R. Deriche, D. Le Bihan, J.-F. Mangin, C. Poupon, Multiple q-shell diffusion propagator imaging, Medical image analysis 15 (4) (2011) 603–621.

[2.11] A. P. Hosseinbor, M. K. Chung, Y.-C. Wu, A. L. Alexander, Bessel fourier orientation reconstruction (BFOR): An analytical diffusion propagator reconstruction for hybrid diffusion imaging and computation of q-space indices, NeuroImage 64 (2013) 650–670.

[2.12] L. Ning, C.-F. Westin, Y. Rathi, Estimating diffusion propagator and its moments using directional radial basis functions, IEEE Trans Med Imag 34 (10) (2015) 2058–2078.

[2.13] A. V. Avram, J. E. Sarlls, A. S. Barnett, E. Özarslan, C. Thomas, M. O. Irfanoglu, E. Hutchinson, C. Pierpaoli, P. J. Basser, Clinical feasibility of using mean apparent propagator (MAP) MRI to characterize brain tissue microstructure, NeuroImage 127 (2016) 422–434.

[2.14] R. H. Fick, D. Wassermann, E. Caruyer, R. Deriche, MAPL: Tissue microstructure estimation using Laplacian-regularized MAP-MRI and its application to HCP data, NeuroImage 134 (2016) 365–385.

[2.15] A. P. Hosseinbor, M. K. Chung, Y.-C. Wu, J. O. Fleming, A. S. Field, A. L. Alexander, Extracting quantitative measures from EAP: A small clinical study using BFOR, in: Med Image Comput Comput Assist Interv, Vol. 7511, Springer, 2012, pp. 280–287.

[2.16] R. H. Fick, M. Daianu, M. Pizzolato, D. Wassermann, R. E. Jacobs, P. M. Thompson, T. Town, R. Deriche, Comparison of biomarkers in transgenic alzheimer rats using multi-shell diffusion MRI, in: International Conference on Medical Image Computing and Computer-Assisted Intervention, Springer, 2016, pp. 187–199.

[2.17] A. S. Bernstein, Advanced diffusion mri techniques: Methodological development and clinical application, Ph.D. thesis, The University of Arizona (2019).

[2.18] S. Aja-Fernández, R. de Luis-García, M. Afzali, M. Molendowska, T. Pieciak, A. Tristán-Vega, Micro-structure diffusion scalar measures from reduced MRI acquisitions, PLOS-ONE 15 (3) (2019) e0229526.

[2.19] P. Callaghan, C. Eccles, Y. Xia, Nmr microscopy of dynamic displacements: k-space and q-space imaging, Journal of Physics E: Scientific Instruments 21 (8) (1988) 820.

[2.20] P. J. Basser, J. Mattiello, D. LeBihan, MR diffusion tensor spectroscopy and imaging, Biophysical journal 66 (1) (1994) 259–267.

[2.21] P. J. Basser, Relationships between diffusion tensor and q-space MRI, Magnetic Resonance in Medicine 47 (2) (2002) 392–397.

[2.22] R. G. Gallager, Principles of digital communication, Cambridge University Press Cambridge, Cambridge,UK, 2008.

[2.23] M. Descoteaux, E. Angelino, S. Fitzgibbons, R. Deriche, Apparent Diffusion Profile estimation from High Angular Resolution Diffusion Images: estimation and applications, Magn. Reson. Med. 56 (2) (2006) 395–410.

[2.24] S. Aja-Fernández, T. Pieciak, A. Tristán-Vega, G. Vegas-Sánchez-Ferrero, V. Molina, R. de Luis-García, Scalar diffusion-MRI measures invariant to acquisition parameters: a first step towards imaging biomarkers, Magn. Reson. Imag. 53 (2018) 123–133.

[2.25] A. Tristán-Vega, A novel framework for the study of neural architectures in the human brain with diffusion MRI, Ph.D. thesis, Universidad de Valladolid, Valladolid, Spain, https://www.lpi.tel.uva.es/thesis (2009).

[2.26] E. Özarslan, B. C. Vemuri, T. H. Mareci, Generalized scalar measures for diffusion MRI using trace, variance, and entropy, Magn Reson Med 53 (4) (2005) 866–876.

[2.27] D. S. Tuch, Q–Ball imaging, Magn Reson Med 52 (2004) 1358–1372.

[2.28] E. Ziegler, M. Rouillard, E. André, T. Coolen, J. Stender, E. Balteau, C. Phillips, G. Garraux, Mapping track density changes in nigrostriatal and extranigral pathways in Parkinson's disease, Neuroimage 99 (2014) 498–508.

[2.29] S. L. Risacher, A. J. Saykin, J. D. West, L. Shen, H. A. Firpi, B. C. McDonald, Baseline mri predictors of conversion from mci to probable ad in the adni cohort, Curr Alzheimer Res 6 (4) (2009) 347-361.

[2.30] A. Zavaliangos-Petropulu, T. M. Nir, S. I. Thomopoulos, R. I. Reid, M. A. Bernstein, B. Borowski, C. R. Jack Jr., M. W. Weiner, N. Jahanshad, P. M. Thompson, Diffusion mri indices and their relation to cognitive impairment in brain aging: The updated multi-protocol approach in adni3, Frontiers in Neuroinformatics 13 (2019) 2.

[2.31] C. Atkinson-Clement, S. Pinto, A. Eusebio, O. Coulon, Diffusion tensor imaging in Parkinson's disease: Review and meta-analysis, Neuroimage: Clinical 16 (2017) 98–110.

[2.32] J.-D. Tournier, R. Smith, D. Raffelt, R. Tabbara, T. Dhollander, M. Pietsch, D. Christiaens, B. Jeurissen, C.-H. Yeh, A. Connelly, Mrtrix3: A fast, flexible and open software framework for medical image processing and visualisation, NeuroImage 202 (2019) 116137. doi:https://doi.org/10.1016/j.neuroimage.2019.116137.

[2.33] S. Smith, M. Jenkinson, H. Johansen-Berg, et al., Tract-based spatial statistics: Voxelwise analysis of multi-subject diffusion data, Neuroimage 31 (2006) 1487–1505.

[2.34] S. Mori, S. Wakana, P. C. Van Zijl, L. Nagae-Poetscher, MRI atlas of human white matter, Elsevier, 2005.

[2.35] G. Barrio-Arranz, R. de Luis-García, A. Tristán-Vega, M. Martín-Fernández, S. Aja-Fernández, Impact of MR acquisition parameters on DTI scalar indexes: a tractography based approach, PloS one 10 (10) (2015) e0137905.

3

Moment-based representation of the diffusion inside the brain from reduced DMRI acquisitions: generalized AMURA

Santiago Aja-Fernández, Tomasz Pieciak, Carmen Martín-Martín, Álvaro Planchuelo-Gómez, Rodrigo de Luis-García and Antonio Tristán-Vega

Laboratorio de Procesado de Imagen (LPI), ETSI Telecomunicación, Universidad de Valladolid, Spain

Abstract: AMURA (Apparent Measures Using Reduced Acquisitions) was originally proposed as a method to infer micro-structural information from single-shell acquisitions in diffusion MRI. It reduces the number of samples needed and the computational complexity of the estimation of diffusion properties of tissues by assuming the diffusion anisotropy is roughly independent on the b-value. This simplification allows the computation of simplified expressions and makes it compatible with standard acquisition protocols commonly used even in clinical practice. The present work proposes an extension of AMURA that allows the calculation of general moments of the diffusion signals that can be applied to describe the diffusion process with higher accuracy. We provide simplified expressions to analytically compute a set of scalar indices as moments of arbitrary orders over either the whole 3-D space, particular directions, or particular planes. The existing metrics previously proposed for AMURA (RTOP, RTPP and RTAP) are now special cases of this generalization. An extensive set of experiments is performed on public data and a clinical clase acquired with a standard type acquisition. The new metrics provide additional information about the diffusion processes inside the brain.

Originally published as: *Aja-Fernández, Santiago and Pieciak, Tomasz and Martín-Martín, Carmen and Planchuelo-Gómez, Álvaro and de Luis-García, Rodrigo and Tristán-Vega, Antonio, Moment-based representation of the diffusion inside the brain from reduced DMRI acquisitions: generalized AMURA, Medical Image Analysis, 102356, 2022*

3.1 Introduction

The name Diffusion Magnetic Resonance Imaging (DMRI) describes a set of diverse MRI imaging techniques with the ability of extracting *in vivo* relevant information regarding the random, anisotropic diffusion of water molecules that underlie the structured nature of

different living tissues [3.1, 3.2, 3.3]. It has attracted an extraordinary interest among the scientific community over the last two decades due to the relationships found between a number of neurological and neurosurgical pathologies and alterations in the white matter as revealed by an increasing number of DMRI studies [3.4, 3.5, 3.6, 3.7, 3.8].

In practice, in order to estimate the properties of the diffusion from the acquired data, different techniques can be adopted, being the diffusion tensor [3.9, DT] the most common in clinical studies. However, the diffusion mechanisms cannot be fully described by DT because of the oversimplified Gaussian fitting. More evolved techniques with more degrees-of-freedom have been proposed, such as Diffusion Kurtosis Imaging [3.10, DKI] or methods based on High Angular Resolution Diffusion Imaging [3.11, 3.12, 3.13, HARDI]. The trend over the last decade has been to acquire a large number of diffusion-weighted images distributed over several shells (i.e. with several gradient strengths) and with moderate-to-high b-values to estimate more advanced diffusion descriptors, such as the Ensemble Average diffusion Propagator [3.14, 3.15, 3.16, 3.17, EAP]. This estimation relies on model-free, non parametric approaches that can accurately describe most of the relevant diffusion phenomena.

Regardless of the method selected for estimating the diffusion properties, in order to be used in clinical studies, the information provided is usually translated into a set of scalar metrics such as: the Fractional Anisotropy (FA) or Mean Diffusivity (MD) [3.18, 3.19] for the DT approach, the Kurtosis coefficient for DKI [3.10, 3.20] or the return-to-origin (RTOP), the return-to-plane (RTPP), return-to-axis probabilities (RTAP) and mean-squared-displacement (MSD) [3.21, 3.14, 3.15, 3.22, 3.16], or the Propagator Anisotropy (PA) [3.15] for EAP imaging.

There are two main limitations with those techniques that rely on the estimation of the EAP: (1) the need of acquiring very large data sets with many $\mathbf{q}$–space samples in different shells; and (2) the estimation of the EAP involves important computational burdens with very long processing times. These two issues have slowed down the generalization of this methodology among the clinical community, despite the relevance of its scalar measures in the description of the brain micro-structure, see for instance [3.23, 3.24, 3.25, 3.26]. In order to overcome these problems, in [3.27, 3.28] authors proposed a new technique called "Apparent Measures Using Reduced Acquisitions" (AMURA) for the computation of EAP imaging-related markers, namely RTOP, RTPP, RTAP and PA without explicitly calculating the EAP. AMURA can mimic the sensitivity of EAP-based measures to microstructural changes when a reduced amount of data distributed in a few shells (even one) is available. In order to do so, AMURA assumes a prior model for the behavior of the radial $\mathbf{q}$–space instead of trying to numerically describe it, yielding simplified expressions that can be computed easily even from single-shell acquisitions. It has proved its potential in some preliminary studies with clinical data (Parkinson and Mild Cognitive Impairment [3.27, 3.28]) and recently in real clinical studies in migraine and headache [3.29, 3.30].

The present work proposes a generic formulation of AMURA that allows the calculation of generalized moments that can be better suited to describe certain anatomies, both healthy and pathological. The existing metrics (RTOP, RTPP and RTAP) can be seen as special cases of this generalization. To that end, the same constrained model for radial diffusion used by [3.27] is adopted here, i.e., the diffusion anisotropy is assumed to be independent of the actual b-value of the measured shells. We use this simplification to derive alternative

simplified expressions for the moments of the acquired magnitude signal and the EAP from single-shell acquisitions.

Our hypothesis is that the new metrics based on moments representation provide extra information about the diffusion that can highlight additional interesting properties of certain brain structures compared to AMURA. In order to evaluate whether the calculation of general moments can be used as an alternative approach to standard AMURA in the analysis of specific brain regions, an extensive set of experiments was performed on data acquired with a typical acquisition protocol employed in a clinical context.

3.2 Background

3.2.1 The Diffusion signal

The EAP, $P(\mathbf{R})$, is the three dimensional Probability Density Function (PDF) of the water molecules inside a voxel moving an effective distance $\mathbf{R}$ in an effective time τ. It is related to the normalized magnitude image provided by the MRI scanner, $E(\mathbf{q})$, by the Fourier transform [3.31]:

$$P(\mathbf{R}) = \int_{\mathbb{R}^3} E(\mathbf{q}) \exp(-2\pi j \mathbf{q}^T \mathbf{R}) d\mathbf{q}. \tag{3.1}$$

The inference of exact information on the $\mathbf{R}$–space would require the sampling of the whole $\mathbf{q}$–space to use the Fourier relationship between both spaces.

In order to obtain an analytical solution from a reduced number of acquired images, a model for the diffusion behavior must be adopted. The most common techniques rely on the assumption of a Gaussian diffusion profile and a steady state regime of the diffusion process that yields to the well-known Diffusion Tensor (DT) approach. Alternatively, a more general expression for $E(\mathbf{q})$ can be used [3.12, 3.27]:

$$E(\mathbf{q}) = \exp\left(-4\pi^2 \tau q^2 D(\mathbf{q})\right) = \exp\left(-b \cdot D(\mathbf{q})\right), \tag{3.2}$$

where the positive function $D(\mathbf{q}) = D(q, \theta, \phi) > 0$ is the Apparent Diffusion Coefficient (ADC), $b = 4\pi^2 \tau \|\mathbf{q}\|^2$ is the so-called b-value and $q = \|\mathbf{q}\|$, $\theta \in [0, 2\pi)$, and $\phi \in [0, \pi]$ are the angular coordinates in the spherical system. According to [3.32], in the mammalian brain this mono-exponential model is predominant for values of b up to $2,000$ s/mm^2 and it can be extended to higher values (up to $3,000$ s/mm^2) if appropriate multi-compartment models of diffusion are used.

3.2.2 Advanced diffusion measures from single shell acquisitions: AMURA

Despite the advantages of the EAP-based measures, the calculation of these scalars usually requires long execution and acquisition times, together with very large b-values and a large number of diffusion gradients, not always available in commercial scanners and generally discarded in the clinical routine. To solve these problems, AMURA has been developed in [3.27, 3.28]. This approach allows the estimation of simplified versions of EAP-related scalars without the explicit calculation of the EAP, using a lower number of samples, even with a

single-shell acquisition scheme. AMURA considers that, if the amount of data is reduced, a restricted diffusion model consistent with single-shell acquisitions must be assumed: the ADC does not depend on the magnitude of $\mathbf{q}$ (i.e., it is roughly independent on the b-value) within the range of b-values probed, so that $D(\mathbf{q}) = D(\mathbf{u})$, where $\mathbf{u} \in \mathcal{S}$ is a unit direction in space where $||\mathbf{u}|| = 1$ and $\mathbf{q} = q\mathbf{u}$. This way Eq. (3.2) becomes:

$$E(\mathbf{q}) = E(q\mathbf{u}) = \exp\left(-4\pi^2\tau q^2\ D(\mathbf{u})\right). \tag{3.3}$$

This methodology allows shorter MRI acquisitions and very fast calculation of scalars. From Eq. (3.3), AMURA proposed a particular implementation of scalar measures. Since the mono-exponential model only holds within a limited range around the measured b-value, the measures derived this way must be seen as *apparent* values at a given b-value, related to the original ones but dependent on the selected shell. The main metrics defined in AMURA are:

1. **Return-to-origin probability (RTOP):** also known as probability of zero displacement, it is related to the probability density of water molecules that minimally diffuse within the diffusion time τ [3.33, 3.21, 3.34]. It is defined as the value of $P(\mathbf{R})$ at the origin, related to the volume of the signal $E(\mathbf{q})$:

$$\begin{aligned} \text{RTOP} &= \int_{\mathbb{R}^3} E(\mathbf{q}) d\mathbf{q} \\ &= \frac{1}{(4\pi)^2\tau^{3/2}}\ C_{0,0}\left\{D(\mathbf{u})^{-3/2}\right\}. \end{aligned} \tag{3.4}$$

   where $C_{0,0}\left\{H(\mathbf{u})\right\}$ is the zeroth-order coefficient of a spherical harmonics (SH) expansion of signal $H(\mathbf{u})$, defined as:

$$C_{0,0}\left\{H(\mathbf{u})\right\} = \frac{1}{\sqrt{4\pi}} \int_{\mathcal{S}} H(\mathbf{u}) d\mathbf{u}, \tag{3.5}$$

   where $\mathcal{S}$ denotes the surface of a sphere of radius one.

2. **Return-to-plane probability (RTPP)**: defined as

$$\text{RTPP} \quad = \quad \int_{\mathbb{R}} E(q\mathbf{r}_{||}) dq = \sqrt{\frac{\pi}{4\pi^2\tau}} \sqrt{\frac{1}{D(\mathbf{r}_{||})}} \tag{3.6}$$

   where $\mathbf{r}_{||}$ denotes the direction of maximal diffusion. This measure is known to be a good indicator of restrictive barriers in the axial orientation, and it is related to the mean pore length [3.15, 3.35, 3.23].

3. **Return-to-axis probability (RTAP)**:

$$\begin{aligned} \text{RTAP} &= \int_{\mathbf{q} \perp \mathbf{r}_{||}} E(\mathbf{q}) d\mathbf{q} \\ &= \frac{1}{2 \cdot 4\pi^2\tau} \mathcal{G}\left\{D(\mathbf{u})^{-1}\right\}(\mathbf{r}_{||}) \end{aligned} \tag{3.7}$$

   where $\mathbf{q} \perp \mathbf{r}_{||}$ is the set of directions perpendicular to $\mathbf{r}_{||}$ and $\mathcal{G}\left\{D(\mathbf{u})^{-1}\right\}(\mathbf{r}_{||})$ is the Funk-Radon Transform (FRT) [3.36] of $D(\mathbf{u})^{-1}$ evaluated at $\mathbf{r}_{||}$, the direction

of maximum diffusion. The RTAP is an indicator of restrictive barriers in the radial orientation [3.15, 3.37, 3.38].

4. **Apparent Propagator Anisotropy (APA)**: quantifies how much the propagator diverges from the closest isotropic one. For AMURA, we can define:

$$\text{APA}_0 = \sqrt{1 - \frac{4}{\sqrt{\pi}} \frac{\left[C_{0,0}\left\{(D(\mathbf{u}) + D_{\text{AV}})^{-3/2}\right\}\right]^2}{C_{0,0}\left\{D(\mathbf{u})^{-3/2}\right\} \cdot D_{\text{AV}}^{-3/2}}}, \tag{3.8}$$

where $D_{\text{AV}} = \frac{1}{\sqrt{4\pi}} C_{0,0}\{D(\mathbf{u})\}$. To better distribute the output values in the range $[0, 1]$, the APA is transformed by a contrast enhancement function as described in [3.15].

3.3 Methods

As previously stated, the information provided by the EAP is expressed in terms of scalar indices or metrics to be usable in practice. In [3.15, 3.16], the authors suggest the use of radial moments, i.e. integrals computed over $P(\mathbf{R})$ and weighted by powers of the radial coordinate. Following a similar rationale, the authors in [3.39] propose the computation of similar moments over $E(\mathbf{q})$. Indices like RTAP and RTPP can be computed as either line or plane integrals over $\mathbf{R}$ which translate to either plane or line integrals over $\mathbf{q}$. Thus, in [3.39] the diffusion is characterized in a multishell approach through the computation of moments on either the $\mathbf{R}$ or the $\mathbf{q}$ domain. In this work, we will restrict ourselves to the assumptions of AMURA, specifically the simplified diffusion in Eq. (3.3) and considering only one acquired shell, i.e., only one b-value is available for the computation of the metrics.

3.3.1 Generalized Moments of $E(\mathbf{q})$

First, we consider those moments over the signal defined in the $\mathbf{q}$ domain.

1. **Full moments:** We define the full moments of $E(\mathbf{q})$ as those computed by integration in the whole 3-D space:

$$\Upsilon^p = \int_{\mathbb{R}^3} q^p E(\mathbf{q}) d\mathbf{q}. \tag{3.9}$$

Note that, with this definition, RTOP $= \Upsilon^0$ and qMSD $= \Upsilon^2$ ($\mathbf{q}$–space mean-squared-displacement [3.16]). By using the simplification in Eq. (3.3), we can write Eq. (3.9) in spherical coordinates and integrate with respect to the radial component q:

$$\begin{aligned} \Upsilon^p &= \int_0^\infty \int_{\mathcal{S}} q^{2+p} \exp(-4\pi^2 \tau q^2 \cdot D(\mathbf{u}))\, d\mathbf{u}\, dq \\ &= \frac{1}{2}\Gamma\left(\frac{3+p}{2}\right) \frac{1}{(4\pi^2\tau)^{\frac{3+p}{2}}} \int_{\mathcal{S}} D(\mathbf{u})^{-\frac{3+p}{2}} d\mathbf{u}, \end{aligned} \tag{3.10}$$

the integral being convergent only if $p > -3$. Using the zeroth-order coefficient of a SH expansion to calculate the integral over the surface of the unit sphere $\mathcal{S}$, we can write:

$$\Upsilon^p = \Gamma\left(\frac{3+p}{2}\right)\frac{\sqrt{\pi}}{(4\pi^2\tau)^{\frac{3+p}{2}}}C_{0,0}\left\{D(\mathbf{u})^{-\frac{3+p}{2}}\right\}, \quad p > -3. \tag{3.11}$$

The units of the full moment Υ^p are $[\mathrm{mm}^{-p-3}]$.

2. **Axial moments:** We define the axial moments as those computed as a line integral along a given direction:

$$\Upsilon^p_{||} = \int_{\mathbb{R}} q^p E(q\mathbf{r}_{||})dq, \tag{3.12}$$

where $\mathbf{r}_{||}$ denotes the direction of maximal diffusion. With this definition, RTPP $= \Upsilon^0_{||}$. Once more, we can use the simplification in Eq. (3.3) and therefore:

$$\begin{aligned}\Upsilon^p_{||} &= \int_{-\infty}^{\infty} q^p \exp(-4\pi^2\tau q^2 D(\mathbf{r}_{||}))dq \\ &= \frac{1}{(4\pi^2\tau)^{\frac{1+p}{2}}}\Gamma\left(\frac{1+p}{2}\right)D(\mathbf{r}_{||})^{-\frac{1+p}{2}}, \quad p > -1,\end{aligned} \tag{3.13}$$

where $D(\mathbf{r}_{||})$ is the value of the diffusion signal $D(\mathbf{q})$ at the maximum diffusion direction $\mathbf{r}_{||}$. Again, the condition $p > -1$ ensures the convergence of the integral. The axial moment $\Upsilon^p_{||}$ is measured in $[\mathrm{mm}^{-p-1}]$.

3. **Planar moments:** We define the planar moments as those computed as surface integrals in a plane perpendicular to a desired direction containing the origin:

$$\Upsilon^p_{\perp} = \int_{\mathbf{q}\perp\mathbf{r}_{||}} q^p E(\mathbf{q})d\mathbf{q}, \tag{3.14}$$

where $\mathbf{q} \perp \mathbf{r}_{||}$ is the set of directions perpendicular to $\mathbf{r}_{||}$ (the one with maximal diffusion). With this definition, RTAP $= \Upsilon^0_{\perp}$. In order to simplify the equation, we use again the simplification in Eq. (3.3). Let θ be the angle that parameterizes the equator perpendicular to the maximum diffusion direction, $\{\mathbf{u}_{\perp}(\theta), \theta \in [0, 2\pi)\} \equiv \{\mathbf{u} : \mathbf{u} \perp \mathbf{r}_{||}, \|\mathbf{u}\| = 1\}$, and $D(\mathbf{u}_{\perp}(\theta))$ the diffusion signal at that equator. Since $D(\mathbf{u}_{\perp}(\theta))$ does not depend on the radial component, the previous integral can be developed into:

$$\begin{aligned}\Upsilon^p_{\perp} &= \int_0^{\infty}\int_0^{2\pi} \exp(-4\pi^2\tau q^2 D(\mathbf{u}_{\perp}(\theta)))\; q^{p+1}\; d\theta\; dq \\ &= \frac{1}{2}\frac{1}{(4\pi^2\tau)^{\frac{p+2}{2}}}\Gamma\left(\frac{2+p}{2}\right)\int_0^{2\pi} D(\mathbf{u}_{\perp}(\theta))^{-\frac{2+p}{2}}d\theta.\end{aligned} \tag{3.15}$$

By assuming $p > -2$ we can guarantee the integral is convergent. The FRT operator allows a more compact notation:

$$\Upsilon^p_{\perp} = \frac{1}{2}\frac{1}{(4\pi^2\tau)^{\frac{p+2}{2}}}\Gamma\left(\frac{2+p}{2}\right)\mathcal{G}\left\{D(\mathbf{u})^{-\frac{2+p}{2}}\right\}(\mathbf{r}_{||}), \quad p > -2. \tag{3.16}$$

The units of the planar moment $\Upsilon^p_{\perp}$ are $[\mathrm{mm}^{-p-2}]$.

Measure	Numerical Implementation
Full moments of $E(\mathbf{q})$	$\Upsilon^p = \Gamma\left(\frac{3+p}{2}\right) \frac{\sqrt{\pi}}{(4\pi^2\tau)^{\frac{3+p}{2}}} C_{0,0}\left\{D(\mathbf{u})^{-\frac{3+p}{2}}\right\},\ p > -3$
Axial moments of $E(\mathbf{q})$	$\Upsilon^p_{\|\|} = \frac{1}{(4\pi^2\tau)^{\frac{1+p}{2}}} \Gamma\left(\frac{1+p}{2}\right) D(\mathbf{r}_{\|\|})^{-\frac{1+p}{2}},\ p > -1$
Planar moments of $E(\mathbf{q})$	$\Upsilon^p_{\perp} = \frac{1}{2} \frac{1}{(4\pi^2\tau)^{\frac{p+2}{2}}} \Gamma\left(\frac{2+p}{2}\right) \mathcal{G}\left\{D(\mathbf{u})^{-\frac{2+p}{2}}\right\}(\mathbf{r}_{\|\|}),\ p > -2$
Full moments of $P(\mathbf{R})$	$\upsilon^p = \frac{\Gamma\left(\frac{p+3}{2}\right)}{q^p \pi^{p+1}} C_{0,0}\left\{D^{\frac{p}{2}}(\mathbf{u})\right\},\ p > -3$

Tab. 3.1.: Survey of the moments of $E(\mathbf{q})$ and $P(\mathbf{R})$ calculated with AMURA.

3.3.2 Generalized (full) moments of $P(\mathbf{R})$

A closed form expression of $P(\mathbf{R})$ cannot be attained in the general case from the mono-exponential model of $E(\mathbf{q})$. Even so, full moments analogous to those defined for $E(\mathbf{q})$ can be explicitly computed. In precise terms, we define the p-th full moment of $P(\mathbf{R})$ as:

$$\upsilon^p = \int_{\mathbb{R}^3} R^p P(\mathbf{R}) d\mathbf{R}. \tag{3.17}$$

where $R = |\mathbf{R}|$. Using spherical coordinates, we can rewrite it to:

$$\upsilon^p = \int_{\mathcal{S}} \left(\int_0^\infty R^{p+2} P(R\mathbf{r}) dR \right) d\mathbf{r},\ \ p > -3, \tag{3.18}$$

where $\mathbf{r} \in \mathcal{S}$ is a unitary direction in space and, therefore, $\mathbf{R} = R\mathbf{r}$ and $|\mathbf{r}| = 1$. If we consider the mono-exponential model in Eq. (3.3) we can solve the integral, see 3.A:

$$\upsilon^p = \frac{\Gamma\left(\frac{p+3}{2}\right)}{2q^p \pi^{p+\frac{3}{2}}} \int_{\mathcal{S}} D^{\frac{p}{2}}(\mathbf{u}) d\mathbf{u},\ p > -3. \tag{3.19}$$

Following the Eq. (3.19), $\mathrm{MSD} = \upsilon^2$. Using the zeroth-order coefficient of a SH expansion to calculate the integral over the surface of the unit sphere $\mathcal{S}$, we can write:

$$\upsilon^p = \frac{\Gamma\left(\frac{p+3}{2}\right)}{q^p \pi^{p+1}} C_{0,0}\left\{D^{\frac{p}{2}}(\mathbf{u})\right\}. \tag{3.20}$$

The full moment υ^p is given in $[\mathrm{mm}^p]$.

3.3.3 Survey

An overview of the different moments proposed in this section, together with their specific numerical implementations, is presented in Table 1. In addition, 3.B provides the analogous expressions for DT representation.

3.4 Materials

In order to test the proposed measures the following datasets were used:

- **Human Connectome Project (HCP) MGH database** [3.40, 3.41][1]: specifically volumes MGH1007, MGH1010, MGH1016, MGH1026 and MGH1030, acquired on a Siemens 3T Connectom scanner (Siemens, Erlangen, Germany) equipped with a custom-made 64-channel head coil and gradient coil capable of producing a maximum gradient strength at 300 mT/m. The data were acquired with a mono-polar Stejskal–Tanner pulsed gradient spin-echo echo planar imaging (EPI) with (repetition time/time echo) $\mathrm{TR/TE} = 8800/57$ ms and accelerated with the Generalized Autocalibrating Partially Parallel Acquisition (GRAPPA) protocol at phase partial Fourier 6/8. The acquisition protocol included four b-values at $\{1000, 3000, 5000, 10,000\}$ s/mm^2 sampled at 64, 64, 128 and 256 directions respectively, 40 non-diffusion acquisitions at $b = 0$, voxel resolution $1.5 \times 1.5 \times 1.5$ mm^3, pixel bandwidth 1984 Hz/pixel, acquisition matrix 140×140 with 96 slices covering each volume, and pulse separation time/diffusion gradients length $\Delta/\delta = 21.8/12.9$ ms.
- **Human Connectome Project (HCP) WU-Minn test-retest database:** [3.42, 3.41]: Thirty-seven subjects were used after excluding seven cases from the database due to incompatibilities between test and retest acquisitions (excluded volumes: 135528, 137128, 151526, 169343, 179548, 192439, 601127, 660951). All subjects were scanned with a customized Siemens 3T Connectome Skyra scanner (Siemens, Erlangen, Germany) equipped with a 32-channel head coil and gradient coil with a maximum gradient strength at 100 mT/m. The data were acquired using the multiband approach with a multiband factor of 3, $\mathrm{TR/TE} = 5520/89.5$ ms. The acquisition protocol included three b-values at $\{1000, 2000, 3000\}$ s/mm^2, each shell sampled in 90 non-collinear directions, 18 repetitions of the baseline acquisition ($b = 0$), voxel resolution $1.25 \times 1.25 \times 1.25$ mm^3, pixel bandwidth 1490 Hz/pixel, 140 slices covering each volume, and pulse separation time/diffusion gradients length $\Delta/\delta = 43/10.6$ ms.
- **Multishell data acquired at CUBRIC (CBR)**[2]: 14 healthy volunteers scanned on a 3T Siemens Prisma scanner (maximum gradient strength at 80 mT/m) with a pulsed-gradient spin-echo (PGSE) sequence. Three shells were acquired at $b = \{1200, 3000, 5000\}$ s/mm^2 with 60 directions per value. The voxel resolution is 1.5$\times$ 1.5$\times$1.5 mm. Other acquisition parameters are: TE=80 ms, TR=4500 ms, $\Delta/\delta = 38.3/19.5$ ms, parallel imaging acquisition (GRAPPA2) with sum of squares combination and 32 channels.
- **Episodic Migraine Database (EMDb)**: as described in [3.7, 3.8]. For this paper we will consider a total of 50 healthy controls (HCs) at the age of 36.1 $\pm$ 13.2 (39F, 11M) and 51 patients with Episodic Migraine (EM) at the age of 36.6 $\pm$ 7.9 (44F,

[1] Data obtained from the Human Connectome Project (HCP) database (`ida.loni.usc.edu/login.jsp`). The HCP project (Principal Investigators: Bruce Rosen, M.D., Ph.D., Martinos Center at Massachusetts General Hospital; Arthur W. Toga, Ph.D., University of Southern California, Van J. Weeden, MD, Martinos Center at Massachusetts General Hospital) is supported by the National Institute of Dental and Craniofacial Research (NIDCR), the National Institute of Mental Health (NIMH) and the National Institute of Neurological Disorders and Stroke (NINDS). HCP is the result of efforts of co-investigators from the University of Southern California, Martinos Center for Biomedical Imaging at Massachusetts General Hospital (MGH), Washington University, and the University of Minnesota.

[2] `www.cardiff.ac.uk/cardiff-university-brain-research-imaging-centre/research/projects/cross-scanner-and-cross-protocol-diffusion-MRI-data-harmonisation`

7M) and duration of migraine 13.1y $\pm$ 10.5y. The study was approved by the Ethics Committee of the Hospital Clínico Universitario de Valladolid (PI: 14-197). The inclusion criteria of EM follow the International Classification of Headache Disorders guidelines [3.43]. MRI acquisition was performed with a Philips Achieva 3 T MRI unit (Philips Healthcare, Best, The Netherlands), using a 32-channel head coil in the MRI facility at the Universidad de Valladolid (Valladolid, Spain). The parameters of the diffusion-weighted acquisition are as follows: $\mathrm{TR/TE} = 9000/86$ ms, flip angle = 90^o, single-shell acquisition with 61 gradient directions and $b = 1000\ \mathrm{s/mm^2}$, one baseline volume, 128×128 matrix size, spatial resolution of $2 \times 2 \times 2$ mm^3 and 66 slices that cover the whole brain. Both T1 and diffusion-weighted data were collected between May 2014 and July 2018 in a unique MRI session, starting with the T1 scan. For a single subject, the time for both scans was approximately 18 minutes. The data were preprocessed following a standard pipeline: denoising, correction for eddy currents and motion and correction for B1 field inhomogeneity, and Gibbs ringing artifact. The MRtrix software [3.44] was employed to carry out these steps. A whole brain mask for each subject was also calculated from data.

3.5 Experiments and Results

3.5.1 Setting-up of the experiments

AMURA and MiSFIT measures were calculated using the dMRI-Lab[3] toolbox and MATLAB 2020a. As explained above, AMURA measures rely on the expansion of spherical functions at a given shell in the basis of SH. Even SH orders up to 6 were fitted with a Laplace-Beltrami penalty $\lambda = 0.006$. The direction of maximum diffusion $\mathbf{r}_{||}$ was computed as the principal eigenvector of the diffusion tensor calculated from the same data set as the AMURA. The FRT was numerically computed as described in [3.45]: the spherical function –$D(\mathbf{u})$– was first spanned in the basis of SH up to the desired order L; then, we exploited the property of SH being eigenfunctions for the FRT by applying constant factors –FRT eigenvalues– to the SH coefficients. As a result, we got the SH coefficients of the analytically computed FRT of the original signal, which could now be evaluated for any orientation at will (and, in particular, for $\mathbf{r}_{||}$).

3.5.2 Behavior of moments for varying orders

A preliminary visual assessment of the different metrics was performed using one single slice from the HCP volume MGH1007. The proposed measures were calculated using a single shell at $b = 3000\ \mathrm{s/mm^2}$. Fig. 3.1 provides a qualitative insight in the behavior of moments computed in the $\mathbf{q}$ and $\mathbf{R}$ domains. Each kind of moment (full, axial, or planar) admits a different range of variation for its order depending on the convergence of the corresponding integral. Accordingly, we have probed a range including inverse (negative), positive and fractional orders in all cases. Since their ranges of variation are very different

[3] www.lpi.tel.uva.es/dmrilab

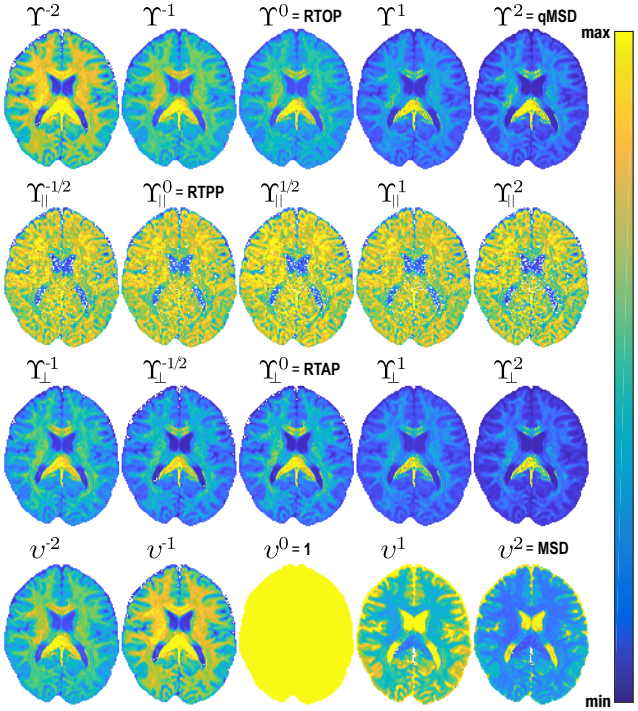

Fig. 3.1.: Moments of different kinds for different orders p computed over the composite attenuation signal over subject HCP MGH1007. Each moment has been normalized to its own range for visualization purposes. Top to bottom: full moments (Υ^p); axial moments for the maximum diffusion direction ($\Upsilon^p_{||}$); planar moments for the maximum diffusion direction ($\Upsilon^p_{\perp}$) and full moments of the EAP (υ^p). These indices include RTOP, qMSD, RTPP, RTAP and MSD.

from each other depending on the order and the kind of moment, all the slices shown have been min-max normalized.

First of all, note that the popular RTOP, RTPP and RTAP could be already calculated with the original formulation of AMURA. Here, we can see them as special values of the considered moments. Full moments Υ^p, for instance, show a different range of quantification of the variation of the white matter as a function of the order p. Axial moments $\Upsilon^p_{||}$ result in very noisy maps with a reduced anatomical coherence, an effect that can also be seen in RTPP, even when calculated with more shells and more advanced methods [3.39]. These moments are especially sensitive to the signal-to-noise ratio (SNR). Planar moments $\Upsilon^p_{\perp}$, on the other hand, exhibit a behavior very similar to the full moments. Anatomical structures in white matter are distinguishable even for negative and not even orders. Finally, moments of $P(\mathbf{R})$, υ^p, show a behavior different to the previous ones. Note that $\upsilon^0 = 1$ since it is the integral of the whole EAP, which represents a PDF. On the other hand, note that, from an implementation point of view, υ^p are defined as positive powers of $D(\mathbf{u})$, while the moments of $E(\mathbf{q})$ are defined over negative powers, hence the visual differences.

Next, we will focus in the values of the different moments in one particular area of the brain, the CC. Different AMURA metrics were calculated on HCP volumes MGH1016, MGH1026 and MGH1030 using a single shell at $b = 5000\ \mathrm{s/mm^2}$ for higher contrast. The CC was extracted using the registration of the the subject's FA (calculated at $b = 1000\ \mathrm{s/mm^2}$)

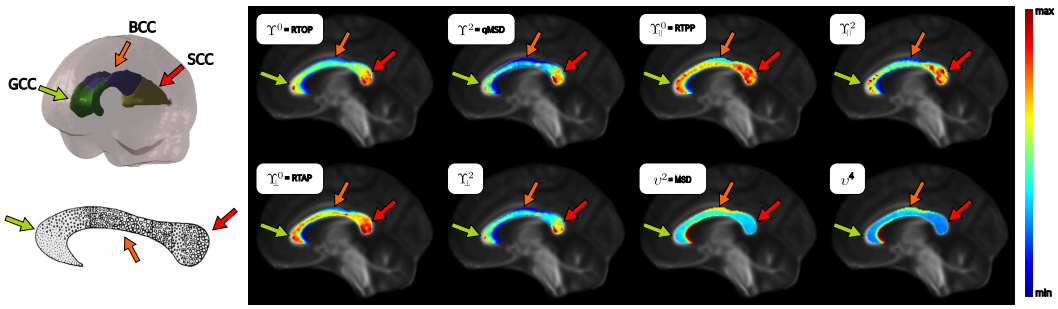

Fig. 3.2.: Values of different moments calculated with AMURA on the CC for the average of volumes MGH1016, MGH1026 and MGH1030 using a single-shell at $b = 5000\,\mathrm{s/mm^2}$ in the standard space, sagittal view. The values of the measures are displayed over the FA for reference. Scheme of the fiber distribution in the corpus callosum extracted from [3.46] with marked regions: the genu corpus callosum (GCC), the body corpus callosum (BCC) and the splenium corpus callosum (SCC).

to a common template using the FSL 6.0.4 (Analysis Group, FMRIB, Oxford, UK.; `https://fsl.fmrib.ox.ac.uk/fsl/fslwiki`; [3.47]), applying the JHU WM atlas [3.48] and then averaging the measures over three subjects. Specifically, we linearly registered the FA to the template FMRIB58 (a high-resolution FA average over 58 subjects) with a voxel resolution of $1 \times 1 \times 1\ \mathrm{mm}^3$ [3.49, 3.50] using twelve degrees of freedom and normalized correlation as the cost function. We then applied a non-linear registration procedure to correct the matching of the subject's FA to the template. Once the FAs were registered to the common space, we warped the AMURA based measures to the standard space using trilinear interpolation. The values of the different metrics over the CC are depicted in Fig. 3.2 for a single sagittal view. Once more, the metrics have been min-max normalized in order to show a similar range of values. A 3D rendering of the CC is shown for reference.

According to previous analyses [3.51, 3.46], the CC presents different fiber structure configurations for the three different parts: the genu CC (GCC), the body CC (BCC) and the splenium CC (SCC). The different regions have a wide variety of diffusion properties, distributed in an uneven manner along this structure, as reflected in the scheme in Fig. 3.2-left, extracted from [3.46]. In Fig. 3.2, those moments based on $E(\mathbf{q})$ reflect the differences in the diffusion properties for the different parts of the CC. This difference is more noticeable with higher order moments, like Υ^2, $\Upsilon^2_{||}$ and $\Upsilon^2_{\perp}$. On the contrary, this effect is not reflected on the moments of $P(\mathbf{R})$.

3.5.3 DT vs. AMURA

Some of the moments presented in this study can also be implemented using the DT approach, as described in 3.B. In this section we will show how AMURA provides distinct representations than DT does, which will potentially lead to markers more sensitive to anatomical changes. Different measures were calculated on volume MGH1007 using a single shell at two different b-values: $b = 1000\,\mathrm{s/mm^2}$ and $b = 3000\,\mathrm{s/mm^2}$. For the sake of visual comparison, Fig. 3.3 shows respective slices of different moments calculated with DT and with AMURA for $b = 3000\,\mathrm{s/mm^2}$ with identical scaling, so that they can be directly compared, together with the voxel-wise joint 2-D histograms for both considered shells.

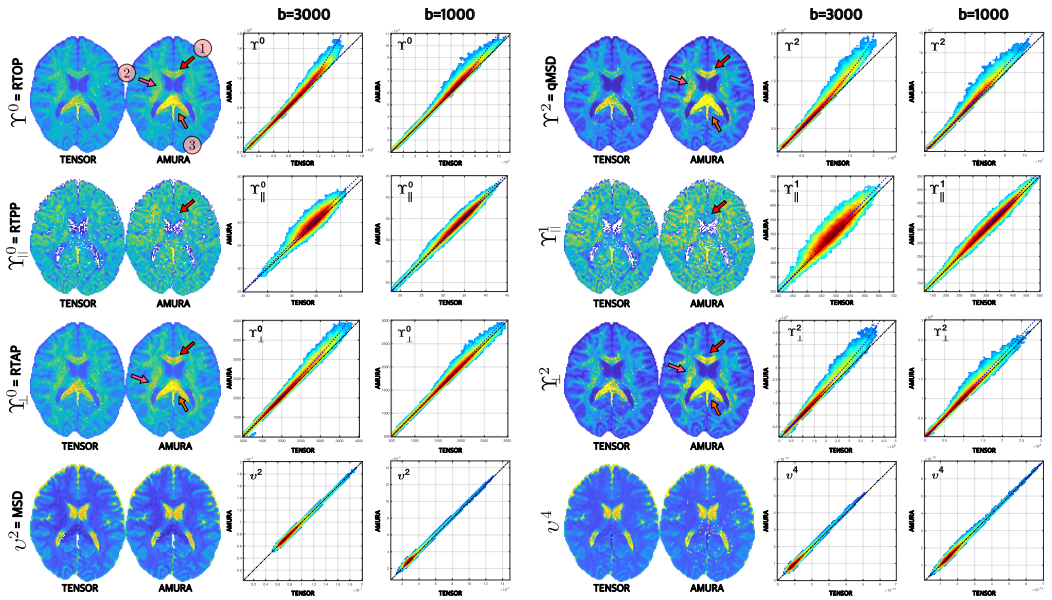

Fig. 3.3.: Comparison of scalar measurements computed with either the DT (left) or AMURA (right) over subject HCP MGH1007 at $b = 3000\ \mathrm{s/mm^2}$. The same scale is used for both two approaches in all cases. Joint 2-D histograms for the comparison at $b = 3000\ \mathrm{s/mm^2}$ and $b = 1000\ \mathrm{s/mm^2}$ are shown in each case. Arrows highlight prominent differences between the DT and AMURA: (1) genu of corpus callosum, (2) centrum semiovale and (3) splenium of the corpus callosum.

While the structure of the anatomical maps look quite similar with the two approaches, and their ends of scale are also coherent, AMURA systematically shows greater values than the DT at the corpus callosum (CC, 1 and 3) and the centrum semiovale (2).

The centrum semiovale is a region with a complex fiber configuration in terms of crossing fibers: there is a conjunction of structures with different alignment, like anterior-posterior (cingulum and superior longitudinal fasciculus), left-right (corpus callosum) and superior-inferior (corticospinal tract). It is known to be an area prone to produce false positives in tractography [3.52]. Thus, the adjustment of a Gaussian model (like the DT) will be subject to underestimation of the diffusion in this region. A more general model like AMURA, despite also being based on an mono-exponential decay, will produce higher values, more coherent with actual structures.

The divergence of values in the CC is explained by a different effect. In that area, the fibers follow a similar main direction, with high anisotropy. However, the underlying structure is a bit more complex than most tracts in white matter, since it shows a greater curvature. The resolution of the DMRI data is not enough to discriminate this subvoxel curvature, especially in approaches like DT, where only one predominant direction is considered. Actually, in [3.52], the authors report analogous problems with tractography in the CC due to this same effect. In addition, full and planar moments calculated with the DT are an inverse function of the smallest eigenvalues (see 3.B). In those areas with higher anisotropy, like the CC, where the second and third eigenvalues are particularly low, the effect of noise could bias them to higher values, a well-known effect in the DT when estimated using a least-squares

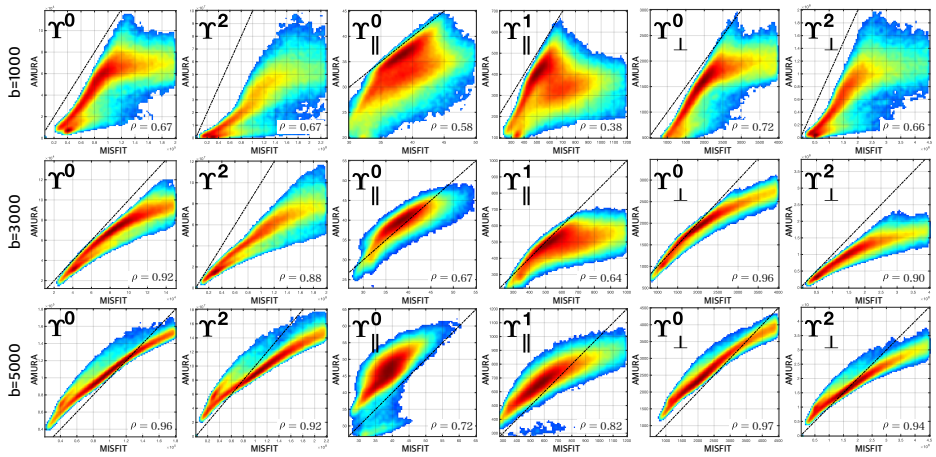

Fig. 3.4.: Comparison of the moments of $E(\mathbf{q})$ computed with AMURA and MiSFIT. A joint 2-D histogram is shown in each case, together with the respective Pearson's correlation coefficient, for quantitative assessment. AMURA is calculated using a single shell with the b-value specified on the left side of each row. MiSFIT is calculated using three shells.

approach [3.53, 3.54, 3.55]. As a consequence, metrics like RTOP and RTAP will show lower values in those areas when calculated with the DT.

On the other hand, note that the moments based on $P(\mathbf{R})$ show almost no difference between both implementations.

Paying attention to the voxel-wise joint 2-D histograms, the DT approach consistently shows an underestimation of the greater values when compared to AMURA, specifically in the full and planar moments of $E(\mathbf{q})$. This mismatch is more significant at $b = 3000\ \mathrm{s/mm^2}$, whereas for $b = 1000\ \mathrm{s/mm^2}$ the differences remain, but to a smaller degree. The histograms show that DT and AMURA diverge when the b-value grows. On the other hand, values for the moments of $P(\mathbf{R})$ are almost the same for both implementations. This effect, once again, could be easily explained by the fact that v^p is calculated over positive powers of $D(\mathbf{u})$.

3.5.4 Comparison with multishell metrics

The *apparent* moments calculated with AMURA are now compared to the same *actual* moments calculated with a multishell approach where the radial information of $\mathbf{q}$ is taken into account, specifically Micro-Structure-adaptive convolution kernels and dual Fourier domains Integral Transforms (MiSFIT) [3.39]. For both methods, volume MGH1010 is considered. AMURA is calculated independently for three separated shells at $b = \{1000, 3000, 5000\}\ \mathrm{s/mm^2}$ while MiSFIT is calculated using the three available shells at once. Fig. 3.4 shows the voxel-wise joint 2-D histogram for the moments of $E(\mathbf{q})$. For each moment, Pearson's correlation coefficient between both methods is calculated. There are clearly differences, since both methods are based on very different initial assumptions. However, for higher b-values, full and planar moments of the $E(\mathbf{q})$ show a very strong correlation between the estimation with AMURA using only one shell and the multishell calculation given by MiSFIT. In some cases, that correlation exceeds the 90%, which basically

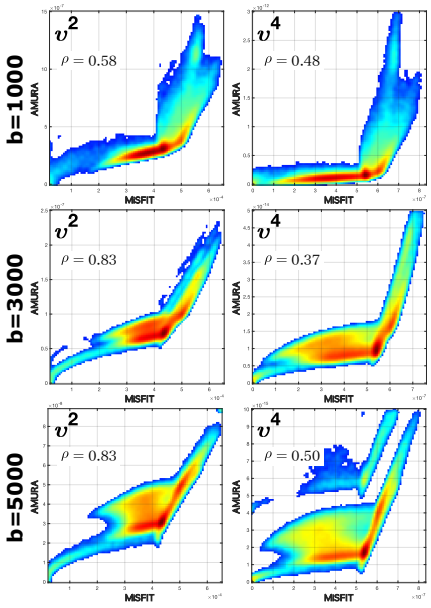

Fig. 3.5.: Comparison of the moments of $P(\mathbf{R})$ computed with AMURA and MiSFIT. A joint 2-D histogram is shown in each case, together with the respective Pearson's correlation coefficient, for quantitative assessment. AMURA is calculated using a single shell with the b-value specified on the left side of each row. MiSFIT is calculated using three shells.

means that those methods are measuring very similar information. However, the mapping of both methods is not linear, with AMURA showing a reduced contrast when compared to MiSFIT, especially for the highest values. Axial moments are the ones showing more differences with greater dispersion.

All the measures show a low correlation when AMURA is calculated at $b = 1000\ \mathrm{s/mm^2}$, which is expected, since the underlying features measured by the estimated moments are better visible at higher b-values. This experiment shows that the best performance of AMURA is achieved for higher b-values, where the correlation with multishell methods is stronger. In addition, the correlation seems weaker when higher order moments are considered.

Fig. 3.5 shows the voxel-wise joint 2-D histogram for the moments of $P(\mathbf{R})$. Results here are weaker than the previous case. This, once more, shows the inability of AMURA to properly estimate the moments of $P(\mathbf{R})$. While the moments of $E(\mathbf{q})$ could provide equivalent information when calculated from a single shell, for a proper estimation of the moments of $P(\mathbf{R})$ experimental results points to the need of multishell information.

3.5.5 Variability of measures depending on the b-value

Next, since AMURA provides *apparent* measures at a given shell, we tested the dependency of different moments on the b-value. To put this to the test, the variability with the b-value is probed using five whole volumes from the CBR data with the following procedure: Each AMURA moment was calculated at $b = 3000\ \mathrm{s/mm^2}$ on the white matter and outliers are removed. Then, that moment was clustered in fivedifferent groups inside using k-means

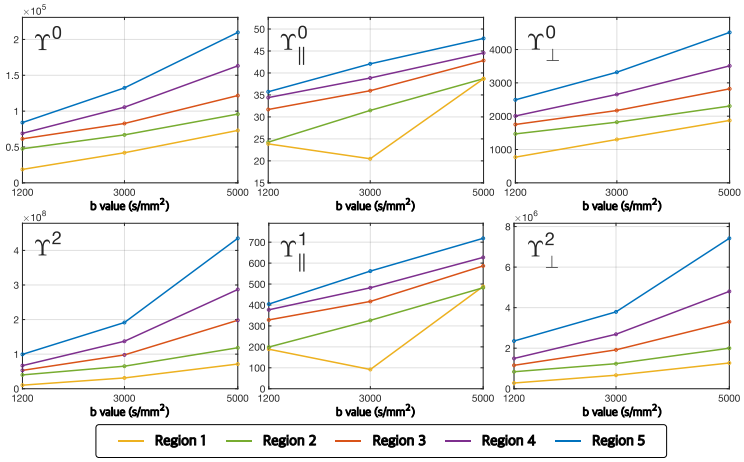

Fig. 3.6.: Evolution of the proposed measures with the b-value using data acquired with a 3T Prisma scanner (CBR dataset). The volume has been clustered in five different sets (for each metric at $b = 3000\ \mathrm{s/mm^2}$) and the median of each set is shown. Each color represents the median value inside each ROI (1 to 5).

algorithm. Each voxel in the white matter was assigned to the closest cluster using the minimum distance. As a result, the whole volume was divided into six different region-of-interests (ROIs) of similar value of the moment at $b = 3000\ \mathrm{s/mm^2}$. Then, the variability with the b-value was probed by computing the different AMURA measures with each of the available shells at $b = 1200\ \mathrm{s/mm^2}$, $b = 3000\ \mathrm{s/mm^2}$, or $b = 5000\ \mathrm{s/mm^2}$. All the proposed measures were computed for each considered case, and the median value inside each of the six clusters was calculated and depicted in Fig. 3.6.

All the considered measures show an indubitable dependence on the b-value. There is a monotonical behavior of each cluster for full and planar moments where the value grows with b. However, the separation between clusters remains for different b-values. This suggests that differences detected by these measures can be detected when using different shells This is not exactly the case for axial moments, where the cluster with lowest value shows a different behavior, decreasing for $b = 3000\ \mathrm{s/mm^2}$. This is motivated by the very noisy nature of this cluster, see for instance Fig. 3.1. The lowest values of the axial moments are prone to more variability than higher values.

3.5.6 Test-retest reproducibility analysis

Next, we evaluate the variability of the moments of AMURA using the HCP WU-Minn test-retest database. This database facilitates subsampling of the data by choosing the first k ($k < N$) diffusion gradient directions out of N samples, so that we subsampled the original data (90 directions) to 45, 30 and 15 gradients subsets per single-shell. To improve the SNR of the baseline (i.e. the non-diffusion weighted data), we averaged all together 18 non-diffusion weighted volumes. We estimated then AMURA measures for each subject, b-value and all four different numbers of gradient directions (i.e. 90, 45, 30 and 15 samples per each shell). We also estimated DTs from $b = 1000\ \mathrm{s/mm^2}$ data using the FSL [3.47]. Hither, the same sampling coverage was employed as the one used for AMURA measures. We

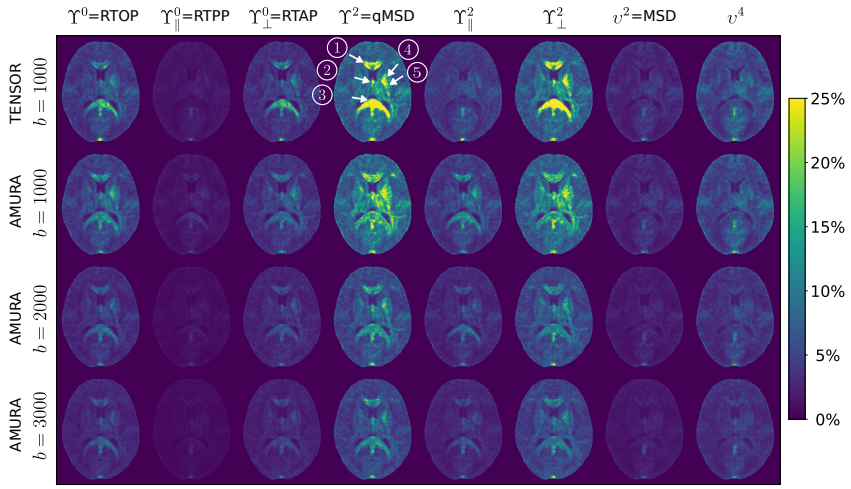

Fig. 3.7.: Median CV maps (defined in %), $\mathrm{CV}(\mathbf{x})$, of the moments of $E(\mathbf{q})$ and $P(\mathbf{R})$ in the standard space calculated across thirty-seven subjects from the HCP WU-Minn test-retest database. The moments were retrieved from single-shell data at $b = 1000$ s/mm^2 (DT; top) and separately for $b = 1000, 2000$ and 3000 s/mm^2 under the AMURA framework, all using 30 gradient directions per a single-shell. The arrows show the following WM regions: (1) genu of corpus callosum, (2) fornix, (3) splenium of the corpus callosum, (4) left anterior limb of the internal capsule and (5) left posterior limb of the internal capsule.

retrieved then the FA, full/axial/planar moments of $E(\mathbf{q})$ and full moments of the diffusion propagator $P(\mathbf{R})$ directly from tensor eigenvalues estimated at each data subsampling level. The FA calculated from fully-sampled data served for the two-step registration process of each subject to the common space as mentioned before. Similarly, we warped all AMURA and DTI based measures to the standard space using trilinear interpolation. The coefficient of variation (CV) is defined in the standard space for each subject, measure and subsampling ratio as the sample standard deviation across two sessions (i.e. test and retest) divided by the sample mean across sessions, and eventually multiplied by 100 to get the percentage score

$$\mathrm{CV}_s(\mathbf{x}) = \frac{\text{sample std. dev}_s(\mathbf{x})}{\text{sample mean}_s(\mathbf{x})} \cdot 100\ [\%] \quad \text{for} \quad s = 1, \ldots, S, \tag{3.21}$$

where $\mathrm{CV}_s(\mathbf{x})$ is a position dependent ($\mathbf{x}$-dependent) CV of a measure under a specified acquistion scenario (i.e. b-value, number of gradient directions) for subject s and S is the number of subjects used for the experiment (i.e. $S = 37$ for the HCP WuMinn database). The final CV is aggregated across all subjects using median operation for each measure, acquisition scenario and spatial position $\mathbf{x}$ separately:

$$\mathrm{CV}(\mathbf{x}) = \underset{s=1,\ldots,S}{\text{median}}\ \mathrm{CV}_s(\mathbf{x}). \tag{3.22}$$

Results of two reproducibility experiments are depicted in Figs. 3.7, 3.8 and 3.9. In the former experiment, we compare median CV maps of the moments of $E(\mathbf{q})$ and diffusion propagator $P(\mathbf{R})$ retrieved from a single-shell diffusion MR data with the DT at $b = 1000$ s/mm^2 and AMURA separately for $b = 1000, 2000$ and 3000 s/mm^2, all using 30 gradient directions. Fig. 3.7 presents the median CV, $\mathrm{CV}(\mathbf{x})$, calculated over all thirty-seven subjects from the HCP WU-Minn test-retest database in the standard space (slice 85), including both the

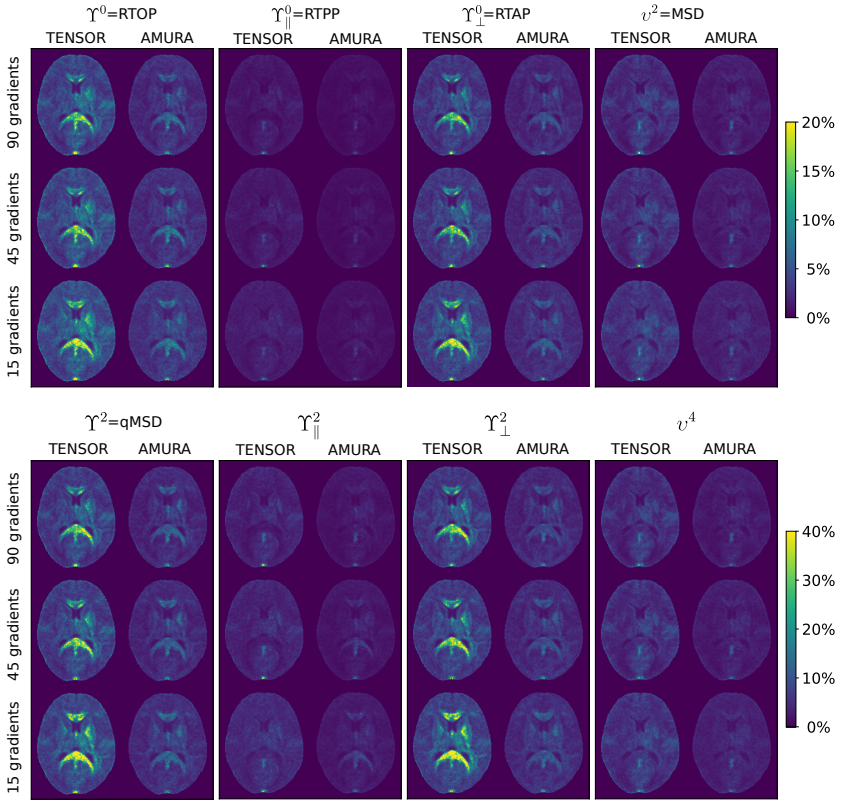

Fig. 3.8.: Comparison of median CV maps, $\mathrm{CV}(\mathbf{x})$, obtained from the HCP WU-Minn test-retest database under different number of diffusion gradient directions employed to calculate the moments of $E(\mathbf{q})$ and $P(\mathbf{R})$, i.e. 90 (fully-sampled data), 45 and 15. The DT-based moments were obtained from a single-shell at $b = 1000\ \mathrm{s/mm^2}$, while the AMURA framework was applied to the data at $b = 3000\ \mathrm{s/mm^2}$.

DT and AMURA. The smallest CV amongst all cases is observed for the zeroth-order axial moment of $E(\mathbf{q})$ (RTPP) and the second-order full moment of diffusion propagator $P(\mathbf{R})$ (MSD), while the highest one is noticeable for the second-order full and planar moments (qMSD, $\Upsilon^2_{\perp}$), especially in highly anisotropic regions such as the corpus callosum (genu and splenium), fornix and anterior/posterior limb of the internal capsule (see the arrows in Fig. 3.7). The CVs for the AMURA at $b = 1000\ \mathrm{s/mm^2}$ are comparable to those obtained from the DT, but in the former case, the CV is decreased with the higher b-value regime. Importantly, the CV increases with the positive moment's order consistently for all types of moments of $E(\mathbf{q})$ and $P(\mathbf{R})$.

The latter reproducibility experiment matches the median CV maps and their histograms determined with the DT and AMURA under the varying number of diffusion gradients used to calculate the moments of $E(\mathbf{q})$ and $P(\mathbf{R})$ starting from fully-sampled volumes (90 directions per shell) and then subsampled data to 45 and 15 directions, respectively. Here, we contrast AMURA measures calculated at $b = 3000\ \mathrm{s/mm^2}$ to DT-based ones from $b = 1000\ \mathrm{s/mm^2}$ (see Fig. 3.8). Generally, both the AMURA and DT exhibit robustness due to a decreasing number of diffusion gradient directions. However, we can observe an increase in the CV obtained from the DT with 15 gradient directions, which is notably prominent in the region of the SCC, including full Υ^p and planar $\Upsilon^p_{\perp}$ moments. Notice we modified the scale in

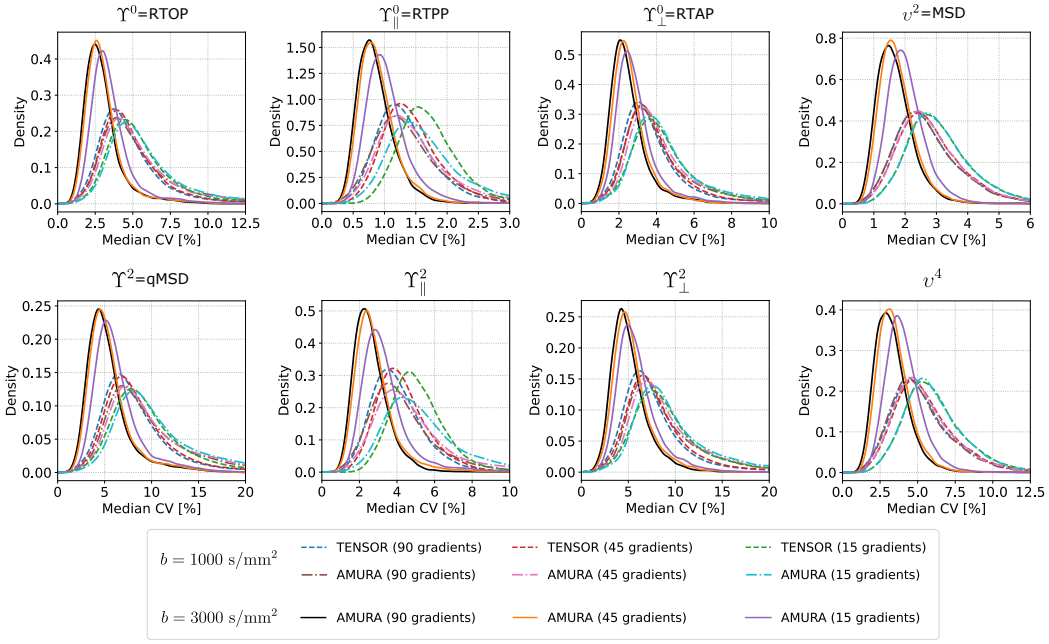

Fig. 3.9.: The histograms of median CV maps for DT- and AMURA-based moments obtained from randomly three subjects from the HCP WU-Minn test-retest database under different numbers of diffusion gradient directions employed to calculate the moments of $E(\mathbf{q})$ and $P(\mathbf{R})$, i.e. 90 (fully-sampled data), 45 and 15. The DT-based moments were obtained from a single-shell at $b = 1000$ s/mm^2, while the AMURA framework was applied to the data at $b = 3000$ s/mm^2. Each curve presents a kernel density estimated plot for the histogram of the CV map of the measure under a specified method and the number of gradient directions used to calculate the parameter.

Fig. 3.8 to delineate the differences between the methods across varying number of gradients. Next, for each measure retrieved with DTI at $b = 1000$ s/mm^2 and AMURA at $b = 1000$ and 3000 s/mm^2, we calculated the histogram from the median CV map aggregated from 37 subjects, $\mathrm{CV}(\mathbf{x})$, over the brain area of a representative slice (slice 85). We applied then a kernel density estimation method with a bandwidth selection using Scott's Rule to generate smoothly varying curves and put them together for each measure in Fig. 3.9. In both the AMURA and DT, we observe shifts in histogram peaks towards higher median CV value, especially once the number of gradients reduce to 15. Nonetheless, the changes in estimated density plots are consistent across all evaluated measures and acquisition scenarios with the advantage of AMURA-based measures under a higher b-value.

3.5.7 Clinical data: Episodic Migraine

Finally, in order to test the capability of the new measures to be used in clinical studies, we have selected a very specific pathology, the EM, in which differences in the white matter are particularly hard to find, compared to other frequently assessed disorders such as Alzheimer's disease or schizophrenia. Details about the nature and etiology of migraine can be found elsewhere [3.56, 3.43]. To better understand migraine pathophysiology, diverse modalities of MRI have been employed in literature, being especially relevant those based on DMRI [3.57, 3.58, 3.59]. One particular study, carried out with the same database we will use

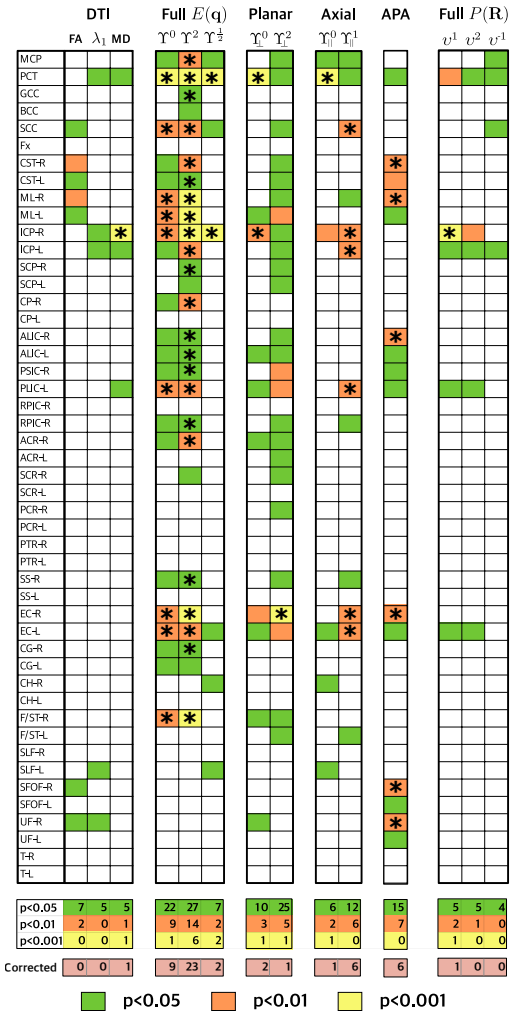

Fig. 3.10.: Episodic migraine (EM) vs. healthy controls (HC): two-sample t-tests for different measures calculated for EMDb database at $b = 1000\ \mathrm{s/mm^2}$ and at each of 48 ROIs defined by the ICBM-DTI-81 atlas (the lower the better). The p-values represent the probability that the measure has identical means for both controls and patients. Differences with statistical significance above 95% are highlighted in green, above 99% in amber and above 99.9% in yellow. At the bottom, the number of regions showing significant differences between EM and HC for each measure. We have carried out the correction for multiple comparisons for each measure following the Benjamini-Hochberg false discovery rate (FDR) procedure. Regions with statistically significant differences between both groups after correction are marked with a star (*).

in this work [3.7], found significantly lower axial diffusivity (AD=λ_1) and MD values in chronic migraine (CM) compared to EM using tract-based spatial statistics (TBSS) [3.60], but no statistically significant differences were found between EM and HCs. In a recent study [3.29] significant differences between patients with EM and HC were found using the RTOP calculated with AMURA over a single shell of $b = 1000\ \mathrm{s/mm^2}$. Patients with EM showed lower RTOP values than HC in 24 out of 48 the assessed regions from the ICBM-DTI-81 White Matter Atlas [3.61].

Hence, to test the moments with a different order, we will carry out a region-oriented analysis of the database in order to search for differences between EM and HC. For all the volumes, the FA was calculated using MRtrix [3.44] from the data collected at $b = 1000\ \mathrm{s/mm^2}$. The FA maps of all the volumes were warped to a common template using the standard TBSS pipeline [3.60]. The same transformation was applied to all the metrics considered for the experiment. A ROIs-based analysis was carried out: 48 different ROIs were identified on the subjects using the JHU WM atlas [3.48]. The average value of the metrics on the FA-skeleton inside each ROI was calculated within the 2% and 98% percentiles. Note that the measures are only calculated over the skeleton to obtain a more robust measure. Then we carried out a two-sample-two-tailed, pooled variance t-test between HC and EM patients for each of the measures considered at each of the 48 ROIs. We corrected these results for multiple comparisons for each diffusion descriptor following the Benjamini-Hochberg False Discovery Rate (FDR) procedure. Note that our purpose is not to carry out a complete clinical study but to analyze the behavior of each measure separately. Thus, results may vary with those reported in literature, especially considering that the statistical comparisons are distinct in the present study, and they should not be roughly interpreted to determine clinical differences (which have already been validated elsewhere [3.7, 3.29]).

Fourteen different measures were considered for the analysis: three DT-based measures (FA, AD, MD) and 11 AMURA-based (APA, Υ^0 (RTOP), Υ^2 (qMSD), $\Upsilon^{1/2}$, $\Upsilon^0_{||}$ (RTPP), $\Upsilon^1_{||}$, $\Upsilon^0_{\perp}$ (RTAP), $\Upsilon^2_{\perp}$, υ^1, υ^2 (MSD) and υ^{-1}). Fig. 3.10 shows a p-value scheme for the 48 ROIs considered for each of the measures. Those ROIs that exhibit differences with statistical significance (before multiple comparison correction and FDR) above 95% ($p < 0.05$) are highlighted in green, above 99% ($p < 0.01$) in amber, and above 99.9% ($p < 0.001$) in yellow. Those ROIs that exhibit differences with statistical significance after multiple comparison correction and FDR are marked by a star (*). In the bottom of the figure the number of regions of each kind for every measure are also shown.

Basic metrics based on the DT show a limited amount of differences, with only one ROI with statistically significant differences for the MD and none for the FA and AD after the FDR correction. This result is consistent with the literature in which, after proper statistical corrections, none are found. For the sake of comparison, another anisotropy metric has been added, PA calculated with AMURA, which can be seen as an alternative to the FA. In this particular experiment PA proves to be more sensitive to changes than FA, coherently with results reported in [3.28].

On the other hand, AMURA-based RTOP shows differences in nine regions after the correction for multiple comparisons. Once more, this is totally compatible with what we have seen in previous studies [3.7]: AMURA can detect changes between EM and HC where DTI cannot. In addition, qMSD (Υ^2) shows a behavior similar to RTOP but, in this particular case, it provides a higher number of statistically significant differences (23 ROIs vs. 9, respectively, after the FDR correction), which is related to the higher number of statistically significant results for lower p-values set as threshold for statistical significance (see *Full* $E(\mathbf{q})$, first two columns of Fig. 3.10). All the ROIs in qMSD show consistently smaller p-values than those in RTOP. Otherwise, the use of a non even moment like $\Upsilon^{1/2}$ does not seem particularly advantageous within this study.

RTAP and RTPP show a limited number of regions with differences after the FDR correction, in line with the findings in the literature. These two metrics would require a higher b-value in order to be more discriminant. However, in the planar case, note that when the order

of the moments increases the number of statistically significant differences also increases, considering the unadjusted and the corrected results. For teh axial case, this effect is only visible in the unadjusted case.

Finally, the moments of the $P(\mathbf{R})$ exhibit a behavior very similar to the DT indices, with only one region with statistically significant differences after the FDR correction, considering simultaneously the three measures. Actually, v^2 can be seen as a version of the MD with different weighting.

3.6 Discussion and conclusions

AMURA was originally proposed as a method to infer micro-structural information from single-shell acquisitions, with no need to specifically calculate the whole EAP. As stated in the original paper [3.27], the metrics provided by this method must be seen as *apparent* versions of the original metrics for a specific shell. The method was initially intended to be used for high b-values (over 2000 s/mm^2), since that is the regime in which measures like RTOP, RTPP and RTAP are better described. However, recent studies, like the one in [3.29], have shown its good performance even for DTI-like acquisitions with b-values around 1000 s/mm^2. In its original formulation, AMURA provided only a small amount of metrics: RTOP, RTPP, RTAP and APA. In this work, we have generalized them in order to provide a greater set of measures based on the moments of $E(\mathbf{q})$ and $P(\mathbf{R})$. The original AMURA metrics can be seen as particular cases of the new proposal calculating new generic moments.

In this sense, AMURA aims at generically describing the diffusion signal through the computation of arbitrary order moments, analogously to the proposal in [3.62]. There, the authors propose a framework to generate rotationally-invariant features from the SH coefficients fitted to the diffusion signal. These features are directly linked with the MD, FA, or the volume of the spherical signal, and can be directly derived from single-shell acquisitions as well. AMURA is not directly defined over the SH coefficients, but this mathematical formalism is only used for the purpose of efficient numerical calculus. Moreover, AMURA attains an alternative description beyond rotation invariants through the computation of planar and axial (i.e. directional) moments.

These generalizations are not just a simple mathematical effort to provide a theoretical framework to AMURA. On the contrary, the new measures allow to better quantify different aspects of the diffusion in the brain, dealing with different features of the diffusion process and being particularly sensitive to the restricted components of such diffusion and better suited to deal with multiple meso-structure diffusion components than DT-based metrics. As we have shown in Fig. 3.10, different ponderations of the same signal will yield to different results and, in the case of clinical studies, could yield to discover new variability patterns in some pathologies, as we have illustrated in the case of migraine.

Although AMURA only needs one shell in order to calculate the different measures, the information provided is not the same obtained from the DT. Differences can be clearly seen in Fig. 3.3 and the test-retest experiment. The use of the DT assumes not only a Gaussian decay, but also a single-bundle meso-structure, while AMURA uses a generic $D(\mathbf{u})$ that could take into account arbitrary fiber bundles orientations. In the experiment carried out, we could see that the DT approach underestimates the values of the moments in those regions in

which there is a complex fiber structure, like the centrum semiovale and the corpus callosum. In the former, different alignments and crossing-fiber structures cannot be properly described by the DT, while in the latter, the source of error is the high sub-voxel curvature of the fibers. Nevertheless, according to this particular experiment, moments calculated over the $E(\mathbf{q})$ are better estimated using a non-parametric orientation distribution, especially those moments of higher order. Results in this experiment are coherent with those obtained using more complex schemes, like MiSFIT (see Fig. 4 and 5 in [3.39]).

These results are also confirmed when we compared the *apparent* moments provided by AMURA with the *actual* moments estimated by a multishell approach, specifically MiSFIT. Although there are some clear differences in Fig. 3.4, for higher b-values, full and planar moments of the $E(\mathbf{q})$ show high correlation between both techniques. AMURA scalars present a reduced contrast when compared to MiSFIT, especially for the highest values of each moment. On the other hand, axial moments are the least robust ones, since they are computed over the $\mathbf{q}$-space samples along the maximum diffusion direction, for which the attenuation is maximal and the SNR dramatically decreases. We can conclude that AMURA does not produce totally analogous values to EAP-based approaches, one issue already raised in [3.27]. However, the large correlations between both methods suggest that these measures are not considering totally different diffusion features, but very close ones. Once again, the goal of AMURA is not estimating the exact same values as EAP-based methods. Nevertheless, a shifted version of a given moment as the ones provided, could also be equally valuable when studying diffusion.

The reproducibility study showed, in general, a good agreement between test and retest acquisitions verified over 37 subjects. The AMURA measures retrieved at $b = 1000\ \mathrm{s/mm^2}$ presented a similar behavior to the DT but with a smaller variation in those areas with higher FA, coherently with the previous experiment. In addition, once the b-value increases, starting from $b = 2000\ \mathrm{s/mm^2}$, our results suggest that AMURA outperforms the DT equivalents in terms of CV. These results seem promising once applying the non-zeroth-order moments of $E(\mathbf{q})$ and $P(\mathbf{R})$ to clinical studies under the higher b-value regime, like those studies where the primary zeroth-order EAP-based moments have already been implemented and showed an advantage over the standard protocols [3.24, 3.23, 3.25, 3.26, 3.63]. One can observe amplified CV values for highly anisotropic brain regions, principally for the DT based measures, i.e. corpus callosum, fornix and limb of the internal capsule (see Fig. 3.7). The exaggerated values are remarkably noticeable with the full Υ^p and planar $\Upsilon^p_\perp$ moments, especially the second-order ones. This effect can be explained on the ground of the tensor equations in 3.B, as in the case of prolate tensors, we observe a positive/negative bias on the second/third eigenvalue, while in oblate tensors, representing crossing fibers, the second and third eigenvalues are generally underestimated [3.64]. Therefore, special care must be taken once using higher-order moments, especially under the low b-value regime, as it might introduce a potential bias in the cohort studies. Nevertheless, the AMURA framework exhibits the robustness to a greatly limited number of the samples in the $\mathbf{q}$–space domain (e.g. only 15 samples per shell), allowing to significantly shorten the acquisition time while preserving the same amount of information. Notice that using only 15 gradient directions, the DT-based moments show intensified CV once compared to fully-sampled data with 90 directions (see Fig. 3.8). Although no studies were performed on the influence of confounding factors on DT-based moments, one can presume that at least 30 gradient directions are suggested for robust estimation, like in the case of FA parameter [3.65].

The robustness of AMURA-based moments has been quantitatively confirmed using the histogram-based study presented in Fig. 3.9. The peak values of kernel density estimated curves are only slightly shifted towards increased median CV value once reducing the number of gradients to only 15 directions. Overall, the reproducibility and robustness to a reduced acquisition scenario experiments allowed recognizing the potential application of the AMURA approach in studies concerning the variability of the brain anatomy, such as longitudinal or lifespan studies, in which a high level of reproducibility is a must.

Finally, in the migraine experiment, AMURA shows a better performance than DT metrics, although we must clarify that this could not be the case for every other study. We have selected one for which, according to the literature, AMURA succeeds in finding differences where the DT could not. But in the same study [3.29], AMURA could find almost no differences between EM and CM, while the DT succeeds. This effect talks about complementary measures, rather than competitive. On the other hand, this experiment allows us to better understand the behavior of different orders and kinds of moments of AMURA. According to the results in Fig. 3.10, the use of higher order moments in $\mathbf{q}$–space provides smaller p-values and allows finding a higher number of statistically significant differences between groups. This could be motivated by the fact that differences between EM and HC are subtle and these moments precisely highlight them. In general, the use of different moments could provide meaningful insight to different phenomenons of diffusion in the tissues, though further validation of AMURA moments is required to postulate them as clinical biomarker candidates.

Furthermore, metrics derived with AMURA have also shown larger correlation with multishell moments when higher b-values where considered. The acquisition of one single shell at b-values over 2000 s/mm^2 is not totally compatible with DT estimation, but it is consistent with single-shell HARDI techniques, in which the ODF is estimated and then some metrics could be derived, such as the ADC, the MD, the generalized FA (GFA) or the apparent fiber density (AFD) [3.66]. Once more, scalars derived from the ODF and moments from AMURA can be calculated together without extra-cost and be used complementarily in practical studies. The complementary nature of GFA and APA, for instance, was already shown in [3.28].

With regard to those moments based on the $P(\mathbf{R})$, they showed themselves not particularly interesting for clinical studies to the extent of the present paper: Fig. 3.3 shows a very high correlation between these indices calculated with either AMURA or the DT, putting at stake the added value of AMURA over DT in this case. When compared with a multishell approach like MiSFIT, these moments calculated with AMURA present a very low correlation with the actual values. In addition, the results of the migraine experiment also show a discriminant power similar to the DT-based measures and no added value. Thus, we must conclude that AMURA is not able to properly estimate the moments of $P(\mathbf{R})$. Unlike moments based on $E(\mathbf{q})$, for which a unique value of $\|\mathbf{q}\|$ allows to extrapolate an apparent behavior for the entire $\mathbf{q}$-space through modeling, a unique $\|\mathbf{q}\|$ sample does not allow a proper description of the bandwidth of the dual domain $\mathbf{R}$: results obtained with just one shell, although feasible from a theoretical point of view, do not provide significant information.

The computation of moments as proposed in this paper is based on the same implementation as in the original AMURA paper [3.27], hence it shares similar pros and cons: since the reconstruction of the EAP is not explicitly required, the computation of scalar measurements will not impose a computational burden to the standard protocols; an entire volume can

be processed in minutes or even seconds, so that a whole database for a clinical study can be processed in the order of few hours. On the other hand, one major drawback of these measures is the same pointed out in [3.27]: the explicit assumption of a specific radial behavior for the diffusion, which cannot fit the whole $\mathbf{q}$–space. As a consequence, the selection of a single shell will make the anatomical features dependent on the selected b-value and, consequently, they must be considered *apparent*. This effect was confirmed by experiment in Fig. 3.6 and it implies that, in clinical studies, the results can be compared against each other only if the same b-value is preserved across data sets. However, despite the dependence with the b-value, the *apparent* moments calculated with AMURA have also shown a great correlation with the *actual* moments calculated with a multishell approach, especially for higher b-values.

All in all, the newly introduced AMURA moments can be easily integrated into the processing pipeline of currently existing single-shell DMRI protocols and databases to unveil anatomical details that may remain hidden in traditional DT-based studies. Their simplicity and fast calculation make them proper complementary metrics for clinical studies.

Appendices

3.A Calculation of full moments of $P(\mathbf{R})$

3.A.1 Fourier Transform in spherical coordinates

Let $D(\mathbf{u}) > 0$ be the diffusivity for a given *shell* $q = q_0$. Using the mono-exponential model, the diffusion signal can be defined as:

$$E(\mathbf{q}) = E(q\mathbf{u}) = \exp\left(-\frac{q^2}{q_0^2} D(\mathbf{u})\right), \tag{3.23}$$

where $\mathbf{u} \in \mathcal{S}$ is a unit direction in space. Since both $E(\mathbf{q})$ and $P(\mathbf{R})$ are real signals, the Eq. (3.1) may as well be established in terms of cosine functions instead of complex exponentials. Besides, it is convenient to represent the integrals in spherical coordinates:

$$\begin{aligned} P(\mathbf{R}) = P(R\mathbf{r}) &= \int_{\mathcal{S}} \left(\int_0^{\infty} q^2 E(q\mathbf{u}) \cos\left(2\pi q R \mathbf{u}^T \mathbf{r}\right) dq \right) d\mathbf{u} \\ &= \int_{\mathcal{S}} \left(\int_0^{\infty} q^2 \exp\left(-\frac{q^2}{q_0^2} D(\mathbf{u})\right) \cos\left(2\pi q R \mathbf{u}^T \mathbf{r}\right) dq \right) d\mathbf{u}, \end{aligned} \tag{3.24}$$

where $\mathbf{r} \in \mathcal{S}$ is a unit direction independent on $\mathbf{u}$. The inner integral in the variable q can be explicitly solved to yield (see section 3.952, Eq. (4) in [3.67]):

$$P(R\mathbf{r}) = \frac{\sqrt{\pi} q_0^3}{4} \int_{\mathcal{S}} D^{-\frac{3}{2}}(\mathbf{u}) \left(1 - \frac{2\left(\pi q_0 R \mathbf{u}^T \mathbf{r}\right)^2}{D(\mathbf{u})}\right) \exp\left(-\frac{\left(\pi q_0 R \mathbf{u}^T \mathbf{r}\right)^2}{D(\mathbf{u})}\right) d\mathbf{u}. \tag{3.25}$$

3.A.2 Explicit computation of full moments

The p-th full moment of the diffusion propagator is defined as:

$$\upsilon^p \triangleq \int_{\mathbb{R}^3} R^p P(\mathbf{R}) d\mathbf{R} = \int_{\mathcal{S}} \left(\int_0^\infty R^{p+2} P(R\mathbf{r}) dR \right) d\mathbf{r}, \tag{3.26}$$

where the integral is already represented in spherical coordinates. By casting Eq. (3.25) into the previous expression, the order of the integrals can be exchanged at convenience to obtain:

$$\upsilon^p = \frac{\sqrt{\pi} q_0^3}{4} \int_{\mathcal{S}} D^{-\frac{3}{2}}(\mathbf{u}) \int_0^\infty R^{p+2} \int_{\mathcal{S}} \left(1 - \frac{2\left(\pi q_0 R \mathbf{u}^T \mathbf{r}\right)^2}{D(\mathbf{u})} \right) \exp\left(- \frac{\left(\pi q_0 R \mathbf{u}^T \mathbf{r}\right)^2}{D(\mathbf{u})} \right) d\mathbf{r}\, dR\, d\mathbf{u}. \tag{3.27}$$

The innermost integral in the variable $\mathbf{r}$ can then be computed using regular spherical coordinates by just aligning their 'z' axis (i.e. the origin of the polar angle $\theta = 0$) with each $\mathbf{u}$, so that $\mathbf{u}^T \mathbf{r} = \cos\theta$:

$$\begin{aligned} & \int_{\mathcal{S}} \left(1 - \frac{2\left(\pi q_0 R \mathbf{u}^T \mathbf{r}\right)^2}{D(\mathbf{u})} \right) \exp\left(- \frac{\left(\pi q_0 R \mathbf{u}^T \mathbf{r}\right)^2}{D(\mathbf{u})} \right) d\mathbf{r} \\ = & \int_0^{2\pi} \int_0^{\pi} \left(1 - \frac{2\left(\pi q_0 R \cos\theta\right)^2}{D(\mathbf{u})} \right) \exp\left(- \frac{\left(\pi q_0 R \cos\theta\right)^2}{D(\mathbf{u})} \right) \sin\theta\, d\phi\, d\theta \\ = & \ 2\pi \int_{-1}^{1} \left(1 - \frac{2\left(\pi q_0 R s\right)^2}{D(\mathbf{u})} \right) \exp\left(- \frac{\left(\pi q_0 R s\right)^2}{D(\mathbf{u})} \right) ds = 4\pi \exp\left(- \frac{\left(\pi q_0 R\right)^2}{D(\mathbf{u})} \right) \end{aligned} \tag{3.28}$$

where the last integral is solved with the change of variable $s = \cos(\theta)$. This result is casted into Eq. (3.27) to obtain:

$$\upsilon^p = \pi^{\frac{3}{2}} q_0^3 \int_{\mathcal{S}} D^{-\frac{3}{2}}(\mathbf{u}) \int_0^\infty R^{p+2} \exp\left(- \frac{\left(\pi q_0 R\right)^2}{D(\mathbf{u})} \right) dR\, d\mathbf{u} = \frac{\Gamma\left(\frac{p+3}{2}\right)}{2 q_0^p \pi^{p+\frac{3}{2}}} \int_{\mathcal{S}} D^{\frac{p}{2}}(\mathbf{u}) d\mathbf{u}, \tag{3.29}$$

whose convergence is assured if $p > -3$. The latter integral has to be numerically computed for each acquired signal, which can be trivially attained by expanding $D^{\frac{p}{2}}$ over $\mathcal{S}$ using SHs. This way, the integral becomes a scaled version of the DC component, $C_{0,0}$, of such expansion:

$$\upsilon^p = \frac{\Gamma\left(\frac{p+3}{2}\right)}{2 q_0^p \pi^{p+\frac{3}{2}}} \int_{\mathcal{S}} D^{\frac{p}{2}}(\mathbf{u}) d\mathbf{u} = \frac{\Gamma\left(\frac{p+3}{2}\right)}{2 q_0^p \pi^{p+\frac{3}{2}}} 2\sqrt{\pi} C_{0,0} \left\{ D^{\frac{p}{2}}(\mathbf{u}) \right\} = \frac{\Gamma\left(\frac{p+3}{2}\right)}{q_0^p \pi^{p+1}} C_{0,0} \left\{ D^{\frac{p}{2}}(\mathbf{u}) \right\}. \tag{3.30}$$

3.B Calculation of the moments using the diffusion tensor

If a Gaussian diffusion propagator is assumed, $P(\mathbf{R})$ is a mixture of independent and (nearly) identically distributed bounded cylinder statistics and, by virtue of the central limit

theorem, their superposition is Gaussian distributed. The measured signal in the $\mathbf{q}$–space is the (inverse) Fourier transform of the PDF and it can be expressed as:

$$E(\mathbf{q}) = \mathcal{F}^{-1}\left\{P(\mathbf{R})\right\}(\mathbf{q}) = \exp\left(-4\pi^2\tau\mathbf{q}^T\mathcal{D}\mathbf{q}\right), \tag{3.31}$$

which represents the well-known Stejskal–Tanner equation [3.68]. The diffusion tensor $\mathcal{D}$ is the anisotropic covariance matrix of the Gaussian PDF $P(\mathbf{R})$, and therefore it is a symmetric, positive–definite matrix with real, positive eigenvalues ($\lambda_1 \geq \lambda_2 \geq \lambda_3$) and orthonormal eigenvectors.

We can use this model to estimate the generalized moments of $E(\mathbf{q})$ and $P(\mathbf{R})$ defined in sections 3.3.1 and 3.3.2. For the sake of simplicity, only the even moments are calculated (the only ones with closed-form expressions):

1. Full moments of $E(\mathbf{q})$:

$$\Upsilon^p = \frac{1}{(4\pi^2\tau)^{\frac{3+p}{2}}}\sum_{k=0}^{p/2}\sum_{m=0}^{k}\binom{p/2}{k}\binom{k}{m}\frac{\Gamma\left(\frac{1}{2}+k-m\right)\Gamma\left(\frac{1}{2}+m\right)\Gamma\left(\frac{1}{2}+\frac{p}{2}-k\right)}{\lambda_1^{\frac{p}{2}+\frac{1}{2}-k}\,\lambda_2^{k-m+\frac{1}{2}}\,\lambda_3^{m+\frac{1}{2}}} \tag{3.32}$$

   This solution is valid for $p \geq 0$ and only for p integer and even. Some specific values are:

$$\begin{aligned}\Upsilon^0 &= \frac{\pi^{3/2}}{(4\pi^2\tau)^{3/2}}\frac{1}{\sqrt{\lambda_1\lambda_2\lambda_3}} && \text{(RTOP)};\\ \Upsilon^2 &= \frac{\pi^{3/2}}{2(4\pi^2\tau)^{5/2}}\frac{\lambda_1\lambda_2+\lambda_2\lambda_3+\lambda_1\lambda_3}{(\lambda_1\lambda_2\lambda_3)^{3/2}} && \text{(qMSD)}.\end{aligned}$$

2. Axial moments of $E(\mathbf{q})$:

$$\Upsilon^p_{||} = \frac{\Gamma\left(\frac{1+p}{2}\right)}{(4\pi^2\tau)^{\frac{1+p}{2}}\lambda_1^{\frac{1+p}{2}}}. \tag{3.33}$$

   This solution is valid for $p > -1$. For example:

$$\begin{aligned}\Upsilon^0_{||} &= \frac{\sqrt{\pi}}{\sqrt{4\pi^2\tau}}\frac{1}{\sqrt{\lambda_1}} && \text{(RTPP)};\\ \Upsilon^2_{||} &= \frac{\sqrt{\pi}}{2(4\pi^2\tau)^{3/2}}\frac{1}{\lambda_1^{3/2}}.\end{aligned}$$

3. Planar moments of $E(\mathbf{q})$:

$$\Upsilon^p_{\perp} = \frac{1}{(4\pi^2\tau)^{\frac{p}{2}+1}}\sum_{k=0}^{p/2}\binom{p/2}{k}\frac{\Gamma\left(\frac{1}{2}+k\right)\Gamma\left(\frac{1}{2}+\frac{p}{2}-k\right)}{\lambda_2^{-k+\frac{p}{2}+\frac{1}{2}}\,\lambda_3^{k+\frac{1}{2}}}. \tag{3.34}$$

   This solution is valid for $p \geq 0$ and only for p integer and even. Some specific values are

$$\begin{aligned}\Upsilon^0_{\perp} &= \frac{\pi}{4\pi^2\tau}\frac{1}{\sqrt{\lambda_2\lambda_3}} && \text{(RTAP)};\\ \Upsilon^2_{\perp} &= \frac{\pi}{2(4\pi^2\tau)^2}\frac{\lambda_2+\lambda_3}{(\lambda_2\lambda_3)^{3/2}}.\end{aligned}$$

4. Full moments of $P(\mathbf{R})$:

$$\begin{aligned} \upsilon^p &= \frac{1}{q_0^p \pi^{3+p}} \sum_{k=0}^{p/2} \sum_{m=0}^{k} \phi^{\upsilon}_{pkm} \lambda_1^{\frac{p}{2}-k} \, \lambda_2^{k-m} \, \lambda_3^m; \qquad (3.35) \\ \phi^{\upsilon}_{pkm} &= \binom{p/2}{k} \binom{k}{m} \Gamma\left(\frac{1}{2}+k-m\right) \Gamma\left(\frac{1}{2}+m\right) \Gamma\left(\frac{1}{2}+\frac{p}{2}-k\right). \end{aligned}$$

This solution is valid for $p \geq 0$ and only for p integer and even. Some specific values are:

$$\begin{aligned} \upsilon^0 &= 1; \\ \upsilon^2 &= \tfrac{1}{2\pi^2 q_0^2}(\lambda_1+\lambda_2+\lambda_3) \qquad \text{(MSD)}; \\ \upsilon^4 &= \tfrac{1}{4\pi^4 q_0^4}\left[2(\lambda_1^2+\lambda_2^2+\lambda_3^2)+(\lambda_1+\lambda_2+\lambda_3)^2\right]. \end{aligned}$$

Software

The full implementation of the methods here included are part of the dMRI-Lab toolbox and it may be downloaded for MATLAB© (The MathWorks, Inc., Natick, MA) and GNU Octave, together with use-case examples and test data, from: `http://www.lpi.tel.uva.es/dmrilab`.

Acknowledgments

This work was supported by Ministerio de Ciencia e Innovación of Spain with research grant RTI2018-094569-B-I00. Tomasz Pieciak acknowledges the Polish National Agency for Academic Exchange for grant PN/BEK/2019/1/00421 under the Bekker programme and the Ministry of Science and Higher Education (Poland) under the scholarship for outstanding young scientists (692/STYP/13/2018). Álvaro Planchuelo-Gómez was supported by Junta de Castilla y León (Spain) and the European Social Fund (ID: 376062, Base de Datos Nacional de Subvenciones).

Extra data for this project was provided by (1) the *Human Connectome Project* (HCP; Principal Investigators: Bruce Rosen, M.D., Ph.D., Arthur W. Toga, Ph.D., Van J. Weeden, MD). HCP funding was provided by the National Institute of Dental and Craniofacial Research (NIDCR), the National Institute of Mental Health (NIMH), and the National Institute of Neurological Disorders and Stroke (NINDS). HCP data are disseminated by the Laboratory of Neuro Imaging at the University of Southern California; (2) Cardiff University Brain Research Imaging Centre, provided by Chantal Tax. The data were acquired at the UK National Facility for In Vivo MR Imaging of Human Tissue Microstructure funded by the EPSRC (grant EP/M029778/1), and The Wolfson Foundation.

Conflict of interest

The authors declare no conflict of interest. The funders had no role in the design of the study; in the collection, analyses or interpretation of data; in the writing of the manuscript or in the decision to publish the results.

Bibliography

[3.1] J.-D. Tournier, S. Mori, A. Leemans, Diffusion tensor imaging and beyond, Magn. Reson. Med. 65 (6) (2011) 1532.

[3.2] H.-E. Assemlal, D. Tschumperlé, L. Brun, K. Siddiqi, Recent advances in diffusion MRI modeling: Angular and radial reconstruction, Med. Image Anal. 15 (4) (2011) 369–396.

[3.3] A. De Luca, A. Ianus, A. Leemans, M. Palombo, N. Shemesh, H. Zhang, D. C. Alexander, M. Nilsson, M. Froeling, G.-J. Biessels, et al., On the generalizability of diffusion MRI signal representations across acquisition parameters, sequences and tissue types: chronicles of the MEMENTO challenge, Neuroimage 240 (2021) 1–17.

[3.4] M. Rovaris, M. Filippi, Diffusion tensor MRI in multiple sclerosis, J. Neuroimaging 17 (s1) (2007) 27S–30S.

[3.5] M. Bester, J. Jensen, J. Babb, A. Tabesh, L. Miles, J. Herbert, R. Grossman, M. Inglese, Non-gaussian diffusion MRI of gray matter is associated with cognitive impairment in multiple sclerosis, Mult. Scler. J. 21 (7) (2015) 935–944.

[3.6] O. Pasternak, C.-F. Westin, B. Dahlben, S. Bouix, M. Kubicki, The extent of diffusion MRI markers of neuroinflammation and white matter deterioration in chronic schizophrenia, Schizophr. Res. 161 (1) (2015) 113–118.

[3.7] Á. Planchuelo-Gómez, D. García-Azorín, Á. L. Guerrero, S. Aja-Fernández, M. Rodríguez, R. de Luis-García, White matter changes in chronic and episodic migraine: a diffusion tensor imaging study, J. Headache Pain 21 (1) (2020) 1–15.

[3.8] Á. Planchuelo-Gomez, D. Garcia-Azorin, A. L. Guerrero, S. Aja-Fernández, M. Rodriguez, R. de Luis-Garcia, Structural connectivity alterations in chronic and episodic migraine: A diffusion magnetic resonance imaging connectomics study, Cephalalgia 40 (4) (2020) 367–383.

[3.9] P. J. Basser, J. Mattiello, D. LeBihan, MR diffusion tensor spectroscopy and imaging, Biophys. J. 66 (1) (1994) 259–267.

[3.10] J. H. Jensen, J. A. Helpern, A. Ramani, H. Lu, K. Kaczynski, Diffusional kurtosis imaging: The quantification of non-gaussian water diffusion by means of magnetic resonance imaging, Magn. Reson. Med. 53 (6) (2005) 1432–1440.

[3.11] D. S. Tuch, T. G. Reese, M. R. Wiegell, V. J. Wedeen, Diffusion MRI of complex neural architecture, Neuron 40 (2003) 885–895.

[3.12] E. Özarslan, T. M. Sepherd, B. C. Vemuri, S. J. Blackband, T. H. Mareci, Resolution of complex tissue microarchitecture using the Diffusion Orientation Transform (DOT), Neuroimage 31 (2006) 1086–1103.

[3.13] E. J. Canales-Rodríguez, C.-P. Lin, Y. Iturria-Medina, C.-H. Yeh, K.-H. Cho, L. Melie-García, Diffusion orientation transform revisited, Neuroimage 49 (2) (2010) 1326–1339.

[3.14] M. Descoteaux, R. Deriche, D. Le Bihan, J.-F. Mangin, C. Poupon, Multiple q-shell diffusion propagator imaging, Med. Image Anal. 15 (4) (2011) 603–621.

[3.15] E. Özarslan, C. G. Koay, T. M. Shepherd, M. E. Komlosh, M. O. Irfanoğlu, C. Pierpaoli, P. J. Basser, Mean apparent propagator (MAP) MRI: a novel diffusion imaging method for mapping tissue microstructure, Neuroimage 78 (2013) 16–32.

[3.16] L. Ning, C.-F. Westin, Y. Rathi, Estimating diffusion propagator and its moments using directional radial basis functions, IEEE Trans. Med. Imag. 34 (10) (2015) 2058–2078.

[3.17] T. D. Haije, E. Özarslan, A. Feragen, Enforcing necessary non-negativity constraints for common diffusion MRI models using sum of squares programming, Neuroimage 209 (2020) 116405.

[3.18] P. Basser, C. Pierpaoli, Microstructural features measured using diffusion tensor imaging, J. Magn. Reson. 111 (3) (1996) 209–219.

[3.19] C.-F. Westin, S. E. Maier, H. Mamata, A. Nabavi, F. A. Jolesz, R. Kikinis, Processing and visualization for diffusion tensor MRI, Med. Image Anal. 6 (2) (2002) 93–108.

[3.20] H. Lu, J. H. Jensen, A. Ramani, J. A. Helpern, Three-dimensional characterization of non-gaussian water diffusion in humans using diffusion kurtosis imaging, NMR Biomed. 19 (2) (2006) 236–247.

[3.21] Y.-C. Wu, A. S. Field, A. L. Alexander, Computation of diffusion function measures in q-space using magnetic resonance hybrid diffusion imaging, IEEE Trans. Med. Imag. 27 (6) (2008) 858–865.

[3.22] A. P. Hosseinbor, M. K. Chung, Y.-C. Wu, A. L. Alexander, Bessel fourier orientation reconstruction (BFOR): An analytical diffusion propagator reconstruction for hybrid diffusion imaging and computation of q-space indices, Neuroimage 64 (2013) 650–670.

[3.23] I. Boscolo Galazzo, L. Brusini, S. Obertino, M. Zucchelli, C. Granziera, G. Menegaz, On the viability of diffusion MRI-based microstructural biomarkers in ischemic stroke, Front. Neurosci. 12 (2018) 92.

[3.24] L. Brusini, S. Obertino, I. B. Galazzo, M. Zucchelli, G. Krueger, C. Granziera, G. Menegaz, Ensemble average propagator-based detection of microstructural alterations after stroke, Int. J. Comput. Assist. Radiol. Surg. 11 (9) (2016) 1585–1597.

[3.25] K. Ma, X. Zhang, H. Zhang, X. Yan, A. Gao, C. Song, S. Wang, Y. Lian, J. Cheng, Mean apparent propagator-MRI: a new diffusion model which improves temporal lobe epilepsy lateralization, Eur. J. Radiol. 126 (2020) 108914.

[3.26] H. Le, W. Zeng, H. Zhang, J. Li, X. Wu, M. Xie, X. Yan, M. Zhou, H. Zhang, M. Wang, et al., Mean apparent propagator MRI is better than conventional diffusion tensor imaging for the evaluation of Parkinson's disease: a prospective pilot study, Front. Aging Neurosci. 12.

[3.27] S. Aja-Fernández, R. de Luis-García, M. Afzali, M. Molendowska, T. Pieciak, A. Tristán-Vega, Micro-structure diffusion scalar measures from reduced MRI acquisitions, PloS one 15 (3) (2020) e0229526.

[3.28] S. Aja-Fernández, A. Tristán-Vega, D. K. Jones, Apparent propagator anisotropy from single-shell diffusion MRI acquisitions, Magn. Reson. Med. 85 (5) (2021) 2869–2881.

[3.29] Á. Planchuelo-Gómez, D. García-Azorín, Á. L. Guerrero, R. d. Luis-García, M. Rodríguez, S. Aja-Fernández, Alternative microstructural measures to complement diffusion tensor imaging in migraine studies with standard MRI acquisition, Brain Sci. 10 (10) (2020) 711.

[3.30] Á. Planchuelo-Gómez, R. Luis-García, D. García-Azorín, Á. L. Guerrero, A. Tristan-Vega, S. Aja-Fernández, AMURA with single-shell acquisitions detects additional white matter properties compared to the diffusion tensor in patients with persistent headache after COVID-19, in: Iberian ISMRM 1st Conference, 2021, p. 84.

[3.31] P. Callaghan, C. Eccles, Y. Xia, NMR microscopy of dynamic displacements: k-space and q-space imaging, J. Phys. E Sci. Instrum. 21 (8) (1988) 820.

[3.32] P. J. Basser, Relationships between diffusion tensor and q-space MRI, Magn. Reson. Med. 47 (2) (2002) 392–397.

[3.33] Y. Assaf, A. Mayk, Y. Cohen, Displacement imaging of spinal cord using q-space diffusion-weighted MRI, Magn. Reson. Med. 44 (5) (2000) 713–722.

[3.34] A. P. Hosseinbor, M. K. Chung, Y.-C. Wu, J. O. Fleming, A. S. Field, A. L. Alexander, Extracting quantitative measures from EAP: A small clinical study using BFOR, in: Med Image Comput Comput Assist Interv, Vol. 7511, Springer, 2012, pp. 280–287.

[3.35] L. Brusini, S. Obertino, M. Zucchelli, I. B. Galazzo, G. Krueger, C. Granziera, G. Menegaz, Assessment of mean apparent propagator-based indices as biomarkers of axonal remodeling after stroke, in: Medical Image Computing and Computer-Assisted Intervention – MICCAI 2015, Springer International Publishing, 2015, pp. 199–206.

[3.36] D. S. Tuch, Q–Ball imaging, Magn. Reson. Med. 52 (2004) 1358–1372.

[3.37] M. Zucchelli, L. Brusini, C. A. Méndez, A. Daducci, C. Granziera, G. Menegaz, What lies beneath? Diffusion EAP-based study of brain tissue microstructure, Med. Image Anal. 32 (2016) 145–156.

[3.38] S. Karmacharya, B. Gagoski, L. Ning, R. Vyas, H. Cheng, J. Soul, J. Newberger, M. Shenton, Y. Rathi, P. Grant, Advanced diffusion imaging for assessing normal white matter development in neonates and characterizing aberrant development in congenital heart disease, NeuroImage: Clinical 19 (2018) 360 – 373.

[3.39] A. Tristán-Vega, S. Aja-Fernández, Efficient and accurate EAP imaging from multi-shell dMRI with micro-structure adaptive convolution kernels and dual Fourier integral transforms (MiS-FIT), Neuroimage 227 (2021) 117616.

[3.40] Q. Fan, T. Witzel, A. Nummenmaa, K. R. Van Dijk, J. D. Van Horn, M. K. Drews, L. H. Somerville, M. A. Sheridan, R. M. Santillana, J. Snyder, et al., MGH–USC Human Connectome Project datasets with ultra-high b-value diffusion MRI, Neuroimage 124 (2016) 1108–1114.

[3.41] S. Moeller, P. Pisharady Kumar, J. Andersson, M. Akcakaya, N. Harel, R. Ma, X. Wu, E. Yacoub, C. Lenglet, K. Ugurbil, Diffusion imaging in the post HCP era, J. Magn. Reson. Imaging 54 (1) (2021) 36–57.

[3.42] D. C. Van Essen, S. M. Smith, D. M. Barch, T. E. Behrens, E. Yacoub, K. Ugurbil, W.-M. H. Consortium, et al., The WU-Minn human connectome project: An overview, Neuroimage 80 (2013) 62–79.

[3.43] Y. Zhang, Q. Kong, J. Chen, L. Li, D. Wang, J. Zhou, International classification of headache disorders 3rd edition beta-based field testing of vestibular migraine in china: Demographic, clinical characteristics, audiometric findings and diagnosis statues, Cephalalgia 36 (3) (2016) 240–248.

[3.44] J.-D. Tournier, R. Smith, D. Raffelt, R. Tabbara, T. Dhollander, M. Pietsch, D. Christiaens, B. Jeurissen, C.-H. Yeh, A. Connelly, MRtrix3: A fast, flexible and open software framework for medical image processing and visualisation, Neuroimage 202 (2019) 116137.

[3.45] M. Descoteaux, E. Angelino, S. Fitzgibbons, R. Deriche, Regularized, fast, and robust analytical Q-Ball imaging, Magn. Reson. Med. 58 (2007) 497–510.

[3.46] F. Aboitiz, J. Lopez Calderon, J. Montiel, Long distance communication in the human brain: Timing constraints for inter-hemispheric synchrony and the origin of brain lateralization, Biol. Res. 36 (2003) 89–99.

[3.47] S. M. Smith, M. Jenkinson, M. W. Woolrich, C. F. Beckmann, T. E. Behrens, H. Johansen-Berg, P. R. Bannister, M. De Luca, I. Drobnjak, D. E. Flitney, et al., Advances in functional and structural MR image analysis and implementation as FSL, Neuroimage 23 (2004) S208–S219.

[3.48] S. Mori, S. Wakana, P. C. Van Zijl, L. Nagae-Poetscher, MRI atlas of human white matter, Elsevier, 2005.

[3.49] M. Jenkinson, S. Smith, A global optimisation method for robust affine registration of brain images, Med. Image Anal. 5 (2) (2001) 143–156.

[3.50] M. Jenkinson, P. Bannister, M. Brady, S. Smith, Improved optimization for the robust and accurate linear registration and motion correction of brain images, Neuroimage 17 (2) (2002) 825–841.

[3.51] F. Aboitiz, A. Scheibel, R. Fisher, E. Zaidel, Fiber composition of the human corpus callosum, Brain Res. 598 (1992) 143–53.

[3.52] T. R. Knösche, A. Anwander, M. Liptrot, T. B. Dyrby, Validation of tractography: Comparison with manganese tracing, Hum. Brain Mapp. 36 (10) (2015) 4116–4134.

[3.53] J. A. Farrell, B. A. Landman, C. K. Jones, S. A. Smith, J. L. Prince, P. C. van Zijl, S. Mori, Effects of signal-to-noise ratio on the accuracy and reproducibility of diffusion tensor imaging–derived fractional anisotropy, mean diffusivity, and principal eigenvector measurements at 1.5t, J. Magn. Reson. Imaging 26 (3) (2007) 756–767.

[3.54] S. Aja-Fernández, M. Niethammer, M. Kubicki, M. E. Shenton, C.-F. Westin, Restoration of DWI data using a Rician LMMSE estimator, IEEE Trans. Med. Imaging. 27 (10) (2008) 1389–1403.

[3.55] A. Tristán-Vega, S. Aja-Fernández, C.-F. Westin, Least squares for diffusion tensor estimation revisited: Propagation of uncertainty with Rician and non-Rician signals, Neuroimage 59 (4) (2012) 4032–4043.

[3.56] Z. Katsarava, D. C. Buse, A. N. Manack, R. B. Lipton, Defining the differences between episodic migraine and chronic migraine, Curr. Pain Headache Rep. 16 (1) (2012) 86–92.

[3.57] X. L. Li, Y. N. Fang, Q. C. Gao, E. J. Lin, S. H. Hu, L. Ren, M. H. Ding, B. N. Luo, A diffusion tensor magnetic resonance imaging study of corpus callosum from adult patients with migraine complicated with depressive/anxious disorder, Headache 51 (2) (2011) 237–245.

[3.58] D. Yu, K. Yuan, W. Qin, L. Zhao, M. Dong, P. Liu, X. Yang, J. Liu, J. Sun, G. Zhou, et al., Axonal loss of white matter in migraine without aura: a tract-based spatial statistics study, Cephalalgia 33 (1) (2013) 34–42.

[3.59] C. D. Chong, T. J. Schwedt, Migraine affects white-matter tract integrity: a diffusion-tensor imaging study, Cephalalgia 35 (13) (2015) 1162–1171.

[3.60] S. Smith, M. Jenkinson, H. Johansen-Berg, et al., Tract-based spatial statistics: Voxelwise analysis of multi-subject diffusion data, Neuroimage 31 (2006) 1487–1505.

[3.61] S. Mori, K. Oishi, H. Jiang, L. Jiang, X. Li, K. Akhter, K. Hua, A. V. Faria, A. Mahmood, R. Woods, et al., Stereotaxic white matter atlas based on diffusion tensor imaging in an ICBM template, Neuroimage 40 (2) (2008) 570–582.

[3.62] M. Zucchelli, S. Deslauriers-Gauthier, R. Deriche, A computational framework for generating rotation invariant features and its application in diffusion MRI, Med. Image Anal. 60 (2020) 101597.

[3.63] J. Moody, D. Dean III, S. Kecskemeti, S. Johnson, B. Bendlin, A. Alexander, Assessing white matter microstructural changes associated with aging & dementia using mean apparent propagator (MAP) MRI, in: Proc. Intl. Soc. Mag. Reson. Med., 2021, p. 1922.

[3.64] B. Whitcher, D. S. Tuch, J. J. Wisco, A. G. Sorensen, L. Wang, Using the wild bootstrap to quantify uncertainty in diffusion tensor imaging, Hum. Brain Mapp. 29 (3) (2008) 346–362.

[3.65] D. K. Jones, The effect of gradient sampling schemes on measures derived from diffusion tensor MRI: a Monte Carlo study, Magn. Reson. Med. 51 (4) (2004) 807–815.

[3.66] M. Descoteaux, High angular resolution diffusion imaging (HARDI), Wiley encyclopedia of electrical and electronics engineering (1999) 1–25.

[3.67] I. S. Gradshteyn, I. M. Ryzhik, Table of integrals, series, and products, Academic press, 2014.

[3.68] E.-O. Stejskal, J.-E. Tanner, Spin diffusion measurements: Spin echoes in the presence of a time-dependent field gradient, J. Chem. Phys. 42 (1965) 288–292.

4

Viability of AMURA biomarkers from single-shell diffusion MRI in Clinical Studies

Carmen Martín-Martín[1], Álvaro Planchuelo-Gómez[1,4], Ángel L. Guerrero[2,3], David García-Azorín[2], Antonio Tristán-Vega[1], Rodrigo de Luis-García[1] and Santiago Aja-Fernández[1]

[1] *Laboratorio de Procesado de Imagen (LPI), Universidad de Valladolid, Valladolid, Spain*
[2] *Headache Unit, Dept. of Neurology, Hospital Clínico Universitario de Valladolid, Spain*
[3] *Department of Medicine, Universidad de Valladolid, Valladolid, Spain*
[4] *Cardiff University Brain Research Imaging Centre (CUBRIC), Cardiff University, Cardiff, UK*

Abstract: Diffusion Tensor Imaging (DTI) is the most employed method to assess white matter properties using quantitative parameters derived from diffusion MRI, but it presents known limitations that restrict the evaluation of complex structures. The objective of this study was to validate the reliability and robustness of complementary diffusion measures extracted with a novel approach, Apparent Measures Using Reduced Acquisitions (AMURA), with a typical diffusion MRI acquisition from a clinical context in comparison with DTI with application to clinical studies. Fifty healthy controls, 51 episodic migraine and 56 chronic migraine patients underwent single-shell diffusion MRI. Four DTI-based and eight AMURA-based parameters were compared between groups with tract-based spatial statistics to establish reference results. On the other hand, following a region-based analysis, the measures were assessed for multiple subsamples with diverse reduced sample sizes and their stability was evaluated with the coefficient of quartile variation. To assess the discrimination power of the diffusion measures, we repeated the statistical comparisons with a region-based analysis employing reduced sample sizes with diverse subsets, decreasing 10 subjects per group for consecutive reductions, and using 5001 different random subsamples. For each sample size, the stability of the diffusion descriptors was evaluated with the coefficient of quartile variation. AMURA measures showed a greater number of statistically significant differences in the reference comparisons between episodic migraine patients and controls compared to DTI. In contrast, a higher number of differences was found with DTI parameters compared to AMURA in the comparisons between both migraine groups. Regarding the assessments reducing the sample size, the AMURA parameters showed a more stable behavior than DTI, showing a lower decrease for each reduced sample size or a higher number of regions with significant differences. However, most AMURA parameters showed lower stability in relation to higher coefficient of quartile variation values than the DTI descriptors, although two AMURA measures showed similar values to DTI. For the synthetic signals, there were AMURA measures with similar quantification to DTI, while other showed similar behavior. These findings suggest that AMURA presents favorable characteristics to identify differences of specific microstructural properties between clinical groups in regions with complex fiber architecture and lower dependency on the sample size or assessing technique than DTI.

Originally published as: *armen Martín-Martín, Álvaro Planchuelo-Gómez, Ángel L. Guerrero, David García-Azorín, Antonio Tristán-Vega, Rodrigo de Luis-García and Santiago Aja-Fernández, Viability of AMURA biomarkers from single-shell diffusion MRI in clinical studies, Frontiers in Neuroscience, VOl 17, 2023 DOI=10.3389/fnins.2023.1106350*

4.1 Introduction

Diffusion Magnetic Resonance Imaging (dMRI) is an imaging modality employed to assess diverse in vivo physiological and pathological conditions of the human body in clinical studies. It has been widely used in the study of the brain and neurological disorders [4.42, 4.21, 4.29, 4.23]. It allows the characterization of the diffusivity of water molecules within the tissue, providing information about the microscopic configuration and structural connectivity of the brain, especially inside the white matter (WM).

The most relevant feature of dMRI is its ability to measure directional variance, i.e., anisotropy, which, inside the brain, is related to structural connectivity between areas. The most common methodology to estimate the anisotropy is via the diffusion tensor (DT) [4.11, 4.51].

In order to use it in clinical studies, the information provided by the DT must be translated into some scalar measures that describe different features of diffusion within every voxel. That way, metrics like fractional anisotropy (FA) were defined and widely employed to characterize damaged tissues in multiple neurological and psychiatric disorders [4.28, 4.12, 4.31, 4.24]. However, from the early stages of DT imaging (DTI), it was clear that the Gaussian assumption oversimplifies the diffusion process.

In the past few decades, many techniques have been proposed to overcome the limitations of DTI, usually requiring the acquisition of larger amounts of diffusion data [4.8, 4.35]. Most of these techniques rely on the estimation of more advanced diffusion descriptors, such as the Ensemble Average diffusion Propagator (EAP), which is the probability density function of the motion of the water molecules within a voxel [4.37, 4.47, 4.50].

A complete analysis of the EAP requires many diffusion-weighted images (DWI) with several (moderate to high) b-values in a multi-shell acquisition. The information provided by the EAP is usually adapted to scalar measures that describe different aspects of diffusion. The most frequently employed measures are the return-to-origin probabilities (RTOP), return-to-plane probabilities (RTPP), return-to-axis probabilities (RTAP) and the propagator anisotropy (PA) [4.37, 4.34, 4.53, 4.17, 4.25].

The accurate estimation of these measures requires the calculation of the EAP, which commonly involves: (1) long acquisition times; (2) several shells with large b-values, which may be difficult to acquire in many commercial MRI scanners; and (3) heavy computational burdens with very long processing times. These three issues have hindered the general adoption of EAP-related metrics in the clinical routine, despite the growing interest in the exploration of their potential applicability [4.9, 4.14, 4.13, 4.55].

To overcome these limitations and facilitate the widespread use of advanced diffusion metrics in clinical studies, a new approach called Apparent Measures Using Reduced Acquisitions (AMURA) has been recently proposed [4.1, 4.2, 4.3]. The method allows the estimation of

diffusion measures such as RTOP, RTAP and PA, while reducing the number of necessary samples and the computational cost. AMURA can mimic the sensitivity of EAP-based measures to microstructural changes when only a small number of shells (even one) is available. To do so, AMURA assumes a prior model for the behavior of the radial q-space instead of trying to numerically describe it, yielding simplified expressions that can be computed easily even from single-shell acquisitions.

One additional advantage of AMURA is that it can be easily integrated into the processing pipeline of current existing single-shell dMRI protocols and databases to unveil anatomical details that may remain hidden in traditional DT-based studies. AMURA has proved its potential in some exploratory studies with clinical data focusing on Parkinson's disease and Mild Cognitive Impairment [4.1, 4.3], as well a recent clinical study on migraine [4.41].

In this work we aim to assess the viability of different diffusion descriptors extracted with AMURA for the study of a neurological disorder in DTI-type datasets. Note that, initially, AMURA was designed to work with b-values over 2000 s/mm^2, since the effects measured with RTOP, RTPP and RTAP were better showed at higher values of b. However, results in clinical data have shown its potential at lower b-values [4.2]. Thus, we will explore the viability of these technique to model DTI-type acquisitions, i.e., dMRI datasets acquired with those protocols usually employed for the estimation of DTI and its derived parameters, such as fractional anisotropy (FA) or mean diffusivity (MD). These acquisitions are commonly single-shell, and only include one non-zero b-value, usually in the order of $b = 1000$ s/mm^2.

We have selected migraine as a case study. Migraine is an attractive pathology for the evaluation of the quality of alternative diffusion metrics, since the differences between patients and controls that have been found using dMRI in the literature are scarce and subtle [4.40]. In migraine, differences are usually hard to find in comparison with other disorders such as schizophrenia or Alzheimer's disease, and they require a large number of subjects per group and good quality data. Thus, migraine will allow us to check the capability of different techniques to detect subtle changes.

Migraine is a disabling primary disorder characterized by recurrent episodes of headache, which usually last 4-72 hours and present at least two of the following four characteristics: moderate to severe pain intensity, unilateral location, pulsating quality, and aggravation with physical activity (Third edition of the International Classification of Headache Disorders, ICHD-3). A common distinction when studying migraine is made between episodic migraine (EM), in which patients suffer from headache less than 15 days per month, and chronic migraine (CM), in which patients suffer from headache at least 15 days per month.

A recent study identified statistically significant differences in migraine using advanced diffusion measures calculated with AMURA [4.41]. This study identified higher RTOP values in CM patients compared to EM, and lower RTPP values in EM compared to HC.

Given the fact that AMURA-derived measures have shown promising results for the characterization of subtle WM changes in migraine, the main objective of this study was the assessment of the reliability and the robustness of AMURA metrics acquired with a typical acquisition employed in a clinical context. Our purpose is to validate the viability of these metrics for clinical studies even when acquisition protocols are suboptimal for this methodology. Specifically, we will use migraine as a case study and DTI-type acquisitions, where only one shell is acquired at $b = 1000$ s/mm^2.

4.2 Materials and Methods

4.2.1 Advanced diffusion measures from single shell acquisitions: AMURA

AMURA was proposed in [4.1] as a methodology to calculate advanced diffusion metrics from reduced acquisitions compatible with commercial scanners and general clinical routine. It allows the estimation of different diffusion-related scalars using a lower number of samples with a single-shell acquisition scheme. AMURA considers that, if the amount of data is reduced, a restricted diffusion model consistent with single-shell acquisitions must be assumed: the (multi-modal) apparent diffusivity does not depend on the b-value, so that a mono-exponential behavior is observed for every spatial direction. According to [4.10], in the mammalian brain, the mono-exponential model is predominant for values of b up to 2000 s/mm^2 and it can be extended to higher values (up to 3000 s/mm^2) if appropriate multi-compartment models of diffusion are employed.

This methodology allows shorter MRI acquisitions and very fast calculation of scalars. Since the mono-exponential model only holds within a limited range around the measured b-value, the measures derived this way must be seen as *apparent* values at a given b-value, related to the original ones but dependent on the selected shell. The AMURA metrics used in this work are [4.1, 4.2, 4.3]:

1. Return-to-origin probability (RTOP), also known as probability of zero displacement, it is related to the probability density of water molecules that minimally diffuse within the diffusion time τ.
2. Return-to-plane probability (RTPP), which is a good indicator of restrictive barriers in the axial orientation.
3. Return-to-axis probability (RTAP), an indicator of restrictive barriers in the radial orientation.
4. Apparent Propagator Anisotropy (APA), an alternative anisotropy metric. It quantifies how much the propagator diverges from the closest isotropic one.
5. Diffusion Anisotropy (DiA), an alternative derivation of APA.
6. Generalized Moments, specifically we will consider the full moments of order 2 (q-space Mean Square Displacement, qMSD) and $1/2$ ($\Upsilon^{1/2}$).

4.2.2 Dataset

Participants

The sample of this study was originally composed of 56 patients with CM, 54 patients with EM and 50 healthy controls (HC) that participated in previous studies [4.40, 4.39]. Three patients with EM were discarded due to misregistration errors.

Inclusion criteria included diagnosis of EM or CM following the ICHD-3 (all the available versions), stable clinical situation, and first screening related to migraine just before the

recruitment. Exclusion criteria were use of preventive treatments before the MRI acquisition, migraine onset in people older than 50 years, recently developed migraine (less than one year), frequent painful conditions, psychiatric and neurological disorders different to migraine, and pregnancy. Further details are available at [4.40].

The local Ethics Committee of Hospital Clínico Universitario de Valladolid approved the study (PI: 14-197). Additionally, all participants read and signed a written consent form prior to their participation.

The detailed demographic and clinical features of the three groups are shown in Table 4.1. No statistically significant differences in age or gender were found between the three groups. Patients with CM showed significantly higher duration of migraine, frequency of headache and migraine attacks and medication overuse, and a lower presence of aura.

Tab. 4.1.: Clinical and demographic characteristics of healthy controls (HC), episodic migraine (EM) and chronic migraine (CM).

	HC (n=50)	EM (n=51)	CM (n=56)	Statistical test
Gender, male/female	11/39 (22/78%)	7/44 (14/86%)	6/50 (11/89%)	$\chi^2_{(2,N=157)} = 2.74$, p = .25 †
Age (years)	36.1 ± 13.2	36.6 ± 7.9	38.1 ± 8.7	$\chi^2_{(2)} = 2.79$, p = .25‡
Duration of migraine history (years)		13.1 ± 10.5	19.6 ± 10.4	U = 932.5, p = .002◇
Time from onset of chronic migraine (months)			24.5 ± 32.9	
Headache frequency (days/month)		3.6 ± 1.9	23.3 ± 6.3	U = 40.0, p < .001◇
Migraine frequency (days/month)		3.6 ± 1.9	13.9 ± 6.9	U = 99.5, p < .001◇
Medication overuse		0 (0%)	42 (75%)	p < .001*
Aura		9 (18%)	1 (2%)	p = .006*

†Chi-square test. ‡Kruskal-Wallis test. ◇Mann-Whitney U test. *Fisher's exact test. Data are expressed as means ± SD.

MRI acquisition

For patients with migraine, the images were acquired at least 24 hours after the last migraine attack and before two weeks after the clinical visit to the headache unit. High resolution 3D T1-weighted followed by DWI were acquired using a Philips Achieva 3T MRI unit (Philips Healthcare, Best, The Netherlands) with a 32-channel head coil . The acquisition of T1-weighted images was carried out using a Turbo Field Echo sequence with the following parameters: repetition time (TR) = 8.1 ms, echo time (TE) = 3.7 ms, flip angle = 8^o, 256×256 matrix size, spatial resolution of $1 \times 1 \times 1$ mm^3 and 160 sagittal slices covering the whole brain.

The acquisition parameters for DWI were TR = 9000 ms, TE = 86 ms, flip angle = 90^o, 61 diffusion gradient orientations, one baseline volume, b-value = 1000 s/mm^2, 128×128 matrix size, spatial resolution of $2 \times 2 \times 2$ mm^3 and 66 axial slices covering the whole brain.

All the images were acquired in the same session with a total acquisition time of 18 minutes.

4.2.3 Analysis of the data

dMRI preprocessing

Image preprocessing steps consisted of 1) denoising based on the Marchenko-Pastur Principal Component Analysis procedure [4.49], 2) eddy currents and motion correction and 3) correction for B1 field inhomogeneity. The MRtrix software [4.46] was employed to carry out these steps, using the *dwidenoise*, *dwipreproc* and *dwibiascorrect* tools [4.49, 4.7, 4.44, 4.54]. Further, a whole brain mask for each subject was obtained with the *dwi2mask* tool [4.18].

Diffusion measures estimation

Two groups of diffusion measures were extracted. The former group is composed of three DTI classical metrics: FA, MD, axial diffusivity (AD) and radial diffusivity (RD). We considered only these measurements as they are the ones employed in most previous studies, particularly in the literature migraine, with no studies applying other measurements excluding the one carried out with this sample or the use of kurtosis [4.26].

These measures were estimated at each voxel using the *dtifit* tool from the FSL software [4.27]. FA measures the degree of anisotropy in the diffusion of water molecules inside each voxel, which reflects the degree of directionality of water diffusivity. MD is the average magnitude of water molecules diffusion. AD measures the water diffusion in the principal direction of WM fibers. RD describes the perpendicular diffusion of the principal direction [4.38].

The latter group includes the seven proposed q-space metrics calculated with AMURA: RTOP, RTAP, RTPP, APA, qMSD, DiA and $\Upsilon^{1/2}$. The measures were calculated using dMRI-Lab[1] and MATLAB 2020a. AMURA measures rely on the expansion of spherical functions at a given shell in the basis of spherical harmonics (SH). Even SH orders up to 6 were fitted with a Laplace-Beltrami penalty $\lambda = 0.006$. A fixed value of $\tau = 70$ms has been assumed for all the AMURA metrics. A visual comparison of the DTI and AMURA measures is shown in Figure 4.1.

[1]Available at `www.lpi.tel.uva.es/dmrilab`.

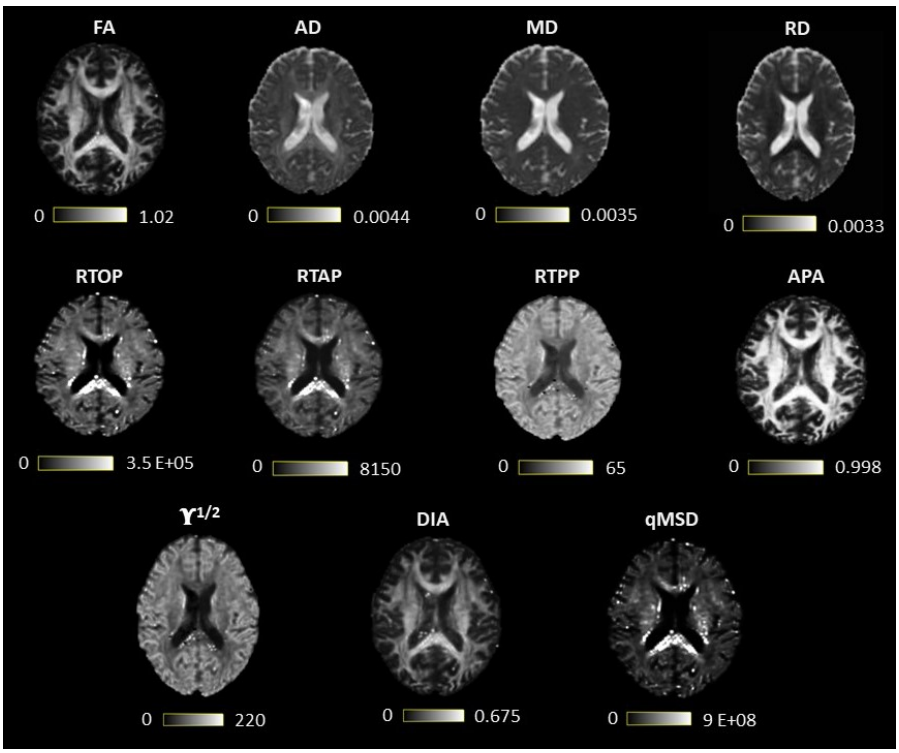

Fig. 4.1.: Visual comparison of diffusion tensor imaging (DTI) and measures from apparent measures using reduced acquisitions (AMURA). The first row contains the DTI measures, and the last two, the AMURA metrics.

4.2.4 Experiment with synthetic data

The main hypothesis of this work is that AMURA metrics are able to detect different diffusion properties than DTI in the white matter. In order to quantify this assumption, an illustrative synthetic experiment was carried out. We simulated a simple diffusion model that diverges from the diffusion tensor (DT). The simplest case is a 2-compartment model in which we considered that the main anisotropic diffusion was ruled by a zeppelin-shaped compartment [4.5] and there was an isotropic compartment that stands for the free water fraction [4.48]:

$$S(b) = f \cdot Z_p(b, d_{||}, d_{\perp}) + (1 - f) \cdot \exp(-bD_0)$$

where $Z_p()$ is the zeppelin compartment, D_0 is the diffusivity of free water at body temperature (nearly $3.0 \cdot 10^{-6}$ μm^2/s), $d_{||}$ (μm^2/s) and $d_{\perp}$ (μm^2/s) are the parallel and perpendicular diffusivities that model the zeppelin and $(1 - f)$ is the free-water fraction.

For the experiment, different values of f were considered, ranging from 0.3 to 1. The value of $d_{||}$ was fixed and $d_{\perp}$ was changed as a function of f for two different cases

1. The FA obtained after estimating the DT from $S(b)$ is constant.

2. The MD obtained after estimating the DT from $S(b)$ is constant.

Sixty-one gradient directions and b=1,000 s/mm^2 were considered. DTI and AMURA metrics were calculated from the synthetic signal.

In comparison with previous studies that assessed EAP-derived measures [4.20, 4.55], we employed a simpler model due to the different objective of our study. The previous studies were focused on a detailed characterization of the microstructure with the assessment of the sensitivity of the EAP measures under different conditions with a three-compartment model. The intracellular volume fraction and dispersion were additionally included compared to our experiment for the three-compartment model. In our study, the main objective was the assessment of AMURA measures compared to DTI in the context of clinical studies, i.e., comparison between clinical groups, with a reduced dMRI acquisition. Therefore, this synthetic experiment worked as a proof of concept to appreciate different properties of the AMURA and DTI measures, and not as a detailed analysis of the parameters in relation to microstructural features.

4.2.5 Statistical analysis

ROI analysis and TBSS

To test the capability of AMURA measures at b = 1000 s/mm2 to be used in clinical studies, two different statistical analyses were considered: a region-oriented analysis and tract-based spatial statistics (TBSS) assessment. For both approaches, statistical differences between EM, CM and HC were assessed with two-by-two comparisons. Forty-eight different regions of interest (ROIs) were identified using the Johns Hopkins University ICBM-DTI-81 White Matter Atlas (JHU WM) [4.36]. The first steps of the two assessing methods were common. The FA volumes were non-linearly registered to the Montreal Neurological Institute (MNI) space using the JHU WM template as reference. In the MNI space, the mean FA image for all the subjects was extracted and it was used to generate the white matter skeleton using a minimum FA value of 0.2. For each subject, the FA values were projected to the skeleton. For all the non-FA measures, the same registration used for the FA maps and projection to the skeleton obtained from the FA volumes were carried out.

For the ROI-based analysis, to obtain more robust measures, the average value of the metrics for each subject was obtained using voxels exclusively included in the white matter skeleton within the 2% and 98% percentiles of the corresponding skeleton values. Then we carried out a two-sampled-two-tailed, pooled variance t-test between each pair of groups (EM-HC, CM-HC and EM-CM) for every measure and ROI.

The TBSS approach was conducted to mimic a clinical study following the basic procedure implemented in [4.41, 4.40]. In this assessment, the statistical comparisons were conducted using the `randomise` tool from FSL [4.33], which performs a permutation test. Specifically, 5000 permutations and the threshold-free cluster enhancement (TFCE) procedure were employed [4.45]. Briefly, TFCE enhances zones of the voxelwise statistic maps that show spatial contiguity to obtain spatial clusters without using specific values to delimitate different spatial areas with similar values. We considered that an atlas-defined region presented statistically significant differences, after family-wise error correction and TFCE, when the voxels with differences contained a volume greater than 30 mm^3. Each ROI from the atlas could be part of one or more clusters defined by the TFCE procedure, i.e., TFCE

was applied independently from the JHU WM atlas and the voxels for each region were extracted within the defined clusters by TFCE.

The threshold for statistical significance for all the statistical assessments was $p < 0.05$. It is worth noting that the purpose of the ROI-based analysis was not to carry out a complete and accurate clinical study, but to analyze the behavior of each measure separately. Thus, the results in this case were not corrected for multiple comparisons, causing some variations with the results reported in the literature. For the same reason, clinical covariates were not included in all the statistical comparisons.

Further, in relation to the ROI-based analysis, Cohen's D value was calculated over the different ROIs to quantify the effect size of the different DTI and AMURA scalars. In addition, the Cohen's D value was obtained for the full WM to better describe what happened with each measure in the whole brain.

Resampling of diffusion measures

To better understand the discrimination power of each measure, we analyzed their statistical significance in relation to the number of subjects in each group, i.e., the sample size. To that end, a resampling experiment was carried out. The number of subjects of each group (EM, CM and HC) was progressively decreased from the original number to 10 subjects in each group, reducing five subjects for each iteration. For each iteration, 5001 different subsamples were randomly obtained following a bootstrapping procedure. For each subsample, the ROI-based approach described in section 4.2.5, i.e., the uncorrected t-tests of the diffusion descriptors from each JHU WM atlas ROI within the WM skeleton, was repeated. Specifically, for the tests with statistically significant differences in the reference comparisons with the whole sample, two-by-two comparisons between HC, EM and CM groups were carried out. For each ROI, diffusion metric and specific configuration, a ROI was considered to have significant differences if at least the two-by-two comparison in 2501 out of the 5001 subsamples showed $p < 0.05$, value established as threshold for statistical significance, as in the whole sample. No kind of statistical correction was used for this experiment considering that our purpose was to study the behavior of the different metrics with the sample size.

Analysis of stability

The coefficient of quartile variation (CQV) was used to measure the stability across groups. The CQV is a measure of homogeneity [4.6] and it was used to assess the inter-subject variability, considering the diverse sample sizes from the analysis described in the previous section. The CQV is one of the most robust statistical measures as it depends on the quartiles, being less sensitive to outliers. Its use is as follows:

$$\text{CQV} = \frac{Q_3 - Q_1}{Q_3 + Q_1} \cdot 100 \tag{4.1}$$

where Q_1 and Q_3 are the first and third quartile, respectively.

The CQV is calculated for each group and ROI, considering as figure of merit the median value of all the CQV of the different 5001 subsamples used in this experiment. The 95% confidence interval (95% CI) was set taking the 2.5 and 97.5 percentiles of the whole CQV

values for each group of values. This 95% CI was compared between the diverse measures and regions for each sample size.

4.3 Results

4.3.1 Experiment with synthetic data

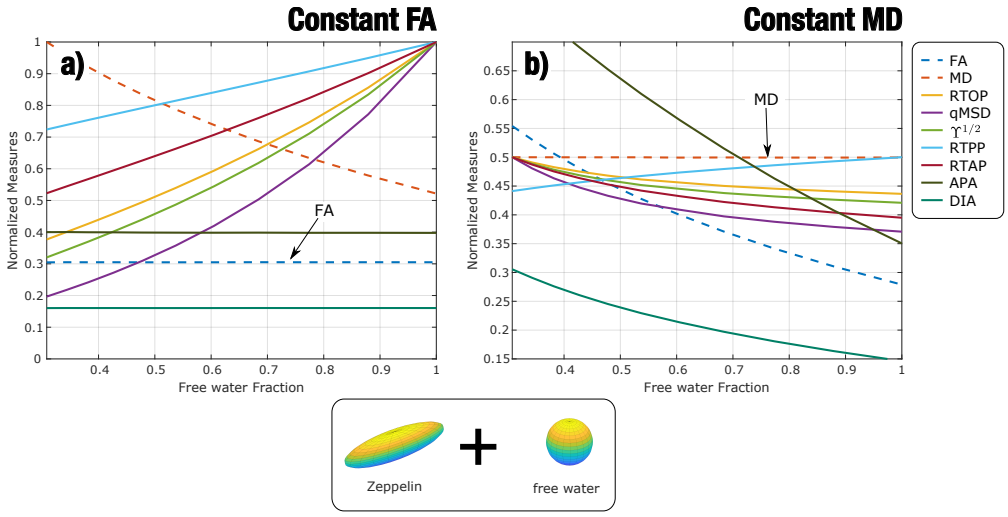

Fig. 4.2.: Experiment with synthetic data: a two-compartment model is considered, zeppelin + free water. The parameters of the zeppelin are modified so that the estimated diffusion tensor in every case shows: a) constant FA; b) constant MD. AMURA metrics have been calculated. Measures are normalized for better visualization.

Results for the experiment with synthetic data are gathered in Fig. 4.2: constant FA (Fig. 4.2-a) and constant MD (Fig. 4.2-b). All measures have been normalized for better visualization and comparison. When FA is set to constant, in this simple scenario, anisotropy-related metrics (PA and DiA) behave similarly. The other AMURA metrics detect the underlying change and grow with f, presenting qMSD, $\Upsilon^{1/2}$ and RTOP similar but higher slopes of opposite sense compared to MD, which decreases with f, begin the change of the RTAP almost identical to the one shown by the MD. On the other hand, when MD is set to constant, Fig. 4.2-b, all the AMURA measures are able to detect the changes in the signal, and the DiA presented a similar steep rate compared to the FA, and higher steep rate values were appreciated in the case of APA. This example illustrates that, although interpretation of some AMURA measures can be similar to DTI measures, they are not really quantifying the diffusion signal in the same way. The variety of AMURA measures allows not only to detect similar patterns compared to DTI, but also to find complementary results.

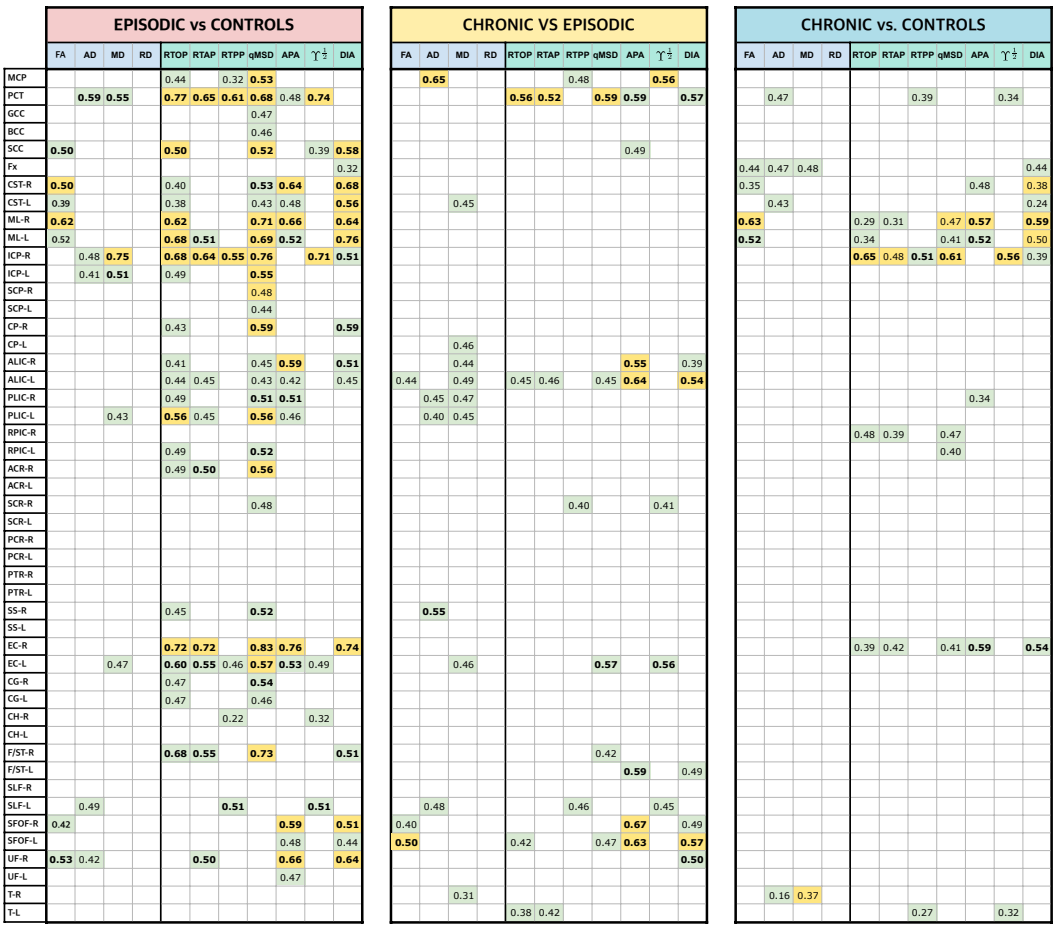

	EPISODIC vs CONTROLS										
	FA	AD	MD	RD	RTOP	RTAP	RTPP	qMSD	APA	$\Upsilon^{\frac{1}{2}}$	DIA
MCP					0.44		0.32	**0.53**			
PCT		**0.59**	**0.55**		**0.77**	**0.65**	**0.61**	**0.68**	0.48	**0.74**	
GCC								0.47			
BCC								0.46			
SCC	**0.50**				**0.50**			**0.52**		0.39	**0.58**
Fx											0.32
CST-R	**0.50**				0.40			**0.53**	**0.64**		**0.68**
CST-L	0.39				0.38			0.43	0.48		**0.56**
ML-R	**0.62**				**0.62**			**0.71**	**0.66**		**0.64**
ML-L	0.52				**0.68**	**0.51**		**0.69**	**0.52**		**0.76**
ICP-R		0.48	**0.75**		**0.68**	**0.64**	**0.55**	**0.76**		**0.71**	**0.51**
ICP-L		0.41	**0.51**		0.49			**0.55**			
SCP-R								0.48			
SCP-L								0.44			
CP-R					0.43			**0.59**			**0.59**
CP-L											
ALIC-R					0.41			0.45	**0.59**		**0.51**
ALIC-L					0.44	0.45		0.43	0.42		0.45
PLIC-R					0.49			**0.51**	**0.51**		
PLIC-L			0.43		**0.56**	0.45		**0.56**	0.46		
RPIC-R											
RPIC-L					0.49			**0.52**			
ACR-R					0.49	**0.50**		**0.56**			
ACR-L											
SCR-R								0.48			
SCR-L											
PCR-R											
PCR-L											
PTR-R											
PTR-L											
SS-R					0.45			**0.52**			
SS-L											
EC-R					**0.72**	**0.72**		**0.83**	**0.76**		**0.74**
EC-L			0.47		**0.60**	**0.55**	0.46	**0.57**	**0.53**	0.49	
CG-R					0.47			**0.54**			
CG-L					0.47			0.46			
CH-R							0.22			0.32	
CH-L											
F/ST-R					**0.68**	**0.55**		**0.73**			**0.51**
F/ST-L											
SLF-R											
SLF-L		0.49					**0.51**			**0.51**	
SFOF-R	0.42								**0.59**		**0.51**
SFOF-L									0.48		0.44
UF-R	**0.53**	0.42				**0.50**			**0.66**		**0.64**
UF-L									0.47		
T-R											
T-L											

	CHRONIC VS EPISODIC										
	FA	AD	MD	RD	RTOP	RTAP	RTPP	qMSD	APA	$\Upsilon^{\frac{1}{2}}$	DIA
MCP		**0.65**					0.48			**0.56**	
PCT					**0.56**	**0.52**		**0.59**	**0.59**		**0.57**
GCC											
BCC											
SCC									0.49		
Fx											
CST-R											
CST-L			0.45								
ML-R											
ML-L											
ICP-R											
ICP-L											
SCP-R											
SCP-L											
CP-R											
CP-L			0.46								
ALIC-R			0.44						**0.55**		0.39
ALIC-L	0.44		0.49		0.45	0.46		0.45	**0.64**		**0.54**
PLIC-R		0.45	0.47								
PLIC-L		0.40	0.45								
RPIC-R											
RPIC-L											
ACR-R											
ACR-L											
SCR-R							0.40			0.41	
SCR-L											
PCR-R											
PCR-L											
PTR-R											
PTR-L											
SS-R		**0.55**									
SS-L											
EC-R											
EC-L			0.46					**0.57**		**0.56**	
CG-R											
CG-L											
CH-R											
CH-L											
F/ST-R								0.42			
F/ST-L									**0.59**		0.49
SLF-R											
SLF-L		0.48					0.46		0.45		
SFOF-R	0.40								**0.67**		0.49
SFOF-L	**0.50**				0.42			0.47	**0.63**		**0.57**
UF-R											**0.50**
UF-L											
T-R			0.31								
T-L					0.38	0.42					

	CHRONIC vs. CONTROLS										
	FA	AD	MD	RD	RTOP	RTAP	RTPP	qMSD	APA	$\Upsilon^{\frac{1}{2}}$	DIA
MCP											
PCT		0.47					0.39			0.34	
GCC											
BCC											
SCC											
Fx	0.44	0.47	0.48								0.44
CST-R	0.35								0.48		0.38
CST-L		0.43									0.24
ML-R	**0.63**				0.29	0.31		0.47	**0.57**		**0.59**
ML-L	**0.52**				0.34			0.41	**0.52**		0.50
ICP-R					**0.65**	0.48	**0.51**	**0.61**		**0.56**	0.39
ICP-L											
SCP-R											
SCP-L											
CP-R											
CP-L											
ALIC-R											
ALIC-L											
PLIC-R									0.34		
PLIC-L											
RPIC-R					0.48	0.39		0.47			
RPIC-L								0.40			
ACR-R											
ACR-L											
SCR-R											
SCR-L											
PCR-R											
PCR-L											
PTR-R											
PTR-L											
SS-R											
SS-L											
EC-R					0.39	0.42		0.41	**0.59**		**0.54**
EC-L											
CG-R											
CG-L											
CH-R											
CH-L											
F/ST-R											
F/ST-L											
SLF-R											
SLF-L											
SFOF-R											
SFOF-L											
UF-R											
UF-L											
T-R		0.16	0.37								
T-L							0.27			0.32	

Tab. 4.2.: Results of the ROI-based statistical analysis and Cohen's D: EM vs HC, CM vs EM and CM vs. HC. Two-sample t-tests for DTI and AMURA measures and each of the ROIs defined by the JHU WM atlas. The p-values represent the probability that a certain measure has identical means for both groups. ROIs exhibiting differences with statistical significance above 95% ($p < 0.05$) are marked in green and above 99% ($p < 0.01$) in amber. The Cohen's D of those ROIs showing statistical differences is included.

4.3.2 ROI based statistical analysis

Eleven different measures were considered for the analysis: four DT-based measures (FA, AD, MD, RD) and seven AMURA-based (RTOP, RTAP, RTPP, qMSD, $\Upsilon^{1/2}$, APA and DiA). Table 4.2 shows a p-value scheme for the 48 ROIs considered for each of the measures. Those ROIs that exhibit differences with statistical significance above 95% ($p < 0.05$) are highlighted in green and above 99% ($p < 0.01$) in amber. The size of the effect (Cohen's D) is shown for those ROIs with significant differences (in bold face those values in which $D > 0.5$).

Note that those metrics based on the DT showed a limited amount of differences with only three ROIs with statistically significant differences above 99% for EM vs CM, two for CM vs EM and two for CM vs HC. In the EM vs HC comparisons, the highest differences between AMURA and DTI metrics, with a a greater number of statistically significant results for AMURA, were found: even in those cases in which the DT found differences, like the pontine

crossing tract (PCT), the equivalent AMURA metrics showed a smaller p-value and higher effect sizes. RTOP, qMSD and DiA were the metrics providing a higher number of statistically significant differences with the higher significance (see amber ROIs) and the greater effect size.

Regarding the other two sets of comparisons (CM-EM and CM-HC), AMURA metrics showed no clear higher number of differences compared to DTI metrics. In fact, AD and MD were able to detect more differences in the comparisons between CM and EM, coherently with previous studies [4.40]. This case suggests the complementary nature of DTI and AMURA. As shown in the preliminary example, both methods are quantifying different microstructure effects. Thus, AMURA seems more sensitive to changes between EM and controls, while DTI seems more sensitive to changes between the two types of migraine.

It is important to note that in all three comparisons, RD did not find any significant differences in any ROI, which is consistent with the findings reported in [4.40]. Therefore, to streamline the presentation of data in the figures and tables that follow, RD will be omitted in the following experiments.

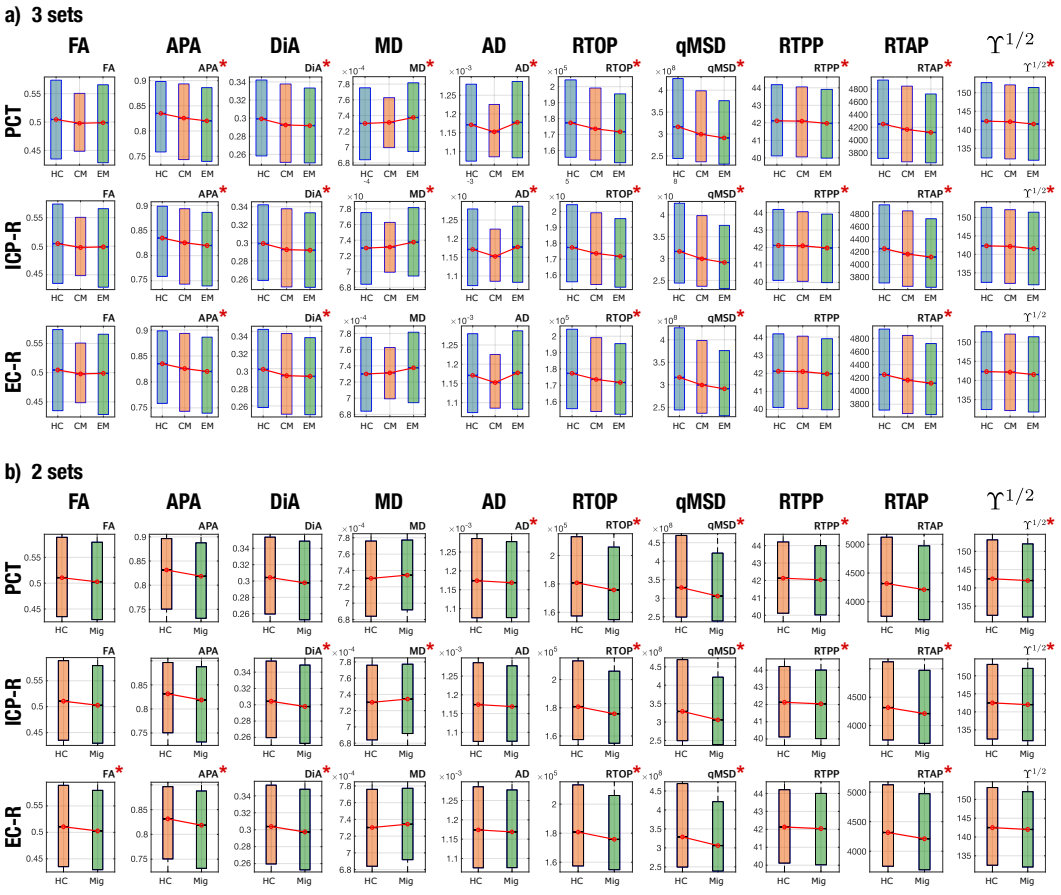

Fig. 4.3.: Boxplots of the distribution of different measures for EM, CM and HC for three specific regions: PCT, ICP-R and EC-R. The star marks those regions with statistically significant differences in the ROI analysis.

To better understand the behavior of both sets of measures, let us deeply analyze three specific regions. We selected the PCT, right inferior cerebellar peduncle (ICP-R) and the right external capsule (EC-R) for being the ones with the highest number of differences and the greatest effect sizes in Table 4.2. For each ROI, a box plot of the three groups is shown for each measure in Fig. 4.3-a. The boxes mark the median and 25 and 75 percentiles of the values of the different measures over the skeleton of the FA for all the subjects in each group. For better visualization, the median of each group is marked in red. The box plots are repeated in Fig. 4.3-b merging EM and CM in a single group that includes all migraine patients.

In the PCT, regarding DTI, the statistical analysis found differences between EM and HC for MD and AD, and between CM and HC for AD, but no differences were found between both migraine groups. In Fig. 4.3-a we can see that, actually, MD showed a higher median value of EM and CM when compared with HC. These differences were kept in Fig. 4.3-b when considering the joint migraine group. On the other hand, AMURA showed significan differences between EM-HC and CM-EM. Only RTPP (a metric related to AD) and $\Upsilon^{1/2}$ Regarding the other two sets of comparisons (CM-EM and CM-HC), AMURA metrics showed no clear higher number of differences compared to DTI metrics. In fact, AD and MD were able to detect more differences in the comparisons between CM and EM. This would mean that AMURA better discriminates EM in this ROI. According to Fig. 4.3-a, that is precisely what is happening. See, for instance, RTOP and qMSD. In both cases, there is almost no difference between HC and CM, while EM shows smaller median and a reduced variance. On the other hand, RTPP behaves more similarly to AD: both migraine groups were similar but differ from the control-group.

For the ICP-R, according to Table 4.2, MD and AD differences were found for the EM-HC case, AMURA found differences for EM-HC and CM-HC and no differences were found for CM-EM. If we check Fig. 4.3-a we can see that both migraine groups presented similar values in this ROI. Statistically significant differences were found between CM and HC, presenting the RTOP, qMSD and RTAP lower values in CM.

A similar effect can be observed in the EC-R, where no differences were found for DTI parameters, but for AMURA in the comparisons between HC and the two migraine groups. If we see Fig. 4.3-a, we can observe that AMURA metrics (RTOP and qMSD, for instance) discriminated CM and HC better than MD and AD. While in the MD and AD cases there is a reduction in the variance of the CM group, the change in the median is smaller, compared to CM and EM. If we pay attention to Fig. 4.3-b, we can see migraine and HC showed similar AD and MD values, while differences could be appreciated with RTOP, qMSD and RTAP.

4.3.3 Effect size

In Table 4.2 the values of the Cohen's D were shown for those ROIs with significant differences. Fig. 4.4 shows the absolute value of Cohen's D for eight selected ROIs (those with the largest number of differences) and for the three group comparisons.

The comparison between EM and HC, the AMURA metrics showed the largest effect sizes as measured by larger Cohen's D values. Specifically, qMSD, RTOP and DiA were consistently getting values over 0.5 (the threshold for medium effect) and, in some cases, near 0.8. In the right external capsule (EC-R), for instance, most AMURA metrics showed a moderate-large

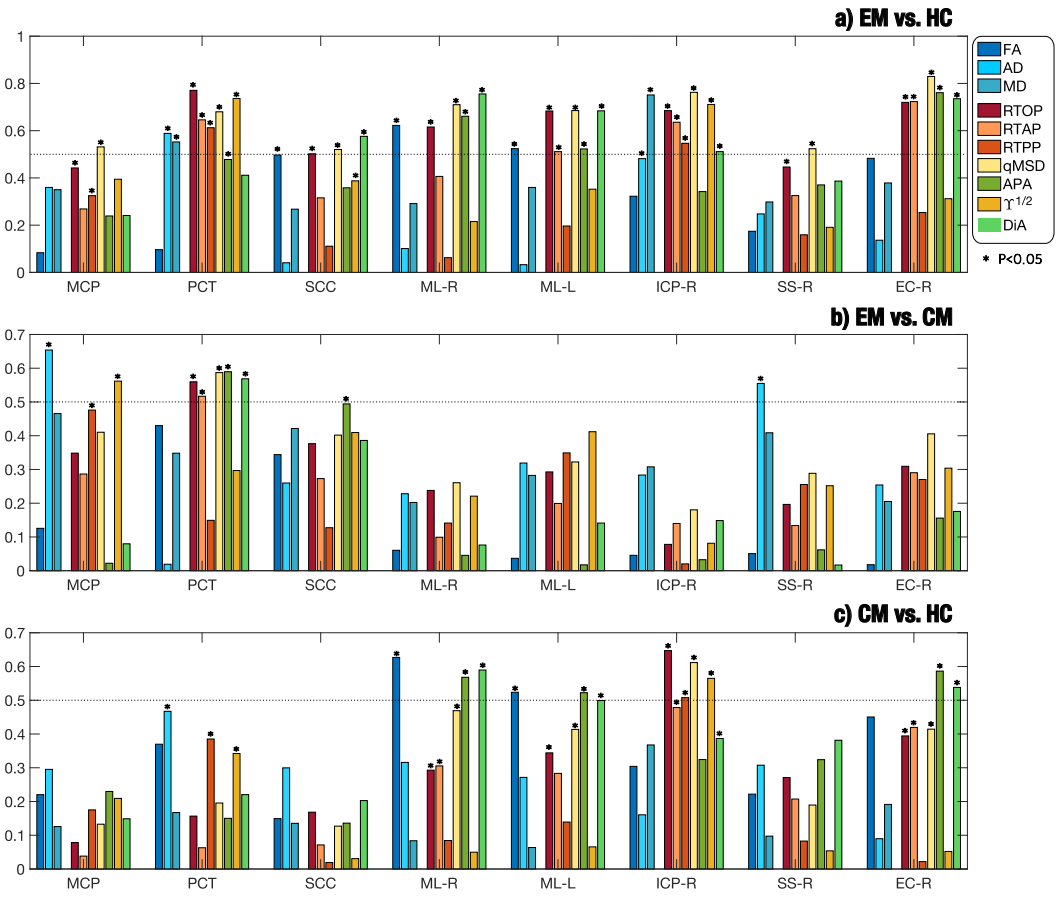

Fig. 4.4.: Absolute value of effect sizes (absolute Cohen's d) for associations between a) EM and HC; b) EM and CM; c) CM and HC. Different DTI and AMURA metrics are considered for eight selected ROIs (MCP, PCT, SCC, ML-R, ML-L, ICP-R, SS-R EC-R) according to the JHU WM Atlas.

effect size while DTI metrics did not get to 0.5. Even in those regions where DTI values showed statistical differences and a moderate effect (PCT, ML-R), AMURA outperformed them. There is only one case, the MD in the ICP-R, where a DTI metric showed a moderate effect size. However, if we check Table 4.2, we can see that the effect size for MD is 0.75, but this value was slightly lower than the value for the qMSD (0.75 vs. 0.76).

Regarding the comparison between CM and EM (Fig. 4.4-b), most measures showed low effect sizes, both for DTI and AMURA. The middle cerebral peduncle (MCP) for the AD and the right sagittal stratum (SSR) showed Cohen's D values over 0.5 for the AD, while AMURA only achieved medium effects in the pontine crossing tract (PCT).

Finally, in the comparison between CM and HC (Fig. 4.4-c), the right external capsule (EC-R), the right medial lemniscus (ML-R) and the left medial lemniscus (ML-L), the APA and the DiA reached absolute values of Cohen's D higher than 0.5, showing at the same time significant differences. FA also showed moderate effect in ML-R and ML-L, while RTOP, qMSD and $\Upsilon^{1/2}$ showed values over 0.5 in the right inferior cerebellar peduncle (ICP-R).

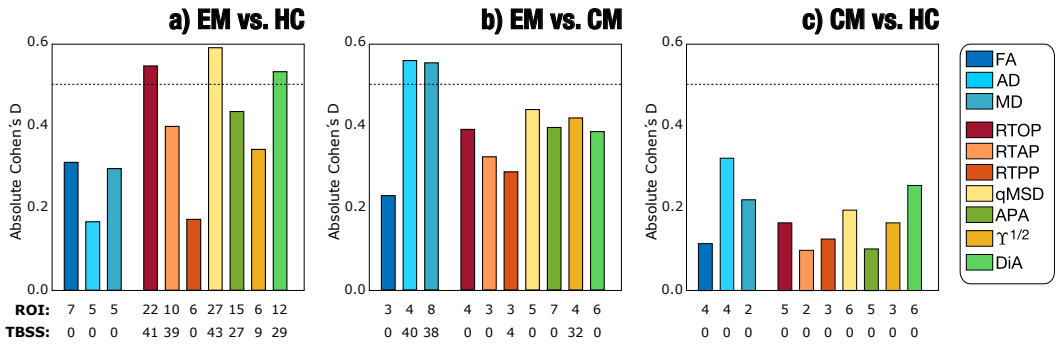

Fig. 4.5.: Absolute value of Cohen's D values for the three group comparisons in the Full WM: a) Episodic Migraine (EM) vs. Healthy Controls (HC); b) EM vs. Chronic Migraine (CM); c) CM vs. HC. DTI and AMURA measures are depicted. For each measure, the total number of ROIs that presented statistically significant differences obtained with the ROI and TBSS statistical approaches are also noted.

It is also interesting to analyze the behavior of each measure over the whole WM. Fig. 4.5 shows the absolute Cohen's D in the whole WM for each measure. The biggest effect sizes were obtained for the comparison between EM vs. HC for AMURA. Coherently, this comparison also produced the highest number of ROIs with significant differences. The qMSD or the RTOP measures reached absolute Cohen's D values close to 0.6, and respectively 27 and 22 ROIs with significant differences for the ROI analysis, 43 and 41 in TBSS. On the other hand, the comparison between CM and HC presented the lowest Cohen's D values, none of them reaching 0.5. Regarding the comparison between CM and EM, the AD, MD were the measures with greatest Cohen's D values, over 0.5.

4.3.4 Change of the sample size

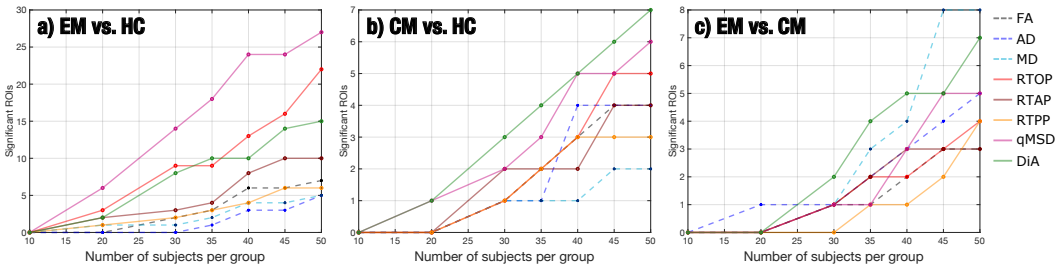

Fig. 4.6.: Number of ROIs with statistically significant differences by the resampling of diffusion measures reducing the number of subjects per group (sample size). A) Episodic Migraine (EM) vs. Healthy Controls (HC). B) Chronic Migraine (CM) vs. HC. C) CM vs. EM. No statistical correction was considered. For each case the median of 5001 permutations considered.

Fig. 4.6 shows the effects of changing the sample size for different DTI and AMURA-based measures for the three comparisons considered. We have selected 8 out of 11 metrics for better visualization of the graphics. Among the DTI measures, results with MD showed a relatively high number of ROIs with statistically significant differences using bigger samples

a) EM vs HC

ROI	N=50	N=25		
	FA	FA	APA	DiA
PCT				
SCC				
CST-R				
CST-L				
ML-R				
ML-L				
ICP-R				
ICP-L				
PLIC-L				
ACR-L				
SLF-L				
SFOF-R				
UF-R				

N=50		N=25					
MD	AD	MD	AD	RTOP	RTAP	qMSD	RTPP	$\Upsilon^{1/2}$

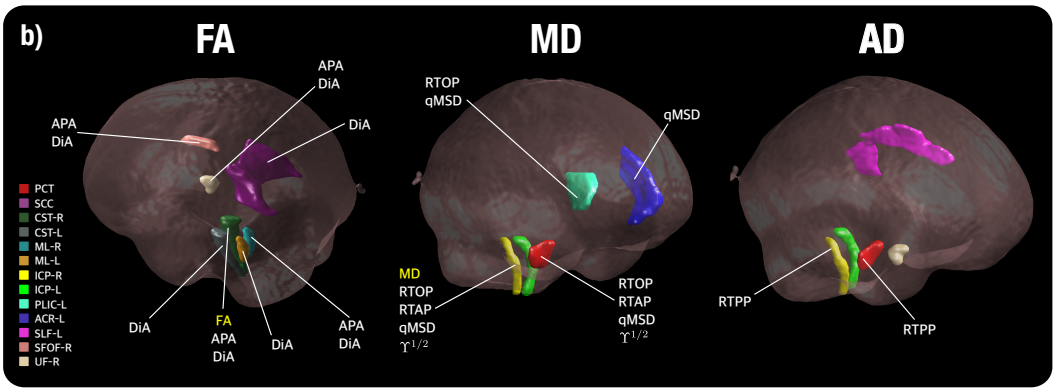

Fig. 4.7.: Significant ROIs found for a reduced sample size ($N = 25$). a) Table of ROIs found at $N = 25$ compared to the original sample size (EM vs HC). In amber, the ROIS with differences for DTI at the original sample size; in red, those ROIS with differences for DTI for a reduced sample size ($N = 25$); in green, those ROIS with differences for AMURA for a reduced sample size ($N = 25$). b) The 13 ROIs detected by DTI at the original sample size are shown in the white matter. For each ROI, we have added the label of those metrics that show significant differences for a sample size of $N = 25$.

sizes, especially for the EM-CM comparison, as can be seen in Figure Fig. 4.6-c. However, even in that case, the number of significant ROIs drastically decreased for a group sample size of 40. In addition, few ROIs with statistically significant differences were found for the rest of DTI measures and for the other two group comparisons, in any sample size, which made the assessment of the relationship between DTI measures and sample size unfeasible.

Results showed a stable behavior of AMURA measures in relation to the sample size, which can be understood as a linear dependence between the group sample size and the number of statistically significant ROIs. In Fig 4.6-a, this behavior can be better understood and interpreted in measures such as qMSD, which was the most robust one in the comparison between EM and HC. Furthermore, RTOP, qMSD and DiA also showed a robust behavior in the CM vs HC comparison. Notice that AMURA measures reached the lack of statistical significance ROIs for a group sample size of 10. However, when reducing the sample size to half ($N = 25$), most AMURA metrics still were able to find differences between groups, while only a few differences remained for the DTI case.

In order to better understand this effect, we now analyze the behavior of the measures in selected ROIS. We have chosen, according to results in Table 4.2, those 13 regions in which DTI measures showed differences with the original sample size for EM vs. HC, see Fig. 4.7-a.

For those 13 ROIs, in 7 of them FA showed significant differences for $N = 50$, 5 for MD and 5 for AD (see ROIs marked in amber). Then, we look at the results for those specific ROIs for a reduced sample size of $N = 25$. Note that, in that case, when the number of subjects is reduced to half, the FA was only able to detect one ROI (out of 7), MD only one (out of 5) and AD none (ROIs marked in red). When we look to the AMURA metrics, we see that they were able to still keep most of those differences even for a reduced sample size (see ROIs marked in green): DiA and APA, anisotropy measures similar to the FA, were able to respectively find 4 and 7 out of the original 7 FA ROIs. RTAP, and $\Upsilon^{1/2}$ succeed in finding 2 of the 5 MD ROIs, while RTOP finds 3 and qMSD 4 of them. In addition, with RTPP, 2 out of the 5 AD ROIs were identified for the reduced sample size. All in all, for this comparison, AMURA outperformed DTI in keeping the differences even for a smaller sample size.

As an illustration, in Fig, 4.7-b, the 13 considered ROIS are depicted. For each ROI, the metrics that showed significant differences for a sample size of $N = 25$ are displayed.

4.3.5 TBSS (original sample)

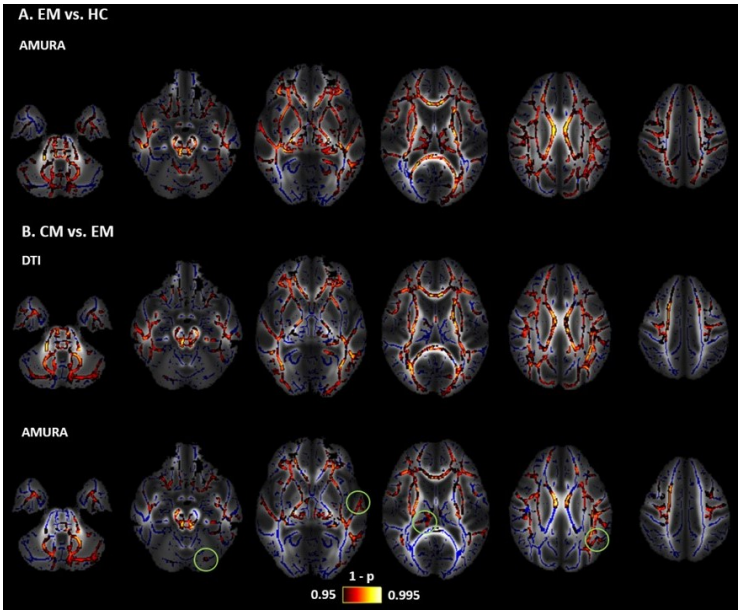

Fig. 4.8.: Results of TBSS analysis: statistically significant clusters of voxels distinguishing between DTI and AMURA approaches. Mean FA image at the background, FA skeleton coloured in blue and significant ROIs coloured in red-yellow. A) Episodic Migraine (EM) vs. Healthy Controls (HC): merged AMURA measures (RTOP, RTAP, APA, qMSD, $\Upsilon^{1/2}$ and DiA). B) CM vs. EM: merged DTI (AD and MD) and AMURA (RTPP, and $\Upsilon^{1/2}$) measures. DTI measures do not detect any significant ROI either in EM vs. HC nor CM vs. HC. Green circles showed the areas where AMURA measures showed differences in group comparisons where the DTI ones did not.

As we have previously staed, the ROI analysis carried out in the previous sections could be an illustrative example of the performance of the different metrics and it gives a valuable insight on the relation among them. However, since no statistical correction was considered,

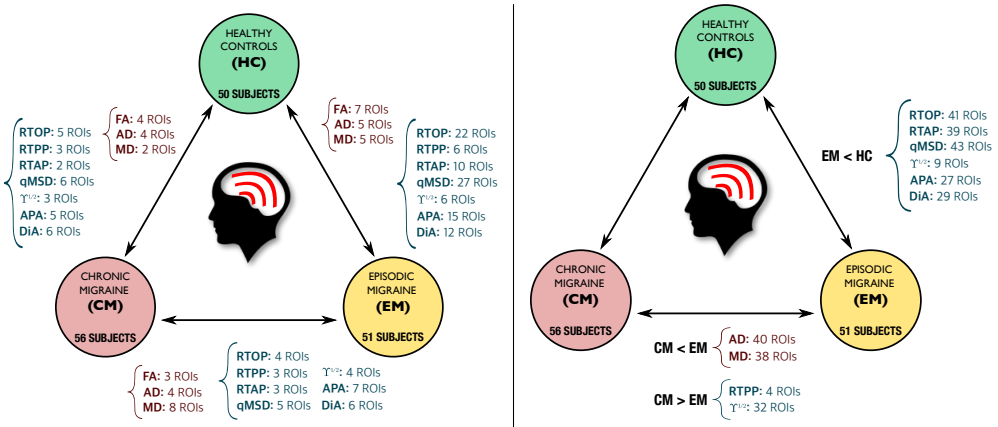

(a) ROI analysis (b) TBSS analysis

Fig. 4.9.: Summary of the statistically significan differences found with DTI (in red) and AMURA measures (in dark blue) for the comparison of the three groups. (a) ROI based analysis (no statistical correction). (b) TBSS analysis (with family-wise error correction).

the results could not be acceptable for clinical studies. Thus, in order to mimic an actual clinical study, we have now repeated the analysis using TBSS for the three comparisons.

Using the DTI measures (FA, MD, AD and RD), statistically significant differences between CM and EM patients were observed for two parameters. Patients with CM showed lower AD and MD values than EM in 40 and 38 out of 48 regions from the JHU-WM Atlas, respectively. No statistically significant differences were found using DTI measures between EM and HC or between CM and HC.

For the AMURA metrics, the comparison between patients with EM and HC showed the highest number of parameters with statistically significant differences. Significant lower RTOP, RTAP, qMSD, APA, DiA and $\Upsilon^{1/2}$ values in EM compared to HC were found in 41, 39, 43, 27, 29, and 9 ROIs out of 48, respectively. Concerning the comparison between both groups of patients, higher values in CM compared to EM were identified for the RTPP and $\Upsilon^{1/2}$ in 4 and 32 regions, respectively.

Fig. 4.8 shows the TBSS results including all the ROIs that presented statistically significant differences together with the FA skeleton. On the one hand, for EM vs. HC and CM vs. HC comparisons, all the AMURA measures which showed significant differences are merged and depicted in the figure, that is, RTOP, RTAP, APA, qMSD, $\Upsilon^{1/2}$ and only DiA for EM vs. HC. On the other hand, DTI and AMURA measures can be distinguished in the last CM vs. EM comparison. For DTI, the merged measures depicted are AD and MD, while for AMURA are RTPP and $\Upsilon^{1/2}$. As it can be seen, AMURA measures showed differences in group comparisons where the DTI ones did not, as shown in the green circles. A summary with the previous TBSS results regarding the number of ROIs and the group comparisons can be found in Fig. 4.9.

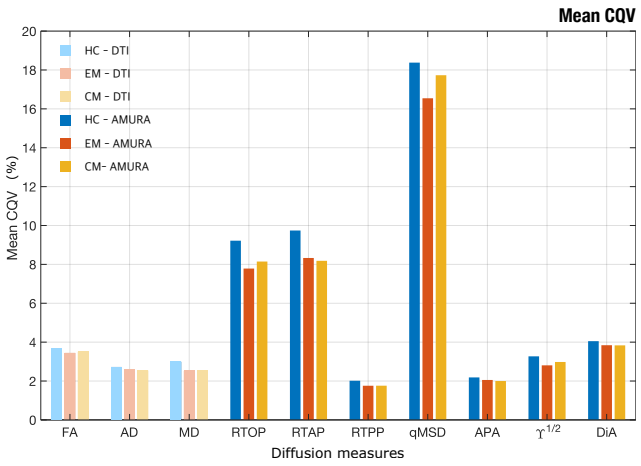

Fig. 4.10.: Mean CQV for each group of study considering the 48 ROIs of JHU-WM atlas. Healthy Controls (HC), Episodic Migraine (EM) and Chronic Migraine (CM). DTI and AMURA measures are shown. The measures with the higher stability have lower CQV.

4.3.6 Analysis of stability

Fig. 4.10 depicts the average values of CQV for all the DTI and AMURA-based diffusion measures. The measures with the highest stability (lowest CQV) were the RTPP and the APA, with an approximate average CQV of 2% considering all the regions. Other measures with relatively high stability were the three DTI measures (FA, MD and AD), $\Upsilon^{1/2}$ and DIA, with CQV average values between 2% and 5%. The remaining DTI and AMURA descriptors (RD, RTAP and RTOP), presented a moderate-high stability, with CQV average values between 5% and 10%. The descriptor with the lowest stability was the qMSD, with CQV average values between 15% and 20%.

Regarding the comparisons between the three groups of interest, after reducing the group sample size to 45 subjects, the assessment of the CQV 95% CI showed that the HC presented a general higher variability than patients with EM and CM. The parameters with a higher number of regions with statistically significant differences between HC and migraine patients according to the 95% CI were the three AMURA measures (RTOP, RTPP and RTAP) and the MD, with 14-22 regions presenting differences. Additionally, in the comparison between HC and CM, the CQV of APA or $\Upsilon^{1/2}$ were significantly higher in HC than CM in 13 regions. The number of regions with CQV differences between CM and EM was lower compared to the comparison between HC and the patient groups. FA and MD were the descriptors with a higher number of regions (nine) that showed higher variance in EM compared to CM, and MD was also the parameter with more regions (eight) with significantly higher variance in CM.

4.4 Discussion and conclusions

In this study, we assessed the viability of advanced diffusion descriptors obtained with a novel approach, AMURA, in comparison with traditional DTI parameters. To this end,

their capability to discriminate difference between clinical groups of interest was compared, together with the stability of these results for reduced sample sizes. Using synthetic and real data with a single-shell and low b-value, we observed that AMURA is sensitive to changes of parameters associated with the dMRI signal, showing a higher capability of discrimination between clinical groups, even for decreased sample sizes. Specifically, with AMURA we detected a larger number of ROIs with statistically significant differences between groups, or results complementary to those identified with DTI, presenting higher effect size but lower stability than DTI metrics.

Advanced diffusion descriptors such as RTOP, RTAP and APA have shown to be useful for the analysis of the WM of the brain [4.1, 4.41, 4.40]. However, their conventional calculation requires acquisition protocols including several b-values, a high number of diffusion gradient directions and very long processing times. This makes them unfeasible for their use in clinical practice or in many commercial MRI scanners. Besides, the use of these metrics in retrospective studies is usually impossible since the acquisition protocols do not allow for it.

AMURA was proposed to allow the estimation of apparent versions of these advanced diffusion measures from reduced acquisitions [4.1, 4.2, 4.3]. It provides a fast and straightforward method to compute them from a single shell and very short processing times. Metrics calculated with AMURA have shown a high correlation with measures calculated using a multishell approach, such as MAP-MRI[4.37], MAPL[4.19] or MiSFIT[4.47], for high b-values (at least 2000 s/mm^2). For lower values, these measures show a weaker correlation since the underlying features measured are better visible at higher b-values [4.1, 4.2]. However, we hypothesized that AMURA metrics can still provide useful information at lower b-values, complementary to that obtained from DTI-based measures. This paper focuses precisely on that hypothesis and tries to elucidate whether AMURA-based measures obtained from standard DTI-type acquisitions are useful in group studies.

To that end, we have resorted to migraine as our target pathology, because of several reasons. First, diffusion MRI studies in the literature show that differences between patients and HC, or between different groups of patients (EM vs. CM) are subtle, as studies using small sample sizes have often reported no differences and even contradictory findings have been published [4.39, 4.16, 4.22, 4.15, 4.30, 4.32, 4.43].

To study the viability of AMURA-based measures, two different statistical analysis were carried out, including a ROI-based analysis and conventional TBSS, together with the assessment of the behavior of the diverse measures from reduces sample sizes and of the stability. We show that AMURA measures obtained from DTI-type acquisitions were able to successfully find statistically significant differences between the three groups under study (HC, EM and CM), including differences that were not detected using DTI-based measures. Although AMURA showed additional differences between groups in a preliminary previous study [4.41], the magnitude of the additional differences, particularly those between EM and HC, was unexpected.

With a single-shell and low b-value acquisition, AMURA shows itself as a method complementary to DTI, as reflected by the results from the TBSS analysis (Figure 4.9-(b)). On the one hand, DTI-based AD and MD showed a good performance for the comparison between EM and CM, with a great number of ROIs with statistically significant differences, while AMURA-based measures detected equivalent but a lower number of differences. On the

other hand, in the comparison between EM and HC, differences were only found using AMURA-based measures, and in a relatively large number of ROIs. The reason of these differences may be that both techniques represent changes associated with diverse pathophysiological mechanisms, as shown in the example with synthetic data, where only AMURA was able to identify changes of the free water fraction. Further studies on disorders with better characterized pathophysiology than migraine must be carried out to understand the different sensitivity to varied biological processes of DTI and AMURA.

Regarding the behavior of the DTI and AMURA measures in the synthetic experiment for diverse free water fractions, some AMURA parameters showed higher sensitivity to the free water changes. For constant FA, qMSD, $\Upsilon^{1/2}$ and RTOP presented higher changes for small changes of the free water fraction than the MD, while DiA and APA remained constant. For constant MD, DiA and FA showed similar changes and the APA showed higher changes than the FA, without constant values of any AMURA parameter. These results suggest that AMURA can better determine differences caused by changes of free water fraction in comparison with DTI, as some parameters presented higher sensitivity. Therefore, the consequence would be that AMURA measures may be able to find subtler differences between clinical groups compared to DTI, in line with previously reported results in migraine [4.41].

The complementary nature of DTI- and AMURA-based measures is confirmed by the ROI-based analysis (Table 4.2 and Figure 4.9-a). In the comparison between CM and EM, for instance, the MD was the metric that detected a higher number of regions with statistically significant differences, but there were some ROIs with differences exclusively identified by one or more AMURA-based measures (e.g., the PCT). In the same way, there were ROIs with differences exclusively found with the MD or AD (e.g., the SS-R), and ROIs with differences identified by both DTI- and AMURA-based measures (e.g., the EC-L).

If we focus on those regions selected in Figure 4.3 (PCT, ICP-R and EC-R) we can better understand what is happening with the behavior of the distribution of the different metrics inside the selected ROIs. First, let us focus on the anisotropy measures, FA, APA and DiA. According to Table 4.2 there are no differences between groups for the FA for any of the three ROIs. On the other hand, APA and DiA reflected differences for EM vs HC (for the three ROIs), for EM vs. CM (in the PCT) and CM vs HC (both in EC-R). These results are confirmed by the boxplots in Figure 4.3, where AMURA-anisotropy measures were able to better separate the three groups. It is of interest to note that when migraine is considered as a single set, results are more similar for the three metrics, confirming that anisotropy differences between controls are migraine were really present. Regarding the other metrics, AD and MD were able to find significant differences in most cases for the three ROIs, according to Table 4.2. However, AMURA metrics always find the same differences but with a greater size effect. As an example of this, we can focus on the PCT for EM vs HC, where we can see that all the metrics succeed in finding differences but with different effect sizes.

All in all, from the results in Table 4.2 and Figure 4.3, we can see that the behavior of AMURA and DTI is similar, although MD and AD showed a lower variance for the CM group. The separation between the groups follows very similar trends within the three ROIs considered. However, AMURA manages to better find these existing differences, and with a larger effect size.

The sensitivity of AMURA-based measures was analyzed by further comparing the effect size found in the different comparisons between groups. A classical method to determine the magnitude of the differences between groups is Cohen's D, which considers the variability of the sample in relation to the average value. As illustrated in Figures 4.4 and 4.5, DTI-based and AMURA-based measures showed comparable effect sizes for the EM-CM and CM-HC comparisons. In the first case, DTI-based AD and MD reached medium effect sizes (0.5) (for the whole WM), while Cohen's D for FA barely exceeded small effect size threshold (0.2). For this last comparison, Cohen's D for AMURA-based measures varied between the small and the medium effect thresholds. For the comparison between CM and EM, however, Cohen's D values were notably lower for all measures, barely reaching 0.3 for DTI-based AD. Finally, regarding the comparison between EM and HC, while DTI-based FA and MD reached Cohen's D values around 0.3, AMURA-based RTOP, qMSD and DIA reached values over 0.5. These differences in effect sizes among different measures and different group comparisons offer a good explanation for the results shown in Table 4.2 and Figure 4.9.

Whereas it may be tempting to think about EM and CM as different degrees of the same pathological process, recent results [4.39, 4.16] support the hypothesis of EM and CM being different entities at the microstructural level, each accompanied by different changes in the WM. Following this hypothesis, DTI-based measures seem well-fitted to detect WM changes in CM, while AMURA-based methods perform remarkably well for the changes that occur in EM. Although the interpretation of changes in DTI or AMURA-based measures is not straightforward, results suggest that WM changes in EM with respect to HC (specifically, lower RTOP and RTAP) might be related to changes in the transverse diffusivity, while changes in CM with respect to EM (such as higher RTPP and lower AD) might be more related to changes in the diffusivity in the axonal or main direction. As previously stated, the complementary use of DTI and AMURA may be useful to detect changes of different nature using data obtained with a low b-value and single-shell acquisition. The specific pathophysiological mechanisms related to changes of diverse essence in AMURA must be assessed in future studies.

Considering the difficulty to obtain large sample sizes in group studies, it is important to assess the behavior of the diverse diffusion measures when the number of subjects per group is reduced. As depicted in Fig. 4.6, both DTI-based and AMURA-based measures shared the expected trend, meaning that the number of ROIs with statistically significant differences decreases as the sample size is reduced. However, as shown in the experiment in Fig. 4.7, when the number of samples is reduced to half, DTI metrics were no longer able to detect the differences between groups in most ROIs, whereas AMURA could. From the 13 ROIs considered in the experiment, DTI lost 11 of them when reducing the sample size, while AMURA only lost 2 of them. This effect favors the usage of AMURA metrics in studies with a small sample size.

The assessment of the stability provides another interesting perspective for the evaluation and comparison between different diffusion measures. The diffusion measures that showed higher stability (lower CQV) were AMURA-based APA and RTPP, and the DTI-based measures, while AMURA-based qMSD seems to present low stability. This high variability was expected, since qMSD is a quadratic measure, so it must show a greater range of variability. Interestingly, it presented a relatively high number of regions with statistically significant differences in the comparisons of both migraine groups against controls for diverse sample sizes despite their low stability. Therefore, the results of this study suggest that qMSD is able

to characterize specific microstructural properties that are particularly difficult to find with other parameters. Moreover, as it has been suggested previously in this section, differences between both groups of patients with migraine and controls may be qualitatively distinct compared to the differences between CM and EM. Furthermore, qMSD is especially sensitive to short diffusion time scales [4.34].

It is important to note that the AMURA-based measures employed in this paper must be considered as apparent values at a given b-value, and their interpretation in terms of the microstructure properties may be different from that of the original EAP-based diffusion measures. Although the relationship between AMURA-based measures and their original counterparts deserves further study, in this paper we deliberately chose not to pursue this comparison to focus on the viability of AMURA-based measures to complement DTI in scenarios where EAP-based measures cannot be obtained.

This study presents limitations that must be pointed out. First, the pathophysiological interpretation of the different trends of the AMURA-based measures is not totally clear, so a description of the microstructural properties according to the values of each measure cannot be provided. As mentioned previously, the apparent nature of AMURA-based measures and their complex relationship with the original EAP-based measures prevent the direct adoption of interpretations from those EAP-based measures. Microstructural studies like those conducted for DTI-based measures [4.4, 4.52] are needed to fully understand the results obtained with AMURA.

Furthermore, the results obtained in this study cannot be directly translated to other pathologies affecting the WM of the brain. Even though AMURA can be expected to be a useful information to detect differences in group studies targeting other diseases, further research is needed to confirm that.

In conclusion, this study showed that the new AMURA-based measures can be easily integrated in group studies using single-shell dMRI acquisition protocols, and they can reveal WM changes that may remain hidden with traditional DT-based measures. The wide variety of AMURA, a fast and relatively simple approach, provides measures that allow to extract values that are able to find differences between groups for restricted sample sizes and dMRI acquisition protocols.

Conflict of Interest Statement

The authors declare that the research was conducted in the absence of any commercial or financial relationships that could be construed as a potential conflict of interest.

Author Contributions

Carmen Martín-Carmen Martín: Validation, Formal analysis, Investigation, Writing - original draft, Writing - review & editing. **Álvaro Planchuelo-Gómez:** Methodology, Validation, Formal analysis, Investigation, Data curation, Writing - original draft, Writing - review & editing. **Ángel L. Guerrero:** Methodology, Validation. **David García-Azorín:** Methodology, Validation. **Antonio Tristán-Vega:** Methodology, Validation, Formal analysis, Supervision,

Project administration, Funding acquisition. **Rodrigo de Luis-García:** Methodology, Validation, Formal analysis, Investigation, Writing - original draft, Supervision, Project administration, Funding acquisition. **Santiago Aja-Fernández:** Conceptualization, Methodology, Software, Validation, Formal analysis, Investigation, Writing - original draft, Writing - review & editing, Supervision, Project administration, Funding acquisition.

Funding

This work was supported by Ministerio de Ciencia e Innovación PID2021-124407NB-I00 and TED2021-130758B-I00, funded by MCIN/AEI/10.13039/501100011033 and the European Union “NextGenerationEU/PRTR", being MCIN: Ministerio de Ciencia e Innovación; AEI: Agencia Estatal de Investigación (with DOI 10.13039/501100011033); and PRTR: “Plan de Recuperación, Transformación y Resiliencia".

Data Availability Statement

The datasets used for this study belong to Hospital Clínico Universitario (Valladolid) and cannot be made public. Researchers may request access to them by contacting the corresponding author.

Bibliography

[4.1] Aja-Fernández, S., de Luis-García, R., Afzali, M., Molendowska, M., Pieciak, T., and Tristán-Vega, A. (2020). Micro-structure diffusion scalar measures from reduced MRI acquisitions. *PLoS One* 15, e0229526

[4.2] Aja-Fernández, S., Pieciak, T., Martín-Martín, C., Planchuelo-Gómez, Á., de Luis-García, R., and Tristán-Vega, A. (2022). Moment-based representation of the diffusion inside the brain from reduced DMRI acquisitions: Generalized AMURA. *Medical Image Analysis* 77, 102356

[4.3] Aja-Fernández, S., Tristán-Vega, A., and Jones, D. K. (2021). Apparent propagator anisotropy from single-shell diffusion MRI acquisitions. *Magnetic resonance in medicine* 85, 2869–2881

[4.4] Alexander, A. L., Lee, J. E., Lazar, M., and Field, A. S. (2007). Diffusion tensor imaging of the brain. *Neurotherapeutics* 4, 316–329

[4.5] Alexander, D. C. (2008). A general framework for experiment design in diffusion MRI and its application in measuring direct tissue-microstructure features. *Magnetic Resonance in Medicine: An Official Journal of the International Society for Magnetic Resonance in Medicine* 60, 439–448

[4.6] Altunkaynak, B. and Gamgam, H. (2019). Bootstrap confidence intervals for the coefficient of quartile variation. *Communications in Statistics-Simulation and Computation* 48, 2138–2146

[4.7] Andersson, J. L. and Sotiropoulos, S. N. (2016). An integrated approach to correction for off-resonance effects and subject movement in diffusion MR imaging. *Neuroimage* 125, 1063–1078

[4.8] Assemlal, H.-E., Tschumperlé, D., Brun, L., and Siddiqi, K. (2011). Recent advances in diffusion MRI modeling: Angular and radial reconstruction. *Medical image analysis* 15, 369–396

[4.9] Avram, A. V., Sarlls, J. E., Barnett, A. S., Özarslan, E., Thomas, C., Irfanoglu, M. O., et al. (2016). Clinical feasibility of using mean apparent propagator (MAP) MRI to characterize brain tissue microstructure. *NeuroImage* 127, 422–434

[4.10] Basser, P. J. and Jones, D. K. (2002). Diffusion-tensor MRI: theory, experimental design and data analysis–a technical review. *NMR in Biomedicine: An International Journal Devoted to the Development and Application of Magnetic Resonance In Vivo* 15, 456–467

[4.11] Basser, P. J., Mattiello, J., and LeBihan, D. (1994). MR diffusion tensor spectroscopy and imaging. *Biophysical journal* 66, 259–267

[4.12] Bette, S., Huber, T., Wiestler, B., Boeckh-Behrens, T., Gempt, J., Ringel, F., et al. (2016). Analysis of fractional anisotropy facilitates differentiation of glioblastoma and brain metastases in a clinical setting. *European journal of radiology* 85, 2182–2187

[4.13] Boscolo Galazzo, I., Brusini, L., Obertino, S., Zucchelli, M., Granziera, C., and Menegaz, G. (2018). On the viability of diffusion MRI-based microstructural biomarkers in ischemic stroke. *Frontiers in neuroscience* 12, 92

[4.14] Brusini, L., Obertino, S., Galazzo, I. B., Zucchelli, M., Krueger, G., Granziera, C., et al. (2016). Ensemble average propagator-based detection of microstructural alterations after stroke. *International journal of computer assisted radiology and surgery* 11, 1585–1597

[4.15] Chong, C. D. and Schwedt, T. J. (2015). Migraine affects white-matter tract integrity: a diffusion-tensor imaging study. *Cephalalgia* 35, 1162–1171

[4.16] Coppola, G., Di Renzo, A., Tinelli, E., Petolicchio, B., Di Lorenzo, C., Parisi, V., et al. (2020). Patients with chronic migraine without history of medication overuse are characterized by a peculiar white matter fiber bundle profile. *The journal of headache and pain* 21, 1–8

[4.17] Descoteaux, M., Deriche, R., Le Bihan, D., Mangin, J.-F., and Poupon, C. (2011). Multiple q-shell diffusion propagator imaging. *Medical image analysis* 15, 603–621

[4.18] Dhollander, T., Raffelt, D., and Connelly, A. (2016). Unsupervised 3-tissue response function estimation from single-shell or multi-shell diffusion MR data without a co-registered T1 image. In *ISMRM Workshop on Breaking the Barriers of Diffusion MRI* (ISMRM Lisbon, Italy), vol. 5

[4.19] Fick, R. H., Wassermann, D., Caruyer, E., and Deriche, R. (2016). MAPL: Tissue microstructure estimation using Laplacian-regularized MAP-MRI and its application to HCP data. *NeuroImage* 134, 365–385

[4.20] Fick, R. H. J., Pizzolato, M., Wassermann, D., Zucchelli, M., Menegaz, G., and Deriche, R. (2016). A sensitivity analysis of q-space indices with respect to changes in axonal diameter, dispersion and tissue composition. In *2016 IEEE 13th International Symposium on Biomedical Imaging (ISBI)*. 1241–1244. doi:10.1109/ISBI.2016.7493491

[4.21] Galbán, C., Hoff, B., Chenevert, T., and Ross, B. (2017). Diffusion MRI in early cancer therapeutic response assessment. *NMR in biomedicine* 30, e3458

[4.22] Gomez-Beldarrain, M., Oroz, I., Zapirain, B. G., Ruanova, B. F., Fernandez, Y. G., Cabrera, A., et al. (2016). Right fronto-insular white matter tracts link cognitive reserve and pain in migraine patients. *The journal of headache and pain* 17, 1–12

[4.23] Goveas, J., O'Dwyer, L., Mascalchi, M., Cosottini, M., Diciotti, S., De Santis, S., et al. (2015). Diffusion-MRI in neurodegenerative disorders. *Magnetic resonance imaging* 33, 853–876

[4.24] Herbert, E., Engel-Hills, P., Hattingh, C., Fouche, J.-P., Kidd, M., Lochner, C., et al. (2018). Fractional anisotropy of white matter, disability and blood iron parameters in multiple sclerosis. *Metabolic brain disease* 33, 545–557

[4.25] Hosseinbor, A. P., Chung, M. K., Wu, Y.-C., and Alexander, A. L. (2013). Bessel fourier orientation reconstruction (bfor): An analytical diffusion propagator reconstruction for hybrid diffusion imaging and computation of q-space indices. *NeuroImage* 64, 650–670

[4.26] Ito, K., Kudo, M., and Sasaki, M. (2016). Detection of changes in the periaqueductal gray matter of patients with episodic migraine using quantitative diffusion kurtosis imaging: preliminary findings. *Neuroradiology* 58, 115–120. doi:10.1007/s00234-015-1603-8

[4.27] Jenkinson, M., Beckmann, C. F., Behrens, T. E., Woolrich, M. W., and Smith, S. M. (2012). FSL. *Neuroimage* 62(2), 782–790

[4.28] Kochunov, P., Williamson, D., Lancaster, J., Fox, P., Cornell, J., Blangero, J., et al. (2012). Fractional anisotropy of water diffusion in cerebral white matter across the lifespan. *Neurobiology of aging* 33, 9–20

[4.29] Mekkaoui, C., Reese, T. G., Jackowski, M. P., Bhat, H., and Sosnovik, D. E. (2017). Diffusion MRI in the heart. *NMR in Biomedicine* 30, e3426

[4.30] Messina, R., Rocca, M. A., Colombo, B., Pagani, E., Falini, A., Comi, G., et al. (2015). White matter microstructure abnormalities in pediatric migraine patients. *Cephalalgia* 35, 1278–1286

[4.31] Mole, J. P., Subramanian, L., Bracht, T., Morris, H., Metzler-Baddeley, C., and Linden, D. E. (2016). Increased fractional anisotropy in the motor tracts of Parkinson's disease suggests compensatory neuroplasticity or selective neurodegeneration. *European radiology* 26, 3327–3335

[4.32] Neeb, L., Bastian, K., Villringer, K., Gits, H. C., Israel, H., Reuter, U., et al. (2015). No microstructural white matter alterations in chronic and episodic migraineurs: a case–control diffusion tensor magnetic resonance imaging study. *Headache: The Journal of Head and Face Pain* 55, 241–251

[4.33] Nichols, T. and Holmes, A. P. (2002). Nonparametric permutation tests for functional neuroimaging: a primer with examples. *Human Brain Mapp* 15, 1–25

[4.34] Ning, L., Westin, C.-F., and Rathi, Y. (2015). Estimating diffusion propagator and its moments using directional radial basis functions. *IEEE transactions on medical imaging* 34, 2058–2078

[4.35] Novikov, D. S., Fieremans, E., Jespersen, S. N., and Kiselev, V. G. (2019). Quantifying brain microstructure with diffusion MRI: Theory and parameter estimation. *NMR in Biomedicine* 32, e3998

[4.36] Oishi, K., Zilles, K., Amunts, K., Faria, A., Jiang, H., Li, X., et al. (2008). Human brain white matter atlas: identification and assignment of common anatomical structures in superficial white matter. *Neuroimage* 43, 447–457

[4.37] Özarslan, E., Koay, C. G., Shepherd, T. M., Komlosh, M. E., İrfanoğlu, M. O., Pierpaoli, C., et al. (2013). Mean apparent propagator (MAP) MRI: a novel diffusion imaging method for mapping tissue microstructure. *NeuroImage* 78, 16–32

[4.38] Pelletier, A., Periot, O., Dilharreguy, B., Hiba, B., Bordessoules, M., Chanraud, S., et al. (2016). Age-related modifications of diffusion tensor imaging parameters and white matter hyperintensities as inter-dependent processes. *Frontiers in aging neuroscience* 7, 255

[4.39] Planchuelo-Gómez, Á., García-Azorín, D., Guerrero, Á. L., Aja-Fernández, S., Rodríguez, M., and de Luis-García, R. (2020). Structural connectivity alterations in chronic and episodic migraine: A diffusion magnetic resonance imaging connectomics study. *Cephalalgia* 40, 367–383

[4.40] Planchuelo-Gómez, Á., García-Azorín, D., Guerrero, Á. L., Aja-Fernández, S., Rodríguez, M., and de Luis-García, R. (2020). White matter changes in chronic and episodic migraine: a diffusion tensor imaging study. *The journal of headache and pain* 21, 1–15

[4.41] Planchuelo-Gómez, Á., García-Azorín, D., Guerrero, Á. L., de Luis-García, R., Rodríguez, M., and Aja-Fernández, S. (2020). Alternative microstructural measures to complement diffusion tensor imaging in migraine studies with standard MRI acquisition. *Brain Sciences* 10, 711

[4.42] Rovaris, M., Gass, A., Bammer, R., Hickman, S. J., Ciccarelli, O., Miller, D. H., et al. (2005). Diffusion MRI in multiple sclerosis. *Neurology* 65, 1526–1532. doi:10.1212/01.wnl.0000184471.83948.e0

[4.43] Shibata, Y., Ishiyama, S., and Matsushita, A. (2018). White matter diffusion abnormalities in migraine and medication overuse headache: A 1.5-t tract-based spatial statistics study. *Clinical Neurology and Neurosurgery* 174, 167–173

[4.44] Smith, S. M., Jenkinson, M., Woolrich, M. W., Beckmann, C. F., Behrens, T. E., Johansen-Berg, H., et al. (2004). Advances in functional and structural MR image analysis and implementation as FSL. *Neuroimage* 23, S208–S219

[4.45] Smith, S. M. and Nichols, T. E. (2009). Threshold-free cluster enhancement: addressing problems of smoothing, threshold dependence and localisation in cluster inference. *Neuroimage* 44, 83–98

[4.46] Tournier, J.-D., Smith, R., Raffelt, D., Tabbara, R., Dhollander, T., Pietsch, M., et al. (2019). MRtrix3: A fast, flexible and open software framework for medical image processing and visualisation. *Neuroimage* 202, 116137

[4.47] Tristán-Vega, A. and Aja-Fernández, S. (2021). Efficient and accurate EAP imaging from multi-shell dMRI with micro-structure adaptive convolution kernels and dual fourier integral transforms (MiSFIT). *NeuroImage* 227, 117616

[4.48] Tristán-Vega, A., París, G., de Luis-García, R., and Aja-Fernández, S. (2022). Accurate free-water estimation in white matter from fast diffusion MRI acquisitions using the spherical means technique. *Magnetic Resonance in Medicine* 87, 1028–1035

[4.49] Veraart, J., Novikov, D. S., Christiaens, D., Ades-Aron, B., Sijbers, J., and Fieremans, E. (2016). Denoising of diffusion MRI using random matrix theory. *Neuroimage* 142, 394–406

[4.50] Wedeen, V. J., Hagmann, P., Tseng, W.-Y. I., Reese, T. G., and Weisskoff, R. M. (2005). Mapping complex tissue architecture with diffusion spectrum magnetic resonance imaging. *Magnetic resonance in medicine* 54, 1377–1386

[4.51] Westin, C.-F., Maier, S. E., Mamata, H., Nabavi, A., Jolesz, F. A., and Kikinis, R. (2002). Processing and visualization for diffusion tensor MRI. *Medical image analysis* 6, 93–108

[4.52] Winklewski, P. J., Sabisz, A., Naumczyk, P., Jodzio, K., Szurowska, E., and Szarmach, A. (2018). Understanding the physiopathology behind axial and radial diffusivity changes—what do we know? *Frontiers in neurology* 9, 92

[4.53] Wu, Y.-C., Field, A. S., and Alexander, A. L. (2008). Computation of diffusion function measures in q-space using magnetic resonance hybrid diffusion imaging. *IEEE transactions on medical imaging* 27, 858–865

[4.54] Zhang, Y., Brady, M., and Smith, S. (2001). Segmentation of brain MR images through a hidden Markov random field model and the expectation-maximization algorithm. *IEEE transactions on medical imaging* 20, 45–57

[4.55] Zucchelli, M., Brusini, L., Méndez, C. A., Daducci, A., Granziera, C., and Menegaz, G. (2016). What lies beneath? Diffusion EAP-based study of brain tissue microstructure. *Medical image analysis* 32, 145–156

Part II

Multishell Acquisitions

5

Efficient and accurate EAP imaging from multi-shell dMRI with Micro-Structure adaptive convolution kernels and dual Fourier Integral Transforms (MiSFIT)

Antonio Tristán-Vega, Santiago Aja-Fernández

Laboratorio de Procesado de Imagen (LPI), Universidad de Valladolid, Spain

Abstract: A number of computational techniques have been lately devised to image the Ensemble Average Propagator (EAP) within the white matter of the brain, propelled by the deployment of multi-shell acquisition protocols and databases: approaches like Mean Apparent Propagator Imaging (MAP-MRI) and its Laplacian-regularized version (MAPL) aim at describing the low frequency spectrum of the EAP (limited by the maximum b-value acquired) and afterwards computing scalar indices that embed useful descriptions of the white matter, e. g. the Return-to-Origin, Plane, or Axis Probabilities (RTOP, RTPP, RTAP). These methods resort to a non-parametric, bandwidth limited representation of the EAP that implies fitting a set of 3-D basis functions in a large-scale optimization problem. We propose a semi-parametric approach inspired by signal theory: the EAP is approximated as the spherical convolution of a **Micro-Structure** adaptive Gaussian kernel with a non-parametric orientation histogram, which aims at representing the low-frequency response of an ensemble of coherent sets of fiber bundles at the white matter. This way, the optimization involves just the 2 to 3 parameters that describe the kernel, making our approach far more efficient than the related state of the art. We devise dual **Fourier** domains **Integral Transforms** to analytically compute RTxP-like scalar indices as moments of arbitrary orders over either the whole 3-D space, particular directions, or particular planes. The so-called MiSFIT is both time efficient (a typical multi-shell data set can be processed in roughly one minute) and accurate: it provides estimates of widely validated indices like RTOP, RTPP, and RTAP comparable to MAPL for a wide variety of white matter configurations.

Originally published as: *Antonio Tristán-Vega, Santiago Aja-Fernández, Efficient and accurate EAP imaging from multi-shell dMRI with micro-structure adaptive convolution kernels and dual Fourier Integral Transforms (MiSFIT), NeuroImage Volume 227, 15 February 2021, 117616*

5.1 Introduction

Diffusion Magnetic Resonance Imaging (dMRI) has evolved in parallel with the development of new advances in MRI acquisition and reconstruction for the last two decades. The seminal work by [5.1] on Diffusion Tensor (DT) MRI of the brain exploited the experiment by [5.2] to estimate the Ensemble Average Propagator (EAP) up from six sensitizing gradient directions at a fixed b-value, corresponding to the six Degrees Of Freedom (DOF) of the model. The EAP, i. e. the Probability Density Function (PDF) of water molecules moving a distance $\mathbf{R}$ within an effective time τ, $P(\mathbf{R};\tau)$, was modeled there as a zero-mean Gaussian whose variance was represented by the DT. As soon as MRI devices offered the possibility of acquiring larger data sets with a good number of gradient directions, many authors suggested new ways to estimate the DT with higher accuracy from over-complete data sets [5.3, 5.4, 5.5, 5.6, 5.7, 5.8]. Shortly afterwards, the availability of dense samplings of the orientations space opened the door to resolve complex white matter features like fiber crossings, first with multi-tensor approaches [5.9, 5.10], then with a general family of protocols dubbed High Angular Resolution Diffusion Imaging [5.11, 5.12, HARDI], see [5.13] for a review.

[5.14], in parallel, described Diffusion Spectrum Imaging (DSI) based on a full sampling of both the orientations space and the space of b-values, i. e. the 3-D 'q-space'. Contrarily to HARDI, DSI did not require any sort of modeling assumptions on the behavior of the measured signal, which conferred a great potential upon the new technique. The main pitfall with DSI, however, was the need to acquire an enormous set of MRI volumes to accurately describe the diffusion process without aliasing artifacts, which made it little feasible in practice. By the same time [5.15] laid the groundwork on Compressed Sensing (CS), a new set of reconstruction techniques based on randomized under-samplings, sparse signal representations, and ℓ_1-minimization problems. As long as CS is especially well suited for problems where the Fourier transform of the signal of interest is sampled, its direct application to DSI seemed natural [5.16, 5.17, 5.18].

However, the kind of sampling required by CS raises a number of practical issues, hindering its adoption in clinical or even research environments. On the contrary, the standard nowadays for advanced dMRI acquisitions are multi-shells, i. e., dense samplings of the orientations space arranged in a regular spherical grid for different b-values (often two up to four) describing each a so-called shell. This kind of data is rather easier to acquire even in clinical environments, to the point that several databases with both healthy and diseased subjects have been publicly issued during the last years, e. g.: the Human Connectome Project [5.19, 5.20, 5.21, HCP] or the Public Parkinson's Disease database [5.22, PDD].

The additional information multi-shells provide over HARDI has been exploited in different ways. Several authors have proposed inferring micro-structural intra-voxel information from multiple diffusion compartments by fitting a suitable diffusion model. This set of techniques include Composite Hindered and Restricted Model for Diffusion [5.23, CHARMED], AxCaliber [5.24], Neurite Orientation Dispersion and Density Imaging [5.25, NODDI] and its Bingham-distributed generalization [5.26], or Multi-tissue Constrained Spherical Deconvolution [5.27]. Additionally, other authors have simplified the problem by decoupling the estimation of micro-structure parameters from the meso-structure observations using Spherical Means [5.28, SM] and Multi-Compartment Spherical Means [5.29, MC-SM], Bayesian regression [5.30], or rotationally-invariant features [5.31]. Many of these approaches may

be casted into a general framework where each voxel is modeled as a mixture of an intra-dendrite component, typically described as a zero-transverse diffusion tensor or a restricted cylinder, an extra-dendrite component, typically modeled as a full Gaussian tensor, and a free water component, modeled as an isotropic Gaussian [5.32]. The estimation of the partial volumes and the diffusion characteristics of each component implies a mixed linear-exponential optimization that involves a good number of parameters, which in practice compels the use of fixed typical values for the longitudinal diffusivities inside the axons and 'minimum tortuosity' constraints to keep the problem tractable. These computations-driven restrictions may or may not be realistic.

On the contrary, EAP imaging aims at describing macroscopic representations of the diffusion process, instead of models [5.33], through its voxel-wise 3-D PDF, which should be an ensemble average of the individual PDFs describing each micro-structure compartment. Since there is no need to infer the actual partial volume fractions or characteristics of each individual compartment, the representation can be entirely non-parametric, as well as get rid of bold assumptions. On the other side of the coin, the necessarily limited bandwidth of the q-space sampling (i. e. the restrictions imposed by the maximum b-value acquired) compels EAP imaging to represent just the low frequency spectrum of the EAP by assuming the diffusion signal is either compact supported or it rapidly vanishes outside the range of acquired b-values. As [5.33] have noticed, this signal representation is not consistent with the actual models for intra-axonal diffusivity. The most prominent approaches in this field include Hybrid Diffusion Imaging [5.34, HyDI], multiple q-shell Diffusion Propagator Imaging [5.35, mq-DPI], Bessel-Fourier Orientation Reconstruction [5.36, BFOR], Spherical Polar Fourier reconstruction [5.37, SPFOR], Simple Harmonic Oscillator based Reconstruction and Estimation [5.38, SHORE], Mean Apparent Propagator MRI [5.39, MAP-MRI], directional Radial Basis Functions [5.40, RBF], or Multi-Echo Stimulated Echo Sequence (MESTIM)-based dMRI [5.41]. Recently, the Laplacian-regularized MAP-MRI [5.42, MAPL] has proven its better performance over the original one, becoming widely accepted among the scientific community [5.43, 5.44, 5.45].

Imaging the EAP results in a whole 3-D function per voxel. Computational dMRI is based on computing quantitative measurements from such functions and perform some kind of statistical analysis and/or data mining trusting on the potential sensitivity/specificity of these indices to discriminate two given populations. This approach has been intensively exploited even with primitive DT-MRI studies, for which the Fractional Anisotropy (FA), the Mean Diffusivity (MD), and other tensor-derived scalars are still nowadays the *de facto* standard [5.3]. Within non-parametric EAP imaging, the aforementioned assumption of bandwidth limitation allows to compute a plethora of scalar measurements, typically as some sort of improper integral over the q-space, which can be assumed to faithfully describe just the low frequency behavior of the EAP. Despite this limitation, the Return to Origin Probability (RTOP), the Return to Plane Probability (RTPP), the Return to Axis Probability (RTAP), the Mean Squared Displacement (MSD) computed over the EAP, or its q-space counterpart (qMSD) [5.46, 5.36, 5.40, 5.47], or the Propagator Anisotropy [5.39, PA] have demonstrated a potential in the description of neural architectures [5.48, 5.49] involving a variety of clinical applications related to Alzheimer disease [5.50, 5.43], multiple sclerosis [5.51], stroke [5.52, 5.53], or Parkinson's disease [5.45].

The fundamentals behind EAP imaging are often related to CS-based DSI. Except for HyDI and MESTIM, all other approaches are based on deploying a suitable basis where the EAP is

assumed to be sparse and the radial behavior is described by light tails: Laplace's equation eigenfunctions, Bessel-Fourier's system, or radial basis functions are a few examples. Then, a proper sampling of the q-space allows for a robust reconstruction by means of a possibly constrained, possibly regularized, optimization procedure. Multi-shell samplings, however, are highly structured as opposed to randomized. This implies that only two to four samples in the radial direction, one per measured shell, are usually available to fit a large number of basis functions. As a consequence, a heavy regularization of the problem is required.

In this work, we assume the bandwidth limitation condition to compute EAP measurements commonly used in the literature, as well as propose new ones. As opposed to the related approaches in the state of the art, ours is not based on fitting the EAP in some functions basis, which makes it time efficient at the same time it relaxes the low-frequency constraints imposed by the maximum b-value acquired. Instead, it is based on Micro-Structure-adaptive convolution kernels and dual Fourier domains Integral Transforms (**MiSFIT**). While the angular representation of the signal is still fully non-parametric (since multi-shell samplings grant a dense sampling for this manifold), the radial representation is low-rank, with at most 3 parameters to estimate (since multi-shell samplings usually offer 2 to 4 radial samples). Inspired by the SM technique described by [5.28, 5.54], we eliminate the effect of fiber dispersion inside each voxel to compute a convolution kernel that depends on the low-frequency micro-structure diffusion properties. The signal in the q-space is afterwards expressed as a spherical convolution of the kernel with a non-parametric Orientation Distribution Function (ODF), which is developed in the basis of Spherical Harmonics (SH). Funk-Hecke's theorem can then be used to draw closed forms for the integral transforms arising from our method. This way, we attain a straightforward formulation of *hybrid* moments, including fractional and inverse, computed over both the EAP and the q-space signal that enhance the different contrast of the various diffusion features found in multi-shell dMRI data sets. Such measures come to generalize RTOP, RTPP, RTAP, MSD, or qMSD. Our experiments suggest that MiSFIT can provide accurate estimates of scalar indices commonly found in EAP imaging with higher bandwidth than state of the art methods. At the same time, the decoupled optimization in a low rank non-linear problem for the radial behavior and a model-free, linear problem for the orientation makes MiSFIT extremely time-efficient, beating the computation times of MAPL in two orders of magnitude.

5.2 Spherical convolution model of dMRI

In what follows, we dub $E(\mathbf{q})$ the attenuation signal defined as the Diffusion Weighted Image (DWI) over the unweighted T2 baseline, $E(\mathbf{q}) = S(\mathbf{q})/S_0$. MiSFIT is grounded on describing the (low frequency) radial behavior of $E(\mathbf{q})$ as a low-rank parametric representation in terms of a spherical convolution. We choose a 3-D Gaussian kernel as a universal approximator whose parameters are tuned to the diffusion properties at each voxel. With single-shell acquisitions, [5.54] have proposed a zero-transverse diffusion kernel whose longitudinal diffusivity, $\lambda_{\parallel}$, is inferred from the spherical average $\widehat{E}$ of $E(\mathbf{q})$. With this approach, the convolution kernel becomes constant for the transverse direction giving rise to an EAP with

infinite bandwidth. [5.28] generalize this idea to compute a non-zero transverse diffusivity $\lambda_\perp$:

$$E(\mathbf{q}) \;=\; \iint_{\mathcal{S}} \Phi(\mathbf{v}) \exp\left(-4\pi^2\tau q^2 \left(\left(\mathbf{u}^T\mathbf{v}\right)^2 \left(\lambda_\parallel - \lambda_\perp\right) + \lambda_\perp\right)\right) d\mathbf{v}; \tag{5.1}$$

$$\left\{\widehat{E}(q_i)\right\}_{i=1}^{2} \;=\; \frac{1}{4\pi} \iint_{\mathcal{S}} E(q_i\mathbf{u})\, d\mathbf{u} = \frac{\sqrt{\pi}}{2} \exp(-4\pi^2\tau q_i^2\lambda_\perp) \frac{\operatorname{erf}\left(\sqrt{4\pi^2\tau q_i^2 \left(\lambda_\parallel - \lambda_\perp\right)}\right)}{\sqrt{4\pi^2\tau q_i^2 \left(\lambda_\parallel - \lambda_\perp\right)}} \tag{5.2}$$

where $\mathcal{S} = \{\mathbf{u} \in \mathbb{R}^3 : \|\mathbf{u}\| = 1\}$, $\mathbf{q} = q\mathbf{u}$ for $q = \|\mathbf{q}\| \in \mathbb{R}^+$, and the b-value relates to q through the effective diffusion time τ as: $b = 4\pi^2\tau q^2$. $\Phi(\mathbf{u})$ stands for the ODF. Eq. (5.2) plots two non-linear equations that can be solved for the two unknowns $\lambda_\parallel$ and $\lambda_\perp$. As long as $\lambda_\perp$ is strictly positive, $E(\mathbf{q})$ fulfills the necessary condition of rapidly vanishing for high q and the EAP can be computed as the Fourier transform of eq. (5.1), for the dual variables $\mathbf{q}$ and $\mathbf{R}$, in terms of classical functions:

$$P(\mathbf{R}) = \frac{1}{\sqrt{(4\pi\tau)^3 \lambda_\parallel \lambda_\perp^2}} \iint_{\mathcal{S}} \Phi(\mathbf{v}) \exp\left(-R^2 \frac{\left(\mathbf{r}^T\mathbf{v}\right)^2 \left(1/\lambda_\parallel - 1/\lambda_\perp\right) + 1/\lambda_\perp}{4\tau}\right) d\mathbf{v}, \tag{5.3}$$

where $\mathbf{R} = R\mathbf{r}$ for $\mathbf{r} \in \mathcal{S}$, $R = \|\mathbf{R}\| \in \mathbb{R}^+$. The parameter $\lambda_\parallel$ can be identified with the parallel diffusivity of non-free water (in case both the intra- and extra-axonal components are equal), so it has to be restricted to the range $0 < \lambda_\parallel \leq D_{\text{iso}}$, where D_{iso} is the diffusivity of free water molecules at body temperature (usually fixed to $3.0 \times 10^{-3}\,\text{mm}^2/\text{s}$). The interpretation of $\lambda_\perp$ is not equally intuitive: transverse diffusion is the mixture of, at least, a rapidly decaying extra-axonal component and a heavy tailed intra-axonal component, the latter violating the bandwidth limitation assumption. The term $\lambda_\perp$ does not stand for anyone of them, but instead it represents the overall low frequency behavior of all components for the transverse diffusion. Accordingly, it cannot be interpreted as a micro-structure measurement but as a kernel approximator tuned to the properties of the voxel. For this kernel to accurately represent the white matter, it has to be constrained to prolate tensors, i. e. $0 < \lambda_\perp \leq \lambda_\parallel$.

Finally, the acquisition of three or more shells allows to refine the representation with a volume fraction $1 - f$ that stands for the potential presence of free water:

$${}_cE(\mathbf{q}) \;=\; (1-f) \exp\left(-4\pi^2\tau q^2 D_{\text{iso}}\right) + f\, E(\mathbf{q}); \tag{5.4}$$

$$\left\{{}_c\widehat{E}(q_i)\right\}_{i=1}^{N_s} \;=\; (1-f) \exp(-4\pi^2\tau q_i^2 D_{\text{iso}}) + f\, \widehat{E}(q_i). \tag{5.5}$$

Now, $N_s \geq 3$ non-linear equations are used to infer three parameters ($\lambda_\parallel$, $\lambda_\perp$, and f). This way, the EAP is described by means of three components: the Gaussian **convolution kernel** described by $\lambda_\parallel$ and $\lambda_\perp$ at each voxel, the **ODF** $\Phi(\mathbf{R})$, and the **partial volume fraction** f describing the percentage of the signal actually described by the convolution sum. The next section focuses on the analytical computation of EAP descriptors (quantitative diffusion indices) from this representation.

	Over $E(\mathbf{q})$	Over $P(\mathbf{R})$
Full: $(\nu > -3)$	$\Upsilon^{\nu}\left[\text{mm.}^{-\nu-3}\right] = \iiint_{\mathbb{R}^3_\infty} q^{\nu} E(\mathbf{q}) d\mathbf{q}$	$\upsilon^{\nu}\left[\text{mm.}^{\nu}\right] = \iiint_{\mathbb{R}^3_\infty} R^{\nu} P(\mathbf{R}) d\mathbf{R}$
Axial: $(\nu > -2)$	$\Upsilon_a^{\nu}(\mathbf{u}_0)\left[\text{mm.}^{-\nu-1}\right] = \int_{-\infty}^{\infty} q^{\nu} E(q\mathbf{u}_0) dq$	$\upsilon_a^{\nu}(\mathbf{r}_0)\left[\text{mm.}^{\nu-2}\right] = \int_{-\infty}^{\infty} R^{\nu} P(R\mathbf{r}_0) dR$
Planar: $(\nu > -1)$	$\Upsilon_p^{\nu}(\mathbf{u}_0)\left[\text{mm.}^{-\nu-2}\right] = \iint_{q\mathbf{u}\perp\mathbf{u}_0} q^{\nu} E(q\mathbf{u}) d(q\mathbf{u})$	$\upsilon_p^{\nu}(\mathbf{r}_0)\left[\text{mm.}^{\nu-1}\right] = \iint_{R\mathbf{r}\perp\mathbf{r}_0} R^{\nu} P(R\mathbf{r}) d(R\mathbf{r})$

Tab. 5.1.: Summary of the definitions of the arbitrary order moments used to characterize diffusion along with their units. Each kind of moment has an allowed range for the order $\nu \in \mathbb{R}$ given by the convergence of the respective integral.

5.3 Computational analysis of dMRI with scalar measurements

The rich 3-D information provided by the EAP has to be somehow condensed into scalar indices to be usable in practice, as it has been thoroughly discussed in the literature. [5.39] have suggested the use of so-called 'radial moments', i. e. integrals computed over P and weighted by powers of the radial coordinate, R^n, with $n \in \mathbb{Z}^+$. Since E and P are a Fourier transforms pair, it makes equal sense computing radial moments over E. On the other hand, typical indices like RTAP and RTPP are computed as either line or plane integrals over $\mathbf{R}$, which in turn translate to either plane or line integrals over $\mathbf{q}$ by virtue of the central section theorem. For these reasons, we aim at generically characterizing dMRI through the computation of moments on either the $\mathbf{R}$ or the $\mathbf{q}$ domain, either by integrating in the whole 3-D space, along particular directions, or over planes orthogonal to such directions. Besides, we do not restrict moments to be neither integer nor positive pursuing an even more general description. A summary of the definitions we develop in the following subsections is provided in Table 5.1. There are remarkable relations among these moments, and also with most of the scalar indices commonly used in the literature:

$$\begin{cases} \upsilon^0 = 1; \\ \Upsilon_a^0(\mathbf{u}_0) = \upsilon_p^0(\mathbf{u}_0); \end{cases} \quad \begin{cases} \text{RTOP} = \Upsilon^0; \\ \text{MSD} = \upsilon^2; \\ \text{qMSD} = \Upsilon^2; \end{cases} \quad \begin{cases} \text{RTPP} = \Upsilon_a^0(\mathbf{u}_\parallel) = \upsilon_p^0(\mathbf{u}_\parallel); \\ \text{RTAP} = \Upsilon_p^0(\mathbf{u}_\parallel) = \upsilon_a^0(\mathbf{u}_\parallel), \end{cases} \tag{5.6}$$

where $\mathbf{u}_\parallel$ stands for the direction of maximum diffusion within each voxel. At first instance we will develop on eqs. (5.1) and (5.3) to obtain analytical expressions for the simplest convolution representation. The trivial extension to the composite in eq. (5.4) is briefly discussed at the end of this section.

5.3.1 Full moments

Full moments are those computed by integration in the whole 3-D space. By casting the representation in eq. (5.1) into the definition of Υ^{ν} given in Table 5.1 we can integrate in

spherical coordinates to obtain:

$$\begin{aligned}\Upsilon^{\nu} &= \iint_{\mathcal{S}}\int_{0}^{\infty} q^{\nu}\left(\int\!\!\int_{\mathcal{S}} \Phi(\mathbf{v})\exp\left(-4\pi^2\tau q^2\left(\left(\mathbf{u}^T\mathbf{v}\right)^2\left(\lambda_{\parallel}-\lambda_{\perp}\right)+\lambda_{\perp}\right)\right)d\mathbf{v}\right) q^2\,dq\,d\mathbf{u} \\ &= \left(\int\!\!\int_{\mathcal{S}} \Phi(\mathbf{v})d\mathbf{v}\right)\left(\iint_{\mathcal{S}}\int_{0}^{\infty} q^{\nu+2}\exp\left(-4\pi^2\tau q^2\left(\left(\mathbf{u}^T\mathbf{v}_0\right)^2\left(\lambda_{\parallel}-\lambda_{\perp}\right)+\lambda_{\perp}\right)\right)dq\,d\mathbf{u}\right) \\ &= \iint_{\mathcal{S}}\int_{0}^{\infty} q^{\nu+2}\exp\left(-4\pi^2\tau q^2\left(\left(\mathbf{u}^T\mathbf{v}_0\right)^2\left(\lambda_{\parallel}-\lambda_{\perp}\right)+\lambda_{\perp}\right)\right)dq\,d\mathbf{u},\end{aligned}$$

where the unit direction $\mathbf{v}_0 \in \mathcal{S}$ can be fixed to any arbitrary constant since the value of the integral does not depend on it. At this point we must define a key parameter in our developments:

$$\rho_{\lambda} \triangleq \frac{\lambda_{\perp}}{\lambda_{\parallel}-\lambda_{\perp}} > 0, \tag{5.7}$$

so that explicitly integrating the previous equation in the variable q renders:

$$\begin{aligned}\Upsilon^{\nu} &= \frac{1}{2\left(4\pi^2\tau\lambda_{\perp}\right)^{\frac{\nu+3}{2}}}\Gamma\left(\frac{\nu+3}{2}\right)\iint_{\mathcal{S}}\frac{d\mathbf{u}}{\left(1+\left(\mathbf{u}^T\mathbf{v}_0\right)^2/\rho_{\lambda}\right)^{\frac{\nu+3}{2}}} \\ &= \frac{\pi}{\left(4\pi^2\tau\lambda_{\perp}\right)^{\frac{\nu+3}{2}}}\Gamma\left(\frac{\nu+3}{2}\right)\int_{-1}^{1}\frac{dx}{\left(1+x^2/\rho_{\lambda}\right)^{\frac{\nu+3}{2}}},\end{aligned}$$

since the spherical averaging in the variable $\mathbf{u}$ will not depend on the arbitrary value of $\mathbf{v}_0$. Note the Gamma function is only defined if $\nu > -3$. With this condition, $\lambda_{\perp}$ (and therefore ρ_{λ}) must be strictly positive as well for Υ^{ν} to be finite. Finally, we introduce the new definition:

$$\iota_{\gamma}^{n}(z) \triangleq \int_{-1}^{1}\frac{x^{2n}dx}{\left(1+x^2/z\right)^{\gamma/2}}, \tag{5.8}$$

so that the full moment of order ν computed over E reads:

$$\Upsilon^{\nu} = \frac{\pi}{\left(4\pi^2\tau\lambda_{\perp}\right)^{\frac{\nu+3}{2}}}\Gamma\left(\frac{\nu+3}{2}\right)\iota_{\nu+3}^{0}(\rho_{\lambda}). \tag{5.9}$$

Conversely, we will define the following parameter κ_{λ}:

$$\kappa_{\lambda} \triangleq \frac{\lambda_{\parallel}}{\lambda_{\parallel}-\lambda_{\perp}} > 1, \tag{5.10}$$

so that full moments computed over P are derived from eq. (5.3) in a similar fashion:

$$\upsilon^{\nu} = \frac{(4\tau)^{\frac{\nu}{2}}\lambda_{\perp}^{\frac{\nu+1}{2}}}{\sqrt{\pi\lambda_{\parallel}}}\Gamma\left(\frac{\nu+3}{2}\right)\iota_{\nu+3}^{0}(-\kappa_{\lambda}). \tag{5.11}$$

In this case, the condition $\lambda_{\perp} > 0$ is required so that $\kappa_{\lambda} > 1$ and the integrand of eq. (5.8) does not become singular at $x = \pm 1$ (which will make $\iota_{\gamma}^{n}(-\kappa_{\lambda})$ divergent for $\gamma \geq 2$). The computation of the integral $\iota_{\gamma}^{n}(z)$ defining both Υ^{ν} and υ^{ν} is thoroughly discussed in appendix 5.C. It is worth noticing that any full moment will depend just on $\lambda_{\parallel}$ and $\lambda_{\perp}$, but never on the ODF.

5.3.2 Axial moments

Axial moments are those computed as line integrals along a given direction $\mathbf{u}_0$, as described in Table 5.1. With the representation in eq. (5.1):

$$\begin{aligned}
\Upsilon_a^\nu(\mathbf{u}_0) &= \int_{-\infty}^{\infty} q^\nu \left(\iint_{\mathcal{S}} \Phi(\mathbf{v}) \exp\left(-4\pi^2\tau q^2 \left(\left(\mathbf{u}_0^T\mathbf{v}\right)^2 \left(\lambda_\parallel - \lambda_\perp\right) + \lambda_\perp \right)\right) d\mathbf{v} \right) dq \\
&= \iint_{\mathcal{S}} \Phi(\mathbf{v}) \int_{-\infty}^{\infty} q^\nu \exp\left(-4\pi^2\tau q^2 \left(\left(\mathbf{u}_0^T\mathbf{v}\right)^2 \left(\lambda_\parallel - \lambda_\perp\right) + \lambda_\perp \right)\right) dq\, d\mathbf{v} \\
&= \frac{1}{\left(4\pi^2\tau\lambda_\perp\right)^{\frac{\nu+1}{2}}} \Gamma\left(\frac{\nu+1}{2}\right) \iint_{\mathcal{S}} \frac{\Phi(\mathbf{v})}{\left(1 + \left(\mathbf{u}_0^T\mathbf{v}\right)^2/\rho_\lambda\right)^{\frac{\nu+1}{2}}} d\mathbf{v}, \qquad (5.12)
\end{aligned}$$

where we can find now an explicit dependency with the ODF through the convolution in the variable $\mathbf{v}$. Conversely, the axial moments computed over P are derived from eq. (5.3):

$$\upsilon_a^\nu(\mathbf{r}_0) = \frac{(4\tau)^{\frac{\nu-2}{2}} \lambda_\perp^{\frac{\nu-1}{2}}}{\sqrt{\pi^3\lambda_\parallel}} \Gamma\left(\frac{\nu+1}{2}\right) \iint_{\mathcal{S}} \frac{\Phi(\mathbf{v})}{\left(1 - \left(\mathbf{r}_0^T\mathbf{v}\right)^2/\kappa_\lambda\right)^{\frac{\nu+1}{2}}} d\mathbf{v}. \qquad (5.13)$$

The practical computation of the ODF-dependent integrals defined by the spherical convolutions in eqs. (5.12) and (5.13) is detailed in the next section. In any case, note that axial moments are only defined for $\nu > -1$, for which the Gamma function will be defined.

5.3.3 Planar moments

Planar moments are those computed as surface integrals in a plane perpendicular to a desired direction $\mathbf{u}_0$ containing the origin, see Table 5.1. With the representation in eq. (5.1):

$$\begin{aligned}
\Upsilon_p^\nu(\mathbf{u}_0) &= \iint_{q\mathbf{u}\perp\mathbf{u}_0} q^\nu \left(\iint_{\mathcal{S}} \Phi(\mathbf{v}) \exp\left(-4\pi^2\tau q^2 \left(\left(\mathbf{u}^T\mathbf{v}\right)^2 \left(\lambda_\parallel - \lambda_\perp\right) + \lambda_\perp \right)\right) d\mathbf{v} \right) d(q\mathbf{u}) \\
&= \iint_{\mathcal{S}} \Phi(\mathbf{v}) \int_{\mathbf{u}\perp\mathbf{u}_0} \int_0^{\infty} q^{\nu+1} \exp\left(-4\pi^2\tau q^2 \left(\left(\mathbf{u}^T\mathbf{v}\right)^2 \left(\lambda_\parallel - \lambda_\perp\right) + \lambda_\perp \right)\right) dq\, d\mathbf{u}\, d\mathbf{v} \\
&= \frac{1}{2\left(4\pi^2\tau\lambda_\perp\right)^{\frac{\nu+2}{2}}} \Gamma\left(\frac{\nu+2}{2}\right) \iint_{\mathcal{S}} \int_{\mathbf{u}\perp\mathbf{u}_0} \frac{\Phi(\mathbf{v})}{\left(1 + \left(\mathbf{u}^T\mathbf{v}\right)^2/\rho_\lambda\right)^{\frac{\nu+2}{2}}} d\mathbf{u}\, d\mathbf{v}, \qquad (5.14)
\end{aligned}$$

where the integral around the equator $\mathbf{u} \perp \mathbf{u}_0$ stands for the polar coordinate used to integrate in the plane orthogonal to $\mathbf{u}_0$. As noted by [5.55], this is the Funk-Radon transform of the integrand evaluated at $\mathbf{u} = \mathbf{u}_0$. Developing on eq. (5.3) yields the moments over P:

$$\upsilon_p^\nu(\mathbf{r}_0) = \frac{(4\tau)^{\frac{\nu-1}{2}} \lambda_\perp^{\frac{\nu}{2}}}{2\sqrt{\pi^3\lambda_\parallel}} \Gamma\left(\frac{\nu+2}{2}\right) \iint_{\mathcal{S}} \int_{\mathbf{r}\perp\mathbf{r}_0} \frac{\Phi(\mathbf{v})}{\left(1 - \left(\mathbf{r}^T\mathbf{v}\right)^2/\kappa_\lambda\right)^{\frac{\nu+2}{2}}} d\mathbf{u}\, d\mathbf{v}. \qquad (5.15)$$

The computation of the ODF-dependent operands in eqs. (5.14) and (5.15) is detailed in the next section. Planar moments are only defined for $\nu > -2$, for which the Gamma function will be defined.

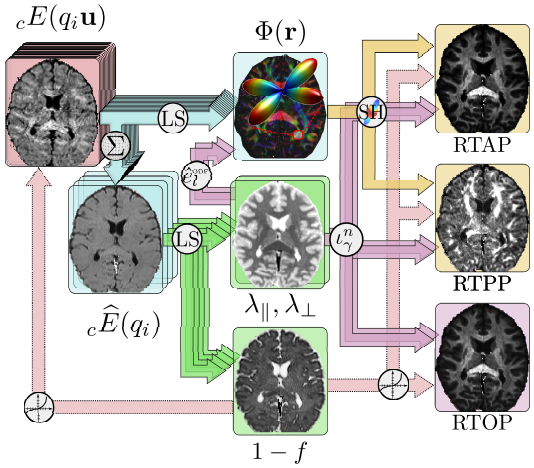

Fig. 5.1.: Graphical abstract of the proposed pipeline for the computational analysis of dMRI based on multi-shell acquisitions.

5.3.4 General moments for the composite representation

The linearity of eq. (5.4), together with the simplicity of the isotropic compartment, allow the trivial extension of the previous expressions to the composite diffusion signal. Hence, each of the full, axial, or planar moments derived in the above will have a composite counterpart described as:

$$\begin{aligned}
{}_c\Upsilon^\nu &= f\cdot\Upsilon^\nu + (1-f)\cdot\frac{2\Gamma\left(\frac{\nu+3}{2}\right)}{\pi^{\nu+2}\left(4\tau D_{\text{iso}}\right)^{\frac{\nu+3}{2}}};\\
{}_c\Upsilon_a^\nu(\mathbf{u}_0) &= f\cdot\Upsilon_a^\nu(\mathbf{u}_0) + (1-f)\cdot\frac{\Gamma\left(\frac{\nu+1}{2}\right)}{\pi^{\nu+1}\left(4\tau D_{\text{iso}}\right)^{\frac{\nu+1}{2}}};\\
{}_c\Upsilon_p^\nu(\mathbf{u}_0) &= f\cdot\Upsilon_p^\nu(\mathbf{u}_0) + (1-f)\cdot\frac{\Gamma\left(\frac{\nu+2}{2}\right)}{\pi^{\nu+1}\left(4\tau D_{\text{iso}}\right)^{\frac{\nu+2}{2}}}.
\end{aligned} \tag{5.16}$$

Or, for the moments computed over P:

$$\begin{aligned}
{}_c\upsilon^\nu &= f\cdot\upsilon^\nu + (1-f)\cdot\frac{2\left(4\tau D_{\text{iso}}\right)^{\frac{\nu}{2}}\Gamma\left(\frac{\nu+3}{2}\right)}{\pi^{\frac{1}{2}}};\\
{}_c\upsilon_a^\nu(\mathbf{r}_0) &= f\cdot\upsilon_a^\nu(\mathbf{r}_0) + (1-f)\cdot\frac{\left(4\tau D_{\text{iso}}\right)^{\frac{\nu-2}{2}}\Gamma\left(\frac{\nu+1}{2}\right)}{\pi^{\frac{3}{2}}};\\
{}_c\upsilon_p^\nu(\mathbf{r}_0) &= f\cdot\upsilon_p^\nu(\mathbf{r}_0) + (1-f)\cdot\frac{\left(4\tau D_{\text{iso}}\right)^{\frac{\nu-1}{2}}\Gamma\left(\frac{\nu+2}{2}\right)}{\pi^{\frac{1}{2}}}.
\end{aligned} \tag{5.17}$$

5.4 Methods

MiSFIT is described end-to-end in Fig. 5.1: the composite multi-shell acquisitions, ${}_cE(q_i\mathbf{u})$, are computed dividing the DWI by the measured unweighted baselines. The composite spherical means, ${}_c\widehat{E}(q_i)$ in eq. (5.5), are obtained from the $0-$th coefficient of the SH

expansions of ${}_cE(q_i\mathbf{u})$ at each shell. These are the N_s samples used to fit the adaptive convolution sum (f, $\lambda_\parallel$, and $\lambda_\perp$) by solving a non-linear Least Squares (LS) problem as in Section 5.4.1. In Section 5.4.3 the ODF, $\Phi(\mathbf{r})$, is drawn by fitting SH coefficients to the non-composite signal $E(q_i\mathbf{u})$ for all the N_s shells: eq. (5.4) allows to isolate $E(q_i\mathbf{u})$ from ${}_cE(q_i\mathbf{u})$ once f is known, so that eq. (5.1) is solved for $\Phi(\mathbf{r})$ via linear LS. The ODF together with the convolution parameters fully describe the EAP, so they are jointly used in Sections 5.4.4 and 5.4.5 to compute the (non-composite) axial moments as in eqs. (5.12) and (5.13) or the (non-composite) planar moments as in eqs. (5.14) and (5.15). On the contrary, full moments depend only on $\lambda_\parallel$ and $\lambda_\perp$, as demonstrated in eqs. (5.9) and (5.11). Finally, the composite moments are computed as in eqs. (5.16) and (5.17).

5.4.1 Inference of the adaptive convolution kernel

Starting at eq. (5.5), we manipulate the terms and take logarithms, so that three unknowns (f, $\lambda_\perp$, and $\delta_\lambda = \lambda_\parallel - \lambda_\perp$) are inferred from N_s measurements via non-linear LS:

$$\min_{f,\lambda_\perp,\delta_\lambda} \frac{1}{2}\sum_{i=1}^{N_s}\left(\log\left(\frac{{}_c\widehat{E}(q_i)-(1-f)\exp(-b_iD_{\text{iso}})}{f}\right)+b_i\lambda_\perp+\log\left(\frac{2\sqrt{b_i\delta_\lambda}}{\sqrt{\pi}\,\text{erf}\left(\sqrt{b_i\delta_\lambda}\right)}\right)\right)^2, \tag{5.18}$$

where $b_i = 4\pi^2\tau q_i^2$. The three variables to infer have to be constrained to physically consistent ranges. In particular, f must be greater than a lower threshold f_0 defined as:

$$f_0 = \max_{i=1,\dots,N_s} \max\left\{1-\frac{{}_c\widehat{E}(q_i)}{\exp(-b_iD_{\text{iso}})},\ 1-\frac{1-{}_c\widehat{E}(q_i)}{1-\exp(-b_iD_{\text{iso}})}\right\}, \tag{5.19}$$

so that the non-free water average $\widehat{E}(q_i)$ computed from the composite average ${}_c\widehat{E}(q_i)$ after eq. (5.5) is still within the range $[0,1]$. Besides, the definition of the moments in Section 5.3 as improper integrals requires the signal $E(\mathbf{q})$ to exhibit fast decaying tails. Cropping the high frequency spectrum is otherwise ubiquitous to EAP imaging, e. g. by using Laplacian penalties [5.42]. Instead, we penalize infinitely prolate shape factors of the convolution kernel, defined as $\lambda_\perp/\delta_\lambda$, which leads to the definitive form of the LS problem:

$$\begin{aligned}&\min_{f,\lambda_\perp,\delta_\lambda} \frac{1}{2}\sum_{i=1}^{N_s}\left(\log\left(\frac{{}_c\widehat{E}(q_i)-(1-f)\exp(-b_iD_{\text{iso}})}{f}\right)+b_i\lambda_\perp+\log\left(\frac{2\sqrt{b_i\delta_\lambda}}{\sqrt{\pi}\,\text{erf}\left(\sqrt{b_i\delta_\lambda}\right)}\right)\right)^2+\mu\frac{\delta_\lambda}{\lambda_\perp},\\ &\text{s. t. :}\quad f_0\le f\le 1;\quad 0\le\lambda_\perp\le D_{\text{iso}}-\delta_\lambda;\quad 0\le\delta_\lambda\le D_{\text{iso}},\end{aligned} \tag{5.20}$$

where $\mu > 0$ is a small constant. The resolution of this LS problem is addressed in appendix 5.A.

5.4.2 Spherical deconvolution and Funk-Hecke's theorem

The keystone of our proposal is the spherical convolution in eq. (5.1). Axial moments as described in eqs. (5.12) and (5.13), or planar moments as described in eqs. (5.14)

and (5.15), rely on this kind of operands as well, all of them obeying the general form:

$$\Psi(\mathbf{u}) = \iint_{\mathcal{S}} \Phi(\mathbf{v})\Lambda(\mathbf{u}^T\mathbf{v})d\mathbf{v}. \tag{5.21}$$

Assuming that Ψ, Φ, and Λ are developed in the basis of (even) SH, $\{Y_l^m(\mathbf{u})\}_{l=0\ (\text{even}),m=-l}^{\infty,l}$, [5.56] first suggested using Funk-Hecke's theorem to solve deconvolution problems within dMRI. In precise terms, let c_l^m be the SH coefficients of $\Psi(\mathbf{u})$ and let ϕ_l^m be the coefficients of $\Phi(\mathbf{u})$:

$$c_l^m = \hat{e}_l\, \phi_l^m, \tag{5.22}$$

where the convolution factors $\hat{e}_l$ are computed, for each rotation invariant kernel Λ, as:

$$\hat{e}_l = 2\pi \int_{-1}^{1} \Lambda(x) P_l(x) dx, \tag{5.23}$$

where $P_l(x)$ are the even-degree Legendre polynomials.

5.4.3 Application to the computation of ODFs

From eq. (5.1), it follows that for each shell described by its b-value, $b_i = 4\pi^2\tau q_i^2$:

$$E(q_i\mathbf{u}) = \iint_{\mathcal{S}} \Phi(\mathbf{v})\, \Lambda_{\text{ODF}}\left(\mathbf{u}^T\mathbf{v}; q_i\right)\, d\mathbf{v} \;:\quad \Lambda_{\text{ODF}}(x; q_i) = \exp\left(-b_i\lambda_\perp\right)\exp\left(-b_i\,\delta_\lambda\,x^2\right), \tag{5.24}$$

where $E(q_i\mathbf{u})$ is obtained from the measured composite signal ${}_cE(q_i\mathbf{u})$ as in eq. (5.4). The convolution factors $\{\hat{e}_l^{\text{ODF}}(q_i)\}_{l=0\ (\text{even})}^{\infty}$ corresponding to this kernel are computed in appendix 5.B. Once this is done, the SH coefficients of the ODF, ϕ_l^m, can be inferred by solving:

$$\frac{1}{4\pi}\hat{e}_0^{\text{ODF}}(q_i) + \sum_{\substack{l=2\\ l\ \text{even}}}^{L}\sum_{m=-l}^{l} \hat{e}_l^{\text{ODF}}(q_i)\,\phi_l^m\, Y_l^m(\mathbf{u}_{i,j}) \simeq E(q_i\mathbf{u}_{i,j}),\ i = 1,\ldots,N_s,\ j = 1,\ldots,N_{g_i} \tag{5.25}$$

where L is the maximum order considered for the SH expansions and $\{\mathbf{u}_{i,j}\}_{j=1}^{N_{g_i}}$ are the N_{g_i} sensitizing gradients acquired at the i-th shell. Note the condition $\phi_0^0\, Y_0^0 = 1/4\pi$ is necessary so that the ODF integrates to 1. Eq. (5.25) can be rewritten in matrix form and solved via linear LS:

$$\begin{bmatrix} \mathbf{B}_1\mathbf{F}_1 \\ \vdots \\ \mathbf{B}_{N_s}\mathbf{F}_{N_s} \end{bmatrix} \boldsymbol{\Phi} \simeq \begin{bmatrix} \mathbf{E}_1 \\ \vdots \\ \mathbf{E}_{N_s} \end{bmatrix} \Rightarrow \boldsymbol{\Phi} = \left(\sum_{i=1}^{N_s} \mathbf{F}_i^T\mathbf{B}_i^T\mathbf{B}_i\mathbf{F}_i + \lambda\mathbf{L}^2\right)^{-1} \left(\sum_{i=1}^{N_s} \mathbf{F}_i^T\mathbf{B}_i^T\mathbf{E}_i\right), \tag{5.26}$$

where $\{\mathbf{B}_i\}_{i=1}^{N_s}$ are $N_{g_i} \times K$ matrices whose (r,c) entry is $[\mathbf{B}_i]_{r,c} = Y_{l(c)}^{m(c)}(\mathbf{u}_{i,r})$. Note we are stacking the double-indexed functions $Y_l^m, l \geq 2$ in order along one single dimension, so that $K = (L+1)(L+2)/2 - 1$. Hence, $\{\mathbf{F}_i\}_{i=1}^{N_s}$ are $K \times K$ diagonal matrices with

$[\mathbf{F}_i]_{c,c} = \hat{e}^{\text{ODF}}_{l(c)}(q_i)$; $\mathbf{\Phi}$ is a $K \times 1$ vector with $[\mathbf{\Phi}]_c = \phi^{m(c)}_{l(c)}$; $\{\mathbf{E}_i\}_{i=1}^{N_s}$ are $N_{g_i} \times 1$ vectors with $[\mathbf{E}_i]_r = E(q_i \mathbf{u}_{i,r}) - \frac{1}{4\pi}\hat{e}^{\text{ODF}}_0(q_i)$; $\mathbf{L}$ is a $K \times K$ diagonal matrix that represents a Laplace-Beltrami penalty, i. e. $[\mathbf{L}]_{c,c} = -l(c)(l(c)+1)$, and $\lambda > 0$ is the regularization parameter. Remarkably, all $\{\mathbf{F}_i\}_{i=1}^{N_s}$ depend on the convolution sum described by $\lambda_\parallel$ and $\lambda_\perp$, meaning that eq. (5.26) implies inverting a $K \times K$ matrix at each imaged voxel.

5.4.4 Application to the computation of axial moments

The following convolution kernel can be identified in eq. (5.12):

$$\Lambda_a(x) = \frac{1}{(1 + x^2/\rho_\lambda)^{\frac{\nu+1}{2}}}, \tag{5.27}$$

whose convolution coefficients are calculated after eq. (5.23):

$$\hat{e}^{a,\nu}_l = 2\pi \int_{-1}^{1} \frac{P_l(x)}{(1 + x^2/\rho_\lambda)^{\frac{\nu+1}{2}}} dx = 2\pi \sum_{n=0}^{l/2} \alpha^{2n}_l \int_{-1}^{1} \frac{x^{2n}}{(1 + x^2/\rho_\lambda)^{\frac{\nu+1}{2}}} dx = 2\pi \sum_{n=0}^{l/2} \alpha^{2n}_l \iota^n_{\nu+1}(\rho_\lambda), \tag{5.28}$$

where $\{\alpha^{2n}_l\}_{n=0}^{l/2}$ are the $2n$-th degree coefficients of the l-th (even) Legendre polynomial and $\iota^n_{\nu+1}(\rho_\lambda)$ is computed for any values of ν and n as described in appendix 5.C. Then:

$$\Upsilon^\nu_a(\mathbf{u}_0) = \frac{2\pi\Gamma\left(\frac{\nu+1}{2}\right)}{(4\pi^2\tau\lambda_\perp)^{\frac{\nu+1}{2}}} \sum_{\substack{l=0 \\ l \text{ even}}}^{L} \left(\sum_{n=0}^{l/2} \alpha^{2n}_l \iota^n_{\nu+1}(\rho_\lambda) \right) \sum_{m=-l}^{l} \phi^m_l \, Y^m_l(\mathbf{u}_0). \tag{5.29}$$

An analogous development on eq. (5.13) yields:

$$\upsilon^\nu_a(\mathbf{r}_0) = \frac{2\,(4\tau)^{\frac{\nu-2}{2}}\,\lambda_\perp^{\frac{\nu-1}{2}}}{\sqrt{\pi\lambda_\parallel}}\,\Gamma\left(\frac{\nu+1}{2}\right) \sum_{\substack{l=0 \\ l \text{ even}}}^{L} \left(\sum_{n=0}^{l/2} \alpha^{2n}_l \iota^n_{\nu+1}(-\kappa_\lambda) \right) \sum_{m=-l}^{l} \phi^m_l \, Y^m_l(\mathbf{u}_0). \tag{5.30}$$

5.4.5 Application to the computation of planar moments

In this case the convolution kernel reads, after eq. (5.14):

$$\Lambda_p(x) = \frac{1}{(1 + x^2/\rho_\lambda)^{\frac{\nu+2}{2}}}. \tag{5.31}$$

Noticeably, for the case of planar moments we need to apply the Funk-Radon transform afterwards, which implies an additional product of the SH coefficients with the eigenvalues of this integral transform, $2\pi(l-1)!!/l!!$, like suggested by [5.57]:

$$\hat{e}^{p,\nu}_l = 2\pi \frac{2\pi(-1)^{l/2}(l-1)!!}{l!!} \int_{-1}^{1} \frac{P_l(x)}{(1 + x^2/\rho_\lambda)^{\frac{\nu+2}{2}}} dx = \frac{4\pi^2(l-1)!!}{l!!} \sum_{n=0}^{l/2} \alpha^{2n}_l \iota^n_{\nu+2}(\rho_\lambda), \tag{5.32}$$

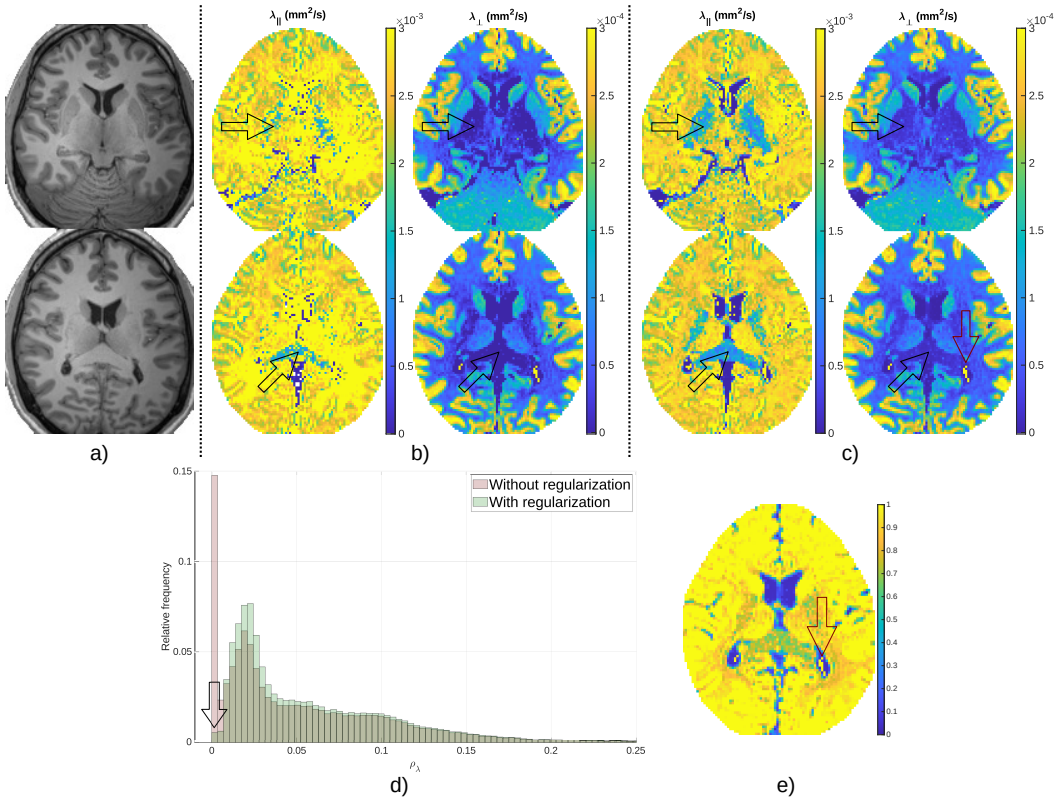

Fig. 5.2.: Problem regularization for two slices of the test volume HCP MGH-1007. T1-weighted images are shown in (a) for anatomical reference. Estimates of the convolution parameters $\lambda_{\parallel}$ and $\lambda_{\perp}$ either without (b) or with (c) regularization. Corresponding histograms of ρ_{λ} are depicted (d) to quantitatively check the effect ('bad values' are those with $\rho_{\lambda} \rightarrow 0$). The fraction f of non-free water is represented in (e) for one of the slices. Black arrows highlight those regions where the regularization has the most noticeable impact. The red arrow highlights representation problems at the csf.

where once again $\iota^{n}_{\nu+2}(\rho_{\lambda})$ is computed as described in appendix 5.C. Planar moments then read:

$$\Upsilon^{\nu}_{p}(\mathbf{u}_0) = \frac{2\pi^2\Gamma\left(\frac{\nu+2}{2}\right)}{\left(4\pi^2\tau\lambda_{\perp}\right)^{\frac{\nu+2}{2}}} \sum_{\substack{l=0 \\ l \text{ even}}}^{L} \frac{(l-1)!!}{l!!} \left(\sum_{n=0}^{l/2} \alpha_l^{2n} \iota^{n}_{\nu+2}(\rho_{\lambda}) \right) \sum_{m=-l}^{l} \phi_l^m \, Y_l^m(\mathbf{u}_0), \quad (5.33)$$

or, developing on eq. (5.15) instead:

$$\upsilon^{\nu}_{p}(\mathbf{r}_0) = \frac{2\sqrt{\pi}\,(4\tau)^{\frac{\nu-1}{2}}\,\lambda_{\perp}^{\frac{\nu}{2}}}{\sqrt{\lambda_{\parallel}}}\,\Gamma\left(\frac{\nu+2}{2}\right) \sum_{\substack{l=0 \\ l \text{ even}}}^{L} \frac{(l-1)!!}{l!!} \left(\sum_{n=0}^{l/2} \alpha_l^{2n} \iota^{n}_{\nu+2}(-\kappa_{\lambda}) \right) \sum_{m=-l}^{l} \phi_l^m \, Y_l^m(\mathbf{u}_0), \quad (5.34)$$

5.5 Experiments and Results

5.5.1 Materials

The experimental work in this paper is intended as a proof of concept, so we avoid large clinical data sets to focus on representative examples. In precise terms:

- We have randomly picked up volume HCP MGH-1007 from the **Human Connectome Project (HCP)** [5.19, 5.20]. These are high quality data acquired on a Siemens 3T Connectome scanner with 4 different shells at $b = \{1,000,\ 3,000,\ 5,000,\ 10,000\}$ s/mm^2, with $\{64,\ 64,\ 128,\ 256\}$ gradient directions each and 40 interleaved unweighted baselines. However, we have removed the outermost shell at $10,000$ s/mm^2 in order to work with more standard (and affordable) acquisitions. The in-plane resolution is 1.5 mm and the slice thickness is 1.5 mm.

- From the **HCP WU-Minn database** [5.21], we have picked up subject 139839, enrolled for both a test and a re-test acquisition sessions. These data comprise 3 shells at $b = \{1,000,\ 2,000,\ 3,000\}$ s/mm^2 with 90 gradient directions each and 18 interleaved unweighted baselines. The in-plane resolution is 1.25 mm and the slice thickness is 1.25 mm.

5.5.2 Experimental set-up

The reported experiments are grouped in two sections: the first set is aimed at qualitatively checking the consistency of the MiSFIT representation, mainly comprising visual assessments of the convolution sum parameters, the ODFs fields, and the computed moments for varying orders. They are related to the expectable outcomes according to the anatomy of the white matter. The second set focuses on evaluating the accuracy and reliability of MiSFIT compared to the state of the art, both qualitatively and quantitatively. We have chosen MAPL as a widely accepted methodology for EAP imaging [5.42], with the implementation provided by python-dipy v1.1.1 (`https://dipy.org/`) for Python 3.8. Pursuing an optimal performance, anisotropic space-shifting with Laplacian penalty and positivity constraints have been used unless otherwise noticed. The Laplacian weighting parameter was fixed with the built-in generalized cross validation approach for a maximum radial order 6. Since MAPL does not explicitly provide free-water estimation, the accuracy of MiSFIT in the computation of f in eq. (5.4) is tested against a home-made version of the ad-hoc method proposed by [5.58] with the parameters suggested by the authors.

Unless otherwise noticed, we have used the expression in eq. (5.4) for MiSFIT in all cases: the parameter μ in eq. (5.20) has been empirically set to a constant value $\mu = 10^{-5}$; the ODFs deconvolution in eq. (5.26) is solved for $L = 8$ and $\lambda = 5 \times 10^{-4}$. To palliate the bias introduced by Rician noise on the computation of spherical means, we use the technique suggested by [5.28, eq. (10)], based on the inversion of Laguerre's polynomials. The standard deviation of noise in the test volume was estimated using the method proposed by [5.59, eq. (25)].

5.5.3 Consistency of the computational diffusion representation

Estimation of the convolution kernel

Though the spherical means have been thoroughly discussed by [5.29, 5.28] within the scope of micro-structure probing, their application to EAP imaging requires $\rho_\lambda > 0$ (and, consequently, $\kappa_\lambda > 1$). The fulfillment of this condition, together with the impact of the regularization of the problem in the anatomical description of the images, are tested in Fig. 5.2. From eq. (5.5), we have solved the problem in eq. (5.20) for either $\mu = 0$ or $\mu = 10^{-5}$. The first scenario generalizes the proposal by [5.28] with a free-water compartment, so the results, as expected, are visually consistent with those reported therein. Noticeably, the parallel kernel parameter $\lambda_\parallel$ is in the same order of magnitude as D_{iso}, meanwhile the transverse parameter $\lambda_\perp$ is one order of magnitude below $\lambda_\parallel$, pointing out to a clearly prolate convolution kernel (this statement holds for the white matter, but not for the cerebro-spinal fluid, csf, or the cortex). For the non-regularized problem, the histogram computed over ρ_λ demonstrates there are a large number of voxels with singular configurations ($\lambda_\perp \to 0$), mostly at the corpus callosum (cc) or the cortico-spinal tract (cst), see black arrows. According to eq. (5.1), such configurations will lead to asymptotically constant tails of $E(\mathbf{q})$ at the transverse direction, which will propagate to all the spatial directions through the spherical convolution. As a consequence, both $E(\mathbf{q})$ and ${}_cE(\mathbf{q})$ will have infinite bandwidth, which is not consistent with the usual premises on EAP imaging. The regularized problem removes such singularities providing a light tails representation of the spectrum of $E(\mathbf{q})$, so that any moment computation will remain well defined. Finally, the estimation of the non-free water fraction f seems mostly coherent across the white matter (close-to-one values) and the csf (close-to-zero values). However, certain csf regions seem corrupted (red arrows), probably due to the ambiguity of the convolution representation in eqs. (5.1) and (5.4) for pure free water, where it should hold $\lambda_\perp \simeq \lambda_\parallel$.

Computation of ODFs fields

After the convolution kernel is computed, the second stage in the pipeline is the computation of the ODFs, illustrated in Fig. 5.3 for a white matter region where several tracts of interest can be identified. As can seen, the computed glyphs are consistent with our prior anatomical knowledge:

- The cc and the cingulum (cg) cross within the ROI highlighted in red, with the cc glyphs spreading upwards with a dominant component along the sagittal-axial direction ('x'-'z' axes), and the cg glyphs piercing the cc along the coronal direction ('y' axis). Besides, fiber crossings are properly described by MiSFIT: within the outermost part of the cc (yellow arrow), the partial volume fraction of the cg is larger than that of the cc, so that the 'green arm' of the glyph becomes more prominent than the 'red arm'. On the contrary, as we move into the cc (blue arrow), its partial volume fraction increases and the 'red arm' becomes larger as compared to the 'green arm'.

- The cst is the most prominent structure inside the ROI highlighted in blue, mostly aligned with the 'z' axis. Nevertheless, MiSFIT is able to properly resolve the fiber crossings with the 'x'-aligned fiber tracts deviating to the cortex across the centrum

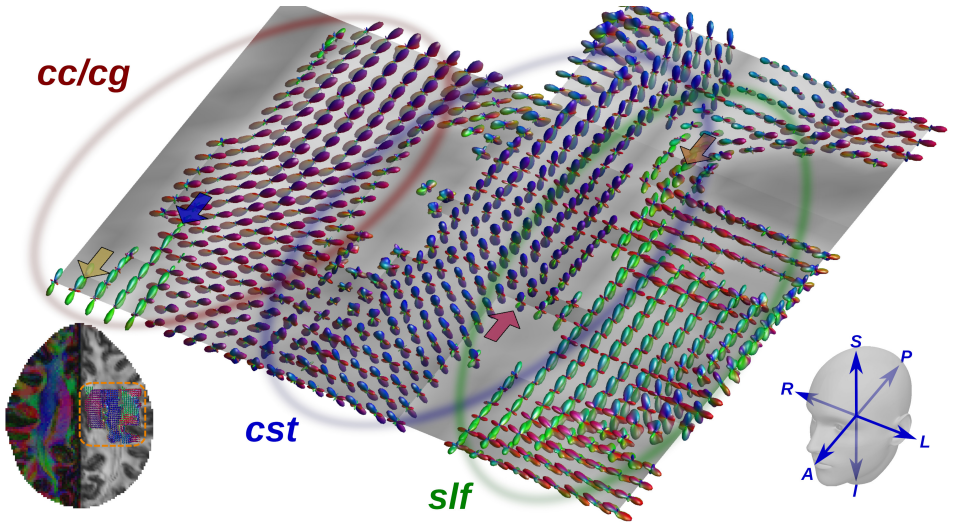

Fig. 5.3.: Detail of the ODFs reconstruction in an axial slice from the test subject HCP MGH-1007. A FA map and a color-by-orientation map extracted from the ODFs field are shown for reference, where we highlight in orange the ROI where the glyphs are shown. Missing glyphs correspond to voxels with an FA below 0.4. Colored arrows point at two-fold fiber crossings (yellow, blue), three-fold fiber crossings (magenta), and small angle fiber crossings (orange).

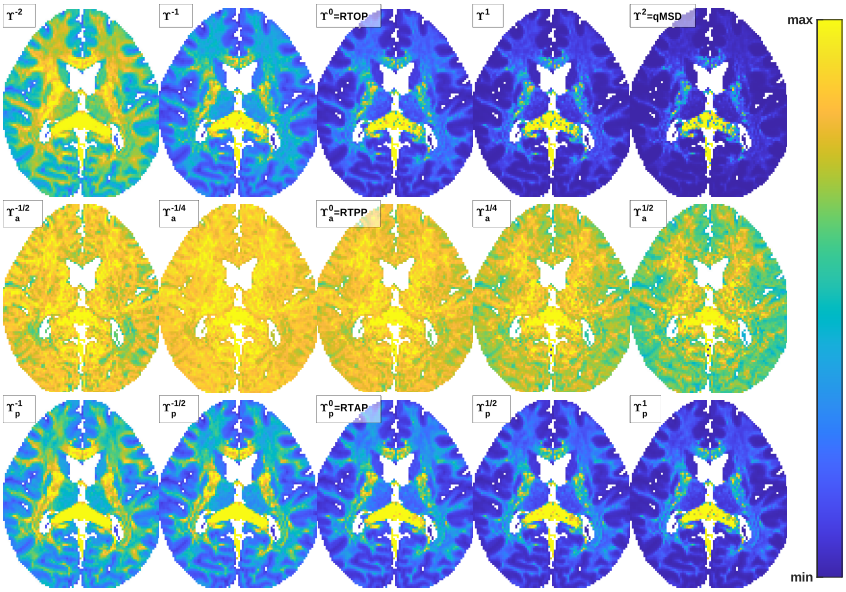

Fig. 5.4.: Moments of different kinds for different orders ν computed over the composite attenuation signal. Each moment has been normalized to its own range, and the csf has been thresholded at $f < 0.5$ for visualization purposes. Top: full moments; middle: axial moments for the maximum diffusion direction; bottom: planar moments for the maximum diffusion direction. This kind of indices include RTOP, qMSD, RTPP, and RTAP.

semiovale, and even the three-bundles crossings involving the superior longitudinal fasciculus (slf) are visible (magenta arrow).

- As we move outwards, the region highlighted in green mostly comprises the slf and

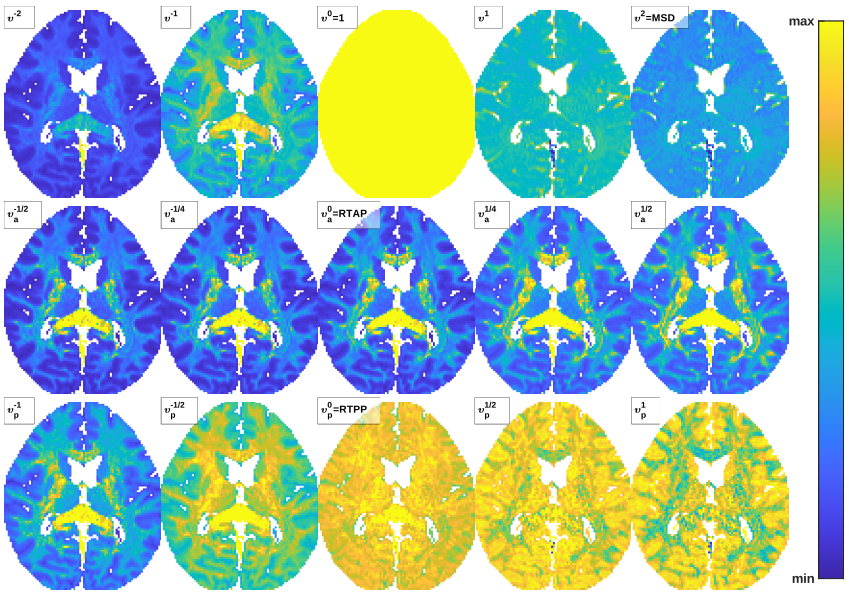

Fig. 5.5.: Moments of different kinds for different orders ν computed over the composite EAP. Each moment has been normalized to its own range, and the csf has been thresholded at $f < 0.5$ for visualization purposes. Top: full moments; middle: axial moments for the maximum diffusion direction; bottom: planar moments for the maximum diffusion direction. This kind of indices include MSD, RTPP, and RTAP.

the fibers directly connecting to the cortex, which explains the fiber crossings in this region. Note that MiSFIT is able to resolve crossings in small angles (orange arrow) corresponding to the curvature of the slf.

For the rest of the white matter regions shown in the axial slice, the color-coded hemisphere (directly computed from the ODFs field) suggests the anatomical consistency of the computed glyphs.

Behavior of each kind of moment for varying orders

The central point in our developments is the characterization of dMRI through scalar measurements. Figs. 5.4 and 5.5 provide a first qualitative insight in the behavior of moments computed respectively from either the composite attenuation signal (Υ-type) or the composite EAP (υ-type). As explained before, each kind of moment (full, axial, or planar) admits a different range of variation for its order ν depending on the convergence of the corresponding integral. Accordingly, we have probed a symmetric range including both negative and positive orders in all cases. Since the units of these moments are millimeters raised to some power depending on ν (see Table 5.1), their ranges of variation are very different from each other, so that all the slices shown in Figs. 5.4 and 5.5 have been min-max normalized. Besides, those voxels with $f < 0.5$ according to eq. (5.4) have been removed for visualization convenience.

First of all, we point out the consistency of the results: the popular RTPP and RTAP can be computed as moments on both the $\mathbf{q}$ domain and the $\mathbf{R}$ domain (RTPP $= \Upsilon_a^0(\mathbf{u}_\parallel) = \upsilon_p^0(\mathbf{u}_\parallel)$, RTAP $= \Upsilon_p^0(\mathbf{u}_\parallel) = \upsilon_a^0(\mathbf{u}_\parallel)$), and accordingly their slices in Figs. 5.4 and 5.5 draw the same

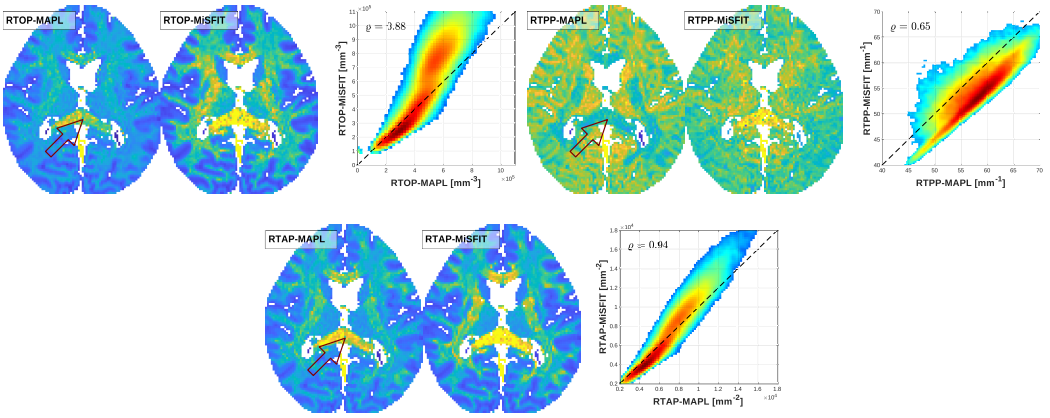

Fig. 5.6.: Comparison of scalar measurements computed with either MAPL (left) or MiSFIT (right): RTOP, RTPP, and RTAP. The same scale is used for both two approaches in all cases, and the csf has been thresholded for visualization comfort. A joint 2-D histogram is shown in each case, together with the respective Pearson's correlation coefficient, for quantitative assessment. Red arrows highlight prominent differences between MAPL and MiSFIT, mostly at the cc.

maps. Of course, υ^0 must evaluate to 1 for any voxel because it is the integral of the EAP, which represents a PDF, over the whole $\mathbb{R}^3$.

As can be seen, different values of ν provide different contrasts for the anatomical details, which is clearly noticeable for full and planar moments but not really evident for axial. This property can be exploited in computational dMRI, since different intra- and inter-tissue contrast levels should lead to different classification patterns. Interestingly, Υ-type moments computed over the attenuation signal seem to provide a higher white matter to gray matter contrast at positive values of ν, meanwhile υ-type moments computed over the EAP do the opposite. Since $\mathbf{q}$ and $\mathbf{R}$ are dual Fourier transform variables, it makes sense their behavior with respect to the sign of ν is somehow complementary.

Axial moments deserve a special attention. As can be seen in Fig. 5.4, the Υ_a-type results in very noisy maps with a reduced anatomical coherence, as it is the case with RTPP. This is probably due to the integration of the q-space along directions for which the diffusivity (thus, the attenuation) is maximal, so that the SNR becomes dramatically worse. This issue does not reproduce for the υ_a^ν-type, for which the axial moments indeed attain consistent descriptions of the white matter.

5.5.4 Comparison to the state of the art in EAP imaging

MiSFIT vs. MAPL: visual assessment

Fig. 5.6 shows respective slices of RTOP, RTPP, and RTAP for both MAPL and MiSFIT with identical scaling, so that they can be directly compared. While the structure of the anatomical maps look quite similar with the two approaches, and their ends of scale are also coherent, MiSFIT seem to estimate larger values than MAPL for RTOP and RTAP, but smaller values for RTPP.

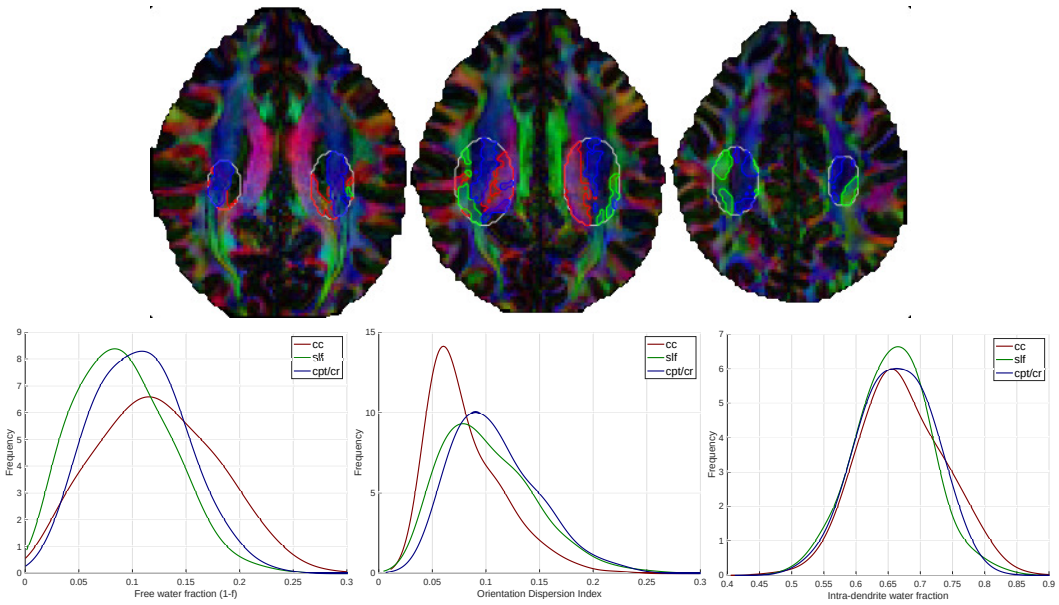

Fig. 5.7.: Setting-up of the numerical comparison of MiSFIT vs. MAPL. An ROI is manually segmented at the centrum semiovale and clustered depending on the principal orientations at each voxel. The NODDI model is used to infer micro-structure parameters, mainly the free-water fraction, the orientation dispersion, and the intra-dendrite vs. extra-dendrite fraction, which are used to stochastically generate synthetic voxels.

Paying attention to the voxel-wise joint 2-D histograms, RTOP and RTAP remain strongly correlated for the low-to-middle range of each parameter, and the discrepancies arise at a higher range. In this latter scenario, MiSFIT consistently over-estimates both RTOP and RTAP with respect to the values computed by MAPL. Even so, the overall Pearson's correlation coefficient is still high enough for the entire range of variation ($\varrho = 0.88$ for RTOP and $\varrho = 0.94$ for RTAP).

On the other hand, RTPP is far noisier than the other measurements, so the resemblance between the two slices is not as evident. Histogram counts show that MiSFIT provides a consistent negative bias with respect to MAPL, and the correlation coefficient is reduced to $\varrho = 0.65$.

A quick look to Fig. 5.6 suggests that the most relevant differences appear at the cc (red arrows), for which both RTOP and RTAP exhibit the highest values. Note the cc comprises highly coherently oriented fiber bundles with small transverse diffusivity, meaning the attenuation signal will slowly decay in the q-space. Since RTOP can de defined as the integral of the attenuation signal in the entire q-space, this issue might be pointing out that MAPL provides a 'lower-pass' estimate than MiSFIT.

MiSFIT vs. MAPL: quantitative evaluation of accuracy

The previous experiment is complemented with a quantitative assessment based on numerical simulations. We aim at designing ground-truth data using a micro-structural model that differs from eq. (5.4) in a substantial manner, at the same time it accounts for the most relevant micro-structural diffusion phenomena. To that end, we have used the python-dmipy

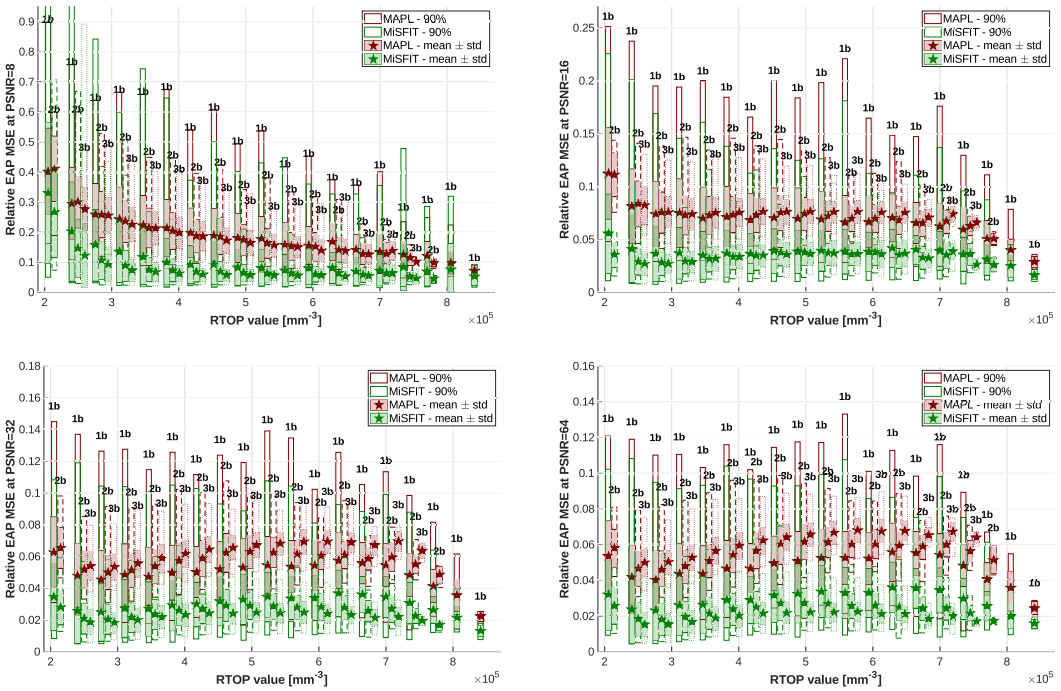

Fig. 5.8.: Errors in the reconstruction of the EAP (or the attenuation signal) with either MAPL or MiSFIT as a function of the ground truth RTOP, for different peak SNRs and for 1, 2, or 3 crossing fiber bundles (1b, 2b, 3b). Missing bars correspond to RTOP values that could not be obtained with the respective configuration. Mean values (stars), standard deviations (solid bars), and 90% confidence intervals (empty bars) are depicted.

package[1] [5.32] to infer realistic parameters for the NODDI approach [5.25] as shown in Fig. 5.7: two ellipsoidal ROIs were symmetrically placed at the centrum semiovale of our test volume, and those voxels with a FA higher than 0.7 were clustered via 3-fold c-means depending on their orientations to obtain the segmentations in Fig. 5.7, top, corresponding to the cc (red), the slf (green) and the corticopontine tract/corona radiata (cpt/cr, blue). NODDI describes a bi-compartmental model with a free-water fraction, analogous to the first term in our eq. (5.4), and a cellular water fraction. For the latter, intra- and extra-dendrite diffusion are respectively described with a singular (zero transverse diffusion) or a non-singular tensor, both aligned with the same direction. This ensemble is convolved with a spherical Watson distribution to account for fiber dispersion parameterized through the Orientation Dispersion Index (ODI). In our case, we have substituted the singular intra-dendrite model with a 'close to singular' tensor, for which the transverse diffusion is set to 1 over 40 times the longitudinal diffusion. Note this fix is mandatory to compute ground truths, since otherwise all the measurements of interest (RTOP, RTPP, RTAP, and the energy of $E(\mathbf{q})$) will be infinite in all cases. Our modified NODDI scheme is used to generate synthetic samples with different configurations:

- The specific NODDI parameters (those in Fig. 5.7, bottom) are randomly generated following the estimated distributions by means of the inverse function method.
- Varying levels of RTOP, RTPP, and RTAP are obtained by uniformly sampling the longitudinal diffusivity within the range $[1.4, 2.8] \times 10^{-3}$ mm^2/s, which both the intra-

[1] `https://dmipy.readthedocs.io`.

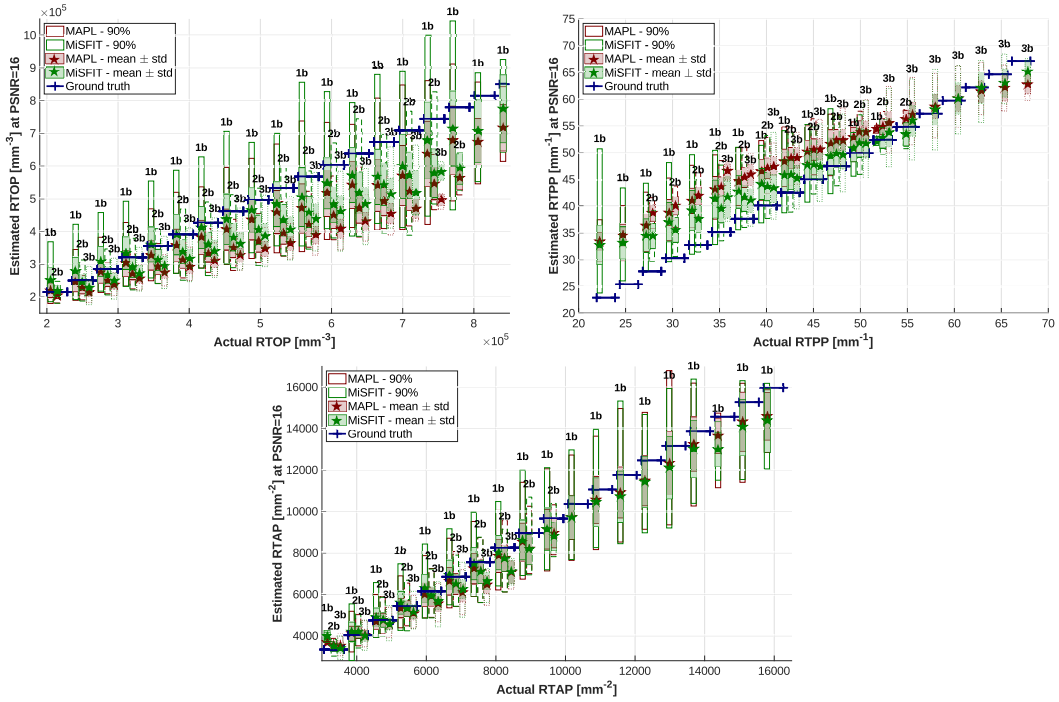

Fig. 5.9.: Estimated RTOP, RTPP, and RTAP vs. ground truth values, for both MAPL and MiSFIT, for a typical peak SNR=16, and for 1, 2, or 3 crossing fiber bundles (1b, 2b, 3b). Missing bars correspond to those ground truth values that could not be obtained with the respective configuration. Mean values (stars), standard deviations (solid bars), and 90% confidence intervals (empty bars) are depicted.

and the extra-dendrite component are set to. The transverse diffusivity for the extra-dendrite component is fixed with the same 'minimum tortuosity' approach used by python-dmipy for parameters estimation.

- The orientation of each simulated bundle (cc, slf, or cpt/cr) is randomly chosen within a cone with aperture 15^o and respective axis $[\sqrt{3}/2, 0, 1/2]^T$, $[0, 1, 0]^T$, or $[0, 0, 1]^T$. They are further combined in three different configurations: 1 bundle (respective volume fractions $\{1, 0, 0\}$), 2 bundles ($\{0.5, 0, 0.5\}$), or 3 bundles ($\{0.35, 0.35, 0.3\}$). Note the longitudinal and transverse diffusivities of these bundles are not linked to each other at all, so we are directly testing the capability of MiSFIT to deal with heterogeneous micro-structural features.

- The resulting signal is sampled in the q-space according to the same scheme found at the HCP MGH-1007 volume, and corrupted afterwards with Rician noise with a peak SNR (defined as the value of the baseline over the standard deviation of noise in the complex domain, σ) of either 8, 16, 32, or 64. Among them, PSNR=16 is the most typical value found in our test volume.

Fig. 5.8 shows the relative Mean Squared Error (rMSE) in the reconstruction of the EAP with either MAPL or MiSFIT as a function of the ground truth RTOP. We choose such

parameterization because RTOP, being the integral of the attenuation signal in the whole q-space, is directly related to the bandwidth of the EAP. According to Parseval's theorem:

$$\text{rMSE} = \frac{\iiint_{\mathbb{R}^3} \left(\widetilde{P}(\mathbf{R}) - P(\mathbf{R})\right)^2 d\mathbf{R}}{\iiint_{\mathbb{R}^3} P(\mathbf{R})^2 \, d\mathbf{R}} = \frac{\iiint_{\mathbb{R}^3} \left(\widetilde{E}(\mathbf{q}) - E(\mathbf{q})\right)^2 d\mathbf{q}}{\iiint_{\mathbb{R}^3} E(\mathbf{q})^2 \, d\mathbf{q}}, \tag{5.35}$$

where $\widetilde{P}(\mathbf{R})$ (or $\widetilde{E}(\mathbf{q})$) stands for the reconstructed signal in each case. As expected, the errors become smaller as the PSNR gets improved, from values of nearly 50% for PSNR=8 and small RTOP to values well below 5% for PSNR=64 at any RTOP. It is worth noticing that MiSFIT consistently outperforms MAPL for almost all the range of PSNR and for any signal bandwidth, with the exception of PSNR=8. In this latter scenario, MiSFIT still provides better estimates on the average, but it shows a greater variability depending on the input RTOP. Noticeably, the behavior of MAPL seems to worsen as the number of crossing fiber bundles increases, but MiSFIT behaves just the opposite. Note that, in the presence of several crossing fibers, each of them may have very different diffusion characteristics, which in principle could compromise the accuracy of eq. (5.4). At the sight of this experiment, however, it does not seem a critical issue. In any case, both MAPL and MiSFIT exhibit quite an estable behavior regardless of the PSNR (with the aforementioned exception for PSNR=8), the input RTOP, and the number of crossing fiber bundles with MiSFIT getting the best rMSE values, in the range of 2.5%.

To check how these errors translate to the scalar measurements of interest in EAP imaging, Fig. 5.9 shows respective results for RTOP, RTPP, and RTAP at PSNR=16, which should be compared to those in Fig. 5.6: while RTAP estimates are virtually identical for both MAPL and MiSFIT, MiSFIT provides higher estimates for RTOP and lower for RTPP than MAPL, which is completely consistent with the joint histograms in Fig. 5.6. Besides, the most prominent discrepancies for RTOP appear in the large range of ground truth RTOP, while for RTPP they appear in the middle range, which is also in good agreement with the histogram shifts in Fig. 5.6. Nonetheless, MiSFIT gets closer than MAPL to the ground truth for both RTOP and RTPP, though both estimates are clearly biased (the bias in RTAP is not equally evident). The likely explanation for the latter is that NODDI yields large bandwidth synthetic signals (due to the close-to-zero transverse diffusion of the intra-dendrite component) that cannot be accurately represented by EAP imaging [5.33]. Finally, the MiSFIT estimates for RTOP and RTAP worsen as the number of crossing fibers increase, but they improve for RTPP. This peculiarity suggests that the deviations of the actual signal from eq. (5.4) have a deeper impact at those directions with weaker diffusivities (note RTPP is the integral along the maximum diffusion direction).

MiSFIT vs. MAPL: test-retest evaluation of reliability

The importance of assessing the reliability of a given measurement aimed at describing individual differences has been recently stressed by [5.60]. Reliability can be defined as the portion of variance comprising both actual inter-subject differences and unwanted contaminants, and its theoretical interest relies on the fact that it states an upper bound for the validity, i. e. the fraction of variance corresponding to actual inter-subject differences. We have devised a simple experiment, using subject HCP WU-Minn-139839, to assess the

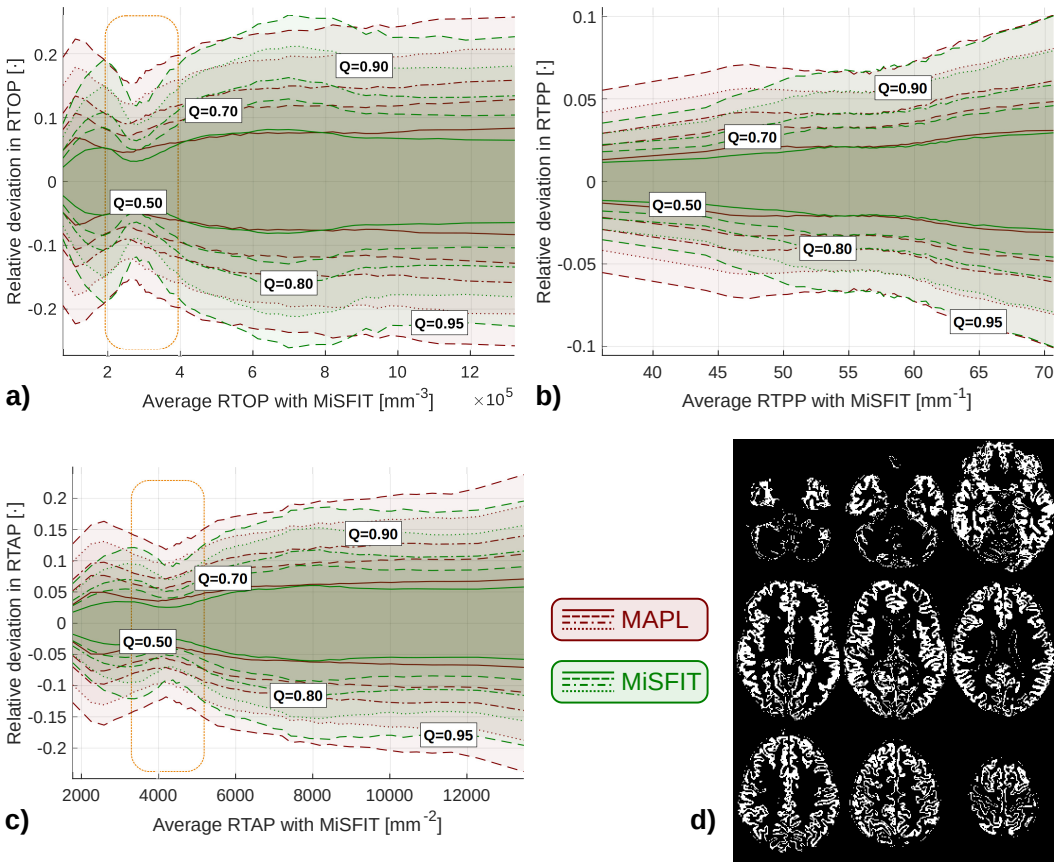

Fig. 5.10.: Reliability of MAPL vs. MiSFIT when computing RTOP (a), RTPP (b), and RTAP (c). The curves represent the relative discrepancies of the scalar indices across the test-retest at voxel clusters defined in terms of each averaged MiSFIT-derived scalar. The anomalous behavior of RTOP and RTAP inside the highlighted windows corresponds to the cortical regions segmented in d).

reliability of MAPL and MiSFIT in terms of the relative discrepancies between test and retest measurements defined as:

$$\delta_{X,\text{method}} = 2\frac{|X_{\text{method}}(\text{test}) - X_{\text{method}}(\text{retest})|}{X_{\text{method}}(\text{test}) + X_{\text{method}}(\text{retest})}, \tag{5.36}$$

where X is one of RTOP, RTPP, or RTAP and 'method' stands for either MAPL or MiSFIT. For each X, the imaged voxels throughout the entire volume are grouped into 100 evenly distributed clusters depending on the average test-retest value obtained with MiSFIT, $(X_{\text{MiSFIT}}(\text{test}) + X_{\text{MiSFIT}}(\text{retest}))/2$. Fig. 5.10 (a–c) shows the 50%, 70%, 80%, 90%, and 95% percentiles of the corresponding $\delta_{X,\text{MAPL}}$ and $\delta_{X,\text{MiSFIT}}$ as a function of the centroid of each aforementioned cluster (the relative deviations are plotted symmetrically since only two test-retest samples are available).

The first thing to notice is the apparent higher reliability of RTPP (b) as compared to RTOP (a) and RTAP (c) despite of its noisier look (see Fig. 5.6). Note the test and retest volumes were not acquired during the same session, so that a potential miss-registration of both volumes is one of the unwanted contaminants that may be present in the experiment. Since

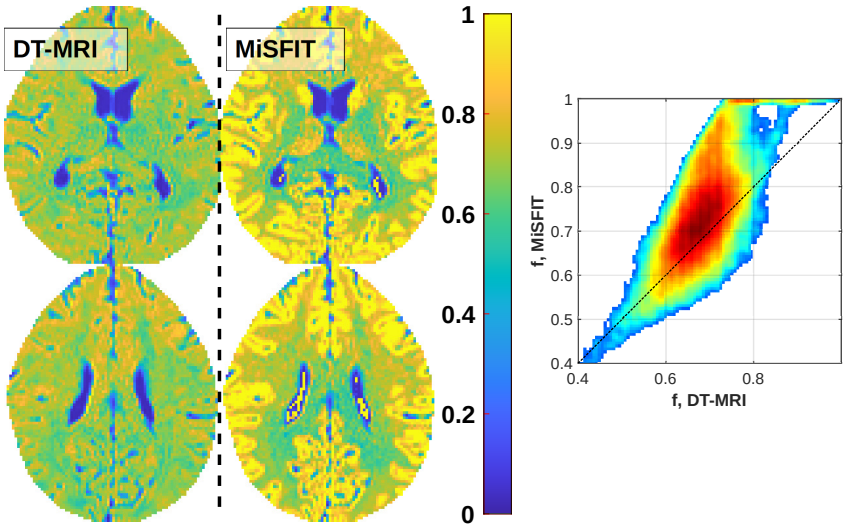

Fig. 5.11.: Inference of the non-free water partial volume fraction with MiSFIT (right-most slices) compared to the *ad hoc* method by [5.58] (left-most slices). The joint histogram refers to the segmented white matter of the whole brain.

RTPP exhibits a much lower local contrast (voxels nearby each other have more similar RTPP than RTOP and RTAP), it is likely that it may better recover from subtle miss-alignments. Next, MAPL and MiSFIT seem to perform approximately the same for all measurements, though MiSFIT consistently beats MAPL for either very large RTOP/RTAP or very small RTPP. According to Fig. 5.6, these are regions corresponding to the most prominent fiber bundles within the white matter. Finally, note that both RTOP and RTAP show an atypical behavior for certain centroids ($2 \cdot 10^5 - 4 \cdot 10^5$ mm^{-3} and $3,500 - 5,000$ mm^{-2}, respectively), for which their reliability notably improves compared to their surrounding values. Fig. 5.10 (d) shows a segmentation of the whole brain based on a raw thresholding of RTOP and RTAP inside these intervals, demonstrating it accurately describes the cortex of the brain: despite EAP imaging mainly focuses on the white matter, its reliability seems to improve inside the gray matter. However, a better reliability does not mean a better validity, since the former is just an upper bound for the latter: once again, the poor local contrast of EAP imaging at the gray matter could likely explain the more predictable behavior at this tissue.

Inference of the non-free water fraction: quantitative evaluation

The inference of the amount of free water at each voxel is an additional capability of our proposal. Fig. 5.11 complements the result in Fig. 5.2 d) with a comparison to the *ad hoc* technique by [5.58]. While the overall structure of the non-free water maps (i. e., f in eq. (5.4)) is comparable for both methods in most of the white matter, MiSFIT strongly differs from the DT-MRI-based method at the gray matter, which we blame on a mismatch of the spherical convolution representation for this tissue. As we have pointed out before, MiSFIT produces corrupted estimates also at the csf due to the ambiguity in the representation. These are the reasons why the joint histograms used for quantitative comparison are restricted to a mask that segments the white matter in each case.

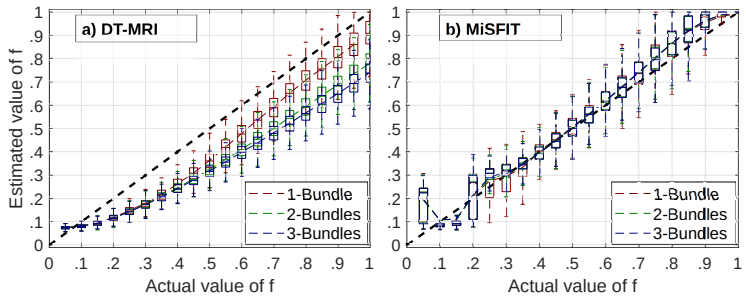

Fig. 5.12.: Quantitative performance of free water estimation in MiSFIT (b) compared to the *ad hoc* method by [5.58] (a). The same sampling scheme and typical peak SNR found at the HCP MGH-1007 volume (16) have been used for the simulations.

These histograms highlight that, while most of the range of f values is similarly estimated by MiSFIT and the DT-MRI method, MiSFIT systematically provides larger estimates for values of f near 1. For a better understanding of this behavior, Fig. 5.12 depicts a simple experiment where we have simulated synthetic voxels as a mixture of either 1, 2, or 3 Gaussian bundles[2] with eigenvalues: λ_1 uniformly distributed within the range $[1.5 \times 10^{-3}, 2 \times 10^{-3}]\,\mathrm{mm}^2/s$, λ_2, λ_3 uniformly distributed within the range $[0.25 \times 10^{-3}, 0.5 \times 10^{-3}]\,\mathrm{mm}^2/s$. The whole ensemble is combined with a free-water isotropic compartment as in eq. (5.4) to generate 1000 realizations for each known value of f. Finally, the signal generated is contaminated with Rician noise for a peak SNR equal to 16. As can be seen, the synthetic experiment is coherent with the visual results in Fig. 5.11 for typical white matter configurations. The DT-MRI-based method systematically under-estimates the amount of confined (non-free) water, f, for almost all the range of inputs. Moreover, its behavior heavily depends on the number of compartments in the voxel, so that in the presence of fiber crossings it becomes less reliable. Conversely, MiSFIT shows the exact same behavior regardless of the number of compartments, probably due to the fact that the spherical averaging removes any dependency with the ODF. For small actual values of f (like those at the csf), however, MiSFIT presents large drifts. Besides, MiSFIT seems to bias the estimate of f towards 1 for high values of the input f, which might explain the saturation of the histograms in Fig. 5.11.

Computational issues

A major strength of MiSFIT relies on its computational efficiency, owing to the fact that the required non-linear optimization involves at most three parameters (f, $\lambda_{\parallel}$, and $\lambda_{\perp}$). Fig. 5.13 depicts a summary of the computation times spent on the analysis of subject HCP MGH-1007 (the background of the image, including the skull, was removed with a mask). All the experiments were run in a laptop equipped with a quad-core Intel© Core™ i7-6500U processor and 8GB RAM. MiSFIT was completely written for Matlab® R2019b[3] running on Kubuntu Linux 19.10, with parallel implementations for the slowest parts. For comparison purposes, MAPL was run in the same machine using the python-dipy package for Python 3.8, which is also mostly parallel.

[2] We choose a simpler model in this experiment because the method by [5.58] is intended for DT-MRI, hence it cannot cope with slow decaying tails of the attenuation signal.

[3] Code available at: `https://www.lpi.tel.uva.es/node/848`

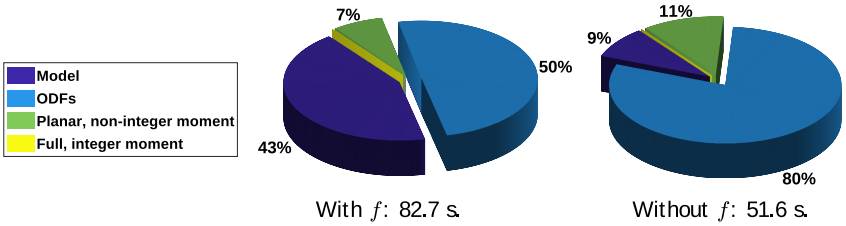

Fig. 5.13.: Computation times required to process the (masked) volume HCP MGH-1007 either (left) or not (right) estimating the non-free water compartment f. Overall execution times refer to a Matlab® coded parallel implementation.

MiSFIT takes tens of seconds to process an entire (masked) volume including kernel estimation, ODFs reconstruction, and computing several moments. Computing the ODFs field is the slowest part, and it takes 50% to 80% of the time. Note the additional estimation of the non-free water compartment for the composite representation in eq. (5.4), compared to the simpler one in eq. (5.1), increases the computation time in roughly 30 seconds. It is worth noticing that the computation of different kinds of moments takes very different amounts of time: planar moments, compared to full moments, require the additional computation of the maximum diffusion direction and additional operations on the SH coefficients; non-integer (including inverse) moments, compared to integer moments, require the explicit computation of Gaussian hypergeometric functions, see Appendix 5.C.

Comparing to MAPL, an analogous analysis takes 80 minutes in case anisotropic weighting is used or 45 minutes otherwise for a fixed value of the Laplacian penalty (i. e. without using generalized cross-validation). In case positivity constraints are enforced, the computation time grows up to nearly 9 hours. Additionally, the more accurate anisotropic weighting technique does not provide ODFs estimates, so that both methods (isotropic and anisotropic) should be run in parallel to simultaneously obtain optimum estimates of moments and ODFs fields.

5.6 Discussion and conclusions

Multi-shell acquisitions are breaking up as a new standard for advanced computational dMRI, far more popular than DSI-like protocols. With this in mind, we have devised a specific approach for EAP imaging of the white matter based on multi-shells. The first noticeable advantage of MiSFIT is its time efficiency: processing a typical volume end-to-end may take in the order of one minute (instead of few hours) in a regular laptop, which makes it appealing for the processing of large clinical databases or even for its implementation in scanner consoles. The keystone of MiSFIT is the decoupling of the radial (variable q) and the angular (variable $\mathbf{u}$) behaviors owing to the SM technique [5.28]: the non-linear estimation of the adaptive convolution kernel involves at most 3 parameters (f, $\lambda_{\parallel}$, and $\lambda_{\perp}$), which can even reduce to 2 ($\lambda_{\parallel}$ and $\lambda_{\perp}$) in case the simplified representation in eq. (5.1) is used. The inference of the ODF at each voxel reduces to a linear LS problem. Compared to methods like MAPL by [5.42], the latter must fit a whole 3-D basis, which is computationally intensive even with parallel computing.

Moreover, since MiSFIT is specifically devised for multi-shell acquisitions (typically comprising 2-4 shells), this is somehow optimal: the radial behavior of the signal is characterized by the convolution kernel (elemental tensor), so that 2-4 radial samples are used to fit 3 parameters (2 for the simplified representation). On the other hand, the orientations space, which is densely sampled in multi-shell acquisitions, is still non-parametric. As opposed, regular EAP imaging techniques are fully non-parametric, implying that 2-4 radial samples must be used to fit a larger number of DOF with the help of regularization or sparsity constraints. Its specific design for multi-shell acquisitions has the additional advantage of making MiSFIT well suited for already existing protocols and public databases [5.20, 5.21].

Although the computation of the EAP based on a convolution sum inferred from spherical means has been suggested by [5.29, 5.28, 5.54], the main novelty of our work relies on its formalization to an efficient framework for the description of the diffusion process based on analytical generalized moments. Nonetheless, the computation of moments of high orders is often problematic with noisy signals: a ν-th order moment over P is related to the ν-th order derivative of E (and vice-versa), which makes it impractical to compute moments with $\nu > 2$ (related to derivatives of higher orders than the Laplacian). MiSFIT grants a compromise solution by describing non-integer (including inverse) moments that correspond to fractional derivatives in the dual domain, either as a 3-D average, along a given direction, or over a plane perpendicular to such direction. This framework provides the means to enhance different diffusion properties (i. e. to reveal different tissue contrasts) at will meanwhile using low order moments to avoid noise amplification: inverse (i. e. negative) moments over P will overweight the values of P near $\mathbf{R} = \mathbf{0}$, thus enhancing proximal diffusion features. On the contrary, direct (i. e. positive) moments over P will assign heavier weights to those values of P farther from the origin, hence enhancing distal diffusion features. As a consequence, the kind of contrast achieved with either $\nu \leq 0$ or $\nu \geq 0$ is completely different. An analogous reasoning applies to those moments computed over E: while $\nu \leq 0$ seems to provide better white matter contrast for P-moments, $\nu \geq 0$ seems more appropriate for E-moments.

The so-called full moments collapse to a function of just the three kernel parameters f, $\lambda_{\parallel}$, and $\lambda_{\perp}$, which makes it questionable if the computation of full moments of arbitrary orders, under our convolution representation, is useful at all beyond a contrast enhancement of these three features. Axial and planar moments, on the contrary, involve the entire representation including the ODF, so that moments of different orders will actually encode different pieces of information. We have considered the maximum diffusion direction for axial and planar moments in all cases, but MiSFIT can equally compute generic moments for any other direction or set of directions. This idea has been already suggested by [5.42]: with the notation used in the present paper, $\upsilon_a^2(\mathbf{r})$, $\forall \mathbf{r} \in \mathcal{S}$ represents an Orientation Probability Density Function (OPDF) as introduced by [5.61, 5.62]. For any other $\nu \neq 2$, $\upsilon_a^\nu(\mathbf{r})$ can be seen as a contrast-enhanced OPDF that can be used to better resolver fiber crossings.

Among the set of generic moments that can be computed, the RTOP, the RTPP, and the RTAP deserve a special attention due to their widespread use in clinical dMRI studies. The quantitative evaluation of MiSFIT as compared to MAPL might suggest the better performance of the former for a wide range of scenarios. However, we have to be careful with the interpretation of such results. First, MAPL is not specifically intended for multi-shell samplings. Since it is non-parametric, we should expect its performance to notably improve with more appropriate sampling schemes (i. e. acquiring more samples at more shells),

which is not necessarily the case for MiSFIT, whose theoretical limit will arise from the deviations of the convolution representation from the true signal.

On the other hand, EAP imaging represents low-pass versions of the diffusion process due to the bandwidth limitation imposed by the maximum b-value acquired. Actual diffusion models, on the contrary, produce infinite-bandwidth signals with heavy tails for $E(\mathbf{q})$ at any direction $\mathbf{u} = \|\mathbf{q}\|$, coming from the contributions of the intra-axonal responses of all the fiber-bundles within the plane orthogonal to $\mathbf{u}$. As a result, the outcomes of both two methodologies cannot be directly compared, since the scalar moments defined as improper integrals over the whole 3-D domain will always become infinite for any true model of diffusion [5.33]. In order to design ground-truth signals, we have overcome this pitfall by modifying the NODDI model to obtain responses with far larger bandwidths than those provided by EAP imaging approaches but still light-tailed. Accordingly, the numerical results reported above do not necessarily mean that MiSFIT is more accurate than MAPL compared to *reality*, but instead they suggest MiSFIT provides descriptions of the white matter with a broader bandwidth than MAPL for a comparable robustness to noise and with a slightly better reliability.

Regarding the estimation of free water, $1-f$, MiSFIT seems accurate at the white matter, but its behavior is not consistent at the gray matter or the csf. As long as we pursue obtaining and/or generalizing scalar indices most usually employed to analyze the white matter, this is generally acceptable. Otherwise, the simpler eq. (5.1) should be used to avoid the ambiguity of eq. (5.4) when $\lambda_\perp \simeq \lambda_\parallel$.

With respect to the limitations of MiSFIT, the use of Funk-Hecke's theorem is a central point to our developments, meaning that representing orientation functions in a basis related to SH is a must. In our experimental set-up, the maximum order of the expansions has been cropped to $L = 8$ in all cases, which entails a well-known issue with high-frequency pruning and ringing artifacts. On the other hand, we have not enforced positivity constraints on the EAP, whose convenience has been recently stressed by [5.63]. Both two issues could be simultaneously addressed with a similar idea as in [5.64], where SH are substituted with Spherical Wavelets (SW) on a non-negative LS problem. Since SW are infinite linear superpositions of SH they are not prone to the ringing artifact, at the same time they allow for similar mathematical developments based on Funk-Hecke's theorem.

The definition of the convolution kernel as a tensor adapted to the micro-structure of the voxel is a key point in MiSFIT as well. Any deviation of actual white matter data from this representation (e. g. two crossing fiber tracts with very different pore characteristics) might turn into a source of inaccuracies. However, the quantitative evaluation with synthetic data has demonstrated this is not an issue in practice, at least in what respects to the computation of moments. Given the limited amount of radial information, a Gaussian convolution is indeed a reasonable 'universal approximator' to fit eq. (5.26). In this scenario, $\Phi(\mathbf{r})$ represents the linear coefficients of the approximator, so that the deviations from the MiSFIT convolution sum will likely translate to miss-representations of the ODF. In what concerns the gray matter, the spherical convolution is not necessarily a good approximator, so the applicability of MiSFIT to such tissues is at stake.

To conclude the comparison with other EAP imaging techniques (MAP-MRI, MAPL, RBFs, mq-DPI, BFOR, *etcetera*), it is fair to say that MiSFIT is only applicable to multi-shell samplings, while the former are sampling-independent and therefore they can work as well with DSI

or CS-oriented data. The experiments reported evidence that MiSFIT is useful in the same range of b-values most usually acquired for EAP imaging, i. e. up to 5,000 s/mm^2, though we have not tested it for special data sets with stronger diffusion gradients (e. g. 10,000 s/mm^2). The range of diffusion times for which the parameters suggested apply should be further investigated as well.

Finally, testing the usefulness of the proposed moments as potential biomarkers for the description of illnesses like Alzheimer's or Parkinson's disease [5.65, 5.66] through white matter analysis is an open field for research. Additionally, the possibility of generalizing standard RTPP or RTAP to moments computed over arbitrary directions offers a wide range of new ways to combine computational dMRI with fiber tracking approaches.

Acknowledgments

This work was supported by the Ministerio de Ciencia e Innovación of Spain with research grant RTI2018-094569-B-I00.

Data collection and sharing for this project was partially provided by the *Human Connectome Project*, `https://ida.loni.usc.edu/login.jsp` (HCP; Principal Investigators: Bruce Rosen, M.D., Ph.D., Martinos Center at Massachusetts General Hospital, Arthur W. Toga, Ph.D., University of Southern California, Van J. Weeden, MD, Martinos Center at Massachusetts General Hospital). HCP funding was provided by the National Institute of Dental and Craniofacial Research (NIDCR), the National Institute of Mental Health (NIMH), and the National Institute of Neurological Disorders and Stroke (NINDS). HCP is the result of efforts of co-investigators from the University of Southern California, Martinos Center for Biomedical Imaging at Massachusetts General Hospital (MGH), Washington University, and the University of Minnesota. HCP data are disseminated by the Laboratory of Neuro Imaging at the University of Southern California.

Data were also provided in part by the Human Connectome Project, WU-Minn Consortium (Principal Investigators: David Van Essen and Kamil Ugurbil; 1U54MH091657) funded by the 16 NIH Institutes and Centers that support the NIH Blueprint for Neuroscience Research; and by the McDonnell Center for Systems Neuroscience at Washington University.

Appendices

5.A Fitting the adaptive convolution kernel

The minimization problem in eq. (5.20) is solved with a modified gradient-projection algorithm [5.67] that ensures the proposed solution belongs to the 3-D feasible region Ω

Inputs: $\{\widehat{E}(q_i), b_i\}_{i=1}^{N_s}$, D_{iso}, μ, τ_0, Δ, M
Outputs: f, $\lambda_\perp$, $\lambda_\parallel$

```
1  Find x_0 = [f_0, λ_⊥,0, δ_λ,0]^T ∈ Ω
2  for n = 0, ..., M − 1
3    Compute: d, J_C, J_P, H_P at x_n
4    Compute τ as in eq. (5.40)
5    Compute x_n+1 as in eq. (5.39)
6    if x_n ∈ ∂Ω and x_n+1 ∉ Ω
7      Compute τ as in eq. (5.42)
8      Compute P as in eq. (5.43)
9      Compute x_n+1 as in eq. (5.41)
10   end if
11   if x_n+1 ∉ Ω
12     x_n+1 = closest x'_n+1 ∈ ∂Ω
13   end if
14   if C(x_n+1) < C(x_n)
15     if ||x_n+1 − x_n|| < Δ
16       BREAK and go to line 24
17     end if
18     τ_0 = τ_0/10
19   else
20     Revert: x_n+1 = x_n
21     τ_0 = 10 τ_0
22   end if
23 end for
24 f = f_n+1, λ_⊥ = λ_⊥,n+1, λ_∥ = λ_⊥ + δ_λ,n+1
```

Tab. 5.2.: Optimization algorithm used to estimate the parameters of the convolution kernel.

whose frontier $\partial\Omega$ is defined by the linear constraints. In precise terms, we rewrite the cost function as:

$$\begin{aligned} C(f, \lambda_\perp, \delta_\lambda) &= \frac{1}{2}\sum_{i=1}^{N_s}\left(\widehat{\mathcal{E}}_{l,i}(f) + b_i\,\lambda_\perp + F(b_i\,\delta_\lambda)\right)^2 + \mu\,P(\lambda_\perp, \delta_\lambda) \\ &= \frac{1}{2}\sum_{i=1}^{N_s} d_i^2\,(f, \lambda_\perp, \delta_\lambda) + \mu\,P(\lambda_\perp, \delta_\lambda), \end{aligned} \tag{5.37}$$

where $\widehat{\mathcal{E}}_{l,i}(f) = \log\left(\left(\widehat{E}_c(q_i) - (1-f)\exp(-b_i\,D_{\text{iso}})\right)/f\right)$, $F(z) = \log\left(2\sqrt{z}/\sqrt{\pi}\text{erf}(\sqrt{z})\right)$, and $P(\lambda_\perp, \delta_\lambda) = \lambda_\perp/\delta_\lambda$. The 3×1 gradient of this cost function reads:

$$\nabla C = \begin{bmatrix} \widehat{\mathcal{E}}'_{l,1} & \dots & \widehat{\mathcal{E}}'_{l,N_s} \\ b_1 & \dots & b_{N_s} \\ b_1\,F' & \dots & b_{N_s}\,F' \end{bmatrix} \begin{bmatrix} d_1 \\ \vdots \\ d_{N_s} \end{bmatrix} + \mu \begin{bmatrix} 0 \\ \partial P/\partial\lambda_\perp \\ \partial P/\partial\delta_\lambda \end{bmatrix} = \mathbf{J}_C\,\mathbf{d} + \mu\mathbf{J}_P. \tag{5.38}$$

We aim at finding configurations for which the gradient becomes null. Far from the frontier $\partial\Omega$, we use Newton's-like iterations:

$$\mathbf{x}_{n+1} - \mathbf{x}_n = -\left(\mathbf{J}_C\mathbf{J}_C^T + \mu\mathcal{H}_P + \tau\mathbf{I}_3\right)^{-1}\left(\mathbf{J}_C\mathbf{d} + \mu\mathbf{J}_P\right), \tag{5.39}$$

where $\mathbf{x} = [f, \lambda_\perp, \delta_\lambda]^T$, $\mathcal{H}_P$ is the 3×3 Hessian of the penalty $P(\lambda_\perp, \delta_\lambda)$, and τ is an adaptive parameter used to fix convergence issues ($\mathbf{I}_d$ stands for the $d \times d$ identity matrix):

$$\tau = \tau_0 \,\text{trace}\left(\mathbf{J}_C\mathbf{J}_C^T + \mu\mathcal{H}_P\right). \tag{5.40}$$

When the current iteration $\mathbf{x}_n$ belongs to the frontier $\partial\Omega$, it is likely that the update in eq. (5.39) will point outside the feasible region Ω, so that it has to be projected [5.67]:

$$\mathbf{x}_{n+1} - \mathbf{x}_n = -\mathbf{P}^T\left(\mathbf{P}\mathbf{J}_C\mathbf{J}_C^T\mathbf{P}^T + \mu\mathbf{P}\mathcal{H}_P\mathbf{P}^T + \tau\mathbf{I}_2\right)^{-1}\mathbf{P}\left(\mathbf{J}_C\mathbf{d} + \mu\mathbf{J}_P\right); \tag{5.41}$$

$$\tau = \tau_0 \,\text{trace}\left(\mathbf{P}\mathbf{J}_C\mathbf{J}_C^T\mathbf{P}^T + \mu\mathbf{P}\mathcal{H}_P\mathbf{P}^T\right), \tag{5.42}$$

where $\mathbf{P}$ is a 2×3 projection matrix that can be derived from the constraints in eq. (5.20):

$$\begin{array}{cccc} f = f_0 \text{ or } f = 1: & \lambda_\perp = 0: & \delta_\lambda = 0: & \lambda_\perp + \delta_\lambda = D_{\text{iso}}: \\ \mathbf{P} = \begin{bmatrix} 0 & 1 & 0 \\ 0 & 0 & 1 \end{bmatrix}; & \mathbf{P} = \begin{bmatrix} 1 & 0 & 0 \\ 0 & 0 & 1 \end{bmatrix}; & \mathbf{P} = \begin{bmatrix} 1 & 0 & 0 \\ 0 & 1 & 0 \end{bmatrix}; & \mathbf{P} = \begin{bmatrix} 1 & 0 & 0 \\ 0 & 1 & -1 \end{bmatrix}. \end{array} \tag{5.43}$$

The final algorithm is sketched in Table 5.2.

5.B Computing the convolution weights to estimate the ODFs

From eqs. (5.23) and (5.24), we aim at computing, for any $b = 4\pi^2\tau q^2$:

$$\hat{e}_l^{\text{ODF}}(q) = 2\pi\exp\left(-b\lambda_\perp\right)\int_{-1}^{1}\exp\left(-b\,\delta_\lambda\,x^2\right)P_l(x)\,dx. \tag{5.44}$$

Obviating the constant $2\pi\exp\left(-b\lambda_\perp\right)$, a well-known property of Legendre polynomials allows us to compute:

$$\begin{aligned} &\int_{-1}^{1}\exp\left(-b\,\delta_\lambda\,x^2\right)P_l(x)dx = \int_{-1}^{1}\exp\left(-b\,\delta_\lambda\,x^2\right)\frac{(2l-1)xP_{l-1}(x) - (l-1)P_{l-2}(x)}{l}dx \\ = \;& \frac{2l-1}{l}\int_{-1}^{1}\exp\left(-b\,\delta_\lambda\,x^2\right)xP_{l-1}(x)dx - \frac{l-1}{l}\int_{-1}^{1}\exp\left(-b\,\delta_\lambda\,x^2\right)P_{l-2}(x)dx, \end{aligned} \tag{5.45}$$

where the second term is proportional to the integral for the previous even degree, $l-2$. For the first term, we can use the differentiation property of Legendre polynomials; for each odd $l \geq 3$:

$$\begin{aligned} &\int_{-1}^{1}\exp\left(-b\,\delta_\lambda\,x^2\right)P_{l-1}(x)dx = \int_{-1}^{1}\exp\left(-b\,\delta_\lambda\,x^2\right)\frac{d}{dx}\frac{P_l(x) - P_{l-2}(x)}{2l-1}dx \\ = \;& \cancel{\exp\left(-b\,\delta_\lambda\,x^2\right)\frac{P_l(x) - P_{l-2}(x)}{2l-1}\Bigg]_{-1}^{1}} + \frac{2b\,\delta_\lambda}{2l-1}\int_{-1}^{1}\exp\left(-b\,\delta_\lambda\,x^2\right)\left(xP_l(x) - xP_{l-2}(x)\right)dx, \end{aligned} \tag{5.46}$$

since all even Legendre polynomials have value 1 at $x = \pm 1$. Developing on the previous result, we can obtain the first term in eq. (5.45) as:

$$\int_{-1}^{1} \exp\left(-b\,\delta_\lambda\,x^2\right) xP_l(x)dx = \frac{2l-1}{2b\,\delta_\lambda}\int_{-1}^{1} \exp\left(-b\,\delta_\lambda\,x^2\right) P_{l-1}(x)dx + \int_{-1}^{1} \exp\left(-b\,\delta_\lambda\,x^2\right) xP_{l-2}(x)dx \quad (5.47)$$

Combining the previous results, Table 5.3 shows a recursive rule to compute the desired integrals for any degree (the results for 0 and 1 were explicitly computed with symbolic calculus software).

l	$\hat{e}_l^{\text{ODF}}(q)$ (l even)	$r_l(q)$ (l odd)
0 / 1	$\frac{2\pi^{3/2}}{\sqrt{b\,\delta_\lambda}}\exp(-b\lambda_\perp)\text{erf}\left(\sqrt{b\,\delta_\lambda}\right)$	$2\pi\exp\left(-b\lambda_\perp\right)\left(\frac{\sqrt{\pi}\,\text{erf}\left(\sqrt{b\,\delta_\lambda}\right)}{2\sqrt{(b\,\delta_\lambda)^3}} - \frac{\exp\left(-b\,\delta_\lambda\right)}{b\,\delta_\lambda}\right)$
≥ 2 / ≥ 3	$\hat{e}_l^{\text{ODF}}(q) = \frac{2l-1}{l}r_{l-1}(q) - \frac{l-1}{l}\hat{e}_{l-2}^{\text{ODF}}(q)$	$r_l(q) = \frac{l-1/2}{b\,\delta_\lambda}\,\hat{e}_{l-1}^{\text{ODF}}(q) + r_{l-2}(q)$

Tab. 5.3.: Recursive rule to compute the convolution factors for the ODFs, $\hat{e}_l^{\text{ODF}}(q)$.

5.C Efficiently computing $\iota_\gamma^n(z)$

We aim at calculating:

$$\iota_\gamma^n(z) = \int_{-1}^{1} \frac{x^{2n}}{\left(1 + x^2/z\right)^{\frac{\gamma}{2}}}dx = \frac{1}{n+1/2}\,{}_2F_1\left(n+\frac{1}{2},\frac{\gamma}{2};n+\frac{3}{2};\frac{-1}{z}\right). \quad (5.48)$$

This result can be checked with any software for symbolic calculus. Though eq. (5.48) provides a closed form in terms of hypergeometric Gaussian functions, its general calculation is computationally intensive and often inaccurate. Instead, we use the recursive rules described by [5.68] to reckon the integrals for any $n \geq 1$ up from $n = 0$:

$$\iota_\gamma^n(z) = \frac{z}{n + \frac{1}{2} - \frac{\gamma}{2}}\left(\left(\frac{z}{z+1}\right)^{\frac{\gamma}{2}-1} - \left(n - \frac{1}{2}\right)\iota_\gamma^{n-1}(z)\right). \quad (5.49)$$

For the special case $n = \frac{\gamma}{2} - \frac{1}{2}$ ($\gamma \in \mathbb{Z}$, $\gamma > 1$), an alternative expression must be used:

$$\iota_\gamma^{\frac{\gamma}{2}-\frac{1}{2}}(z) = \frac{-2z}{\gamma-2}\left(\frac{z}{z+1}\right)^{\frac{\gamma}{2}-1} + z\,\iota_{\gamma-2}^{\frac{\gamma}{2}-\frac{3}{2}}(z). \quad (5.50)$$

The algorithm completes with the computation of the initial terms for $n = 0$. In this case, a recursion for $\gamma \in \mathbb{Z}$ is used [5.68]:

$$\iota_{\gamma+2}^0(z) = \frac{2}{\gamma}\left(\frac{z}{1+z}\right)^{\frac{\gamma}{2}} - \frac{1-\gamma}{\gamma}\iota_\gamma^0(z). \quad (5.51)$$

Inputs: $\gamma \in \mathbb{R}^+ \backslash \{0\}$,
$0 < \lambda_\perp \leq \lambda_\parallel \leq D_{\text{iso}}$
Outputs: $\{\iota_\gamma^n(z)\}_{n=0}^{L/2}$, $L \in \mathbb{Z}$, even,
$L \geq 0$

---

1 Compute $z = \rho_\lambda = \frac{\lambda_\perp}{\lambda_\parallel - \lambda_\perp}$ or $z = -\kappa_\lambda = -\frac{\lambda_\parallel}{\lambda_\parallel - \lambda_\perp}$
2 if $\gamma \in \mathbb{Z}$
3 $\quad \iota_0^0(z) = 2$
4 $\quad \iota_1^0(z) = 2\sqrt{z}\,\operatorname{acsch}\left(\sqrt{z}\right)$ or $2\sqrt{-z}\,\operatorname{acsc}\left(\sqrt{-z}\right)$
5 $\quad \iota_2^0(z) = 2\sqrt{z}\,\operatorname{acot}\left(\sqrt{z}\right)$ or $2\sqrt{-z}\,\operatorname{acoth}\left(\sqrt{-z}\right)$
6 $\quad$ for g from (1 or 2) until $g = \gamma$, 2 by 2:
7 $\quad\quad \iota_g^0(z) = \frac{2}{g-2}\left(\frac{z}{1+z}\right)^{\frac{g-2}{2}} - \frac{3-g}{g-2}\,\iota_{g-2}^0(z)$
8 $\quad$ end for
9 else
10 $\quad \iota_\gamma^0(z) = 2\,{}_2F_1\left(\frac{1}{2}, \frac{\gamma}{2}; \frac{3}{2}; \frac{-1}{z}\right)$
11 end if
12 for $n = 1, 2, \ldots, L/2$
13 $\quad$ if $\gamma \in \mathbb{Z}$ is odd, $\gamma \geq 3$, and $n = \frac{\gamma}{2} - \frac{1}{2}$
14 $\quad\quad$ Compute $\iota_1^0(z)$ as in line 4
15 $\quad\quad$ for g from 3 until $g = \gamma$, 2 by 2
16 $\quad\quad\quad \iota_g^{\frac{g}{2}-\frac{1}{2}}(z) = \frac{-2z}{g-2}\left(\frac{z}{1+z}\right)^{\frac{g}{2}-1} + z\,\iota_{g-2}^{\frac{g}{2}-\frac{3}{2}}(z)$
17 $\quad\quad$ end for
18 $\quad$ else
19 $\quad\quad \iota_\gamma^n(z) = \frac{z}{n+\frac{1}{2}-\frac{\gamma}{2}}\left(\left(\frac{z}{z+1}\right)^{\frac{\gamma}{2}-1} - \left(n - \frac{1}{2}\right)\iota_\gamma^{n-1}(z)\right)$
20 $\quad$ end if
21 end for

Tab. 5.4.: Recursive algorithm to efficiently compute $\iota_\gamma^n(z)$.

Finally, the values for the first $\gamma \in \mathbb{Z}$ and $n = 0$ may be analytically computed:

$$\begin{aligned}
\gamma = 0: &\qquad \iota_0^0(z) = 2; \\
\gamma = 1: &\quad \iota_1^0(z) = 2\sqrt{z}\,\operatorname{acsch}\left(\sqrt{z}\right) = 2\sqrt{-z}\,\operatorname{acsc}\left(\sqrt{-z}\right); \\
\gamma = 2: &\quad \iota_2^0(z) = 2\sqrt{z}\,\operatorname{acot}\left(\sqrt{z}\right) = 2\sqrt{-z}\,\operatorname{acoth}\left(\sqrt{-z}\right).
\end{aligned} \tag{5.52}$$

For $\gamma \notin \mathbb{Z}$, we have to explicitly evaluate ${}_2F_1\left(\frac{1}{2}, \frac{\gamma}{2}; \frac{3}{2}; \frac{1}{z}\right)$. However, since this expression is just the term for $n = 0$, it remains well-behaved and can be efficiently reckoned with accuracy. A summary of the algorithm used to compute $\iota_\gamma^n(z)$ is outlined in Table 5.4.

Bibliography

[5.1] P.J. Basser and C. Pierpaoli. Microstructural and physiological features of tissues elucidated by Quantitative–Diffusion–Tensor MRI. *Journal of Magnetic Resonance*, 111(3):209–219, June 1996.

[5.2] E.-O. Stejskal and J.-E. Tanner. Spin diffusion measurements: Spin echoes in the presence of a time-dependent field gradient. *Journal of Chemical Physics*, 42:288–292, 1965.

[5.3] C.-F. Westin, S.E. Maier, H. Mamata, A. Nabavi, F.A. Jolesz, and R. Kikinis. Processing and visualization for diffusion tensor MRI. *Medical Image Analysis*, 6:93–108, 2001.

[5.4] Murat Aksoy, Chunlei Liu, Michael Moseley, and Roland Bammer. Single-step nonlinear diffusion tensor estimation in the presence of microscopic and macroscopic motion. *Magnetic resonance in Medicine*, 59:1138–1150, 05 2008.

[5.5] Pablo Casaseca-de-la-Higuera, Antonio Tristán-Vega, Santiago Aja-Fernández, Carlos Alberola-López, Carl-Fredrik Westin, and Raúl San-José-Estépar. Optimal real-time estimation in diffusion tensor imaging. *Magnetic Resonance Imaging*, 30(4):506–517, 2012.

[5.6] B. Landman, P.-L. Bazin, J. Prince, and J. Hopkins. Diffusion tensor estimation by maximizing Rician likelihood. In *Procs. of IEEE 11th International Conference on Computer Vision*, pages 1–8, October 2007.

[5.7] Cyril Poupon, Alexis Roche, Jessica Dubois, Jean-François Mangin, and Fabrice Poupon. Real-time MR diffusion tensor and Q-ball imaging using Kalman filtering. *Medical Image Analysis*, 12(5):527–534, 2008.

[5.8] R. Salvador, A. Peña, D.-K. Menon, T.-A. Carpenter, J.-D. Pickard, and E.-T. Bullmore. Formal characterization and extension of the linearized diffusion tensor model. *Human Brain Mapping*, 24:144–155, 2005.

[5.9] B.W. Kreher, J.F. Schneider, I. Mader, E. Martin, J. Henning, and K.A. Il'yasov. Multitensor approach for analysis and tracking of complex fiber configurations. *Magnetic Resonance in Medicine*, 54(5):1216–1225, September 2005.

[5.10] S. Peled, O. Friman, F.A. Jolesz, and C.-F. Westin. Geometrically constrained two–tensor model for crossing tracts in DWI. *Magnetic Resonance in Medicine*, 24(9):1263–1270, 2006.

[5.11] David S. Tuch, Timothy G. Reese, Mette R. Wiegell, Nikos Makris, John W. Belliveau, and Van J. Wedeen. High angular resolution diffusion imaging reveals intravoxel white matter fiber heterogeneity. *Magnetic Resonance in Medicine*, 48(4):577–582, 2002.

[5.12] D.S. Tuch, T.G. Reese, M.R. Wiegell, and V.J. Wedeen. Diffusion MRI of complex neural architecture. *Neuron*, 40:885–895, 2003.

[5.13] Haz-Edine Assemlal, David Tschumperlé, Luc Brun, and Kaleem Siddiqi. Recent advances in diffusion MRI modeling: Angular and radial reconstruction. *Medical Image Analysis*, 15(4):369–396, 2011.

[5.14] V.J. Wedeen, P. Hagmann, W.-Y.I. Tseng, T.G. Reese, and R.M. Weisskoff. Mapping complex tissue architecture with diffusion spectrum imaging. *Magnetic Resonance in Medicine*, 54:1377–1386, 2005.

[5.15] D. L. Donoho. Compressed sensing. *IEEE Transactions on Information Theory*, 52(4):1289–1306, 2006.

[5.16] Marion I. Menzel, Ek T. Tan, Kedar Khare, Jonathan I. Sperl, Kevin F. King, Xiaodong Tao, Christopher J. Hardy, and Luca Marinelli. Accelerated diffusion spectrum imaging in the human brain using compressed sensing. *Magnetic Resonance in Medicine*, 66(5):1226–1233, 2011.

[5.17] Berkin Bilgic, Kawin Setsompop, Julien Cohen-Adad, Anastasia Yendiki, Lawrence L. Wald, and Elfar Adalsteinsson. Accelerated diffusion spectrum imaging with compressed sensing using adaptive dictionaries. *Magnetic Resonance in Medicine*, 68(6):1747–1754, 2012.

[5.18] Robert J Young, Ek T Tan, Kyung K Peck, Mehrnaz Jenabi, Sasan Karimi, Nicole Brennan, Jennifer Rubel, John Lyo, Weiji Shi, Zhigang Zhang, Marcel Prastawa, Xiaofeng Liu, Jonathan I Sperl, Robin Fatovic, Luca Marinelli, and Andrei I. Holodny. Comparison of compressed sensing diffusion spectrum imaging and diffusion tensor imaging in patients with intracranial masses. *Magnetic Resonance Imaging*, 36:24–31, 2017.

[5.19] Qiuyun Fan, Thomas Witzel, Aapo Nummenmaa, Koene R.A. Van Dijk, John D. Van Horn, Michelle K. Drews, Leah H. Somerville, Margaret A. Sheridan, Rosario M. Santillana, Jenna Snyder, Trey Hedden, Emily E. Shaw, Marisa O. Hollinshead, Ville Renvall, Roberta Zanzonico, Boris Keil, Stephen Cauley, Jonathan R. Polimeni, Dylan Tisdall, Randy L. Buckner, Van J. Wedeen, Lawrence L. Wald, Arthur W. Toga, and Bruce R. Rosen. MGH–USC Human Connectome Project datasets with ultra-high b-value diffusion MRI. *NeuroImage*, 124:1108–1114, 2016.

[5.20] Bruce Rosen, Arthur W. Toga, and Van J. Wedeen. The NIH Human Connectome Project data base, 2020. Authors listed are the Principal Investigators of the HCP project. Last visited: 2020/04/01.

[5.21] David C. Van Essen, Stephen M. Smith, Deanna M. Barch, Timothy E.J. Behrens, Essa Yacoub, and Kamil Ugurbil. The WU-Minn Human Connectome Project: An overview. *NeuroImage*, 80:62–79, 2013.

[5.22] Erik Ziegler, Maud Rouillard, Elodie André, Tim Coolen, Johan Stender, Evelyne Balteau, Christophe Phillips, and Gaëtan Garraux. Mapping track density changes in nigrostriatal and extranigral pathways in Parkinson's disease. *Neuroimage*, 99:498–508, 2014.

[5.23] Yaniv Assaf and Peter J. Basser. Composite hindered and restricted model of diffusion (CHARMED) MR imaging of the human brain. *NeuroImage*, 27(1):48–58, 2005.

[5.24] Yaniv Assaf, T. Blumenfeld-Katzir, and Peter J. Basser. Axcaliber: a method for measuring axon diameter distribution from diffusion mri. *Magnetic Resonance in Medicine*, 59:1347–1354, 2008.

[5.25] Hui Zhang, Torben Schneider, Claudia A. Wheeler-Kingshott, and Daniel C. Alexander. NODDI: Practical in vivo neurite orientation dispersion and density imaging of the human brain. *NeuroImage*, 61(4):1000–1016, 2012.

[5.26] Maira Tariq, Torben Schneider, Daniel C. Alexander, Claudia A. Gandini Wheeler-Kingshott, and Hui Zhang. Bingham–NODDI: Mapping anisotropic orientation dispersion of neurites using diffusion MRI. *NeuroImage*, 133:207–223, 2016.

[5.27] Ben Jeurissen, Jacques-Donald Tournier, Thijs Dhollander, Alan Connelly, and Jan Sijbers. Multi-tissue constrained spherical deconvolution for improved analysis of multi-shell diffusion MRI data. *NeuroImage*, 103:411–426, 2014.

[5.28] Enrico Kaden, Frithjof Kruggel, and Daniel C. Alexander. Quantitative mapping of the per-axon diffusion coefficients in brain white matter. *Magnetic Resonance in Medicine*, 75(4):1752–1763, 2016.

[5.29] Enrico Kaden, Nathaniel D. Kelm, Robert P. Carson, Mark D. Does, and Daniel C. Alexander. Multi-compartment microscopic diffusion imaging. *NeuroImage*, 139:346–359, 2016.

[5.30] Marco Reisert, Elias Kellner, Bibek Dhital, Jürgen Hennig, and Valerij G. Kiselev. Disentangling micro from mesostructure by diffusion MRI: A Bayesian approach. *NeuroImage*, 147:964–975, 2017.

[5.31] Dmitry S. Novikov, Jelle Veraart, Ileana O. Jelescu, and Els Fieremans. Rotationally-invariant mapping of scalar and orientational metrics of neuronal microstructure with diffusion MRI. *NeuroImage*, 174:518–538, 2018.

[5.32] Rutger H. J. Fick, Demian Wassermann, and Rachid Deriche. The dmipy toolbox: Diffusion mri multi-compartment modeling and microstructure recovery made easy. *Frontiers in Neuroinformatics*, 13:64, 2019.

[5.33] Dmitry S. Novikov, Valerij G. Kiselev, and Sune N. Jespersen. On modeling. *Magnetic Resonance in Medicine*, 79(6):3172–3193, 2018.

[5.34] Yu-Chien Wu and Andrew L. Alexander. Hybrid diffusion imaging. *Neuroimage*, 36(3):617–629, 2007.

[5.35] Maxime Descoteaux, Rachid Deriche, Denis Le Bihan, Jean-François Mangin, and Cyril Poupon. Multiple q-shell diffusion propagator imaging. *Medical image analysis*, 15(4):603–621, 2011.

[5.36] A Pasha Hosseinbor, Moo K Chung, Yu-Chien Wu, and Andrew L Alexander. Bessel Fourier orientation reconstruction (BFOR): An analytical diffusion propagator reconstruction for hybrid diffusion imaging and computation of q-space indices. *NeuroImage*, 64:650–670, 2013.

[5.37] Sylvain. L Merlet and Rachid Deriche. Continuous diffusion signal, EAP and ODF estimation via compressive sensing in diffusion MRI. *Medical Image Analysis*, 17(5):556–572, 2013.

[5.38] Evren Özarslan, Cheng Guan Koay, and Peter J Basser. Simple harmonic oscillator based reconstruction and estimation for one-dimensional q-space magnetic resonance (1D-SHORE). In *Excursions in Harmonic Analysis*, volume 2, pages 373–399. Springer, 2013.

[5.39] Evren Özarslan, Cheng Guan Koay, Timothy M Shepherd, Michal E Komlosh, M Okan İrfanoğlu, Carlo Pierpaoli, and Peter J Basser. Mean apparent propagator (MAP) MRI: a novel diffusion imaging method for mapping tissue microstructure. *NeuroImage*, 78:16–32, 2013.

[5.40] Lipeng Ning, Carl-Fredrik Westin, and Yogesh Rathi. Estimating diffusion propagator and its moments using directional radial basis functions. *IEEE Trans Med Imag*, 34(10):2058–2078, 2015.

[5.41] Steven H. Baete and Fernando E. Boada. Accelerated radial diffusion spectrum imaging using a multi-echo stimulated echo diffusion sequence. *Magnetic Resonance in Medicine*, 79(1):306–316, 2018.

[5.42] Rutger HJ Fick, Demian Wassermann, Emmanuel Caruyer, and Rachid Deriche. MAPL: Tissue microstructure estimation using Laplacian-regularized MAP-MRI and its application to HCP data. *NeuroImage*, 134:365–385, 2016.

[5.43] Rutger HJ Fick, Madelaine Daianu, Marco Pizzolato, Demian Wassermann, Russell E Jacobs, Paul M Thompson, Terrence Town, and Rachid Deriche. Comparison of biomarkers in transgenic Alzheimer rats using multi-shell diffusion MRI. In *International Conference on Medical Image Computing and Computer-Assisted Intervention*, pages 187–199, Athens, Greece, 2016. Springer.

[5.44] Alexandra Tobisch, Radiger Stirnberg, Robbert L. Harms, Thomas Schultz, Alard Roebroeck, Monique M. B. Breteler, and Tony Stacker. Compressed sensing diffusion spectrum imaging for accelerated diffusion microstructure MRI in long-term population imaging. *Frontiers in Neuroscience*, 12:650, 2018.

[5.45] Santiago Aja-Fernández, Rodrigo de Luis-García, Maryam Afzali, Malwina Molendowska, Tomasz Pieciak, and Antonio Tristán-Vega. Micro-structure diffusion scalar measures from reduced MRI acquisitions. *PLOS ONE*, 15(3):1–25, 3 2020.

[5.46] Partha P Mitra, LL Latour, Robert L Kleinberg, and Christopher H Sotak. Pulsed-field-gradient NMR measurements of restricted diffusion and the return-to-the-origin probability. *Journal of Magnetic Resonance, Series A*, 114(1):47–58, 1995.

[5.47] Y. Wu, A. S. Field, and A. L. Alexander. Computation of diffusion function measures in q-space using magnetic resonance hybrid diffusion imaging. *IEEE Transactions on Medical Imaging*, 27(6):858–865, 2008.

[5.48] Alexandru V Avram, Joelle E Sarlls, Alan S Barnett, Evren Özarslan, Cibu Thomas, M Okan Irfanoglu, Elizabeth Hutchinson, Carlo Pierpaoli, and Peter J Basser. Clinical feasibility of using mean apparent propagator (MAP) MRI to characterize brain tissue microstructure. *NeuroImage*, 127:422–434, 2016.

[5.49] Mauro Zucchelli, Lorenza Brusini, C Andrés Méndez, Alessandro Daducci, Cristina Granziera, and Gloria Menegaz. What lies beneath? Diffusion EAP-based study of brain tissue microstructure. *Medical image analysis*, 32:145–156, 2016.

[5.50] Madelaine Daianu, Russell E Jacobs, Tara M Weitz, Terrence C Town, and Paul M Thompson. Multi-shell hybrid diffusion imaging (HYDI) at 7 Tesla in TgF344-AD transgenic Alzheimer rats. *PloS ONE*, 10(12):e0145205, 2015.

[5.51] A Pasha Hosseinbor, Moo K Chung, Yu-Chien Wu, John O Fleming, Aaron S Field, and Andrew L Alexander. Extracting quantitative measures from EAP: A small clinical study using BFOR. In *International Conference on Medical Image Computing and Computer-Assisted Intervention*, pages 280–287, Nice, France, 2012. Springer.

[5.52] Ilaria Boscolo Galazzo, Lorenza Brusini, Silvia Obertino, Mauro Zucchelli, Cristina Granziera, and Gloria Menegaz. On the viability of diffusion MRI-based microstructural biomarkers in ischemic stroke. *Frontiers in neuroscience*, 12:92, 2018.

[5.53] Lorenza Brusini, Silvia Obertino, Ilaria Boscolo Galazzo, Mauro Zucchelli, Gunnar Krueger, Cristina Granziera, and Gloria Menegaz. Ensemble average propagator-based detection of microstructural alterations after stroke. *International journal of computer assisted radiology and surgery*, 11(9):1585–1597, 2016.

[5.54] A. Tristán-Vega, S. Aja-Fernández, and C.F. Westin. Deblurring of probabilistic ODFs in quantitative diffusion MRI. In *2012 9th IEEE International Symposium on Biomedical Imaging (ISBI)*, pages 932–935, May 2012.

[5.55] D.S. Tuch. Q–Ball imaging. *Magnetic Resonance in Medicine*, 52:1358–1372, 2004.

[5.56] M. Descoteaux, R. Deriche, T. R. Knosche, and A. Anwander. Deterministic and probabilistic tractography based on complex fibre orientation distributions. *IEEE Transactions on Medical Imaging*, 28(2):269–286, 2009.

[5.57] M. Descoteaux, E. Angelino, S. Fitzgibbons, and R. Deriche. Regularized, fast, and robust analytical Q-Ball imaging. *Magnetic Resonance in Medicine*, 58:497–510, 2007.

[5.58] Andrew R. Hoy, Cheng Guan Koay, Steven R. Kecskemeti, and Andrew L. Alexander. Optimization of a free water elimination two-compartment model for diffusion tensor imaging. *NeuroImage*, 103:323–333, 2014.

[5.59] Santiago Aja-Fernández, Antonio Tristán-Vega, and Carlos Alberola-López. Noise estimation in single- and multiple-coil magnetic resonance data based on statistical models. *Magnetic Resonance Imaging*, 27(10):1397–1409, 2009.

[5.60] Xi-Nian Zuo, Ting Xu, and Michael Peter Milham. Harnessing reliability for neuroscience research. *Nature Human Behaviour*, 3:768–771, 2019.

[5.61] A. Tristán-Vega, C.-F. Westin, and S. Aja-Fernández. Estimation of fiber orientation probability density functions in High Angular Resolution Diffusion Imaging. *NeuroImage*, 47(2):638–650, 2009.

[5.62] Antonio Tristán-Vega, Carl-Fredrik Westin, and Santiago Aja-Fernández. A new methodology for the estimation of fiber populations in the white matter of the brain with the Funk–Radon transform. *NeuroImage*, 49(2):1301–1315, 2010.

[5.63] Tom Dela Haije, Evren Özarslan, and Aasa Feragen. Enforcing necessary non-negativity constraints for common diffusion mri models using sum of squares programming. *NeuroImage*, 209:116405, 2020.

[5.64] A. Tristán-Vega and C.F. Westin. Probabilistic ODF estimation from reduced HARDI data with sparse regularization. In *International Conference on Medical Image Computing and Computer-Assisted Intervention*, pages 182–190, Toronot, Canada, 2011. Springer.

[5.65] Christophe Phillips, Gaetan Garraux, and Erik Ziegler. High-quality diffusion-weighted imaging of Parkinson's disease, 2020. Web resource at NITRC. Last visited: 2020/04/01.

[5.66] Michael W. Weiner. The Alzheimer's Disease Neuroimaging Initiative, 2020. Author listed is the Principal Investigator of the ADNI. Last visited: 2020/04/01.

[5.67] David G. Luenberger and Yinyu Ye. *Linear and Nonlinear Programming*. International Series on Operations Research & Management Science. Springer, 3rd edition, 2008.

[5.68] I.S. Gradshteyn and I.M. Ryzhik. *Table of Integrals, Series, and Products*. Academic Press, Elsevier, 7th edition, 2007.

6

Efficient Estimation of Propagator Anisotropy and Non-Gaussianity in multi-shell diffusion MRI with MiSFIT

Guillem París[1], Tomasz Pieciak[1,2], Santiago Aja-Fernández[1], Antonio Tristán-Vega[1]

[1]*Laboratorio de Procesado de Imagen (LPI), Universidad de Valladolid, Valladolid, Spain*
[2]*AGH University of Science and Technology, Krakow, Poland*

Abstract:
Purpose: We seek to reformulate the so-called Propagator Anisotropy (PA) and Non-Gaussianity (NG), originally conceived for the Mean Apparent Propagator diffusion MRI (MAP-MRI), to the Micro-Structure adaptive convolution kernels and dual Fourier Integral Transforms (MiSFIT). These measures describe relevant normalized features of the Ensemble Average Propagator (EAP).
Theory and Methods: First, the indices, which are defined as the EAP's dissimilarity from an isotropic (PA) or a Gaussian (NG) one, are analytically reformulated within the MiSFIT framework. Then a comparison between the resulting maps is drawn by means of a visual analysis, a quantitative assessment via numerical simulations, a test-retest study across the MICRA data set (6 subjects scanned 5 times) and, finally, a computational time evaluation.
Results: Findings illustrate the visual similarity between the indices computed with either technique. Evaluation against synthetic ground truth data, however, demonstrates MiSFIT's improved accuracy. In addition, the test-retest study reveals MiSFIT's higher degree of reliability in most of white matter regions. Finally, the computational time evaluation shows MiSFIT's time reduction up to 2 orders of magnitude.
Conclusions: Despite being a direct development on the MAP-MRI representation, the PA and the NG can be reliably and efficiently computed within MiSFIT's framework. This, together with the previous findings in [6.1], could mean the difference that definitely qualifies diffusion MRI to be incorporated into regular clinical settings.

6.1 Introduction

Diffusion MRI (dMRI) has become an irreplaceable tool for the non-invasive study of the micro- and meso-structure of the white matter (WM) of the brain. While the micro-structure is usually characterized through suitable diffusion models, the description of the meso-structure entails the reconstruction and analysis of the Ensemble Average Propagator (EAP) [6.2], defined as the Probability Density Function of water molecules moving a distance $\mathbf{R}$ within a diffusion time τ [6.3]. The topic covered in this paper focuses on the

latter. Specifically, we address the characterization of the 3-D EAP computed from multi-shell samplings (MSS), i. e. dMRI acquisitions comprising a *small* set of b-values (shells) with a *large* number of diffusion gradients each [6.4].

Reconstructing the 3-D EAP allows to compute several scalar indices that embed useful descriptors of WM. Among them, return-to-origin, return-to-plane or return-to-axis probabilities (respectively, RTOP, RTPP and RTAP), as well as propagator anisotropy (PA) or non-Gaussianity (NG) are the most often used [6.5, 6.6, 6.7]. In the present paper we focus on PA and NG, which come to generalize the popular Fractional Anisotropy (FA) and diffusion Kurtosis.

PA is defined in [6.7] as the distance from the propagator $P(\mathbf{R})$ to its isotropic equivalent. By means of Parseval's theorem, it can also be defined as the distance from the attenuation signal $E(\mathbf{q})$ (the diffusion signal characterized by wave vector $\mathbf{q}$ over the unweighted T2 baseline) to its closest isotropic counterpart, $O(\mathbf{q})$:

$$\text{PA} = \gamma\left(\sin(\angle(E(\mathbf{q}), O(\mathbf{q}))), \epsilon\right) \in [0, 1], \tag{6.1}$$

where:

$$\cos(\angle(E(\mathbf{q}), O(\mathbf{q}))) = \frac{\langle E(\mathbf{q}), O(\mathbf{q})\rangle}{\parallel E(\mathbf{q}) \parallel \parallel O(\mathbf{q}) \parallel}, \tag{6.2}$$

and:

$$\gamma(t, \epsilon) = \frac{t^{3\epsilon}}{1 - 3t^{\epsilon} + 3t^{2\epsilon}}, \tag{6.3}$$

for $\epsilon = 0.4$, which stands for a contrast enhancement of PA within the normalized range $[0, 1]$. PA has shown the ability to characterize morphological and cytoarchitectural attributes, even in Gray Matter (GM) regions where the FA is non-informative [6.8]. Yet, PA offers a more accurate assessment of the anisotropic behavior in crossing fibers regions. Within clinical setups, PA has shown a great potential in the analysis of longitudinal changes within subjects [6.9], the characterization of cognitive impairment after traumatic brain injury (TBI) [6.10], impaired social cognition in autism [6.11], or age-dependent neuronal demise in transgenic Alzheimer rats [6.12].

In turn, NG is defined as the distance from $E(\mathbf{q})$ to its closest Gaussian representation, $G(\mathbf{q})$ [6.7]:

$$\text{NG} = \sin\left(\angle(E(\mathbf{q}), G(\mathbf{q}))\right) \in [0, 1]. \tag{6.4}$$

Though the clinical applicability of NG has not been as thoroughly tested as that of PA, it has been lately proven useful at distinguishing grade II from grade III and IV gliomas [6.13], relevant for the noninvasive preoperative evaluation of tumour pathological grading. Some additional studies on axonal loss and demyelination [6.14], as well as head and neck cancer [6.15, 6.16] are also available.

Though they can be computed resorting to other estimation techniques [6.6], PA and NG naturally arise from MAP-MRI [6.5, 6.7]. Therein, the NG can be easily computed from the energy of the non-DC components, since MAP-MRI develops the diffusion signal by successively refining a Gaussian model. Conversely, the PA is related to the non-DC components of the isotropic, non-voxel adaptive version of MAP-MRI, a.k.a. 3D-SHORE.

In this article, we aim at formulating and evaluating both PA and NG for the newly developed Micro-Structure adaptive convolution kernels and dual Fourier Integral Transforms

(MiSFIT, [6.1]), both of them from the very same signal representation. By taking advantage of the computational efficiency of MISFIT, we expect the already-demonstrated higher accuracy in the RTxP computation w.r.t MAPL (the *de facto* standard, regularized version of MAP-MRI [6.5]) to also be translated for PA and NG. In addition, we also expect this accuracy to result in a higher reliability of the measures, which together with the critical reduction of the computational time, qualify MiSFIT's PA and NG to be incorporated not only in research studies, but also in clinical settings.

6.2 Theory

6.2.1 MiSFIT's signal representation

MiSFIT's composite representation, as it can be seen in [6.1] eq. (4), comprises the aggregate of a free-diffusing isotropic component and a semi-parametric component that accounts for the partial volume fraction $f \in [0,1]$ of constrained diffusion:

$$ {}_cE(\mathbf{q}) = (1-f)\exp(-bD_0) + fE(\mathbf{q}), \tag{6.5}$$

with $\mathbf{q} = q\mathbf{u}$ ($q = \|\mathbf{q}\| \in \mathbb{R}_+$) the wave-vector related to the b-value as $b = 4\pi^2\tau q^2$ and D_0 the diffusivity of free-water at body temperature. The constrained diffusion signal $E(\mathbf{q})$ is drawn as the spherical convolution of a parametric kernel, defined by the longitudinal $\lambda_\parallel$ and transverse $\lambda_\perp$ diffusivities, with a non-parametric Orientation Distribution Function (ODF), Φ:

$$E(\mathbf{q}) = \iint_{\mathcal{S}} \Phi(\mathbf{v}) \exp\left(-b\left((\mathbf{u}^T\mathbf{v})(\lambda_\parallel - \lambda_\perp) + \lambda_\parallel\right)\right) d\mathbf{v}, \tag{6.6}$$

where $\mathcal{S} = \{\mathbf{u} \in \mathbb{R}^3 : \|\mathbf{u}\| = 1\}$. By representing the ODF in the basis of Spherical Harmonics (SH), MiSFIT lastly represents the attenuation signal as:

$$E(q\mathbf{u}) = \sum_{\substack{l=0 \\ l \text{ even}}}^{L} \sum_{m=-l}^{l} \widehat{e}_l^{\text{ODF}}(q)\phi_l^m Y_l^m(\mathbf{u}), \tag{6.7}$$

where $Y_l^m(\mathbf{u})$ are the (even) SH functions, ϕ_l^m stand for the SH coefficients of the ODF, and $\widehat{e}_l^{\text{ODF}}(q)$ are $\lambda_\parallel$ and $\lambda_\perp$-dependent convolution multipliers (see [6.1] for further details). A central part to our developments, as can be easily deduced from eqs. (6.1) and (6.4), is the computation of scalar products between SH-spanned functions like in eq. (6.7). We prove in Appendix A (located in the "Supporting Information") that their calculation relies on the evaluation of the following integral, $\mathcal{I}_l(\rho_\lambda)$, involving the Legendre Polynomials $P_l(x_i)$:

$$\mathcal{I}_l(\rho_\lambda) = \int_{-1}^{1}\int \frac{P_l(x_1)P_l(x_2)}{(2\rho_\lambda + x_1^2 + x_2^2)^{3/2}} dx_1 dx_2, \tag{6.8}$$

for $\rho_\lambda = \lambda_\perp/(\lambda_\parallel - \lambda_\perp)$. These integrals do not admit a closed form. However, since only the first few even orders of l are needed, they can be pre-computed for a wide range of ρ_λ and with an accuracy up to the numerical precision of the machine. Fig. 6.1 shows their values for the first few l.

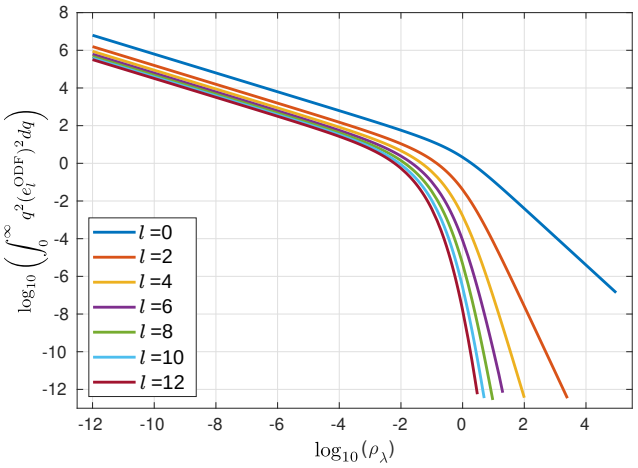

Fig. 6.1.: Numerical values of the integrals $\mathcal{I}_l(\rho_\lambda)$ as described in eq. (6.8).

6.2.2 PA for MiSFIT's composite signal

From the definition in eq. (6.1), we develop into:

$$\sin\left(\angle({}_cE(\mathbf{q}),\ {}_cO(\mathbf{q}))\right) = \sqrt{1-\cos^2\left(\angle({}_cE(\mathbf{q}),\ {}_cO(\mathbf{q}))\right)} \tag{6.9}$$

We demonstrate in Appendix B (in "Supporting Information") that the squared cosine in the last equation leads to:

$$\cos^2\left(\angle({}_cE(\mathbf{q}),\ {}_cO(\mathbf{q}))\right) = \frac{\|{}_cO(q)\|^2}{\|{}_cE(q\mathbf{u})\|^2} = \frac{(1-f)^2O_{\text{iso}} + f^2O_{\text{ani}} + f(1-f)O_{\text{mix}}}{(1-f)^2E_{\text{iso}} + f^2E_{\text{ani}} + f(1-f)E_{\text{mix}}}, \tag{6.10}$$

where the isotropic terms (E_{iso}, O_{iso}), the anisotropic terms (E_{ani}, O_{ani}), and the mixed terms (E_{mix}, O_{mix}) come from the composite representation (i.e. isotropic plus anisotropic parts) in eq. (6.5):

$$\begin{aligned}
O_{\text{ani}} &= (\phi_0^0)^2\pi\delta_\lambda^{-3/2}\mathcal{I}_0(\rho_\lambda);\\
E_{\text{ani}} &= \sum_{l,m}(\phi_l^m)^2\pi\delta_\lambda^{-3/2}\mathcal{I}_l(\rho_\lambda);\\
E_{\text{iso}} &= O_{\text{iso}} = (2D_0)^{-3/2};\\
E_{\text{mix}} &= O_{\text{mix}} = 4\sqrt{\pi}\phi_0^0\Big((D_0+\lambda_\perp)\sqrt{D_0+\lambda_\parallel}\Big)^{-1},
\end{aligned} \tag{6.11}$$

for $\delta_\lambda = \lambda_\parallel - \lambda_\perp$. Therefore, the PA finally reads:

$$\text{PA} = \gamma\left(\sqrt{1 - \frac{\frac{(1-f)^2}{(2D_0)^{3/2}} + \frac{4\sqrt{\pi}f(1-f)}{(D_0+\lambda_\perp)\sqrt{D_0+\lambda_\parallel}}\phi_0^0 + f^2(\phi_0^0)^2\pi\delta_\lambda^{-3/2}\mathcal{I}_0(\rho_\lambda)}{\frac{(1-f)^2}{(2D_0)^{3/2}} + \frac{4\sqrt{\pi}f(1-f)}{(D_0+\lambda_\perp)\sqrt{D_0+\lambda_\parallel}}\phi_0^0 + f^2\sum_{l,m}(\phi_l^m)^2\pi\delta_\lambda^{-3/2}\mathcal{I}_l(\rho_\lambda)}}, \epsilon\right). \tag{6.12}$$

Noticeably, removing the isotropic compartment (i.e. taking $f = 1$) results in a much simpler expression:

$$\text{PA} = \gamma\left(\sqrt{1 - \frac{O_{\text{ani}}}{E_{\text{ani}}}}, \epsilon\right) = \gamma\left(\sqrt{1 - \frac{(\phi_0^0)^2 \pi \delta_\lambda^{-3/2} \mathcal{I}_0(\rho_\lambda)}{\sum_{l,m}(\phi_l^m)^2 \pi \delta_\lambda^{-3/2} \mathcal{I}_l(\rho_\lambda)}}, \epsilon\right). \tag{6.13}$$

Conversely, fitting a voxel with $f = 0$ (i.e. a free-water voxel), results in both $\|_cO(q)\|^2$ and $\|_cE(q\mathbf{u})\|^2$ being equal. Hence, the PA as defined in eq. (6.9), will be 0 as expected.

6.2.3 NG for MiSFIT's composite signal

Now, from the definition in eq. (6.4):

$$\sin(\angle({}_cE(\mathbf{q}),\ {}_cG(\mathbf{q}, \widehat{\mathbf{D}}))) = \sqrt{1 - \left(\frac{\langle {}_cE(\mathbf{q}),\ {}_cG(\mathbf{q}, \widehat{\mathbf{D}})\rangle}{\|{}_cE(\mathbf{q})\| \|{}_cG(\mathbf{q}, \widehat{\mathbf{D}})\|}\right)^2}, \tag{6.14}$$

where ${}_cG(\mathbf{q}, \widehat{\mathbf{D}})$ is the closest Gaussian propagator. In the MiSFIT approach, the equivalent Gaussian propagator is estimated by fitting a tensor to the EAP-based reconstruction of the attenuation signal (for b-values < 2000 s/mm^2). The reason behind this is that computing the actual closest Gaussian propagator (i.e. that which results in the smallest possible Mean Squared Difference, MSD) is not trivial and would require solving a calculus of variations problem that could easily maim the computational efficiency nature upon which MiSFIT is build. Hence, the problem is solved in the logarithmic domain of $E(\mathbf{q})$, to make it convex and permit a closed-form solution, while keeping the computationally-efficient feature that makes MiSFIT desirable for specific settings. Thus, from now on, our implementation of the *closest* Gaussian propagator will be referred to as "DTI-like propagator". More information about the Gaussian propagator and the method chosen to compute it is included in the appendix E.2. (in "Supporting Information"). We demonstrate in Appendix C that the quotient in eq. (6.14) equals:

$$\left(\frac{\langle {}_cE(\mathbf{q}),\ {}_cG(\mathbf{q}, \widehat{\mathbf{D}})\rangle}{\|{}_cE(\mathbf{q})\| \|{}_cG(\mathbf{q}, \widehat{\mathbf{D}})\|}\right)^2 = \frac{\left(\frac{1-f}{\sqrt{|\widehat{\mathbf{D}}+\mathbf{D}_0|}} + f\sum_{l,m}\phi_l^m \xi_l^m\right)^2 \sqrt{8|\widehat{\mathbf{D}}|}}{(1-f)^2 E_{\text{iso}} + f^2 E_{\text{ani}} + f(1-f)E_{\text{mix}}}, \tag{6.15}$$

where $\widehat{\mathbf{D}}$ is the DTI-like propagator; $\mathbf{D}_0 = D_0 I_3$ is D_0 times the identity matrix; $|\cdot|$ stands for the determinant; ξ_l^m are the SH coefficients of a spherical function defined in Appendix C (in "Supporting Information") that depends on $\widehat{\mathbf{D}}$, $\lambda_\parallel$ and $\lambda_\perp$. Finally, the NG reads:

$$\text{NG} = \sqrt{1 - \frac{\left(\frac{1-f}{\sqrt{|\mathbf{D_0}+\widehat{\mathbf{D}}|}} + f\sum_{l,m}\phi_l^m \xi_l^m\right)^2 \sqrt{8|\widehat{\mathbf{D}}|}}{\frac{(1-f)^2}{(2D_0)^{3/2}} + f^2 \sum_{l,m}(\phi_l^m)^2 \pi \delta_\lambda^{-3/2} \mathcal{I}_l(\rho_\lambda) + \frac{4\sqrt{\pi} f(1-f)}{(D_0+\lambda_\perp)\sqrt{D_0+\lambda_\parallel}}\phi_0^0}}. \tag{6.16}$$

Again, evaluating the NG for $f = 1$ yields to a simpler expression:

$$\mathrm{NG} = \sqrt{1 - \left(8\delta_\lambda^3 |\widehat{\mathbf{D}}|\right)^{1/2} \frac{\left(\sum_{l,m} \phi_l^m \xi_l^m\right)^2}{\pi \sum_{l,m} (\phi_l^m)^2 \mathcal{I}_l(\rho_\lambda)}}. \tag{6.17}$$

For values of f other than 0, finding the Gaussian counterpart to the MiSFIT-estimated EAP is not equally easy. This is not an issue within the (anisotropic) MAP-MRI framework, since it represents the diffusion signal as a series of orthogonal cumulants, being the DTI estimation the first one, i.e.:

$$E_{\mathrm{MAP}}(\mathbf{q}) = E_{\mathrm{DTI}}(\mathbf{q}) + E_{\mathrm{MAP}\backslash\mathrm{DTI}}(\mathbf{q}), \tag{6.18}$$

so that the closest Gaussian is just the first addend. As already explained in the beginning of the section, MiSFIT can only compute a "DTI-like" propagator in order not to maim its computational efficiency.

6.3 Methods

6.3.1 Materials

In vivo validation has been carried out using only publicly-available databases:

- The **HCP** (Human Connectome Project)[1] MGH-USC data set (subject 1007) comprises high-quality DWI volumes acquired on a Siemens 3T Connectome Scanner (Siemens, Erlangen, Germany) with maximum gradient strength 300 mT/m. The data were acquired with a spin-echo echo planar imaging (EPI) with TR/TE $= 8000/57$ ms, four different shells at $b = [1000,\ 3000,\ 5000,\ 10000]$ s/mm^2 with $[64,\ 64,\ 128,\ 256]$ diffusion gradients each, and 40 interleaved non-weighted baselines, in-plane resolution 1.5×1.5 mm^2 and slice thickness 1.5 mm, and pulse separation time/diffusion gradients length $\Delta/\delta = 21.8/12.9$ ms. The outermost shell has been removed in order to validate our proposal with more standard acquisitions.
- The **MICRA** (Micro-structural Image Compilation with Repeated Acquisitions) database [6.17] contains five repeated sets of MSS DWI for each of six healthy volunteers. The images were acquired within a two-week period, approximately at the same time for each participant —avoiding potential diurnal effects— on an ultra-strong gradient 3T Connectome MRI scanner using a single-shot spin echo EPI with TR/TE $=$ $3000/59$ ms, six different shells at $b = [200,\ 500,\ 1200,\ 2400,\ 4000,\ 6000]$ s/mm^2, with $[20,\ 20,\ 30,\ 61,\ 61,\ 61]$ gradient directions respectively, in-plane resolution 2×2 mm^2, slice thickness 2 mm and $\Delta/\delta = 24/7$ ms. The data were preprocessed by removing Gibbs ringing artifacts [6.18] (with MRtrix3 [6.19]) and correcting susceptibility-induced distortions (with FSL's `topup`; Analysis Group, FMRIB, Oxford,

[1] Data obtained from the Human Connectome Project (HCP) database (https://ida.loni.usc.edu/login.jsp). The HCP project (Principal Investigators: Bruce Rosen, M.D., Ph.D., Martinos Center at Massachusetts General Hospital; Arthur W. Toga, Ph.D., University of Southern California, Van J. Weeden, MD, Martinos Center at Massachusetts General Hospital) is supported by the National Institute of Dental and Craniofacial Research (NIDCR), the National Institute of Mental Health (NIMH) and the National Institute of Neurological Disorders and Stroke (NINDS). HCP is the result of efforts of co-investigators from the University of Southern California, Martinos Center for Biomedical Imaging at Massachusetts General Hospital (MGH), Washington University, and the University of Minnesota.

UK.; https://fsl.fmrib.ox.ac.uk/fsl/fslwiki [6.20, 6.21]) and B1 field inhomogeneity [6.22] (with MRtrix3).

6.3.2 Implementation details

The fitting procedure for parameters f, $\lambda_{\parallel}$ and $\lambda_{\perp}$ in eqs. (6.5) and (6.6), and the computation of the ODF's SH coefficients, is detailed in [6.1]. We have used $L = 8$ as the maximum order for SH expansions, and empirically set $\mu = 1.2 \cdot 10^{-4}$ as the regularization parameter described therein to avoid singular convolution kernels. To compute $\mathcal{I}_l(\rho_\lambda)$, we have resorted to linear interpolation in the logarithmic domain from the values depicted in Fig. 6.1. The whole MiSFIT framework, including the newly introduced PA and NG, was coded in Matlab® R2019b (The MathWorks, Inc., Natick, MA) and is available for download [2].

The computation of PA and NG with MiSFIT is validated by comparing them with the *de facto* standard in the related literature, i.e. the MAPL as described in [6.5]. We have used the implementation in the DIPY package [3] under Python 3, though the actual code allowing the computation of the PA within the anisotropic MAP-MRI reconstruction was kindly provided by the authors on demand. We use MAPL with positivity constraints and cross-validation for setting the Laplacian penalty term. The maximum order for the basis functions was set to 6.

In both cases, and unless otherwise noticed, both PA and NG have been set up using the entirety of the acquisition's shells.

6.3.3 Ground-truth based evaluation

Numeric comparisons over ground-truth data are based on the methodology originally proposed in [6.1]. A micro-structure model is estimated at representative regions of the WM using NODDI [6.23]. Afterwards, a statistical model is built upon the estimated parameters, and further used to draw random samples that are fed to the forward NODDI model to generate synthetic samples simulating 1, 2, or 3 crossing fibers at will with a known Peak Signal to Noise Ratio (PSNR). As long as the generative model can be sampled for any gradient direction and b-value, ground-truth values are easily obtained for any dMRI measure with arbitrary precision by numerical integration. See [6.1] for further details on this methodology. While the ground truth for the PA is somehow trivial via the SH representation, determining the ground truth of NG implies solving a problem of calculus of variations. So this is transformed into a Least Squares (LS) optimization one by minimizing the squared residuals of a preset number of $\mathbf{q}$-space samples and then solved in the logarithmic domain of $E(\mathbf{q})$, as explained in Section 6.2.3.

[2] http://www.lpi.tel.uva.es/dmrilab
[3] https://dipy.org/

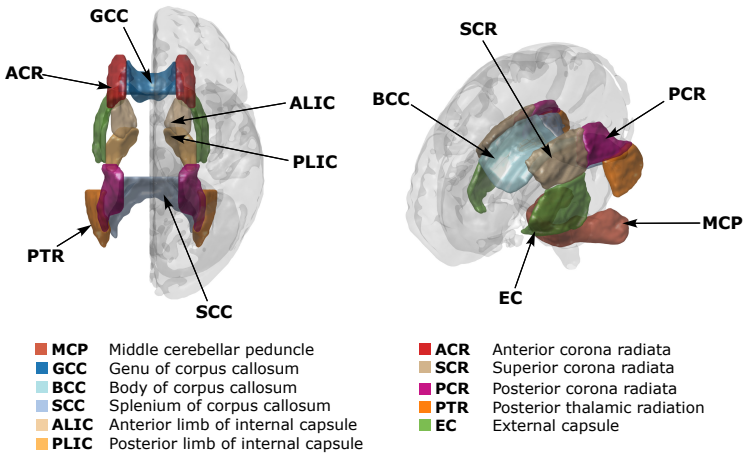

Fig. 6.2.: 3D visualization of the 11 JHU DTI-based labels in standard space. Note that some of the regions are not shown in either subfigure, in order to ease the visualization.

6.3.4 Reliability Study

The repeated acquisitions within MICRA dataset have been used to assess the repeatability of the computed measures (i.e. inter-session variability) and the separability they provide (i.e. inter-subject differences). These complementary properties together characterize the reliability of each method (MiSFIT/MAPL) and measure (PA/NG) [6.24]. Note that DTI's FA and DKI's mean Kurtosis have been included in the table for a wider comparison.

The design of the corresponding experiment is as follows: First, ROIs were back-projected by registering the JHU atlas' labels [6.25] (in MNI152 space) into each subjects' space by means of linear plus nonlinear registration (FSL's [6.26] FLIRT and FNIRT [6.27, 6.28], respectively) of the subject's FA to the JHU atlas, followed by the application of the inverse warping to the JHU labels. An eroded mask of the regions with a kernel of size $2 \times 2 \times 2$ was then computed to palliate the effects of a possible misalignment in the registration, removing tissue regions potentially affected by a partial volume effect, followed by the removal of those values for which the FA in the region yielded outliers (defined as those values falling 1.5 times outside the interquartile range). More information about the outlier rejection procedure is included in the Appendix E.1. within the supporting document. Finally, for each ROI in the subject space, one single-valued representative of each measure was computed as the median value. Fig. 6.2 shows a 3D brain render of the 12 WM regions included in the study (i.e. those in the JHU DTI-based atlas). Note that ROIs in both right and left hemisphere have been merged together into a single region. Repeatability was then computed as the mean across subjects of the variances across sessions, while separability was computed as the variance across subjects of the means across sessions. A Figure of Merit (FoM) was lastly defined as the separability over repeatability ratio. Owing to the limited size of the database, a 200-runs bootstrap analysis over population's subsets was carried out to assess the confidence we can put on such FoM, expressed as its coefficient of variation (CV):

$$\mathrm{CV}_{\mathrm{FoM}} = \left(1 + \frac{1}{4n}\right)\frac{s}{\bar{x}}, \tag{6.19}$$

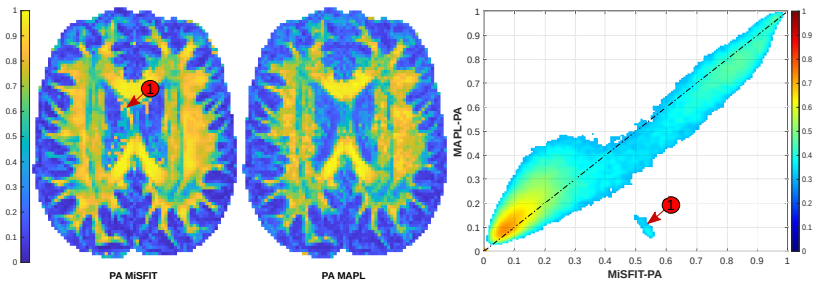

Fig. 6.3.: Comparison of the PA maps obtained with either MiSFIT and MAPL for the third session of the fourth MICRA's subject. Left: visual assessment within the whole range of variation $[0, 1]$. Right: joint 2-D histograms (logarithmic) of MAPL's values vs. MiSFIT's. The high-valued islands within MiSFIT (tag numbered '1') correspond to ambiguous configurations of the convolutional representation of MiSFIT.

with $\bar{x}/s$ the mean/standard deviation over bootstrapped samples, and n the number of bootstrap samples, used in the first term to attain unbiased estimates of the CV.

6.3.5 Computational Time Evaluation

One main advantage of MiSFIT, as compared to MAP-MRI/MAPL, is its computational efficiency, which allows to estimate the EAP two orders of magnitude faster. Nonetheless, the computation of scalar measures from the reconstructed EAP can result in non-negligible computational overloads: while the computation of NG is straightforward after the non-isotropic MAP-MRI signal representation, this is not the case for PA, which requires non-trivial extra calculations.

For this reason, it makes sense to compare how long MiSFIT and MAPL take to compute (1) the signal representation, (2) the PA and (3) the NG. The experiment is carried out with the aforementioned Matlab's (for MiSFIT) and Python DIPY's (for MAPL) implementations running in a quad-core Intel© CoreTM i7-6500U processor with 8GB RAM.

6.4 Results

6.4.1 Visual assessment

Figs. 6.3 and 6.4 compare the computations of PA and NG by MiSFIT and MAPL for the randomly chosen third session of the fourth MICRA's subject. With regard to PA, MAPL presents a noisier behavior (Fig. 6.3, left), specially in those areas with lower anisotropy values —except the ventricles, which MiSFIT clearly fails to delineate. This can also be observed in areas with higher anisotropy, resulting, for example, in some visible discontinuities in the *external capsule* (EC). In comparison, MiSFIT produces a more saturated map, clearly defining the major WM fiber tracts and their limits, making even more distinguishable the anisotropy of diffusion processes in some brain regions. Nonetheless, this contrast saturation

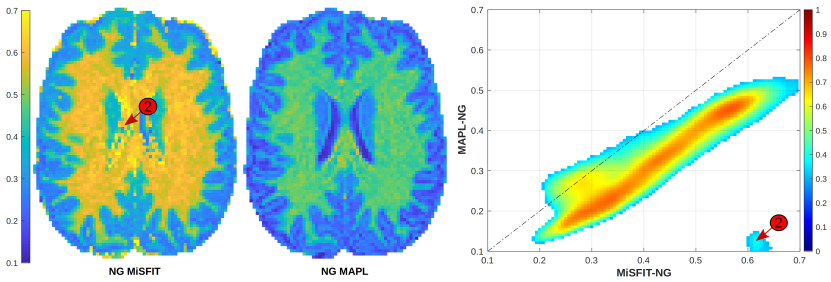

Fig. 6.4.: Comparison of the NG maps obtained with either MiSFIT and MAPL for the third session of the fourth MICRA's subject. Left: visual assessment within the cropped range $[0.1, 0.7]$. Right: joint 2-D histograms (logarithmic) of MAPL's values vs. MiSFIT's. The outliers tagged with '2' correspond to ambiguous configurations of the convolutional representation of MiSFIT.

does not imply, *per se*, a more accurate result. The comparison can also be analysed in terms of the 2D joint histogram (Fig. 6.3, right), which shows a linear correlation between both metrics, only disturbed for lower PA values, where the histogram broadens. As explained in [6.1], MiSFIT's estimation produces artifacts (tagged with number 1) due to ambiguities in highly-isotropic zones (such as the ventricles or the GM), where the optimizer has to decide, in eqs. (6.5) and (6.6), whether $f = 1$ or $\lambda_\perp \simeq \lambda_\parallel$.

For NG, both MiSFIT and MAPL provide outcomes as similar as those found with PA (Fig. 6.4, left), with the exception of the overall negative bias MAPL introduces w.r.t MiSFIT. This shift is more clearly visible in Fig. 6.4, right: MAPL's values are strongly linearly correlated with MiSFIT's, but placed along a line with slope less than 1 and negative bias. Once again, MiSFIT fails to delineate the ventricles due to the ambiguity in the representation, yielding to the outlier tagged as 2 in the histogram.

6.4.2 Quantitative analysis based on ground-truth

The numerical assessment of the accuracy of each method is based on the ground-truth data described in Section 6.3.3: Figs. 6.5 and 6.6 show the similarity of PA and NG, as computed with each of MAPL and MiSFIT, with true values of PA and NG, respectively. Joint 2-D histograms have been computed for different PSNR values (16, 32 and 64). Fig. 6.7 shows the rMSE for PA and NG estimates from both MAPL and MiSFIT as a function of the ground-truth RTOP value, as in [6.1]. This choice is based on the definition of RTOP as the integral of the attenuation signal in the whole $\mathbf{q}$-space:

$$\text{RTOP} = \int_{\mathbb{R}^3} |E(\mathbf{q})|^2 d\mathbf{q}, \tag{6.20}$$

which directly relates RTOP to the bandwidth of the EAP.

For PSNR=64, MiSFIT results in more accurate **PA** maps than MAPL from every possible point of view: Not only depicting smaller variability across the dynamic range, but also resulting in mean values closer to the ground truth. When conditions worsen, e.g. PSNR=16,

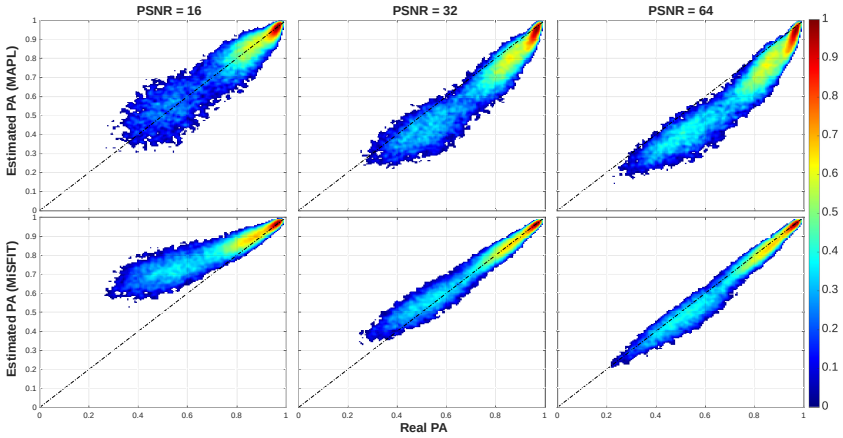

Fig. 6.5.: 2D Joint histogram of the estimated PA (y-axis) against synthetic ground truth values (x-axis) for different PSNR (16 left, 32 middle, 64 right). There exists a significant linear correlation between the estimated and real values, with MiSFIT being clearly more accurate and less variable than MAPL for PSNR > 32.

MiSFIT obtains poorer results, overestimating the anisotropy in highly-isotropic regions. These PA estimates, however, get more accurate the more anisotropic the region is.

Regarding the relative MSE (top of Fig. 6.7), MiSFIT yields to smaller errors, constantly outperforming MAPL values for any given bandwidth, PSNR or fiber bundle configuration. This latter variable is responsible of the poorer behavior of MiSFIT in Fig. 6.5 with PSNR$=16$. Arguably, both PA estimates worsen as the number of crossing fibers increases, which may be caused by the representation's difficulties when computing the isotropic EAP counterpart from bundles that may have different diffusion properties. Notice that, despite the results being worse for the third bundle configuration, they still outperform MAPL's.

The discussion for the **NG** is not equally good to MiSFIT. First of all, the two left-most columns of Fig. 6.6 (PSNR 16 and 32, respectively) show bigger variability across the measure's dynamic range, even for those values with means closer to the ground truth than those reported by MAPL. With respect to MiSFIT, there are multiple sources of error that end up stacking one to each other, the main one is driven by the noise —which causes the metric to be underestimated, specially in regions with high-Gaussianity behavior— but also by the estimated EAP —which affects the non-Gaussian regions estimates— and the DTI-estimated equivalent Gaussian EAP —which is greatly palliated as the fiber crossings increases.

On the other hand, the rMSE depicted from MiSFIT's NG (bottom of Fig. 6.7) seems to be dominated by the EAP reconstruction error, which results in MiSFIT underestimating the NG. This behavior is consistent with the one explained in [6.1] (Fig. 8). Interestingly, the rMSE increases when dealing with single-fiber configurations. This may be caused by MiSFIT's construction: The convolution of the Gaussian kernel with a very prolate but not-completely-sampled ODF (i.e. possibly non-Gaussian) results in Gaussian-like distributions, which yields to underestimated NG results. Alternatively, when adding fibers onto the configuration, the reconstructed EAP function gets smoother over the surface of the sphere, thus getting more accurately defined by the sampling scheme, which in turn leads to more precise estimations of the original EAP. This can also be appreciated in the bottom of Fig. 6.7.

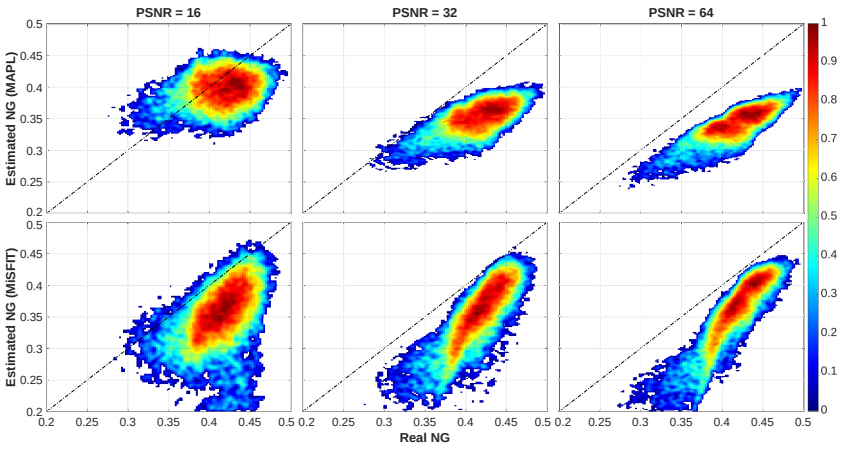

Fig. 6.6.: 2D Joint histogram of the estimated NG (y-axis) against synthetic ground truth values (x-axis) for different PSNR (16 left, 32 middle, 64 right). A linear correlation can be appreciated in both PSNR $= 64$ maps. MiSFIT tends to be more accurate in the high values, while MAPL estimation gets unbiased for lower ones, as well as for PSNR $= 16$.

In order to relate the numerically-obtained results with in-vivo images, the PSNR has been computed for a subject of the MICRA dataset by dividing the filtered (denoised) image by the estimated noise level. Both filtered image and noise level have been computed by using dwidenoise (MRtrix3, Tournier et al., NeuroImage, 2019) on the raw images. Finally, a white matter mask has been crafted by merging all the (previously-eroded) JHU WM labels. The resulting PSNR is 28.12, a usual result for good-quality acquisitions such as MICRA. This result indicates that the in-vivo images in Fig. 2 and 3 (from MICRA dataset) can be related to the middle column in Fig. 4, 5 and 6. In this PSNR range, the MiSFIT's PA portrays a much less variable estimation than MAPL's. MiSFIT tends to overestimate the mid-low PA values, while MAPL tends to subestimate them. MiSFIT's RMSE depicts a better accuracy in either bundle configuration and throughout the entire bandwidth range. Regarding the NG, the variance of the estimation increases significantly, yielding to subestimated results for both MiSFIT and MAPL. Concerning the RMSE, for the lower bandwidth ranges the MiSFIT's NG results in slightly less accurate estimations, which are improved in the mid-to-high bandwidth ranges.

6.4.3 Reliability Study

The results corresponding to the experiment described in Section 6.3.4 are summarized in Tables 6.1 and 6.2. Table 6.1 reports the FoM —the reliability measurement— together with the CV of the repeatability values. Table 6.2 shows the FOM's bootstrapped CV.

The first thing to notice from Table 6.1 is that all FoM values are greater than one, meaning that, for any given ROI, the inter-subject variability of the metrics is greater than the intra-subject variability. Regarding the PA, both MiSFIT and MAPL exhibit the same tendency, yielding to reliability values in the same order of magnitude, with the exception of the GCC where MAPL depicts much greater results than MiSFIT, and the EC where MiSFIT depicts greater results than MAPL. The reliability of the MiSFIT's NG, on the other hand, outperforms MAPL in most regions, for example in the 3 subregions of the *corpus callosum* (CC) —*genu*,

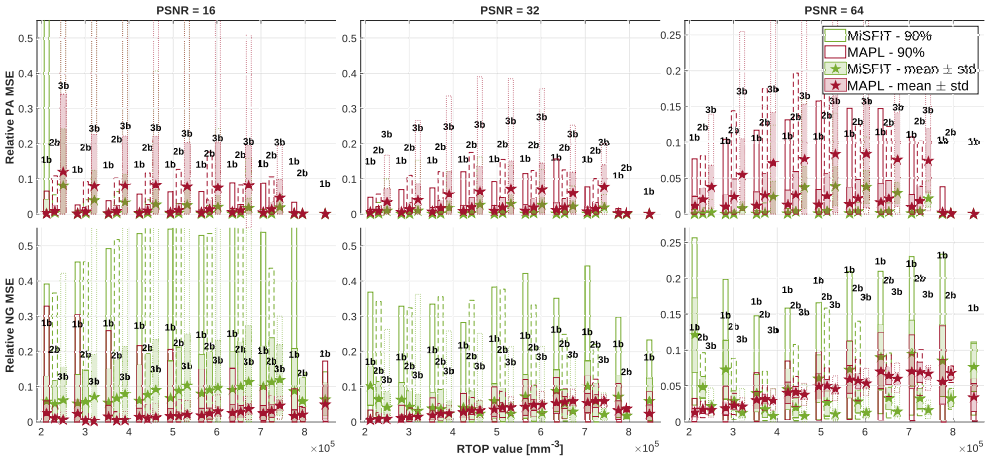

Fig. 6.7.: Estimated relative mean squared error (rMSE) of PA (top) and NG (bottom) as a function of signal's bandwidth (i.e. RTOP), for different PSNR (16 left, 32 middle and 64 right) and 1, 2 or 3 fiber crossing configuration. Missing bars correspond to those fiber bundle configurations for which PA, NG or RTOP values could not be computed. Statistical properties displayed: mean (star-shaped symbol), standard deviation (full-colored box), 90% confidence interval (empty box).

body and *splenium*— which together form one of the biggest connective pathways in the brain.

In terms of repeatability, both measures result in stable outputs throughout the various sessions of a given subject, yielding low CV values. MAPL's PA results in more repeatable values in 6 out of 11 regions while giving virtually equal values for 2 of the rest (BCC and PLIC, with less than 10% difference between both frameworks); whereas MAPL's NG depicts higher repeatability in 5 out of the 11 regions. To widen the comparison with existing and previously-validated measures, the table also includes the reliability and repeatability values for FA (Fractional Anisotropy) and MK (mean Kurtosis) from DTI and DKI frameworks, respectively. As it can be seen, the FA shows the same tendency to that of MAPL and MiSFIT, with the only exceptions being ACR and SCR. Concerning the MK, which outperforms both MAPL and MiSFIT's reliability values in 6 of the regions, it is worth noticing that this measure is not as similar to the NG as the FA is to the PA. That is simply because, by definition, the mean Kurtosis is computed as the mean of individual kurtoses calculated along all gradient directions, whereas NG requires the 3-D EAP and its 3-D Gaussian counterpart to compute the dissimilarity of the projection onto a multidimensional vector; thus being affected by moments with order higher than kurtosis.

The results shown in the previous table are supplemented by the bootstrap-derived coefficients of variation of the reliability values in Table 6.2, which gives us insights about the reliability of the FoM values. For example, we can conclude that repeated acquisitions of the FoM value for the MAPL's PA in the *middle cerebellar peduncle* (MCP, 2.09) yield to variations 0.658 times its mean, thereby making us aware of the variation of such value, and able to question its trustworthiness.

	PA		FA	NG		MK
Region	**MAPL**	**MiSFIT**	**DTI**	**MAPL**	**MiSFIT**	**DKI**
MCP	0.113 / 3.54	0.064 / 2.09	0.184 / 2.64	0.035 / 2.66	0.136 / 3.82	0.039 / 1.44
GCC	0.067 / 13.49	0.151 / 4.59	0.192 / 13.20	0.120 / 3.59	0.070 / 19.74	0.072 / 8.58
BCC	0.057 / 4.66	0.061 / 4.31	0.077 / 7.42	0.087 / 1.98	0.016 / 4.37	0.010 / 11.83
SCC	0.006 / 14.7	0.026 / 10.86	0.018 / 33.42	0.049 / 5.77	0.003 / 40.94	0.025 / 17.46
ALIC	0.078 / 3.04	0.148 / 5.25	0.149 / 2.57	0.056 / 4.00	0.045 / 1.40	0.035 / 13.01
PLIC	0.045 / 6.55	0.049 / 3.72	0.059 / 7.07	0.030 / 3.31	0.015 / 8.43	0.021 / 9.43
ACR	0.152 / 3.42	0.024 / 3.39	0.033 / 11.33	0.026 / 4.55	0.036 / 14.30	0.024 / 14.37
SCR	0.232 / 3.38	0.019 / 3.21	0.067 / 24.30	0.023 / 2.26	0.040 / 35.15	0.017 / 5.32
PCR	0.157 / 3.14	0.034 / 2.00	0.349 / 1.20	0.021 / 2.34	0.152 / 2.12	0.037 / 6.70
PTR	0.192 / 5.05	0.023 / 5.98	0.252 / 2.06	0.036 / 3.42	0.083 / 2.03	0.016 / 18.82
EC	0.729 / 3.39	0.035 / 17.30	0.352 / 5.35	0.075 / 7.1	0.491 / 5.47	0.022 / 18.84

Tab. 6.1.: Repeatability coefficient of variation (‰) over reliability (FoM) values for each of the regions, measures (PA, NG) and methods (MiSFIT, MAPL). DTI's FA and DKI's MK have been added for a wider comparison. Results indicate a good ratio between inter-subject and the intra-subject variability for both measures. On average, MiSFIT's NG obtain slightly better results than MAPL's, e.g. in the *corpus callosum*, while resulting in less reliable PA maps than those obtained with MAPL or DTI's FA.

	PA		FA	NG		MK
Region	**MAPL**	**MiSFIT**	**DTI**	**MAPL**	**MiSFIT**	**DKI**
MCP	0.596	0.658	0.613	0.494	0.225	0.325
GCC	0.385	0.230	0.243	0.318	0.303	0.199
BCC	0.524	0.557	0.588	0.310	0.408	0.437
SCC	0.488	0.431	0.516	0.324	0.293	0.486
ALIC	0.331	0.368	0.332	0.351	0.322	0.322
PLIC	0.719	0.399	0.553	0.409	0.342	0.203
ACR	0.359	0.275	0.416	0.488	0.649	0.323
SCR	0.679	0.522	0.491	0.502	0.488	0.430
PCR	0.256	0.559	0.334	0.378	0.382	0.326
PTR	0.170	0.304	0.333	0.388	0.513	0.586
EC	0.659	0.328	0.276	0.305	0.326	0.201

Tab. 6.2.: Bootstrap-derived CV of the FoM values for each of the regions, measures (PA, NG) and methods (MiSFIT, MAPL), together with the DTI's FA and the DKI's MK, for a wider comparison. The bootstrap was computed by doing 200 runs.

6.4.4 Computational Time Evaluation

Arguably, one notorious factor that conditions the actual clinical applicability of EAP imaging resides in the computational time requirements. Table 6.3 shows the time needed by MiSFIT and MAPL to (1) fit the signal, (2) compute the PA, and (3) compute the NG. As it can be seen, fitting the signal to MAPL requires almost 9 hours for a single DWI MICRA volume with size (110, 110, 66, 266). MiSFIT does so in less than 20 seconds.

As expected, the PA computation is time-consuming for the MAPL approach, which has to recalculate the MAP-MRI isotropic coefficients from those of the anisotropic representation. MiSFIT, on the contrary, only has to take the first SH coefficient to estimate the isotropic counterpart. This process ends up taking MAPL 2 hours 20 minutes in comparison with MiSFIT's 0.345 seconds.

Finally, the NG is easily computed by MAPL, which only has to take the first coefficient (Gaussian) from its series expansion and compute the angular divergence. In this case, MAPL computes the measure in 3.6 seconds while MiSFIT takes 5.8 seconds.

Phases	**MAPL**	**MiSFIT**
Fit Model	8h 36m	**17**s
PA Computation	2h 19m	**1**s
NG Computation	**3**s	6s
Total time	10h 56m	**23**s

Tab. 6.3.: Time consumption on the different phases of the metric's computation. Fitting the MAPL model is three-orders of magnitude more time-expensive than MiSFIT. MAPL requires almost 11 hours for a single DWI volume, in comparison with MiSFIT's 23 seconds, which makes the former unfeasible for clinical applicability.

To sum up, the total time required by either framework to actually produce a meaningful map is no less than 8 hours 30 minutes for MAPL (fit the model and compute the NG) compared with MiSFIT's maximum of 22 seconds (fit the model and compute the NG). Needless to say, this time-consuming difference is of main importance not only in clinical settings, but also in the processing of large data sets that are becoming more common in the dMRI community.

6.5 Discussion

In this paper we have shown how two descriptors of the white matter anatomy, PA and NG, can be computed within MiSFIT with very little computational effort. This way, we have generalized the analysis described in the original work [6.1], based on raw moments, to normalized indices that can be easier to interpret.

Regarding the PA, we have shown that MiSFIT yields to maps comparable to those obtained with MAPL. Yet, according to the numerical simulations, MiSFIT results are more accurate. This remains true in regions with diverse anisotropic behavior, and becomes compromised only when dealing with attenuation signals highly contaminated by noise. The reliability evaluation depicts comparable outcomes for both frameworks; meaning that, in general, none is far superior than the other and result, on average, in estimates almost identical (5.85 for MAPL, 5.70 for MiSFIT). In some particular regions, however, substantial differences can be found. The repeatability assessment, on the other hand, yields to MiSFIT estimates more repeatable than MAPL's (on average, 0.06 and 0.17‰, respectively). Thus, we conclude not only that MiSFIT's PA leads to a desirable stability of measurements throughout the sessions (in its maximum, the average subject's measures of the GCC varies 0.151‰ its mean), but also that its reliability is comparable to that of MAPL.

Concerning the NG, we have shown the high correlation between MiSFIT's and MAPL's estimates, disturbed only by MiSFIT's noisier behavior in Gaussian regions. Overall, MiSFIT exhibits a positive bias compared to MAPL for all the range of NG. According to the numerical simulations in Fig. 6.6, however, both frameworks clearly underestimate the *actual* value of the NG. Paradoxically, the negative bias in MAPL increases with the PSNR. Yet, the (negative) bias introduced by MiSFIT is less severe than MAPL's, which is consistent with the experiment in Fig. 6.4 with real data. Therefore, the large relative errors reported in Fig. 6.7 for the NG (far larger than those for the PA) are likely explained by the bias in the estimation. Similar to PA, both frameworks depict highly repeatable results across intra-subject sessions (0.05‰

for MAPL, 0.10‰ for MiSFIT, averaging across regions). In terms of reliability, MiSFIT's estimates are, on average, far more reliable (12.52 against MAPL's 3.73).

Note the evaluation of the NG based on ground-truth is far more difficult than it is for the PA, since the definition of the NG is tightly related to the MAP-MRI representation: with MAP-MRI, the closest Gaussian is trivially computed as the first addend of the expansion, so that the non-Gaussian part of the EAP is orthogonal to its Gaussian part. This property is unique to MAP-MRI, and does not hold neither for MiSFIT nor for the designed ground-truth signal. Consequently, it remains unclear if our ground truth is actually the desirable target. Given this situation, the reliability analysis grants a valuable quantitative information without the need of a ground-truth. In this sense, MiSFIT outperforms MAPL's estimation of the NG in 7 out of the 11 regions studied, including the CC. Taking also into account that MiSFIT offers a higher dynamic range for the NG, see Fig. 6.4 (left), we postulate that MiSFIT can be an attractive alternative to compute this index.

The numerical validation based on reliability, not just repeatability, is indeed a novel contribution of the present paper, as separability is a desirable property for any anatomical index. We claim that assessing the reliability is mandatory when comparing different dMRI techniques since EAP imaging approaches crop the otherwise infinite bandwidth of the diffusion signal in different ways (see [6.1]), depending on the representation used. The main limitation of the reliability assessment is the need for a robust inter-subject registration, so that the registration error does not become a critical confounding factor. In this sense, the repeatability values added to the analysis together with the computation of bootstrapped FoMs in Table 6.2 gives an idea of the confidence we can put on the results in Table 6.1. As long as the coefficients of variation are relatively large in all cases, we may conclude that more work is needed to pose the assessment of reliability as a state of the art procedure.

A critical issue with previous implementations of both the PA and the NG is their time-consuming nature, unsuited for clinical practice. According to Table 6.3, the time required for processing an entire volume of the MICRA database with MAPL is well over 8 hours when Generalized Cross-Validation and Positivity Constraints are used. For a subject in the HCP database, this time can grow up to 52 hours. Provided that for a clinical study a whole database needs to be processed, researchers will be compelled to use sub-optimal configurations, without positivity constraints, with fixed Laplacian penalty terms, or cropping the maximum order of the basis functions, which will compromise the accuracy of the measures and, in turn, the quality of the study. MiSFIT, on the other hand, is two orders of magnitude faster for any configuration.

To sum up, in this work the PA and NG measures have been introduced, their equations derived for MiSFIT's full composite attenuation signal and their performance within such framework validated. Both measures, with several proven clinical applications, result in consistent and reliable maps. All of this, together with MiSFIT's proven efficiency —capable of modeling the signal and computing both maps in less than a minute compared to MAPL's 11 hours— make the MiSFIT framework qualified for the new standardized dMRI protocol within clinical settings.

Acknowledgments

Guillem París was funded by the Consejería de Educación de Castilla y León and the European Social Fund through the "Ayudas para financiar la contratación predoctoral de personal investigador - Orden EDU/1100/2017 12/12" program. This work was supported by the Ministerio de Ciencia e Innovación of Spain with research grants RTI2018-094569-B-I00 and PID2021-124407NB-I00. Tomasz Pieciak acknowledges the Polish National Agency for Academic Exchange for grant PPN/BEK/2019/1/00421 under the Bekker programme and the Ministry of Science and Higher Education (Poland) under the scholarship for outstanding young scientists (692/STYP/13/2018).

Data collection and sharing for this project was partially provided by the Human Connectome Project, https://ida.loni.usc.edu/login.jsp (HCP; Principal Investigators: Bruce Rosen, M.D., Ph.D.,Martinos Center at Massachusetts General Hospital, Arthur W. Toga, Ph.D., University of Southern California, Van J. Weeden, MD, Martinos Center at Massachusetts General Hospital). HCP funding was provided by the National Institute of Dental and Craniofacial Research (NIDCR), the National Institute of Mental Health (NIMH), and the National Institute of Neurological Disorders and Stroke (NINDS). HCP is the result of efforts of co-investigators from the University of Southern California, Martinos Center for Biomedical Imaging at Massachusetts General Hospital (MGH), Washington University, and the University of Minnesota. HCP data are disseminated by the Laboratory of Neuro Imaging at the University of Southern California.

Appendices

6.A Legendre Polynomials Integration

This section shows the resolution of scalar products between SH-spanned functions, since both PA and NG rely on it. First, take into account that the scalar product of two such functions f and g can be expressed in spherical coordinates as:

$$\langle f(\mathbf{q}), g(\mathbf{q})\rangle = \iiint_{\mathbb{R}^3} f(\mathbf{q})g(\mathbf{q})d\mathbf{q} = \iint_{\mathcal{S}}\int_0^\infty q^2 f(q\mathbf{u})g(q\mathbf{u})dqd\mathbf{u}. \tag{6.21}$$

The squared modulus of f results in $\|f(\mathbf{q})\|^2 = \int_0^\infty q^2 \iint_{\mathcal{S}} \left(f(q\mathbf{u})\right)^2 d\mathbf{u}dq$. Casting the attenuation signal $E(\mathbf{q})$, as in eq.(7), into the previous result, we get:

$$\|E(q\mathbf{u})\|^2 = \int_0^\infty q^2 \iint_{\mathcal{S}} \left(\sum_{l,m} \hat{e}_l^{\text{ODF}}(q)\phi_l^m Y_l^m(\mathbf{u})\right)^2 d\mathbf{u}dq \tag{6.22}$$

$$= \int_0^\infty q^2 \sum_{l,m} \left(\hat{e}_l^{\text{ODF}}(q)\right)^2 (\phi_l^m)^2 dq = \sum_{l,m} (\phi_l^m)^2 \int_0^\infty q^2 \left(\hat{e}_l^{\text{ODF}}(q)\right)^2 dq. \tag{6.23}$$

To simplify, the integral in the variable q will be done separately by first replacing the convolution factors $\hat{e}_l^{\text{ODF}}(q) = 2\pi \int_{-1}^{1} \Lambda_{\text{ODF}}(x,q) P_l(x) dx$, where Λ_{ODF} stands for the convolution kernel in a given shell, see [1]:

$$E(q_i \mathbf{u}) = \iint_{\mathcal{S}} \Phi(\mathbf{v}) \Lambda_{\text{ODF}}(\mathbf{u}^T \mathbf{v}; q_i) d\mathbf{v} \quad : \quad \Lambda_{\text{ODF}}(x, q_i) = \exp(-b_i \lambda_\perp) \exp(-bi \delta_\lambda x^2), \tag{6.24}$$

where $\delta_\lambda = \lambda_{\|} - \lambda_\perp$. Hence, we can continue with the computation in eq. (6.23)

$$\int_0^\infty q^2 (\hat{e}_l^{\text{ODF}}(q))^2 dq = \int_0^\infty q^2 \left(2\pi \int_{-1}^{1} \Lambda_{\text{ODF}}(x,q) P_l(x) dx \right)^2 dq, \tag{6.25}$$

which results in:

$$\int_0^\infty q^2 (\hat{e}_l^{\text{ODF}}(q))^2 dq = 4\pi^2 \iint_{-1}^{1} \left(q^2 \Lambda_{\text{ODF}}(x_1, q) \Lambda_{\text{ODF}}(x_2, q) dq \right) P_l(x_1) P_l(x_2) dx_1 dx_2 \tag{6.26}$$

$$= \frac{\pi}{(4\pi\tau\delta_\perp)^{3/2}} \iint_{-1}^{1} \frac{P_l(x_1) P_l(x_2)}{(2\rho_\lambda + x_1^2 + x_2^2)^{3/2}} dx_1 dx_2 \tag{6.27}$$

$$= \frac{\pi}{(4\pi\tau\delta_\perp)^{3/2}} I_l(\rho_\lambda), \tag{6.28}$$

with $\rho_\lambda = \lambda_\perp / \delta_\lambda$. Although the previous equation does not provide a closed form expression, it shows that the computation of the norm of a function represented as the convolution with an SH-spanned ODF reduces to the numerical pre-calculation of the integral $I_l(\rho_\lambda)$ for a sufficiently large range of ρ_l and for $l = 0, 2, \ldots$ up to the desired order.

6.B Propagator Anisotropy for EAP composite signal

In this section, the formulation of the Propagator Anisotropy, as defined in [5], will be developed for MiSFIT's composite signal. First, let us define $\text{PA} = \gamma\left(\sin(\angle({}_cE(\mathbf{q}), {}_cO(q))), \epsilon\right)$, where $\sin(x)$ will be computed as $\sqrt{1 - \cos^2(x)}$. The isotropic equivalent ${}_cO(q)$ is defined as the directional average of ${}_cE(\mathbf{q})$:

$${}_cO(q) = \frac{1}{4\pi} \int_{\mathcal{S}} {}_cE(q\mathbf{u}) d\mathbf{u}. \tag{6.29}$$

The attenuation signal, in turn, is expressed in terms of SH basis functions as [1]:

$${}_cE(q\mathbf{u}) = (1 - f) \cdot \exp\left(-4\pi^2 \tau q^2 D_0\right) + f \cdot \sum_{l,m} \hat{e}_l^{\text{ODF}}(q) \phi_l^m Y_l^m(\mathbf{u}), \tag{6.30}$$

so that ${}_cO(q)$ is trivially computed from the DC component of the expansion:

$${}_cO(q) = (1 - f) \cdot \exp\left(-4\pi^2 \tau q^2 D_0\right) + f \frac{1}{(4\pi)^{3/2}} \hat{e}_0^{\text{ODF}}(q) \phi_l^m. \tag{6.31}$$

To begin with, the squared module of the composite signal is obtained by integrating, in spherical coordinates (unit sphere $\mathcal{S}$ and radial coordinate q), the squared ${}_cE(q\mathbf{u})$:

$$\|{}_cE(q\mathbf{u})\|^2 = \int_0^\infty q^2 \iint_{\mathcal{S}} \left((1-f)\cdot \exp\left(-4\pi^2\tau q^2 D_0\right) + f\cdot \sum_{l,m} \hat{e}_l^{\text{ODF}}(q)\phi_l^m Y_l^m(\mathbf{u})\right)^2 d\mathbf{u}dq. \tag{6.32}$$

Applying a binomial expansion to eq. (6.32), we get three terms, namely: isotropic, anisotropic and mixed. To ease the readability, the squared composite EAP will be expressed as $({}_cE(q\mathbf{u}))^2 =_c E^2_{\text{iso}}(q\mathbf{u}) +_c E^2_{\text{ani}}(q\mathbf{u}) + 2_cE_{\text{mix}}(q\mathbf{u})$, so that we have:

$$\begin{aligned}
{}_cE^2_{\text{iso}}(q\mathbf{u}) &= (1-f)^2 \exp\left(-8\pi^2\tau q^2 D_0\right) dq; && (6.33)\\
{}_cE^2_{\text{ani}}(q\mathbf{u}) &= f^2 \sum_{l,m} (\hat{e}_l^{\text{ODF}}(q))^2 (\phi_l^m)^2 (Y_l^m(\mathbf{u}))^2; && (6.34)\\
2_cE_{\text{mix}}(q\mathbf{u}) &= 2f(1-f)\exp\left(-4\pi^2\tau q^2 D_0\right) \sum_{l,m} \hat{e}_l^{\text{ODF}}(q)\phi_l^m Y_l^m(\mathbf{u}). && (6.35)
\end{aligned}$$

For each of these operands, respectively:

$$\begin{aligned}
\int_0^\infty q^2 \iint_{\mathcal{S}} {}_cE^2_{\text{iso}}(q\mathbf{u})d\mathbf{u}dq &= (1-f)^2 4\pi \int_0^\infty q^2 \exp\left(-4\pi^2\tau q^2 D_0\right) dq = (1-f)^2 \frac{1}{(8\pi\tau D_0)^{3/2}}; && (6.36)\\
\int_0^\infty q^2 \iint_{\mathcal{S}} {}_cE^2_{\text{ani}}(q\mathbf{u})d\mathbf{u}dq &= f^2 \sum_{l,m} (\phi_l^m)^2 \frac{\pi}{(4\pi\tau\delta_\lambda)^{3/2}} \mathcal{I}_l(\rho_\lambda); && (6.37)\\
\int_0^\infty q^2 \iint_{\mathcal{S}} 2_cE_{\text{mix}}(q\mathbf{u})d\mathbf{u}dq &= 2f(1-f)\int_0^\infty q^2 \exp\left(-4\pi^2\tau q^2 D_0\right) \frac{1}{\sqrt{4\pi}} \hat{e}_0^{\text{ODF}}(q)\phi_0^0 dq, && (6.38)
\end{aligned}$$

where the resolution of the second integral, referring to the purely-anisotropic term $\|{}_cE_{\text{ani}}\|^2$, addresses to Appendix 6.A. The last integral, referring to the integral of the mixed signal ${}_cE_{\text{mix}}(q\mathbf{u})$, is trivially solved since all SH basis, except for Y_0^0, have zero mean. Now, expanding the ODF 0-th SH coefficients in eq. (6.38):

$$\hat{e}_0^{\text{ODF}} = 2\pi \int_{-1}^{1} \Lambda_{\text{ODF}}(x,q) P_0(x) dx, \tag{6.39}$$

where $\Lambda = \exp(-b\lambda_\perp)\exp(-b\delta_\lambda x^2)$ results in:

$$\begin{aligned}
\int_0^\infty q^2 \iint_{\mathcal{S}} 2E_{\text{mix}}(q\mathbf{u})d\mathbf{u}dq &= 8\pi\sqrt{\pi} f(1-f)\phi_0^0 \int_{-1}^{1} \left(\int_0^\infty q^2 \exp\left(-b(D_0+\lambda_\perp+\delta_\lambda x^2)\right) dq\right) dx && (6.40)\\
&= \frac{2\pi^2 f(1-f)}{(4\pi^2\tau)^{3/2}} \phi_0^0 \int_{-1}^{1} \frac{1}{(D_0+\lambda_\perp+\delta_\lambda x^2)^{3/2}} dx && (6.41)\\
&= \frac{2\pi^2 f(1-f)}{(4\pi^2\tau\delta_\lambda)^{3/2}} \phi_0^0 \frac{2}{(D_0/\delta_\lambda+\rho_\lambda)\sqrt{D_0/\delta_\lambda+\rho_\lambda+1}} && (6.42)\\
&= \frac{4\sqrt{\pi} f(1-f)}{(4\pi\tau)^{3/2}} \frac{1}{(D_0+\lambda_\perp)\sqrt{D_0+\lambda_\parallel}} \phi_0^0. && (6.43)
\end{aligned}$$

Finally, adding all the terms and simplifying the expression, we obtain the following result:

$$\|_cE(q\mathbf{u})\|^2 = \frac{1}{(4\pi\tau)^{3/2}}\left(\frac{(1-f)^2}{(2D_0)^{3/2}} + f^2\sum_{l,m}(\phi_l^m)^2\pi\delta_\lambda^{-3/2}\mathcal{I}_l(\rho_\lambda) + \frac{4\sqrt{\pi}f(1-f)}{(D_0+\lambda_\perp)\sqrt{D_0+\lambda_\parallel}}\phi_0^0\right). \tag{6.44}$$

To compute the norm of ${}_cO(q)$, we use the same reasoning as in eq. (6.31), and simply keep the term for $l=0$ in eq. (6.44):

$$\|_cO(q)\|^2 = \frac{1}{(4\pi\tau)^{3/2}}\left(\frac{(1-f)^2}{(2D_0)^{3/2}} + f^2(\phi_0^0)^2\pi\delta_\lambda^{-3/2}\mathcal{I}_0(\rho_\lambda) + \frac{4\sqrt{\pi}f(1-f)}{(D_0+\lambda_\perp)\sqrt{D_0+\lambda_\parallel}}\phi_0^0\right). \tag{6.45}$$

Finally, note that:

$$\begin{aligned}\langle {}_cE(q\mathbf{u}), {}_cO(q)\rangle &= \int_0^\infty q^2 \iint_{\mathcal{S}} {}_cE(q\mathbf{u})\,{}_cO(q)\,d\mathbf{u}dq = \int_0^\infty q^2 \iint_{\mathcal{S}} {}_cE(q\mathbf{u})\frac{1}{4\pi}\iint_{\mathcal{S}} {}_cE(q\mathbf{v})d\mathbf{v}d\mathbf{u}dq \\ &= \frac{1}{4\pi}\int_0^\infty q^2\left(\iint_{\mathcal{S}} {}_cE(q\mathbf{u})d\mathbf{u}\right)\left(\iint_{\mathcal{S}} {}_cE(q\mathbf{v})d\mathbf{v}\right)dq = 4\pi\int_0^\infty q^2\,{}_cO^2(q)dq = \|_cO(q)\|^2\end{aligned} \tag{6.46}$$

hence the squared cosine between both two functions reads:

$$\begin{aligned}\cos^2(\angle({}_cE(\mathbf{q}),{}_cO(q))) &= \frac{\langle {}_cE(q\mathbf{u}), {}_cO(q)\rangle^2}{\|_cE(q\mathbf{u})\|^2\,\|_cO(q)\|^2} = \frac{\|_cO(q)\|^2}{\|_cE(q\mathbf{u})\|^2} \\ &= \frac{\frac{(1-f)^2}{(2D_0)^{3/2}} + \frac{4\sqrt{\pi}f(1-f)}{(D_0+\lambda_\perp)\sqrt{D_0+\lambda_\parallel}}\phi_0^0 + f^2(\phi_0^0)^2\pi\delta_\lambda^{-3/2}\mathcal{I}_0(\rho_\lambda)}{\frac{(1-f)^2}{(2D_0)^{3/2}} + \frac{4\sqrt{\pi}f(1-f)}{(D_0+\lambda_\perp)\sqrt{D_0+\lambda_\parallel}}\phi_0^0 + f^2\sum_{l,m}(\phi_l^m)^2\pi\delta_\lambda^{-3/2}\mathcal{I}_l(\rho_\lambda)}\end{aligned} \tag{6.47}$$

6.C Non-Gaussianity for EAP composite signal

As in the previous Section, we define the NG in terms of the sine between two signals, which is computed from the cosine:

$$\mathrm{NG} = \sin(\angle({}_cE(\mathbf{q}),\ {}_cG(\mathbf{q},\widehat{\mathbf{D}}))) = \sqrt{1-\cos^2(\angle({}_cE(\mathbf{q}),\ {}_cG(\mathbf{q},\widehat{\mathbf{D}})))}, \tag{6.48}$$

where ${}_cG$ is the DTI-like (Gaussian) propagator. The cosine between the signals, in turn, is computed as:

$$\cos(\angle({}_cE(\mathbf{q}),\ {}_cG(\mathbf{q},\widehat{\mathbf{D}}))) = \frac{\langle {}_cE(\mathbf{q}),\ {}_cG(\mathbf{q},\widehat{\mathbf{D}})\rangle}{\|_cE(\mathbf{q})\|\|_cG(\mathbf{q},\widehat{\mathbf{D}})\|}. \tag{6.49}$$

First, we compute the numerator of eq. (6.49) as follows:

$$\langle {}_cE(\mathbf{q}),\ {}_cG(\mathbf{q},\widehat{\mathbf{D}})\rangle = \iiint_{\mathbb{R}^3}\left((1-f)\exp\left(-4\pi^2\tau q^2 D_0\right) + fE(\mathbf{q})\right)\exp\left(-4\pi^2\tau q^2\mathbf{u}^T\widehat{\mathbf{D}}\mathbf{u}\right)d\mathbf{u}, \tag{6.50}$$

where $\widehat{\mathbf{D}}$ is the tensor associated to the DTI-like Gaussian propagator. Developing the multiplication of exponential functions, we obtain:

$$\langle {}_cE(\mathbf{q}),\ {}_cG(\mathbf{q},\widehat{\mathbf{D}})\rangle = (1-f)\iiint_{\mathbb{R}^3} e^{-4\pi^2\tau q^2\mathbf{u}^T(\mathbf{D_0}+\widehat{\mathbf{D}})\mathbf{u}}d\mathbf{u} + f\iint_{\mathcal{S}}\Phi(\mathbf{v})\iiint_{\mathbb{R}^3} e^{-4\pi^2\tau q^2\mathbf{u}^T(\widehat{\mathbf{D}}+\widehat{\mathbf{D}}^{\lambda}_{\mathbf{v}})\mathbf{u}}dqd\mathbf{u}d\mathbf{v}, \tag{6.51}$$

where $\mathbf{D_0} = D_0\mathbf{I}_3$, $\mathbf{I}_3$ is the 3×3 identity matrix and $\widehat{\mathbf{D}}^{\lambda}_{\mathbf{v}}$ is an elemental diffusion tensor with eigenvectors $\lambda_{\parallel}$, $\lambda_{\perp}$, aligned with direction $\mathbf{v}\in\mathcal{S}$. Since the integral of the exponential over $\mathbb{R}^3$ is trivial, we can obtain a simpler solution:

$$\langle {}_cE(\mathbf{q}),\ {}_cG(\mathbf{q},\widehat{\mathbf{D}})\rangle = \frac{1-f}{\sqrt{(4\pi\tau)^3|\mathbf{D_0}+\widehat{\mathbf{D}}|}} + f\iint_{\mathcal{S}}\frac{\Phi(\mathbf{v})}{\sqrt{(4\pi\tau)^3|\widehat{\mathbf{D}}+\widehat{\mathbf{D}}^{\lambda}_{\mathbf{v}}|}}d\mathbf{v}, \tag{6.52}$$

where $|\cdot|$ stands for the determinant of a matrix. Now, expanding the ODF in the SH basis, as $\Phi(\mathbf{v}) = \sum_{l,m}\phi_l^m Y_l^m(\mathbf{v})$, we obtain the following expression:

$$\langle {}_cE(\mathbf{q}),\ {}_cG(\mathbf{q},\widehat{\mathbf{D}}))\rangle = \frac{1-f}{\sqrt{(4\pi\tau)^3|\mathbf{D_0}+\widehat{\mathbf{D}}|}} + f\sum_{l,m}\phi_l^m \underbrace{\iint_{\mathcal{S}}\frac{1}{\sqrt{(4\pi\tau)^3|\widehat{\mathbf{D}}+\widehat{\mathbf{D}}^{\lambda}_{\mathbf{v}}|}}Y_l^m(\mathbf{v})d\mathbf{v}}_{\text{Projection onto SH basis}}. \tag{6.53}$$

The latter integral represents the projection of the corresponding function in the SH basis, hence, it can be accurately computed by LS fitting, for all l and m simultaneously, whenever it is properly sampled over the unit sphere. Such sampling strategy is described in depth in Appendix 6.D and results in:

$$\langle {}_cE(\mathbf{q}),\ {}_cG(\mathbf{q},\widehat{\mathbf{D}})\rangle = \frac{1-f}{\sqrt{(4\pi\tau)^3|\mathbf{D_0}+\widehat{\mathbf{D}}|}} + \frac{f}{(4\pi\tau)^{3/2}}\sum_{l,m}\phi_l^m\xi_l^m, \tag{6.54}$$

where $|\widehat{\mathbf{D}}+\widehat{\mathbf{D}}^{\lambda}_{\mathbf{v}}|^{-1/2} = \sum_{l,m}\xi_l^m Y_l^m(\mathbf{v})$. Finally:

$$\langle {}_cE(\mathbf{q}),\ {}_cG(\mathbf{q},\widehat{\mathbf{D}})\rangle = \frac{1}{(4\pi\tau)^{3/2}}\left(\frac{1-f}{\sqrt{|\mathbf{D_0}+\widehat{\mathbf{D}}|}} + f\sum_{l,m}\phi_l^m\xi_l^m\right). \tag{6.55}$$

The EAP module was computed in eq. (6.45), and the module of the DTI-like Gaussian propagator admits the closed form $\|\ {}_cG\| = (4\pi\tau)^{-3/2}(|2\widehat{\mathbf{D}}|)^{-1/2}$. Hence:

$$\cos^2({}_cE(\mathbf{q}),\ {}_cG(\mathbf{q},\widehat{\mathbf{D}}) = \frac{\left(\frac{1-f}{\sqrt{|\mathbf{D_0}+\widehat{\mathbf{D}}|}} + f\sum_{l,m}\phi_l^m\xi_l^m\right)^2\sqrt{8|\widehat{\mathbf{D}}|}}{\frac{(1-f)^2}{(2D_0)^{3/2}} + f^2\sum_{l,m}(\phi_l^m)^2\pi\delta_{\lambda}^{-3/2}\mathcal{I}_l(\rho_{\lambda}) + \frac{4\sqrt{\pi}f(1-f)}{(D_0+\lambda_{\perp})\sqrt{D_0+\lambda_{\parallel}}}\phi_0^0}. \tag{6.56}$$

6.D Efficient Sampling of Spherical Function

Eq. (6.53) can be seen as a projection onto the SH basis, and can be solved efficiently by *properly* sampling $|\widehat{\mathbf{D}}+\widehat{\mathbf{D}}^{\lambda}_{\mathbf{v}}|^{-1/2}$ in the variable $\mathbf{v}$. This is done by means of a spectral

analysis at each voxel, by making use of the matrix determinant lemma [6.29]:

$$|\mathbf{A} + \mathbf{u}\mathbf{v}^T| = (1 + \mathbf{v}^T\mathbf{A}^{-1}\mathbf{u})|\mathbf{A}|. \tag{6.57}$$

It can be applied by noticing that the elemental tensor $\widehat{\mathbf{D}}^{\lambda}_{\mathbf{v}}$ can be written as:

$$\widehat{\mathbf{D}}^{\lambda}_{\mathbf{v}} = \sqrt{\delta_\lambda}\mathbf{v}\sqrt{\delta_\lambda}\mathbf{v}^T + \lambda_\perp \mathbf{I}_3, \tag{6.58}$$

The proof is straightforward by noticing that both sides of the previous equation have the same eigenvalues and eigenvectors. Applying then the lemma in eq. (6.57):

$$|\widehat{\mathbf{D}} + \widehat{\mathbf{D}}^{\lambda}_{\mathbf{v}}| = \left(1 + \delta_\lambda \mathbf{v}^T(\lambda_\perp \mathbf{I}_3 + \widehat{\mathbf{D}})\mathbf{v}\right)|\lambda_\perp \mathbf{I}_3 + \widehat{\mathbf{D}}|, \tag{6.59}$$

which reduces the problem to compute the determinant of $\lambda_\perp \mathbf{I}_3 + \widehat{\mathbf{D}}$ at each voxel, independent on the variable $\mathbf{v}$. Note that $\widehat{\mathbf{D}}$ is positive (semi)definite and the MiSFIT approach ensures $\lambda_\perp$ is greater than 0, so that eq. (6.59) is always well defined and may be used to draw an arbitrary number of samples for $\mathbf{v} \in \mathcal{S}$. This means the coefficients ξ_l^m can be computed with arbitrary numerical precision up to any desired degree L, with the unique limit being that imposed by computational load constraints.

6.E Other results

This section shows some intermediate results that were not included in the document. Contrarily to the already seen appendices, these are not central to the development of the experiments but show some interesting results that support the steps finally taken.

6.E.1 Outlier Rejection Procedure

The main goal of the outlier rejection is to remove those voxels placed in the edges of the WM regions; thus palliating the effect of misregistration. Fig. S1 shows different methods for outlier removal. As it can be observed, some methods offer a more conservative approach and reject fewer outliers (i.e. standard rejection and mean-based rejection) than others (percentile-based one). The mean-based rejection is too conservative and there is almost no rejection. The two percentile approaches are probably too loose and reject many outliers that are placed in the middle of the WM labels. Therefore, the standard outlier rejection was chosen since it is the one more aligned with our needs: It successfully removes outliers placed on the edges of WM labels to palliate any possible misregistration. Fig. S2 shows the placement of such outliers in several slices of the first session of the subject 1 of the MICRA dataset.

6.E.2 DTI-like Gaussian Approximation

The current way of computing the DTI-like Gaussian propagator is motivated by the computational efficiency that MiSFIT offers. By the way it is formalized, MAPL is built upon

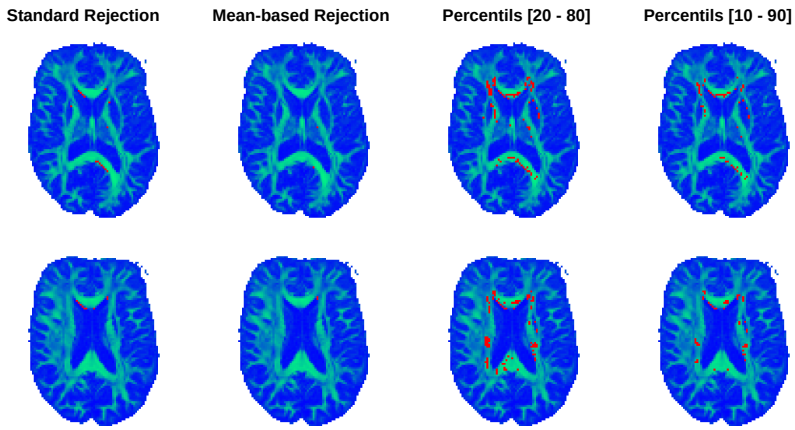

Fig. 6.8.: Outliers (red) overlayed onto several slices of the FA map (Subject 1, session 1), using 4 different outlier rejection methodologies: Standard Rejection, Mean-based Rejection, Percentils [20-80] and Percentils [10-90].

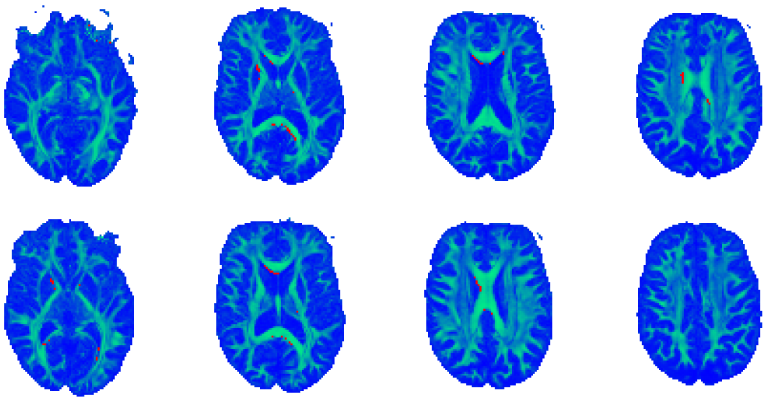

Fig. 6.9.: Outliers (red) overlayed onto several slices of the FA map (Subject 1, session 1), using the standard outlier rejection approach. Note how the outliers are correctly placed in the edges of the WM regions.

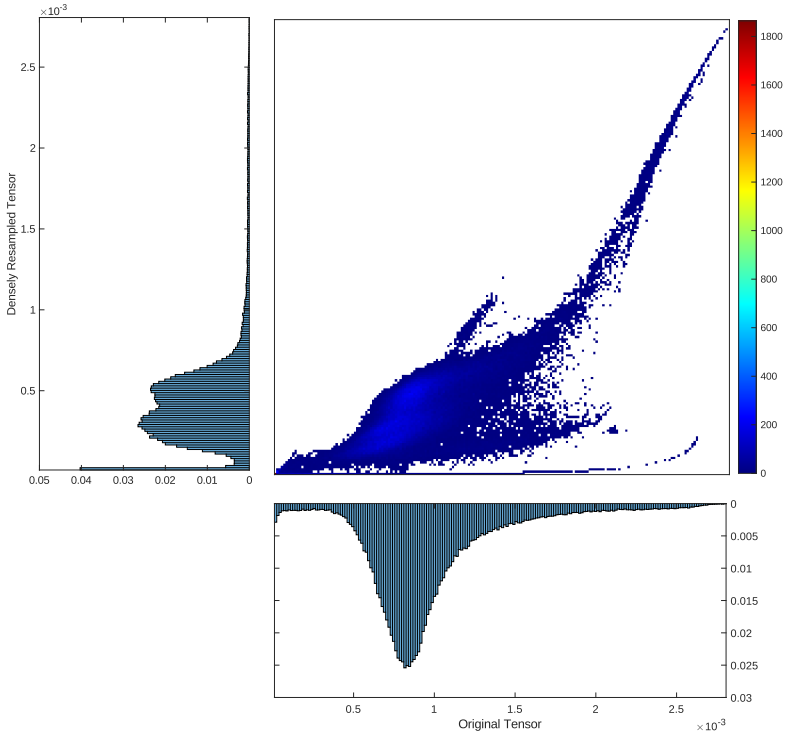

Fig. 6.10.: 2D joint histograms of both DTI representations ($M \times N \times P \times 6$).

successive refinements of the DTI approximation so that the Gaussian equivalent is the diffusion tensor that both (1) best describes the low b-value ($b < 2000\text{s/mm}^2$) regime and (2) mathematically minimizes the cost:

$$\min_{G(q)} \iiint_{\mathbb{R}^3} ||E(q) - G(q)||^2 dq \tag{6.60}$$

In MiSFIT, however, we can only aim at obtaining one of both representations. We could proceed by mimicking Eq. 6.60 via a discretization in a Cartesian lattice, so that the integral might be approximated with arbitrary precision, and the mathematically optimal Gaussian computed by means of (possibly constrained) numerical optimization. Nevertheless, this solution not only would compromise the anatomical interpretation of the NG, since we are no longer measuring deviations from the standard, low b-value DTI approach; but would also involve solving a non-linear non-convex optimization problem, where no optimal solution is assured. Therefore, MiSFIT currently aims at obtaining the Gaussian counterpart that best describes the low b-value regime, by minimizing:

$$\min_{D} \sum_{k=0}^{K} ||b\mathbf{g}_k^T \mathbf{D} \mathbf{g}_k - \ln(\frac{S_k}{S_0})||^2 \tag{6.61}$$

Notice the problem is reformulated in its logarithmic domain, where convexity —and thus, optimality— is assured. Fig. S3 shows the 2D joint histogram of the tensorial signals ($M \times N \times P \times 6$) for both implementations. Also, Fig. S4 show the 2D joint histogram of

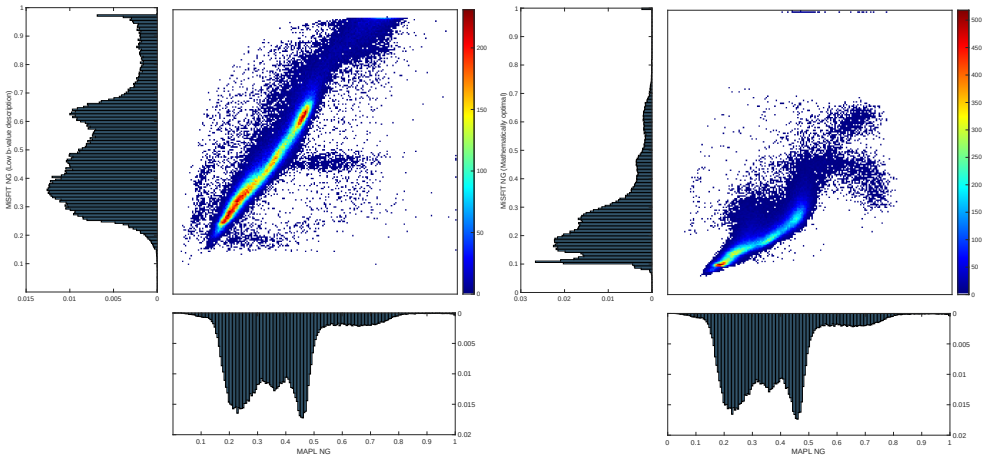

Fig. 6.11.: 2D joint histograms of the NG maps obtained with the two implementations (current implementation, low b-value description, in the left; mathematically optimal, right) against the MAPL's NG. Pearson correlation coefficient is included.

the NG computed with both implementations against the MAPL's map together with both Pearson coefficients. As it can be seen, there is more similarity between MAPL's NG and the current implementation of the NG than the mathematically optimal one.

Bibliography

[6.1] Tristán-Vega A, Aja-Fernández S. Efficient and accurate EAP imaging from multi-shell dMRI with micro-structure adaptive convolution kernels and dual Fourier Integral Transforms (MiSFIT). NeuroImage 2021;227. doi:10.1016/j.neuroimage.2020.117616.

[6.2] Novikov DS, Kiselev VG, Jespersen SN. On modeling 2018. doi:10.1002/mrm.27101.

[6.3] Callaghan PT. Principles of Nuclear Magnetic Resonance Microscopy. Clarendon Press, Oxford, 1991.

[6.4] Wu YC, Alexander AL. Hybrid diffusion imaging. NeuroImage 2007;36:617–629. doi:10.1016/j.neuroimage.2007.02.050.

[6.5] Fick RH, Wassermann D, Caruyer E, Deriche R. MAPL: Tissue microstructure estimation using Laplacian-regularized MAP-MRI and its application to HCP data. NeuroImage 2016;134:365–385. doi:10.1016/j.neuroimage.2016.03.046.

[6.6] Ning L, Westin CF, Rathi Y. Estimating diffusion propagator and its moments using directional radial basis functions. IEEE transactions on medical imaging 2015;34:2058–2078.

[6.7] Özarslan E, Koay CG, Shepherd TM, Komlosh ME, Irfanoglu MO, Pierpaoli C, Basser PJ. Mean apparent propagator (MAP) MRI: A novel diffusion imaging method for mapping tissue microstructure. NeuroImage 2013;78:16–32. doi:10.1016/j.neuroimage.2013.04.016.

[6.8] Galazzo IB, Brusini L, Obertino S, Zucchelli M, Granziera C, Menegaz G. On the viability of diffusion MRI-based microstructural biomarkers in ischemic stroke. Frontiers in Neuroscience 2018;12. doi:10.3389/fnins.2018.00092.

[6.9] Avram AV, Sarlls JE, Barnett AS, Özarslan E, Thomas C, Irfanoglu MO, Hutchinson E, Pierpaoli C, Basser PJ. Clinical feasibility of using mean apparent propagator (MAP) MRI to characterize brain tissue microstructure. NeuroImage 2016;127:422–434. doi:https://doi.org/10.1016/j.neuroimage.2015.11.027.

[6.10] Kraus MF, Susmaras T, Caughlin BP, Walker CJ, Sweeney JA, Little DM. White matter integrity and cognition in chronic traumatic brain injury: A diffusion tensor imaging study. Brain 2007;130:2508–2519. doi:10.1093/brain/awm216.

[6.11] Barnea-Goraly N, Kwon H, Menon V, Eliez S, Lotspeich L, Reiss AL. White matter structure in autism: Preliminary evidence from diffusion tensor imaging. Biological Psychiatry 2004;55:323–326. doi:10.1016/j.biopsych.2003.10.022.

[6.12] Fick RHJ, Daianu M, Pizzolato M, Wassermann D, Jacobs RE, Thompson PM, Town T, Deriche R. Comparison of biomarkers in transgenic alzheimer rats using multi-shell diffusion MRI. Mathematics and Visualization 2017;pp. 187–199. doi:10.1007/978-3-319-54130-3_16.

[6.13] Wang P, Weng L, Xie S, He J, Ma X, LI B, Yuan P, Wang S, Zhang H, Gao Y, Wu Q, Niu G. Primary application of mean apparent propagator-MRI diffusion model in the grading of diffuse glioma. European Journal of Radiology 2021;138:109622. doi:10.1016/j.ejrad.2021.109622.

[6.14] Song SK, Yoshino J, Le TQ, Lin SJ, Sun SW, Cross AH, Armstrong RC. Demyelination increases radial diffusivity in corpus callosum of mouse brain. NeuroImage 2005;26:132–140. doi:https://doi.org/10.1016/j.neuroimage.2005.01.028.

[6.15] Jansen JF, Stambuk HE, Koutcher JA, Shukla-Dave A. Non-Gaussian analysis of diffusion-Weighted MR imaging in head and neck squamous cell carcinoma: A feasibility study. American Journal of Neuroradiology 2010;31:741–748. doi:10.3174/AJNR.A1919.

[6.16] Yuan J, Yeung DKW, Mok GS, Bhatia KS, Wang YXJ, Ahuja AT, King AD. Non-Gaussian analysis of diffusion weighted imaging in head and neck at 3T: a pilot study in patients with nasopharyngeal carcinoma. PloS one 2014;9. doi:10.1371/JOURNAL.PONE.0087024.

[6.17] Koller K, Rudrapatna U, Chamberland M, Raven EP, Parker GD, Tax CMW, Drakesmith M, Fasano F, Owen D, Hughes G, Charron C, Evans CJ, Jones DK. MICRA: Microstructural image compilation with repeated acquisitions. NeuroImage 2021;225:117406. doi:10.1016/j.neuroimage.2020.117406.

[6.18] Kellner E, Dhital B, Kiselev VG, Reisert M. Gibbs-ringing artifact removal based on local subvoxel-shifts. Magnetic resonance in medicine 2016;76:1574–1581.

[6.19] Tournier JD, Smith R, Raffelt D, Tabbara R, Dhollander T, Pietsch M, Christiaens D, Jeurissen B, Yeh CH, Connelly A. MRtrix3: A fast, flexible and open software framework for medical image processing and visualisation. Neuroimage 2019;202:116137.

[6.20] Andersson JL, Skare S, Ashburner J. How to correct susceptibility distortions in spin-echo echo-planar images: application to diffusion tensor imaging. Neuroimage 2003;20:870–888.

[6.21] Smith SM, Jenkinson M, Woolrich MW, Beckmann CF, Behrens TE, Johansen-Berg H, Bannister PR, De Luca M, Drobnjak I, Flitney DE, *et al.* Advances in functional and structural MR image analysis and implementation as FSL. Neuroimage 2004;23:S208–S219.

[6.22] Zhang Y, Brady M, Smith S. Segmentation of brain MR images through a hidden markov random field model and the expectation-maximization algorithm. IEEE Transactions on Medical Imaging 2001;20:45–57.

[6.23] Zhang H, Schneider T, Wheeler-Kingshott CA, Alexander DC. NODDI: Practical in vivo neurite orientation dispersion and density imaging of the human brain. NeuroImage 2012;61:1000–1016. doi:10.1016/j.neuroimage.2012.03.072.

[6.24] Zuo XN, Xu T, Milham MP. Harnessing reliability for neuroscience research. Nature Human Behaviour 2019;3. doi:10.1038/s41562-019-0655-x.

[6.25] Mori S, Oishi K, Jiang H, Jiang L, Li X, Akhter K, Hua K, Faria AV, Mahmood A, Woods R, *et al.* Stereotaxic white matter atlas based on diffusion tensor imaging in an icbm template. Neuroimage 2008;40:570–582.

[6.26] Smith SM, Jenkinson M, Woolrich MW, Beckmann CF, Behrens TE, Johansen-Berg H, Bannister PR, De Luca M, Drobnjak I, Flitney DE, *et al.* Advances in functional and structural mr image analysis and implementation as FSL. Neuroimage 2004;23:S208–S219.

[6.27] Jenkinson M, Smith S. A global optimisation method for robust affine registration of brain images. Medical image analysis 2001;5:143–156.

[6.28] Jenkinson M, Bannister P, Brady M, Smith S. Improved optimization for the robust and accurate linear registration and motion correction of brain images. Neuroimage 2002;17:825–841.

[6.29] Harville DA. Matrix algebra from a statistician's perspective. Springer, 1997. ISBN 038794978X.

7

HYDI-DSI revisited: constrained non-parametric EAP imaging without q-space re-gridding

Antonio Tristán-Vega, Tomasz Pieciak, Guillem París, Justino R. Rodríguez-Galván, Santiago Aja-Fernández

LPI, ETSI Telecomunicación, Universidad de Valladolid, Spain

Abstract: Hybrid Diffusion Imaging (HYDI) was one of the first attempts to use multi-shell samplings of the q-space to infer diffusion properties beyond Diffusion Tensor Imaging (DTI) or High Angular Resolution Diffusion Imaging (HARDI). HYDI was intended as a flexible protocol embedding both DTI (for lower b-values) and HARDI (for higher b-values) processing, as well as Diffusion Spectrum Imaging (DSI) when the entire data set was exploited. In the latter case, the spherical sampling of the q-space is re-gridded by interpolation to a Cartesian lattice whose extent covers the range of acquired b-values, hence being acquisition-dependent. The Discrete Fourier Transform (DFT) is afterwards used to compute the corresponding Cartesian sampling of the Ensemble Average Propagator (EAP) in an entirely non-parametric way. From this lattice, diffusion markers such as the Return To Origin Probability (RTOP) or the Mean Squared Displacement (MSD) can be numerically estimated.

We aim at re-formulating this scheme by means of a Fourier Transform encoding matrix that eliminates the need for q-space re-gridding at the same time it preserves the non-parametric nature of HYDI-DSI. The encoding matrix is adaptively designed at each voxel according to the underlying DTI approximation, so that an optimal sampling of the EAP can be pursued without being conditioned by the particular acquisition protocol. The estimation of the EAP is afterwards carried out as a regularized Quadratic Programming (QP) problem, which allows to impose positivity constraints that cannot be trivially embedded within the conventional HYDI-DSI. We demonstrate that the definition of the encoding matrix in the adaptive space allows to analytically (as opposed to numerically) compute several popular descriptors of diffusion with the unique source of error being the cropping of high frequency harmonics in the Fourier analysis of the attenuation signal. They include not only RTOP and MSD, but also Return to Axis/Plane Probabilities (RTAP/RTPP), which are defined in terms of specific spatial directions and are not available with the former HYDI-DSI. We report extensive experiments that suggest the benefits of our proposal in terms of accuracy, robustness and computational efficiency, especially when only standard, non-dedicated q-space samplings are available.

Originally published as: *Antonio Tristán-Vega, Tomasz Pieciak, Guillem París, Justino R. Rodríguez-Galván, Santiago Aja-Fernández, HYDI-DSI revisited: Constrained non-parametric EAP imaging without q-space re-gridding, Medical Image Analysis, Vol. 84, 102728, 2023.*

7.1 Introduction

Diffusion Magnetic Resonance Imaging (dMRI) allows probing the random movement of water molecules inside human tissues, especially the white matter of the brain, *in vivo*. The basic dMRI sequence comprises two pulsed gradients with duration δ taken apart an idle time Δ, with a re-focusing 180^o RF pulse in between [7.51]. This way, water molecules moving along the applied gradient will experiment a net de-phasing that translates in the attenuation of the acquired T2 signal with respect to the unweighted one (the so-called baseline). The *strength* of this effect, characterized by the so-called b-value, increases linearly with Δ, and quadratically with δ and the magnitude $\|\mathbf{G}\|$ of the gradient applied.

This kind of contrast has been thoroughly used in clinical research to characterize a number of pathologies such as Alzheimer's disease [7.18, 7.24], Parkinson's disease [7.1], Traumatic Brain Injury (TBI) [7.65, 7.40], stroke [7.14, 7.15], multiple sclerosis [7.28], migraine [7.48, 7.47], and many others. Though a minimum of six gradient directions with a constant b-value suffices to probe the meso-structural anisotropy of the white matter, the advent of more sophisticated MRI machinery and acquisition protocols has led into the routine acquisition of advanced data sets with several hundreds of diffusion gradients with varying directions but also varying b-values. Among them, multi-shell data sets, i.e. acquisitions where the acquired gradients are arranged in a regular spherical lattice, have rapidly become the standard. Indeed, several databases with both healthy and diseased subjects have been publicly issued in the last few years [7.29, 7.58, 7.69, 7.23, 7.26, 7.52, 7.34].

Two complementary approaches have focused the recent research on advanced dMRI [7.42]: the first one aims at modeling the diffusion signal as a mixture of micro-structural compartments whose responses can be individually modeled, so that their partial volume fractions and individual features can be disentangled from the diffusion measurements. This group includes, to name but a few, the Composite Hindered and Restricted Model for Diffusion [7.4, CHARMED], the Neurite Orientation Dispersion and Density Imaging [7.68, NODDI], or the Multi-tissue Constrained Spherical Deconvolution [7.32, CSD]. These methods have the advantage of providing directly interpretable micro-structural features, and also explaining both the low and the high b-value regimen of the diffusion signal and, in particular, its slow decaying tails. On the other hand, they give rise to ill-posed optimization problems that are often simplified resorting to modeling assumptions such as minimum tortuosity [7.68, 7.33]. These suppositions, however, have been empirically evidenced to largely deviate from reality [7.35].

The second group of techniques generalize the *classical* Diffusion Tensor Imaging (DTI) approach [7.8, 7.9] by drawing signal representations, as opposed to geometrical models, such as mono-exponentials [7.3, 7.2], multi-exponentials [7.46, 7.10], or DTI distributions [7.54]. In particular, Ensemble Average Propagator (EAP) imaging is a very active research field within this second trend: the EAP, $P(\mathbf{R})$, is a positive, unit-mass, antipodal-symmetric probability density function related to the positive, antipodal-symmetric attenuation signal $E(\mathbf{q}) = S(\mathbf{q})/S_0$ (with $S(\mathbf{q})$ the signal acquired when a gradient wave-vector

$\mathbf{q}$, $\|\mathbf{q}\| \propto \delta \|\mathbf{G}\|$, is applied, and S_0 the unweighted T2 baseline image), as a pair of Fourier transforms [7.16]:

$$P(\mathbf{R}) = \iiint_{\mathbb{R}^3} E(\mathbf{q}) \exp\left(-j2\pi\mathbf{q}^T\mathbf{R}\right) d\mathbf{q} \overset{\tau}{\longleftrightarrow} E(\mathbf{q}) = \iiint_{\mathbb{R}^3} P(\mathbf{R}) \exp\left(j2\pi\mathbf{q}^T\mathbf{R}\right) d\mathbf{R}, \tag{7.1}$$

where $\tau = \Delta - \delta/3$ is the effective diffusion time. For the previous equation to be fulfilled in terms of classical functions, $E(\mathbf{q})$ must rapidly vanish as $\|\mathbf{q}\| \to \infty$, so that it remains square-integrable and $P(\mathbf{R})$ does not comprise Dirac's delta-like singularities [7.43]. As pointed out by [7.42], this issue makes EAP imaging inherently incompatible with actual models for intra-axonal diffusion, as long as the signal produced by confined water compartments is heavy-tailed. Within DTI, the EAP is represented as a zero-mean Gaussian process with covariance matrix D, which is a 3×3 rank-2 tensor, symmetric, positive (semi)-definite, and independent on the effective diffusion time τ [7.8, 7.9]:

$$P_G(\mathbf{R}) = \frac{1}{\sqrt{\det(D)\,(4\pi\tau)^3}} \exp\left(-\frac{\mathbf{R}^T D^{-1}\mathbf{R}}{4\tau}\right) \longleftrightarrow E_G(\mathbf{q}) = \exp\left(-4\pi^2\tau\mathbf{q}^T D\mathbf{q}\right), \tag{7.2}$$

where the b-value is defined as $b = 4\pi^2\tau\|\mathbf{q}\|^2$. Diffusion Spectrum Imaging (DSI) was aimed at avoiding the limitations of the model in eq. (7.2) by attaining a non-parametric sampling of $P(\mathbf{R})$ at a regular Cartesian lattice [7.61]. The straightforward approach is sampling $E(\mathbf{q})$ itself in a regular lattice and using the Discrete Fourier Transform (DFT) to find estimates of $P(\mathbf{R})$, which implies acquiring a huge amount of q-space samples to avoid aliasing artifacts. Alternatively, Compressed Sensing (CS) techniques can be used to vastly reduce this demand [7.12, 7.37, 7.67] as long as a *non-coherent* sampling of the whole q-space is available and the EAP can be sparsely represented in a certain function basis [7.22]. Since we are mostly interested in multi-shell samplings with a relatively small maximum b-value, the former requirement is hardly met.

Many EAP imaging techniques circumvent the lack of a detailed q-space sampling by assuming the EAP and the attenuation signal can be faithfully represented as a superposition of pre-designed basis functions (dictionary atoms) whose 3-D Fourier transforms may be easily characterized. This approach includes multiple q-shell Diffusion Propagator Imaging [7.21, mq-DPI], Bessel-Fourier Orientation Reconstruction [7.27, BFOR], Spherical Polar Fourier reconstruction [7.5, 7.38, SPF], Simple Harmonic Oscillator based Reconstruction and Estimation [7.44, SHORE], Mean Apparent Propagator MRI [7.45, MAP-MRI] and its Laplacian-regularized version [7.25, MAPL], or directional Radial Basis Functions [7.41, RBF]. Patch-based dictionary learning, as opposed to dictionary design, has also been used to low-rank represent the attenuation signal [7.59].

The general idea behind these techniques is that the attenuation signal $E(\mathbf{q})$ can be written as the linear superposition of a relatively small number of parametric continuous functions, whose shape and size parameters can be either pre-defined [7.5, 7.38], learned [7.59], adaptively fitted depending on the diffusion profile at each voxel [7.45, 7.25], or even dynamically computed at the same time as the coefficients of the linear combination [7.41]. Afterwards, the linearity of the Fourier transform can be exploited to apply the same linear combination to the Fourier transforms of the basis functions and conversely represent the EAP as a linear mixture of parametric continuous functions. Provided the reduced number of q-space samples, together with the poor Signal-to-Noise Ratio (SNR) commonly found in

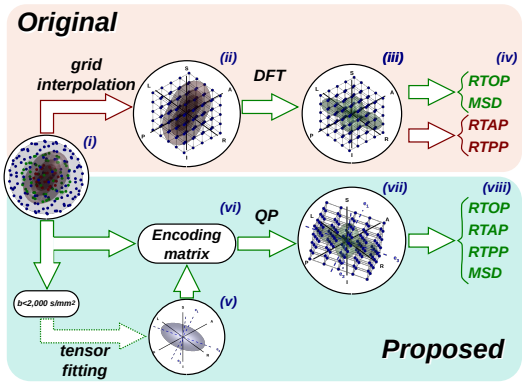

Fig. 7.1.: The original HYDI-DSI vs. our proposal. Red arrows highlight those steps in the original method resorting to numerical interpolation (those we aim to avoid).

dMRI volumes, it is common to find regularization penalties in the estimation of the linear coefficients that describe $E(\mathbf{q})$, as well as constraints such as positivity or unit mass of the EAP [7.19]. More recently, the Micro-Structure adaptive kernels and dual Fourier Integral Transforms [7.55, MiSFIT] has allowed to dramatically reduce the complexity of EAP imaging by representing it as the spherical convolution of a fiber Orientation Distribution Function (fODF) with a Gaussian kernel. Nonetheless, this technique applies only to multi-shell acquisitions, but not to more general protocols.

All the above methods share the same philosophy of representing the low-pass EAP parametrically, as a mixture of continuous domain functions. As opposed, DSI and Hybrid Diffusion Imaging-based DSI [7.62, 7.63, HYDI-DSI] tackle the problem in a different, straightforward way, as it is depicted in Fig. 7.1 (top): the (still low-pass) EAP is no longer represented by means of a collection of parameters describing a continuous mixture, but instead a discrete sampling of the EAP at a regular 3-D lattice (typically $9 \times 9 \times 9$) is pursued. To that end, a corresponding lattice is defined over the attenuation signal domain (*ii*), whose support comes determined by the maximum b-value, b_{max}, acquired in the multi-shell sampling (*i*), i.e. $E(\mathbf{q})$ is assumed to *live* inside $\Omega = [-q_{\text{max}}, q_{\text{max}}]^3 \subset \mathbb{R}^3$, where $q_{\text{max}} = \sqrt{b_{\text{max}}/4\pi^2\tau}$. The values of $E(\mathbf{q})$ at these lattice points are obtained by means of grid interpolation: the convex hull of the sampled data is calculated [7.7], and Delaunay triangulation is used to parcel it [7.60]. The problem then reduces to the linear interpolation of each lattice node depending on the parcel it lies within. Finally, the DFT can be computed to retrieve a $9 \times 9 \times 9$ lattice in the EAP domain (*iii*) with spatial resolution $(1/2q_{\text{max}})^3$ [7.43].

Despite its success in describing the anatomy of the white matter in many situations such as TBI [7.65, 7.40], Alzheimer's disease [7.18], or gender/age-related changes [7.64], this scheme is not free of certain problems. The first one is that the bandwidth of the EAP, defined by Ω, directly depends on the acquisition protocol, and more specifically on the maximum b-value acquired. Indeed, the original HYDI-DSI imposes a specific acquisition protocol with evenly spaced shells up to $b_{\text{max}} \simeq 10,000\,\text{s/mm}^2$, so that the lattice interpolation is rather uniform (meaning that each measured q-space sample will be used equally often for interpolation). Additionally, though the unit-mass constraint of the EAP is guaranteed by the DFT operator by simply placing $E(\mathbf{0}) = 0$, positivity constraints cannot be pursued. Such constraints have been proven especially meaningful within dMRI [7.19]. Finally, the analytical computations of the popular Return to Origin Probability (RTOP) or Mean Squared

Displacement (MSD) are straightforward with HYDI-DSI, but the Return to Axis/Plane Probabilities (RTAP/RTPP) need to be computed as line/plane integrals in the EAP domain, leading to the need for interpolation of the computed lattice values (*iv*).

In the present paper, we explore an alternative approach to get rid of q-space interpolation while maintaining the non-parametric nature of HYDI-DSI, see Fig. 7.1 (bottom). Following the same idea by [7.45], the DTI representation is used to describe the low b-value regime of the attenuation signal (*v*): the eigenvectors and eigenvalues at each voxel are used to rotate and stretch the 3-D space so that the EAP is estimated in an adaptive grid determined by the diffusion properties of the voxel instead of the gradients table (*vii*). The aim is palliating the dependency of the estimated EAP with the acquisition protocol. To avoid the need for q-space interpolation, the sparsely sampled q-space (*i*) is analytically related to the adaptive EAP lattice (*vii*) by means of the so-called encoding matrix (*vi*). This way, the nodal values of the EAP can be directly solved from the q-space samples by solving a Quadratic Programming (QP) problem. The advantage of doing so is two-fold: first, not only unit mass, but also positivity constraints, can be imposed to the EAP. Additionally, by avoiding the computation of the convex hull and Delaunay's triangulation we attain a vast improvement of the overall computational efficiency. Besides, we derive a regularization term based on the energy of the Laplacian of the EAP to deal with low SNR and/or poor sampling density of the q-space. Finally, we demonstrate that the adaptive grid strategy allows the analytical computation of all the RTxP and MSD indices without any further interpolation (*viii*).

The remainder of the paper is organized as follows. Section 7.2 details steps *v*–*vii* in Fig. 7.1 (bottom), namely: the arrangement of the adaptive 3-D lattice based on the DTI approximation (Section 7.2.1), the definition of the encoding matrix (Sections 7.2.2 and 7.2.3), and the QP problem statement (Section 7.2.4). Section 7.3 details step *viii*, i. e. the computation of the RTxP and MSD. Section 7.4 describes the numerical implementation of the proposed method and the parameters involved. The qualitative and quantitative evaluation of the proposal is addressed in Section 7.5. Finally, in Section 7.6 we provide some additional insights into the potential and the limitations of our proposal, as well as its differences and similarities with the related state of the art.

7.2 EAP reconstruction from scattered multi-shell data

7.2.1 Adapting the Cartesian grid to the voxel properties

The DTI model provides a good approximation of the diffusion process for b-values under $2,000\,\mathrm{s/mm^2}$. We will assume our q-space sampling includes at least one shell suitable for DTI, so that a diffusion tensor D can be estimated at each voxel to accurately describe the low b-values regime:

$$D = \Theta\Lambda\Theta^T;\;\; \Theta = [\mathbf{u}_1, \mathbf{u}_2, \mathbf{u}_3];\;\; \Lambda = \begin{bmatrix} \lambda_1 & 0 & 0 \\ 0 & \lambda_2 & 0 \\ 0 & 0 & \lambda_3 \end{bmatrix}, \tag{7.3}$$

where $0 \leq \lambda_1 \leq \lambda_2 \leq \lambda_3$ are the three real, non-negative eigenvalues of D and $\mathbf{u}_1$, $\mathbf{u}_2$, and $\mathbf{u}_3$ are their respective 3×1, unit-norm, mutually orthogonal eigenvectors. Besides, we will

force $\mathbf{u}_3$ to have the proper orientation so that $\mathbf{u}_3 = \mathbf{u}_1 \times \mathbf{u}_2$ and Θ is a rotation matrix (hence $\det(\Theta) = 1$). We can use this rotation afterwards to align the Cartesian lattice where the EAP will be sampled with the principal directions of D: with the change of variable: $\mathbf{R}' = \Theta^T\mathbf{R} \Leftrightarrow \mathbf{R} = \Theta\mathbf{R}'$, the maximum diffusion direction will become aligned with the 'z' axis, while the secondary diffusion directions will align with 'x' and 'y':

$$\begin{aligned} &P_\Theta(\mathbf{R}') = P(\Theta\mathbf{R}') \Leftrightarrow P(\mathbf{R}) = P_\Theta(\Theta^T\mathbf{R}); \\ &E_\Theta(\mathbf{q}') = \iiint_{\mathbb{R}^3} P_\Theta(\mathbf{R}') \exp\left(j2\pi{\mathbf{q}'}^T\mathbf{R}'\right) d\mathbf{R}' \\ &\quad \overset{\mathbf{R}'=\Theta^T\mathbf{R}}{=} \iiint_{\mathbb{R}^3} P(\mathbf{R}) \exp\left(j2\pi{\mathbf{q}'}^T\Theta^T\mathbf{R}\right) d\mathbf{R} = E(\Theta\mathbf{q}'). \end{aligned} \tag{7.4}$$

The meaning of the previous equation is that, without any loss of generality, we can assume the Gaussian approximation of the EAP is aligned with the Cartesian axes ('z' being the maximum diffusion direction). It suffices to apply a voxel-dependent rotation Θ^T to the 'gradients table' of the multi-shell sampling, $\mathbf{u}' = \Theta^T\mathbf{u}$, so that:

$$\begin{aligned} P_{G,\Theta}(\mathbf{R}') &= \frac{1}{\sqrt{\det(\Lambda)\,(4\pi\tau)^3}} \exp\left(-\frac{{\mathbf{R}'}^T\Lambda^{-1}\mathbf{R}'}{4\tau}\right) \\ &= \frac{1}{\sqrt{\lambda_1\lambda_2\lambda_3\,(4\pi\tau)^3}} \exp\left(\frac{-x^2}{4\tau\lambda_1}\right) \exp\left(\frac{-y^2}{4\tau\lambda_2}\right) \exp\left(\frac{-z^2}{4\tau\lambda_3}\right); \\ E_{G,\Theta}(\mathbf{q}') &= \exp\left(-4\pi^2\tau{\mathbf{q}'}^T\Lambda\mathbf{q}'\right) = \exp\left(-4\pi^2\tau\lambda_1 q_x^2\right) \exp\left(-4\pi^2\tau\lambda_2 q_y^2\right) \exp\left(-4\pi^2\tau\lambda_3 q_z^2\right) \end{aligned} \tag{7.5}$$

for $\mathbf{R}' = [x, y, z]^T$ and $\mathbf{q}' = [q_x, q_y, q_z]^T$.

7.2.2 Relating the (rotated) q-space to the (rotated) EAP domain

We will assume the attenuation signal is compact supported, i. e. the value of $E_\Theta(\mathbf{q}')$ vanishes to zero outside the 3-D domain $\Omega = (-\frac{Q_x}{2}, \frac{Q_x}{2}) \times (-\frac{Q_y}{2}, \frac{Q_y}{2}) \times (-\frac{Q_z}{2}, \frac{Q_z}{2}) \subset \mathbb{R}^3$. This allows to arrange a 3-D tiling with shifted versions of $E_\Theta(\mathbf{q}')$ to build a periodic signal in the three coordinates $\{q_x, q_y, q_z\}$:

$$\tilde{q}_u = q_u - Q_u \left\lceil \frac{q_u - Q_u/2}{Q_u} \right\rceil \text{ for } u \in \{x, y, z\} \Rightarrow \widetilde{E}_\Theta(\mathbf{q}') = E_\Theta(\tilde{\mathbf{q}}'), \text{ for } \tilde{\mathbf{q}}' = [\tilde{q}_x, \tilde{q}_y, \tilde{q}_z]^T \tag{7.6}$$

Assuming $\widetilde{E}_\Theta$ has finite power, it can be written in terms of its 3-D Fourier series expansion [7.43]:

$$\widetilde{E}_\Theta(\mathbf{q}') = \sum_{k=-\infty}^{\infty} \sum_{l=-\infty}^{\infty} \sum_{m=-\infty}^{\infty} c_{k,l,m} \exp\left(j2\pi\left(\frac{k}{Q_x}q_x + \frac{l}{Q_y}q_y + \frac{m}{Q_z}q_z\right)\right), \tag{7.7}$$

where the coefficients c_{klm} are computed by projecting $\widetilde{E}_\Theta$ onto each normalized basis function:

$$\begin{aligned} c_{k,l,m} &= \frac{1}{Q}\iiint_\Omega \widetilde{E}_\Theta(\mathbf{q}')\exp\left(-j2\pi\left(\frac{k}{Q_x}q_x+\frac{l}{Q_y}q_y+\frac{m}{Q_z}q_z\right)\right)d\mathbf{q}' \\ &= \frac{1}{Q}\iiint_{\mathbb{R}^3} E_\Theta(\mathbf{q}')\exp\left(-j2\pi\mathbf{q}'^T\mathbf{R}'_{k,l,m}\right)d\mathbf{q}' = \frac{1}{Q}P_\Theta(\mathbf{R}'_{k,l,m}), \end{aligned} \tag{7.8}$$

where $Q = Q_xQ_yQ_z$ and $\mathbf{R}'_{k,l,m} = [k/Q_x, l/Q_y, m/Q_z]^T$ draws a regular lattice in the space of the EAP. Eqs. (7.7) and (7.8) can now be combined to establish the linear relation between the measurements in the q-space and the values of the EAP to estimate. Since $\widetilde{E}_\Theta$ is real and antipodal symmetric, a cosine series expansion may be used:

$$\widetilde{E}_\Theta(\mathbf{q}') = \frac{1}{Q}\sum_{k=-\infty}^{\infty}\sum_{l=-\infty}^{\infty}\sum_{m=-\infty}^{\infty} P_\Theta(\mathbf{R}'_{k,l,m})\cos\left(2\pi\mathbf{q}'^T\mathbf{R}'_{k,l,m}\right). \tag{7.9}$$

7.2.3 Building the encoding matrix

Eq. (7.9) will be used to estimate a Cartesian sampling of the EAP from a spherical multi-shell q-space sampling, $\{\mathbf{q}'_i \in \Omega\}_{i=1}^{N_i}$. Since the available number of q-samples is limited, so it is the number of lattice nodes we can actually estimate for the EAP, and in practice the Fourier series expansion will be cropped to its first few coefficients assuming $\widetilde{E}_\Theta$ is smooth enough:

$$\widetilde{E}_\Theta(\mathbf{q}') \simeq \frac{1}{Q}\sum_{k=-N_x}^{N_x}\sum_{l=-N_y}^{N_y}\sum_{m=-N_z}^{N_z} P_\Theta(\mathbf{R}'_{k,l,m})\cos\left(2\pi\mathbf{q}'^T\mathbf{R}'_{k,l,m}\right), \tag{7.10}$$

so that $2N_x+1$ samples evenly spaced $1/Q_x$ should cover the entire 'x' axis of the EAP domain; $2N_y+1$ samples, one each $1/Q_y$ should cover the 'y' axis; $2N_z+1$ samples, one each $1/Q_z$ should cover the 'z' axis. This means that the compact support of E_Θ is constrained by the number of lattice nodes along each dimension, which in turn is related to the available number of q-space samples, N_i. In precise terms:

- If the EAP is roughly compact supported at (i. e. it has negligible values outside of) the 3-D domain $[-\frac{X}{2},\frac{X}{2}]\times[-\frac{Y}{2},\frac{Y}{2}]\times[-\frac{Z}{2},\frac{Z}{2}]$, sampling its entire support will demand:

$$\frac{N_x}{Q_x}=\frac{X}{2}\Rightarrow Q_x=\frac{2N_x}{X};\qquad \frac{N_y}{Q_y}=\frac{Y}{2}\Rightarrow Q_y=\frac{2N_y}{Y};\qquad \frac{N_z}{Q_z}=\frac{Z}{2}\Rightarrow Q_z=\frac{2N_z}{Z}, \tag{7.11}$$

  so that any q-samples with either $|q_x|>\frac{Q_x}{2}$, $|q_y|>\frac{Q_y}{2}$, or $|q_z|>\frac{Q_z}{2}$ will be discarded since they must be assumed to be 0. Obviously, the larger N_x, N_y, and N_z, the fewer q-samples will need to be discarded. However:

- $N_l = (2N_x+1)(2N_y+1)(2N_z+1)$ should be in the same order as N_i so that the number of parameters to estimate is not vastly greater than the number of measurements (in the absence of regularization, $N_l \leq N_i$ indeed).

Fortunately, the antipodal symmetry of the EAP ($P_\Theta(\mathbf{R}') = P_\Theta(-\mathbf{R}')$) allows to nearly halve the number of Degrees of Freedom (DoF) to estimate. From eq. (7.10), a simple reordering of the addends yields:

$$\begin{aligned} E_\Theta(\mathbf{q}') \simeq \frac{1}{Q}\Bigg(& P_\Theta(\mathbf{0}) + 2\sum_{k=1}^{N_x} P_\Theta(\mathbf{R}'_{k,0,0}) \cos\left(2\pi {\mathbf{q}'}^T \mathbf{R}'_{k,0,0}\right) \\ & +2\sum_{k=-N_x}^{N_x}\sum_{l=1}^{N_y} P_\Theta(\mathbf{R}'_{k,l,0}) \cos\left(2\pi {\mathbf{q}'}^T \mathbf{R}'_{k,l,0}\right) \\ & +2\sum_{k=-N_x}^{N_x}\sum_{l=-N_y}^{N_y}\sum_{m=1}^{N_z} P_\Theta(\mathbf{R}'_{k,l,m}) \cos\left(2\pi {\mathbf{q}'}^T \mathbf{R}'_{k,l,m}\right)\Bigg). \end{aligned} \tag{7.12}$$

Hence, the actual number of DoF to estimate is $n = 1 + N_x + (2N_x+1)N_y + (2N_x+1)(2N_y+1)N_z = (N_l+1)/2$. Now, let us substitute the triple indexing $\{k,l,m\}$ of the lattice with a unique index j by simply stacking its nodes in order:

$$\begin{aligned} \left\{\mathbf{R}'_j\right\}_{j=1}^{n} &= \{\mathbf{R}'_1, \mathbf{R}'_2, \ldots, \mathbf{R}'_n\} \\ &\equiv \Big\{\mathbf{R}'_{0,0,0}, \ldots, \mathbf{R}'_{N_x,0,0}, \mathbf{R}'_{0,1,0}, \ldots, \mathbf{R}'_{N_x,1,0}, \ldots, \mathbf{R}'_{N_x,N_y,0}, \\ &\qquad \mathbf{R}'_{-N_x,-N_y,1}, \ldots, \mathbf{R}'_{N_x,-N_y,1}, \ldots, \mathbf{R}'_{N_x,N_y,1}, \ldots, \mathbf{R}'_{N_x,N_y,N_z}\Big\} \end{aligned} \tag{7.13}$$

The $N_i \times n$ encoding matrix $\mathcal{F}$ relates the $N_i \times 1$ vector of measurements, $\mathbf{E} = [E_\Theta(\mathbf{q}'_1), \ldots, E_\Theta(\mathbf{q}'_{N_i})]^T$, with the $n \times 1$ vector of unknowns, $\mathbf{P} = [P_\Theta(\mathbf{R}'_1), \ldots, P_\Theta(\mathbf{R}'_n)]^T$. After eq. (7.12):

$$\mathbf{E} \simeq \mathcal{F}\,\mathbf{P} \;:\; [\mathcal{F}]_{i,j} = \frac{\kappa_j}{Q} \cos\left(2\pi {\mathbf{q}'_i}^T \mathbf{R}'_j\right), \tag{7.14}$$

where $\kappa_j = 1$ if $j = 0$ or $\kappa_j = 2$ otherwise. Finally, it is worth noticing the actual number of samples N_i may be voxel-dependent in case certain q-space samples lay outside the allowed bandwidth defined by Q_x, Q_y, and Q_z at each voxel.

7.2.4 Estimating the EAP from the encoding matrix

Eq. (7.14) establishes a linear relation between the vector of measurements $\mathbf{E}$ and the vector of unknowns $\mathbf{P}$ that allows solving for the latter with linear Least Squares (LS) techniques. However, two additional requirements must be fulfilled for the solution to be physically meaningful: positivity and unit mass. For the former, we will constrain all the entries of $\mathbf{P}$ to be non-negative. For the latter, we note that the unit mass property of the EAP is equivalent to the attenuation signal evaluating to 1 at the origin $\mathbf{q}'_0 = \mathbf{0}$. Thus, the following QP problem arises:

$$\min_{\mathbf{P}} \; \frac{1}{2}\left\|\mathbf{E} - \mathcal{F}\mathbf{P}\right\|^2 \text{ s. t. } \mathbf{P} \geq 0 \text{ and } f_0^T \mathbf{P} = 1, \tag{7.15}$$

where the $N_l \times 1$ vector $f_0 = \frac{1}{Q}[1, 2, \ldots, 2]^T$ stands for an additional row of the encoding matrix at $\mathbf{q}'_0 = \mathbf{0}$. Nonetheless, these reconstruction problems often require some sort of regularization: first, the measurements vector $\mathbf{E}$ is highly contaminated with noise. This is

addressed by [7.62, 7.63] by just dropping down to 0 those values of the diffusion weighted images below a certain threshold (usually, twice the free-air average signal). In our case, we cannot forget that the actual number of samples, N_i, is voxel-dependent since out-of-bandwidth samples are removed, so that the QP in eq. (7.15) might even become ill-posed. For these reasons, the QP problem will be reformulated as follows:

$$\min_{\mathbf{P}} \frac{1}{2}\|\mathbf{E}-\mathcal{F}\mathbf{P}\|^2+\frac{\lambda}{2}\|\mathcal{L}\mathbf{P}\|^2 \text{ s. t. } \mathbf{P}\geq 0 \text{ and } f_0^T\mathbf{P}=1, \tag{7.16}$$

where $\lambda > 0$ is a *small* positive constant and $\mathcal{L}$ is some linear operator. We will resort to a Laplacian penalty, described in Appendix 7.A, as a popular choice to promote the smoothness of the solution [7.20, 7.17, 7.25]. Note eq. (7.16) describes a convex problem, so that a unique optimum exists [7.36].

7.3 Computation of diffusion markers from the Cartesian EAP

Once the EAP is fully sampled in its whole domain, any numerical feature at will can be estimated from it. In this section we derive expressions for several commonly used diffusion markers: the RTOP and MSD, like [7.63] do, but also the RTAP and the RTPP.

7.3.1 RTOP

Since the RTOP (or Po) is defined as the value of the EAP at the origin, it may be trivially computed as:

$$\text{RTOP}=P(\mathbf{0})=P_\Theta(\mathbf{0})=[\mathbf{P}]_1, \tag{7.17}$$

i.e. as the first component of vector $\mathbf{P}$.

7.3.2 RTAP

The RTAP represents the probability of water molecules moving back to the axis following the maximum diffusion direction within a time τ. In our model, such axis reduces to 'z'. The RTAP can be defined either on the EAP domain or the q-space:

$$\text{RTAP}=\int_{-\infty}^{\infty}P_\Theta(\mathbf{R}')\,dz=\int_{-\infty}^{\infty}\int_{-\infty}^{\infty}E_\Theta(\mathbf{q}')\,dq_x\,dq_y=\int_{-Q_x/2}^{Q_x/2}\int_{-Q_y/2}^{Q_y/2}\widetilde{E}_\Theta(\mathbf{q}')\,dq_x\,dq_y. \tag{7.18}$$

The latter expression can be used to derive the RTAP from eq. (7.12):

$$\begin{aligned}\text{RTAP} \;\simeq\; & \frac{1}{Q}\left(\int_{\frac{-Q_x}{2}}^{\frac{Q_x}{2}}\int_{\frac{-Q_y}{2}}^{\frac{Q_y}{2}} P_\Theta(\mathbf{0})\,dq_x\,dq_y + 2\sum_{k=1}^{N_x} P_\Theta(\mathbf{R}'_{k,0,0})\int_{\frac{-Q_x}{2}}^{\frac{Q_x}{2}}\int_{\frac{-Q_y}{2}}^{\frac{Q_y}{2}}\cos\left(2\pi{\mathbf{q}'_i}^T\mathbf{R}'_{k,0,0}\right)\,dq_x\,dq_y\right.\\ & + 2\sum_{k=-N_x}^{N_x}\sum_{l=1}^{N_y} P_\Theta(\mathbf{R}'_{k,l,0})\int_{\frac{-Q_x}{2}}^{\frac{Q_x}{2}}\int_{\frac{-Q_y}{2}}^{\frac{Q_y}{2}}\cos\left(2\pi{\mathbf{q}'_i}^T\mathbf{R}'_{k,l,0}\right)\,dq_x\,dq_y\\ & \left. + 2\sum_{k=-N_x}^{N_x}\sum_{l=-N_y}^{N_y}\sum_{m=1}^{N_z} P_\Theta(\mathbf{R}'_{k,l,m})\int_{\frac{-Q_x}{2}}^{\frac{Q_x}{2}}\int_{\frac{-Q_y}{2}}^{\frac{Q_y}{2}}\cos\left(2\pi{\mathbf{q}'_i}^T\mathbf{R}'_{k,l,m}\right)\,dq_x\,dq_y\right)\\ = \;& \frac{1}{Q_z}\left(P_\Theta(\mathbf{0}) + 2\sum_{m=1}^{N_z} P_\Theta(\mathbf{R}'_{0,0,m})\right). \end{aligned} \tag{7.19}$$

Remarkably, eq. (7.19) equals the first order quadrature for the first integral form in eq. (7.18), but it is exact up to the necessary cropping of the Fourier series coefficients.

7.3.3 RTPP

The RTPP represents the probability of water molecules moving back to the plane perpendicular to the maximum diffusion direction within a time τ. Since we assimilate the maximum diffusion direction to the 'z' axis, such domain is trivially described as the 'x'-'y' plane. The RTPP can be defined either on the EAP domain or the q-space:

$$\text{RTPP} = \int_{-\infty}^{\infty}\int_{-\infty}^{\infty} P_\Theta(\mathbf{R}')\,dx\,dy = \int_{-\infty}^{\infty} E_\Theta(\mathbf{q}')\,dq_z = \int_{-Q_z/2}^{Q_z/2}\widetilde{E}_\Theta(\mathbf{q}')\,dq_z. \tag{7.20}$$

The latter expression can be used to derive the RTPP from eq. (7.12):

$$\begin{aligned}\text{RTPP} \;\simeq\; & \frac{1}{Q}\left(\int_{\frac{-Q_z}{2}}^{\frac{Q_z}{2}} P_\Theta(\mathbf{0})\,dq_z + 2\sum_{k=1}^{N_x} P_\Theta(\mathbf{R}'_{k,0,0})\int_{\frac{-Q_z}{2}}^{\frac{Q_z}{2}}\cos\left(2\pi{\mathbf{q}'_i}^T\mathbf{R}'_{k,0,0}\right)\,dq_z\right.\\ & + 2\sum_{k=-N_x}^{N_x}\sum_{l=1}^{N_y} P_\Theta(\mathbf{R}'_{k,l,0})\int_{\frac{-Q_z}{2}}^{\frac{Q_z}{2}}\cos\left(2\pi{\mathbf{q}'_i}^T\mathbf{R}'_{k,l,0}\right)\,dq_z\\ & \left. + 2\sum_{k=-N_x}^{N_x}\sum_{l=-N_y}^{N_y}\sum_{m=1}^{N_z} P_\Theta(\mathbf{R}'_{k,l,m})\int_{\frac{-Q_z}{2}}^{\frac{Q_z}{2}}\cos\left(2\pi{\mathbf{q}'_i}^T\mathbf{R}'_{k,l,m}\right)\,dq_z\right)\\ = \;& \frac{1}{Q_xQ_y}\left(P_\Theta(\mathbf{0}) + 2\sum_{k=1}^{N_x} P_\Theta(\mathbf{R}'_{k,0,0}) + 2\sum_{k=-N_x}^{N_x}\sum_{l=1}^{N_y} P_\Theta(\mathbf{R}'_{k,l,0})\right), \end{aligned} \tag{7.21}$$

which again equals the first order quadrature approximation to the first integral form in eq. (7.20).

7.3.4 MSD

The MSD is the second order, non-central moment of the EAP. Since it will remain invariant to rotations, it can be equally computed from the rotated EAP $P_\Theta(\mathbf{R}')$:

$$\text{MSD} = \iiint_{\mathbb{R}^3} \|\mathbf{R}'\|^2 \, P_\Theta(\mathbf{R}') \, d\mathbf{R}' = \iiint_{\mathbb{R}^3} \left(x^2+y^2+z^2\right) P_\Theta(\mathbf{R}') \, dx \, dy \, dz. \tag{7.22}$$

From the theory on Fourier analysis, this quantity may be equally computed in the q-space by evaluating the (scaled) Laplacian of $E_\Theta(\mathbf{q}')$ at $\mathbf{q}' = \mathbf{0}$ [7.43], as it has been thoroughly exploited in the literature [7.56, 7.57]:

$$\text{MSD} = \frac{-1}{4\pi^2} \Delta_{\mathbf{q}'} E_\Theta(\mathbf{0}) = \frac{-1}{4\pi^2} \Delta_{\mathbf{q}'} \widetilde{E}_\Theta(\mathbf{0}). \tag{7.23}$$

This expression allows a straightforward computation from eq. (7.12):

$$\begin{aligned}
\text{MSD} \simeq \frac{-1}{4\pi^2 Q} \Bigg(& 2 \sum_{k=1}^{N_x} P_\Theta(\mathbf{R}'_{k,0,0}) \, \Delta_{\mathbf{q}'} \cos\left(2\pi {\mathbf{q}'}^T \mathbf{R}'_{k,0,0}\right) \\
& + 2 \sum_{k=-N_x}^{N_x} \sum_{l=1}^{N_y} P_\Theta(\mathbf{R}'_{k,l,0}) \, \Delta_{\mathbf{q}'} \cos\left(2\pi {\mathbf{q}'}^T \mathbf{R}'_{k,l,0}\right) \\
& + 2 \sum_{k=-N_x}^{N_x} \sum_{l=-N_y}^{N_y} \sum_{m=1}^{N_z} P_\Theta(\mathbf{R}'_{k,l,m}) \, \Delta_{\mathbf{q}'} \cos\left(2\pi {\mathbf{q}'}^T \mathbf{R}'_{k,l,m}\right) \Bigg) \Bigg|_{\mathbf{q}'=\mathbf{0}} \\
= \frac{2}{Q} \Bigg(& \sum_{k=1}^{N_x} P_\Theta(\mathbf{R}'_{k,0,0}) \left\|\mathbf{R}'_{k,0,0}\right\|^2 + \sum_{k=-N_x}^{N_x} \sum_{l=1}^{N_y} P_\Theta(\mathbf{R}'_{k,l,0}) \left\|\mathbf{R}'_{k,l,0}\right\|^2 \\
& + \sum_{k=-N_x}^{N_x} \sum_{l=-N_y}^{N_y} \sum_{m=1}^{N_z} P_\Theta(\mathbf{R}'_{k,l,m}) \left\|\mathbf{R}'_{k,l,m}\right\|^2 \Bigg).
\end{aligned} \tag{7.24}$$

Again, the first-order quadrature approximation to the integral in eq. (7.22).

7.4 Numerical methods and algorithm parameters

7.4.1 Bandwidth selection

A key limitation of the original HYDI-DSI is the direct dependence of the bandwidth of the EAP with the particular q-space sampling scheme, which we address here. The lattice where the EAP will be defined will cover a domain that directly depends on the number of lattice points and its bandwidth (i.e. the support $\Omega \subset \mathbb{R}^3$ of the attenuation signal $E(\mathbf{q})$). For example, for the 'x' axis, the EAP will be sampled from $-N_x/Q_x$ to N_x/Q_x. The extent of the EAP domain actually covered can be increased by decreasing Q_x: this implies reducing the bandwidth of the signal, i.e. smoothing the EAP itself. Accordingly, the value of derived indices like RTOP will be artificially reduced due to the convolution of the EAP with a low-pass kernel. Conversely, we can keep a large bandwidth of the EAP by increasing Q_x, but

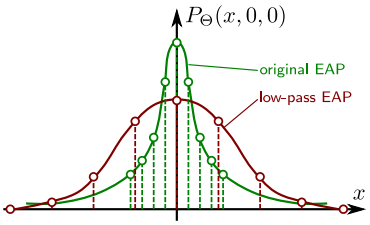

Fig. 7.2.: The effect of wrongly choosing the bandwidth of the EAP for $N_x = 4$: if Q_x is too small (red), the EAP support is fully covered but it becomes low-pass filtered; if Q_x is too large (green), the EAP is kept sharp but its support is not properly sampled.

in this case the maximum value sampled, N_x/Q_x, is likely not to cover a proper extent of the EAP. Fig. 7.2 illustrates these two issues. Of course, we can think of increasing N_x together with Q_x to get full EAP coverage while preserving and adequate bandwidth. But the number of lattice nodes, in the order of $\mathcal{O}(N_x \cdot N_y \cdot N_z)$, cannot be arbitrarily large, but instead it should roughly match the number of available q-space samples even if regularization constraints are imposed.

Since the lattice axes are aligned with the eigenvectors of the low b-value regimen, DTI approximation, it makes sense to scale them according to the respective eigenvalues. For the 'x' axis, the farthest sampled value can be chosen such that the Gaussian tail has decayed to a pre-defined small value $\mu > 0$:

$$\left.\begin{aligned} P_\Theta\left(0,0,0\right) &= \frac{\exp\left(-\frac{1}{4\tau\lambda_1}\left(\frac{0}{Q_x}\right)^2\right)}{\sqrt{\det(\Lambda)\left(4\pi\tau\right)^3}} \\ P_\Theta\left(\frac{N_x}{Q_x},0,0\right) &= \frac{\exp\left(-\frac{1}{4\tau\lambda_1}\left(\frac{N_x}{Q_x}\right)^2\right)}{\sqrt{\det(\Lambda)\left(4\pi\tau\right)^3}} = \mu\, P_\Theta(0,0,0) \end{aligned}\right\} \Rightarrow \frac{Q_x}{2} = \frac{N_x}{4\sqrt{-\tau\lambda_1\log(\mu)}}. \tag{7.25}$$

Note this expression can be otherwise written in terms of maximum b-values to get rid of the diffusion time τ, so that:

$$b_{\text{cut-off},x} = 4\pi^2\tau\left(\frac{Q_x}{2}\right)^2 = \frac{-\pi^2 N_x^2}{4\lambda_1\log(\mu)}; \quad b_{\text{cut-off},y} = \frac{-\pi^2 N_y^2}{4\lambda_2\log(\mu)}; \quad b_{\text{cut-off},z} = \frac{-\pi^2 N_z^2}{4\lambda_3\log(\mu)}. \tag{7.26}$$

It becomes inherent to our approach that q-space samples measured beyond these limits have to be dropped down to avoid aliasing. Consequently, the parameter μ must be appropriately tuned. As a final remark, there is no reason why this same bandwidth tuning cannot be used with the original re-gridding/interpolation approach to define the domain Ω: it suffices to input zeros to the interpolation algorithm at boundary points $\{-Q_x/2, 0, Q_x/2\} \times \{-Q_y/2, 0, Q_y/2\} \times \{-Q_z/2, 0, Q_z/2\} - \mathbf{0}$, and then operate as described by [7.62, 7.63] for an input lattice defined over $\Omega = [-Q_x/2, Q_x/2] \times [-Q_y/2, Q_y/2] \times [-Q_z/2, Q_z/2]$ computed after eq. (7.25). We will put this strategy to the test as described in Section 7.5.2.

7.4.2 Practical implementation

The computation of the Gaussian approximation in eq. (7.5) is accomplished with linearized LS techniques from the q-space samples with $b \leq 2,000\,\text{s/mm}^2$ [7.49]. The bandwidth of the signal, described by $b_{\text{cut-off},e_j}$, will be determined according to eq. (7.26) for an empirically fixed μ. The number of samples along each dimension is a design parameter, but we will use the same sampling as in the original HYDI-DSI approach, i. e. a $9 \times 9 \times 9$ lattice ($N_x = N_y = N_z = 4$) with $N_l = 729$, so that $n = (N_l + 1)/2 = 365$ DoF have to be estimated.

The form of matrix $\mathcal{L}$ in eq. (7.16), describing the Laplacian energy penalty, is described in Appendix 7.A, and the parameter λ will be fixed according to empirical considerations.

Finally, the QP in eq. (7.16) is solved with an *ad hoc* replacement of Matlab's `quadprog` function, based on gradient projection [7.36]. The iterations are initialized with the unconstrained solution of eq. (7.16), which reduces to the computation of $(\mathcal{F}^T\mathcal{F} + \lambda\,\mathcal{L}^T\mathcal{L})^{-1}\mathcal{F}^T\mathbf{E}$, where the matrix to invert is symmetric and positive definite. Such solution is corrected for negative values and normalized to fulfill the unit-mass constraint before feeding the iterations until convergence. Note the QP is convex, so it is always guaranteed to converge to the global optimum. Matlab code can be downloaded as a part of the *dMRI-Lab* toolbox (`http://www.lpi.tel.uva.es/dmrilab`).

7.5 Experiments and results

7.5.1 Materials

The evaluation of the proposal will be based on publicly available databases. Concretely:

- The Human Connectome Project (HCP), MGH database [7.23]: these are high quality data acquired on a Siemens 3T Connectome scanner with 4 different shells at $b = \{1,000,\ 3,000,\ 5,000,\ 10,000\}$ s/mm^2, with $\{64,\ 64,\ 128,\ 256\}$ gradient directions each and 40 interleaved unweighted baselines. The in-plane resolution is 1.5 mm and the slice thickness is 1.5 mm. Other acquisition parameters are: pulse separation time/diffusion gradients length Δ/δ = 21.8/12.9 ms, repetition time TR = 8800 ms, time echo TE = 57 ms. We have randomly chosen subject HCP MGH-1007 for proofs of concept.

- The HCP WU-Minn database [7.58]: these data were acquired with a Siemens 3T Connectome Skyra scanner with a maximum gradient strength at 100 mT/m, 3 shells at $b = \{1,000,\ 2,000,\ 3,000\}$ s/mm^2 with 90 gradient directions each and 18 interleaved unweighted baselines. The in-plane resolution is 1.25 mm and the slice thickness is 1.25 mm. Other acquisition parameters are: Δ/δ = 43/10.6 ms, TR/TE = 5520/89.5 ms. We selected 10 subjects, enrolled for both test and re-test acquisition sessions: 103818, 105923, 111312, 114823 115320, 122317, 125525, 130518, 139839, 143325.

7.5.2 Methods compared

The original method as described by [7.62, 7.63] will be simply referred to as HYDI-DSI. We will use a custom implementation based on Matlab's `griddatan` as the authors suggest. Note, however, that the q-space grid will be rotated at each voxel (but not stretched) before the interpolation, which allows us to align the maximum diffusion direction with the 'z' axis to compute RTAP and RTPP. The proposed method described in this paper will be dubbed HYDI-DSI-QP attending to its numerical implementation as a QP. Besides, we will probe a third method, HYDI-DSI-AB, for which q-space re-gridding and interpolation is used in a lattice defined over an adaptive bandwidth (AB) as described in Section 7.4.1. This way, HYDI-DSI-AB is an intermediate approach that inherits from both HYDI-DSI and HYDI-DSI-QP, and it can indeed be considered as a novel method proposed in the present paper. Finally, we will include comparisons with MAPL [7.25], which is probably the most popular approach within the category of continuous domain, parametric representations of the EAP. We will use Python's `dipy` implementation (`https://dipy.org/`) with anisotropic scaling, positivity constraints, a maximum radial order 4 for the basis functions, and a fixed value 0.2 for the Laplacian weighting. While order 6 is advised by the authors in case isotropic scaling is used, order 4 provides an acceptable trade-off between representation capabilities and computational load in the anisotropic case.

7.5.3 Bandwidth selection

The bandwidth chosen for the signal at each voxel depends on the parameter μ and the lattice size, but not on the particular q-space sampling scheme. Indeed, only those b-values below $2,000\,\mathrm{s/mm^2}$ are actually used to fit the DTI approximation. Accordingly, we have chosen subject HCP MGH-1007 as a representative example to elaborate Fig. 7.3, where the cut-off b-values at each (rotated) axis 'x', 'y', and 'z' are represented at a middle-brain axial slice. We have chosen a typical $9 \times 9 \times 9$ lattice with $N_x = N_y = N_z = 4$, corresponding to $n = 365$ DoF of the EAP. Fig. 7.3 (left) allows to conclude that, unless a extreme value is chosen for μ, such as 0.01, the only samples rejected at $b = 5,000\,\mathrm{s/mm^2}$ and above correspond to the cerebrospinal fluid (CSF). To corroborate this assertion, Fig. 7.3 (right) shows a typical voxel at the CSF (4), for which the estimated bandwidth is smaller than the sampled bandwidth and a large number of samples are dropped out.

On the contrary, even for $\mu = 0.05$, many non-CSF samples at $b = 10,000\,\mathrm{s/mm^2}$ will be discarded for axis 'z'. As it can be inferred from Fig. 7.3 (right, voxel 3), this situation corresponds to prominent, *well packaged* structures (with large Fractional Anisotropy, FA) within the white matter (WM), like the corpus callosum (CC; voxel 3) and the cortico-spinal tract (CST), for which the signal along the main diffusion direction rapidly vanishes: even when the estimated bandwidth is larger than the sampled one at the transverse diffusion plane, the bandwidth for the main diffusion direction crops the sampled one, so that the samples at the North and South poles of the rotated space are discarded. Note this artifact is likely to appear also in the original HYDI-DSI, since the signal at these points will fall below the threshold set as twice the free air signal.

With the same value $\mu = 0.05$, Fig. 7.3 (right, voxels 1 and 2), shows that no samples will be discarded, in general, at the gray matter (GM) or low-FA regions of the WM. For the latter, a low FA value will reflect regions with important partial volume effects due to fiber

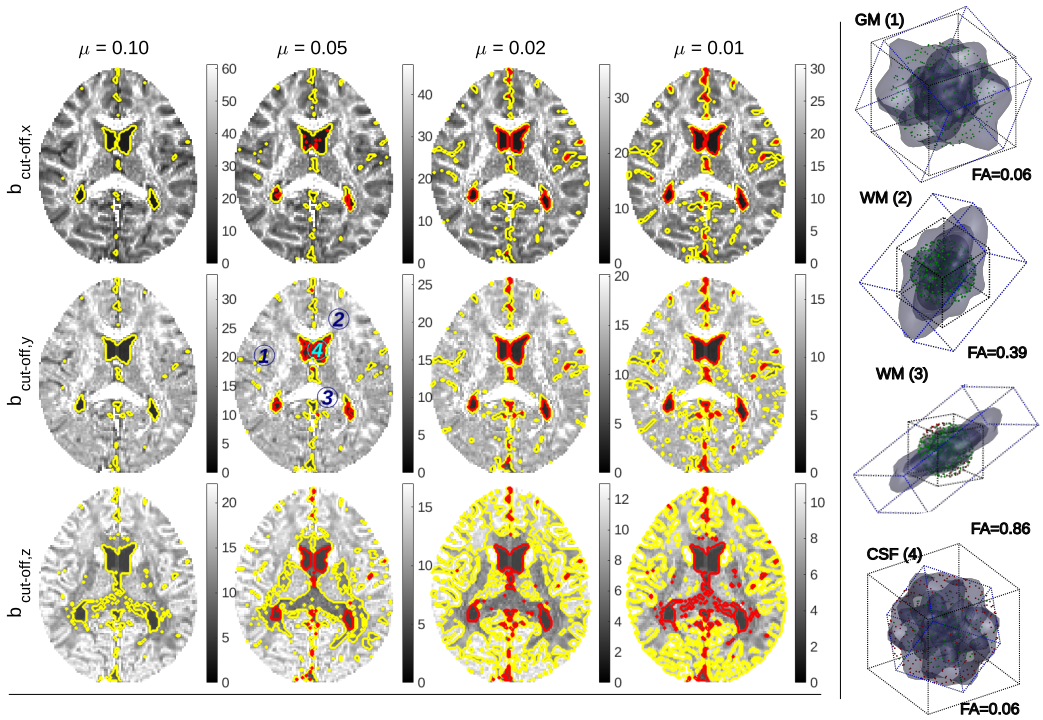

Fig. 7.3.: (Left) Cut-off b-values ($\times 10^3$ s/mm^2) for the three main diffusion directions (top to bottom, on ascending order of the eigenvalues) and for several values of parameter μ, all of them computed over volume HCP MGH-1007 for a fixed lattice size $9 \times 9 \times 9$. Yellow lines correspond to iso-contours at $b_{\text{cut-off},e_j} = 10,000\,\text{s/mm}^2$, and red lines to iso-contours at $b_{\text{cut-off},e_j} = 5,000\,\text{s/mm}^2$. (Right) A detail of the bandwidth selection ($\mu = 0.05$) at four representative voxels located as shown in the left figure. The black bounding boxes represent the original q-space domain given by the maximum b-value $10,000\,\text{s/mm}^2$; blue ones stand for the estimated bandwidths in the rotated space from the DTI approach. The dots represent the acquired b-values and gradients (red: discarded; green: used), and the surfaces depict the actual attenuation signal at each shell.

crossings and/or bending, for which any spatial direction will mix up both restricted and free diffusion.

Finally, $\mu = 0.10$ practically avoids out-of-bandwidth q-space pruning, but this comes at the expense of a poor coverage of the tails of the EAP. In the light of this experiment, we can conclude that applying a threshold $\mu = 0.05$ to the tails of the EAP seems a good trade-off for most of situations.

7.5.4 Regularization parameter selection

The optimal value of the regularization parameter λ in eq. (7.16) is likely to depend on several factors, such as the q-space sampling and the SNR of the data set, the lattice size, or the bandwidth chosen through parameter μ. For this reason, we have explored the same previous values of μ and two data sets with very different characteristics, concretely HCP MGH-1007 and HCP WuMinn-139839, to trace the L-curves in the respective Fig. 7.4 (a) and (b). Besides, in order to keep a reasonable complexity, we have fixed the lattice size once

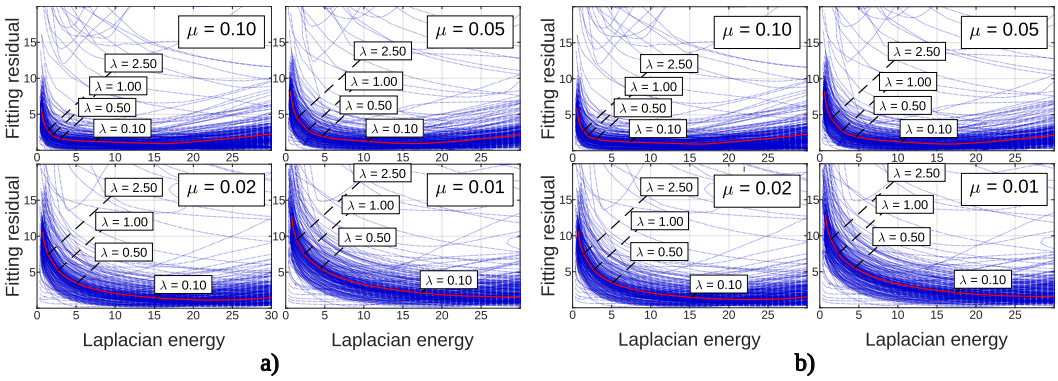

Fig. 7.4.: Fitting residual $\|\mathbf{E} - \mathcal{F}\mathbf{P}\|^2$ vs. Laplacian energy penalty $\|\mathcal{L}\mathbf{P}\|^2$ as a function of the regularization parameter λ, for subjects HCP MGH-1007 (a) and HCP WuMinn-139839 (b) and for several values of μ. The curves represented in dashed, blue lines correspond to a random sub-sample inside the white matter. The red curve in solid line represents the average value inside the white matter.

again to the standard $9 \times 9 \times 9$. The L-curves plot the trade-off between the fitting residual $\|\mathbf{E} - \mathcal{F}\mathbf{P}\|^2$ and the Laplacian energy penalty $\|\mathcal{L}\mathbf{P}\|^2$ as parameter λ varies: for large values of λ, the Laplacian penalty becomes stronger and *smoother* solutions are promoted at the expense of larger residuals. Conversely, for small values of λ the solution will resemble closer the acquired data, but it will likely become physically little plausible. We have focused on the white matter, which has been roughly segmented by thresholding the FA of the DTI approximation at 0.3. First thing to note is that larger bandwidths (i.e. larger μ) translate in smaller residuals, even when less q-space samples are discarded in the QP of eq. (7.16) and hence vector $\mathbf{E}$ has more components. This is an additional reason to avoid an excessive cropping of the large b-value regimen. Next, it seems the behavior of the L-curves is very little dependent on the value of μ, which allows to tune both parameters independently. Finally, the optimal value of λ can be assured to be in the range $[0.1, 2.5]$ in all cases: the corner of the L-curves marks the point where a slight improvement in the residual will come at the expense of an important worsening of the smoothness of the solution (and vice-versa), so the optimal λ should be chosen close to this point. Accordingly, a fixed value $\lambda = 0.50$ seems adequate for both data sets HCP MGH and HCP WuMinn, and it is the fixed value used throughout the paper.

7.5.5 Negativity of unconstrained methods

One main advantage of the HYDI-DSI-QP is the possibility it grants to enforce sampled EAP values to be positive, which is unparalleled for the interpolated methods (HYDI-DSI and HYDI-DSI-AB). Fig. 7.5 is aimed at checking the actual impact of such constraints depending on the number of acquired shells. Once again, subject HCP MGH-1007 has been considered as a representative example: both HYDI-DSI and HYDI-DSI-AB (with $\mu = 0.05$, according to the previous experiment) have been used to compute the EAP at each voxel inside $9 \times 9 \times 9$ lattices, and the percentage of energy corresponding to negative values of the EAP estimated by numerical quadrature. As it can be seen, the presence of negative lobes within the EAP is not a negligible issue. Indeed, it becomes more noticeable as the number of acquired shells decreases (as expected), but also it is more relevant for those white matter regions with

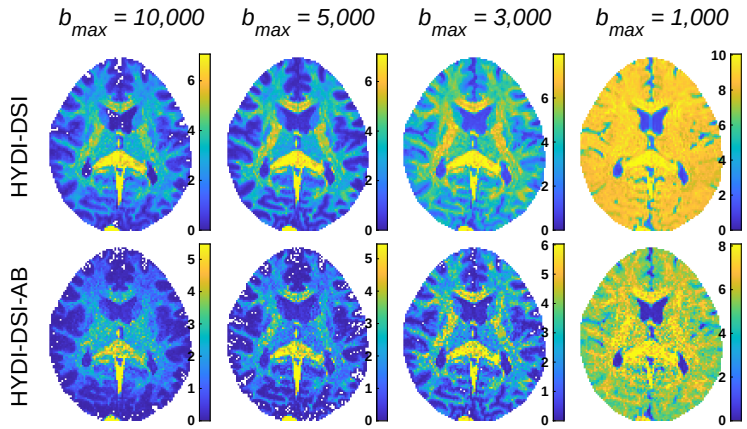

Fig. 7.5.: Percentage of energy corresponding to negative values of the EAP within each voxel for the unconstrained methods: the original HYDI-DSI (top row) and the adaptive bandwidth method, HYDI-DSI-AB (bottom row).

highest anisotropy: in particular, nearly 10% (or more) of the estimated values of the EAP can be negative inside the CC and the CST for any number of acquired shells. Comparing HYDI-DSI with HYDI-DSI-AB, the adaptive bandwidth selection for the latter helps palliating this artifact to some degree. Finally, note the computed percentage of *negative energy* with HYDI-DSI-QP will always be zero by construction.

7.5.6 Accuracy of scalar maps

The quantitative evaluation of dMRI techniques is usually a challenging problem due to the lack of realistic ground-truth data. In this paper we will reuse the original approach conceived by [7.55], where an actual micro-structural model is estimated using the NODDI technique by [7.68] at representative regions of the white matter. The parameters obtained are statistically characterized to draw random samples that are fed to the forward NODDI model to generate synthetic samples simulating 1, 2, or 3 crossing fibers at will with known Peak Signal to Noise Ratio (PSNR). As long as the generative model can be sampled for any arbitrary gradient direction and b-value, ground-truth values are easily obtained for any dMRI measure with arbitrary precision by numerical integration. The reader is addressed to [7.55] for further details on this methodology.

Fig. 7.6 shows Bland & Altman agreement plots [7.13] between the indices (one of RTOP, RTAP, RTPP or MSD) as computed with either of the methods compared (one of MAPL, HYDI-DSI, HYDI-DSI-AB, or HYDI-DSI-QP) and the ground truth. Three different PSNR values were probed, and the plots comprise all possible fiber-crossing configurations in all cases. The q-space sampling scheme is the one found in the HCP MGH database. Since each method will potentially introduce a variable scale-shift for these indices depending on the estimated bandwidth, we use logarithmic plots, i.e.: if the agreement between M_1 and M_2 has to be assessed, we plot y vs. x, where x and y are respectively defined as $x = (\log(M_1) + \log(M_2))/2$ and $y = \log(M_2) - \log(M_1)$. For quantitative assessment, we provide also estimates of the correlation of coefficient and the Normalized Mutual Information (NMI) between x_1 and x_2 in all cases.

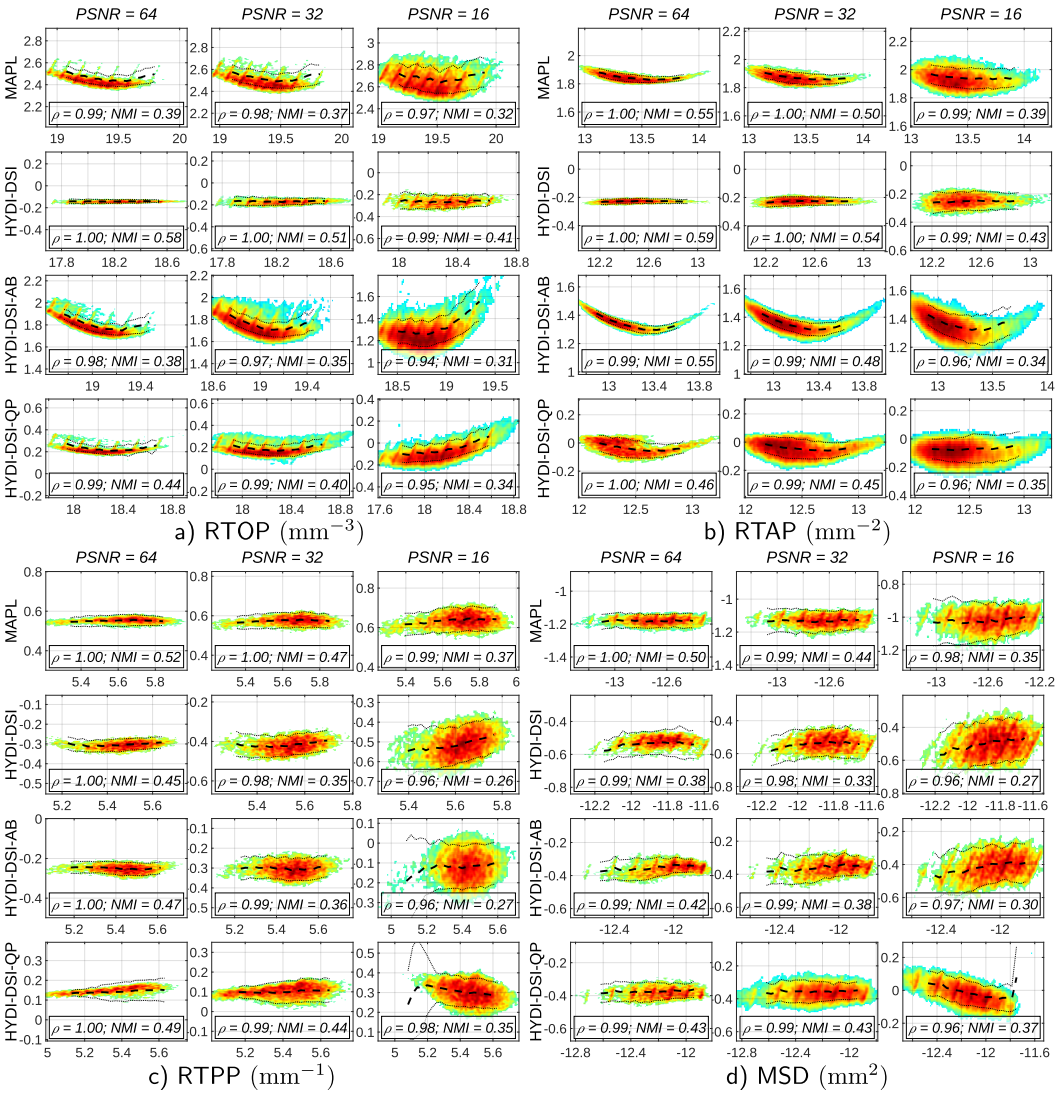

Fig. 7.6.: Bland & Altman agreement plots (logarithmic) between the scalar measures obtained with each of the methods compared (M_1) and the synthetic ground truth (M_2), as a function of the PSNR and for mixed fiber configurations. The scalar measures tested are a) RTOP, b) RTAP, c) RTPP and d) MSD. The 'x' axis represents $(\log(M_1) + \log(M_2))/2$, and the 'y' axis $\log(M_2) - \log(M_1)$. Dashed lines represent median values, whereas dotted lines represent the 10% and 90% percentiles; the correlation coefficient ρ and the Normalized Mutual Information (NMI) are shown for quantitative assessment.

In general terms, all methods attain fairly good results for medium-large PSNR, but their performance obviously worsens as the PSNR decreases. Comparing the proposed HYDI-DSI-QP with the original HYDI-DSI, the former is outperformed, both in terms of correlation and NMI, by the latter for the RTOP and RTAP, but it does overall better with the RTPP and MSD. HYDI-DSI-AB, in turn, does not seem consistently beneficial for any index. Yet, the original HYDI-DSI proves itself extraordinarily robust to noise for RTOP and RTAP, with the plots experiencing very little spreading as the PSNR decreases.

If we compare now with MAPL, its behavior is in general similar to that of HYDI-DSI-QP,

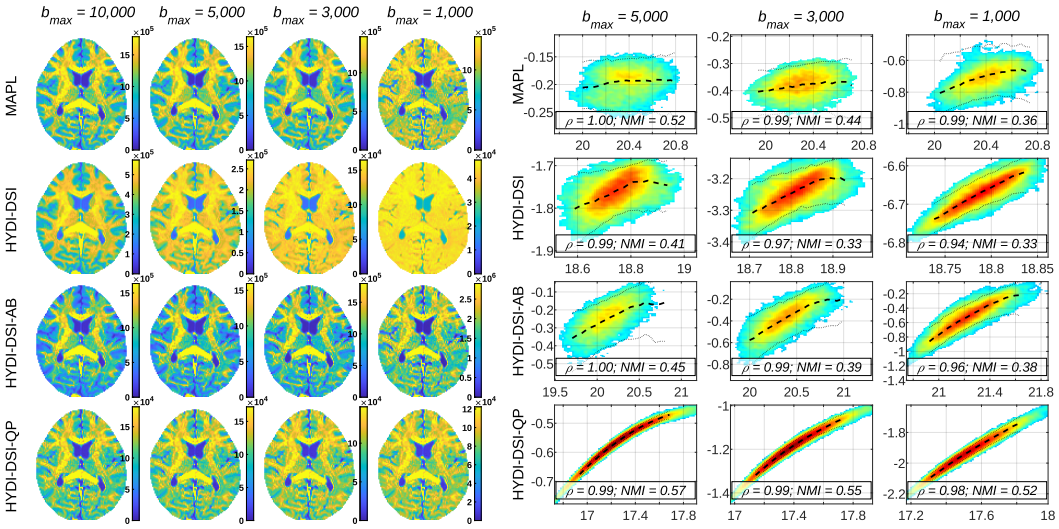

Fig. 7.7.: RTOP values (in mm^{-3}) for subject HCP MGH-1007 using either the four available shells ($b_{\max} = 10,000\,\mathrm{s/mm^2}$), the three innermost shells ($b_{\max} = 5,000\,\mathrm{s/mm^2}$), the two innermost shells ($b_{\max} = 3,000\,\mathrm{s/mm^2}$), or just the innermost shell ($b_{\max} = 1,000\,\mathrm{s/mm^2}$). Left: an illustrative central axial slice. Right: Bland & Altman agreement plots (logarithmic) between the computation with all four shells (x-axis) and the computation with the innermost shells (y-axis) as indicated. The correlation coefficient ρ and the NMI are also shown for quantitative assessment.

though the former performs slightly better than the latter in some scenarios (above all, for RTAP and RTPP) in terms of correlations and NMI. Note, however, that the plots for HYDI-DSI-QP are closer to 0 for all indices and all PSNR values, meaning the scale-shifts induced by our proposed technique are less important than those with all the other methods (except, in some situations, for HYDI-DSI). With regard to this issue, note that MAPL is indeed the worst performer, since it yields to a larger bias than all other methods in all situations.

7.5.7 Sensitivity of scalar maps to the number of acquired shells

One of the aims of the present proposal is reducing the dependency of quantitative dMRI parameters on the q-space sampling scheme by designing a sampling-independent bandwidth. To check this property, we compute the RTOP, RTAP, RTPP and MSD for subject HCP MGH-1007. At first instance, we will use the four available shells up to $b = 10,000\,\mathrm{s/mm^2}$, since the original HYDI-DSI was designed for this range of maximum b-values. This estimate will be set as the bronze standard for each method, and then the outermost shells will be sub-sequentially removed to estimate the same scalar measurements from either three, two, or even one shell.

Fig. 7.7 shows the results for RTOP, both qualitatively (RTOP maps, left) and quantitatively (Bland & Altman plots, right). As it can be seen, the benefit of HYDI-DSI-QP over all other methods compared is now clear: the plots are very well clustered around the median value in all cases demonstrating an outstanding agreement even if only one shell at $b_{\max} = 1,000\,\mathrm{s/mm^2}$ is used, whereas all other methods (especially MAPL) yield widespread cloud

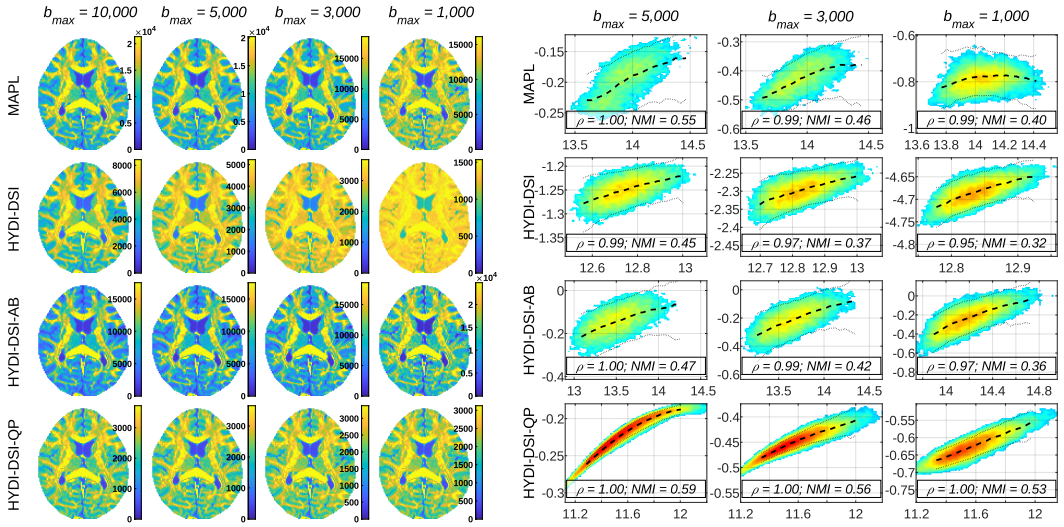

Fig. 7.8.: RTAP values (in mm^{-2}) for subject HCP MGH-1007 using either the four available shells ($b_{\max} = 10,000\,\mathrm{s/mm^2}$), the three innermost shells ($b_{\max} = 5,000\,\mathrm{s/mm^2}$), the two innermost shells ($b_{\max} = 3,000\,\mathrm{s/mm^2}$), or just the innermost shell ($b_{\max} = 1,000\,\mathrm{s/mm^2}$). Left: an illustrative central axial slice. Right: Bland & Altman agreement plots (logarithmic) between the computation with all four shells (x-axis) and the computation with the innermost shells (y-axis) as indicated. The correlation coefficient ρ and the NMI are also shown for quantitative assessment.

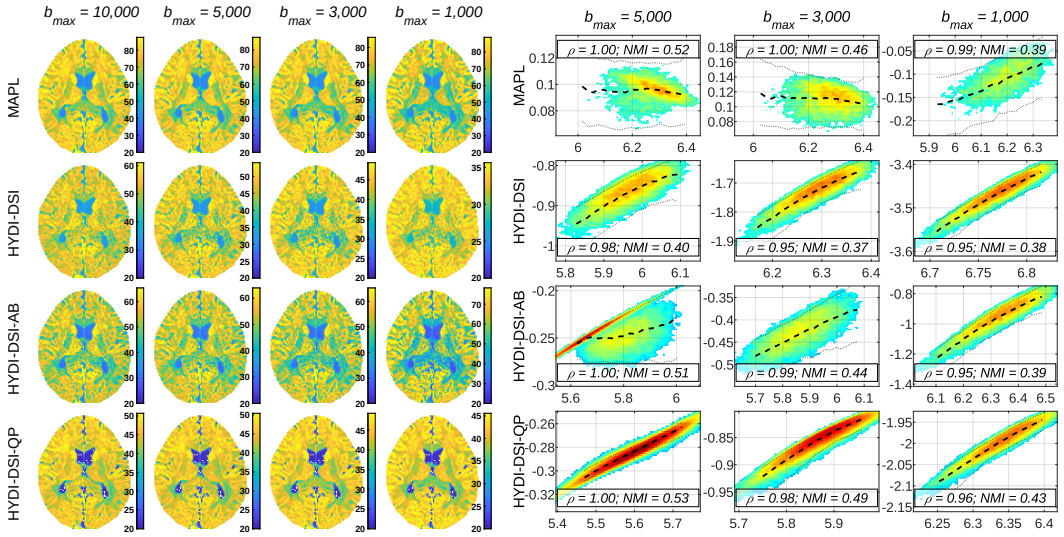

Fig. 7.9.: RTPP values (in mm^{-1}) for subject HCP MGH-1007 using either the four available shells ($b_{\max} = 10,000\,\mathrm{s/mm^2}$), the three innermost shells ($b_{\max} = 5,000\,\mathrm{s/mm^2}$), the two innermost shells ($b_{\max} = 3,000\,\mathrm{s/mm^2}$), or just the innermost shell ($b_{\max} = 1,000\,\mathrm{s/mm^2}$). Left: an illustrative central axial slice. Right: Bland & Altman agreement plots (logarithmic) between the computation with all four shells (x-axis) and the computation with the innermost shells (y-axis) as indicated. The correlation coefficient ρ and the NMI are also shown for quantitative assessment.

points. This conclusion is supported by the fairly larger NMI value attained by HYDI-DSI-QP in all cases (the correlation coefficient is not a conclusive performance index since it becomes

very close to 1 in all cases).

With regard to the scale shifts, HYDI-DSI is extremely sensitive to the removal of the outermost shells (because the estimated bandwidth directly depends on the the maximum b-value itself), meanwhile HYDI-DSI-AB and HYDI-DSI-QP are more robust. Though the estimated bandwidth for these two methods is acquisition protocol-independent, they will be affected by the lack of samples at large b-values as well: with HYDI-DSI-QP, the Laplacian penalty promotes smooth solutions; in the absence of high frequency q-samples to fit, the obvious way in which this condition is fulfilled is producing low-pass responses, which translates in reduced values of RTOP, see Fig. 7.2; with HYDI-DSI-AB, the missing samples are just replaced with a zero padding, which leads also to an artificial bandwidth drift. In this sense, the scales of the parameters estimated with MAPL remain more faithful to those at $b_{\text{max}} = 10,000\,\text{s/mm}^2$ (though, after Fig. 7.6, these scales might be distorted).

Very similar comments arise for the RTAP from Fig. 7.8: HYDI-DSI-QP is able to faithfully reproduce the original results with all four shells even if the sampling scheme is reduced to just one shell, which translates in well clustered plots and noticeably larger NMI values. Yet, HYDI-DSI-QP is able to better preserve the scale of the RTAP across all the experiments as compared to HYDI-DSI and even MAPL, being slightly outperformed only by HYDI-DSI-AB.

For the RTPP, Fig. 7.9 demonstrates that HYDI-DSI-QP is still the best performer, though its actual advantage over the other methods is not equally clear in this case. Besides, and conversely to the RTAP, the scale-shifts induced in the RTPP as the outermost shells are removed is especially noticeable with HYDI-DSI-QP, and only the original HYDI-DSI remains more sensitive. It is worth noticing that the Bland & Altman map for HYDI-DSI-AB at $b_{\text{max}} = 5,000\,\text{s/mm}^2$ presents an artifact in the form of a spread cloud over-imposed to a clearly defined linear cluster. The RTPP can be computed as the integral of $E(\mathbf{q})$ along the main diffusion direction: for those voxels with a large FA, corresponding to a unique, well packaged, fiber bundle (e.g. voxel 3 in Fig. 7.3, right), the signal will very quickly decay for this main direction, so that it will very likely have vanished at $b = 5,000\,\text{s/mm}^2$ and above. Since HYDI-DSI-AB works by zero-padding all the values above b_{max}, the estimates for $b_{\text{max}} = 5,000\,\text{s/mm}^2$ and $b_{\text{max}} = 10,000\,\text{s/mm}^2$ will be exactly the same, which explains the straight line in the figure. For other voxels with smaller FA, the estimates will largely differ due to the zero-padding, which explains the spread cloud.

Finally, the MSD is tested in Fig. 7.10 with similar conclusions: HYDI-DSI-QP provides very well clustered results, demonstrating an outstanding agreement with the whole sampling even if just one shell is used. The NMI values, once again, corroborate the visual inspection. With regard to the scale shifts, in this case HYDI-DSI-AB seems particularly robust, whereas HYDI-DSI-QP and MAPL behave similarly and HYDI-DSI, again, proves itself especially sensitive.

7.5.8 Repeatability and reliability analyses

The importance of computing quantitative indices in a reliable manner within neurosciences has been stressed by [7.70]. According to the authors, such indices not only need to be repeatable for the same subject/anatomy being imaged (i.e. be specific), but they should also reflect meaningful anatomical changes among subjects (i.e. be sensitive). The quantitative assessment of repeatability through test-retest acquisitions has become a

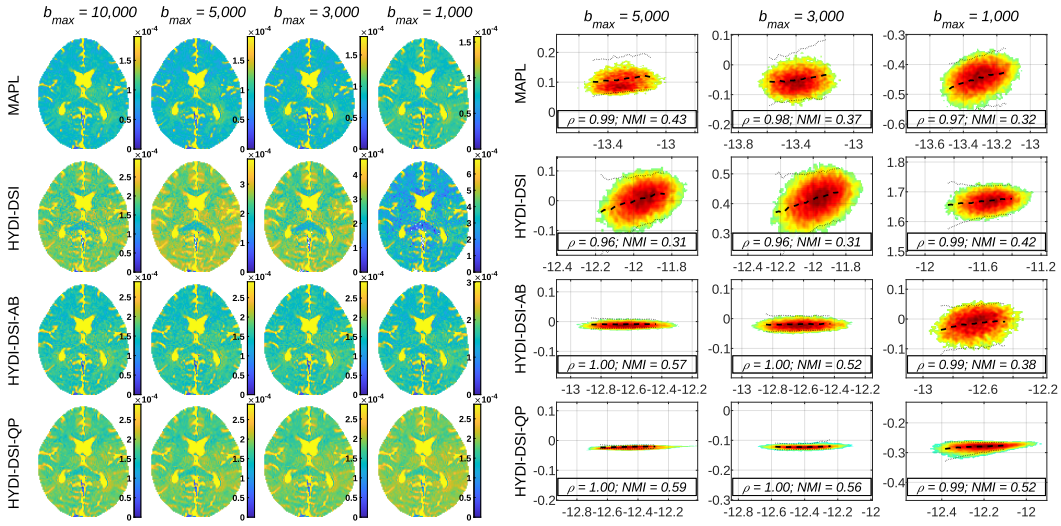

Fig. 7.10.: MSD values (in mm^2) for subject HCP MGH-1007 using either the four available shells ($b_{\max} = 10,000\,\mathrm{s/mm}^2$), the three innermost shells ($b_{\max} = 5,000\,\mathrm{s/mm}^2$), the two innermost shells ($b_{\max} = 3,000\,\mathrm{s/mm}^2$), or just the innermost shell ($b_{\max} = 1,000\,\mathrm{s/mm}^2$). Left: an illustrative central axial slice. Right: Bland & Altman agreement plots (logarithmic) between the computation with all four shells (x-axis) and the computation with the innermost shells (y-axis) as indicated. The correlation coefficient ρ and the NMI are also shown for quantitative assessment.

common topic in dMRI, to the point that several *ad hoc* databases have been designed with this aim [7.34, 7.58]. In particular, we will use the test-retest subset of the HCP WuMinn database in this section.

We calculate the RTOP, RTAP, RTPP and MSD with MAPL, HYDI-DSI, HYDI-DSI-AB and HYDI-DSI-QP. Each combination involves both the test and the retest acquisitions within the data set. All three available shells and all 90 gradient directions per each shell were used. Besides, we estimate the diffusion tensors at $b = 1000\ \mathrm{s/mm}^2$ using the FSL 6.0.4 `dtifit` tool [7.50, Analysis Group, FMRIB, Oxford, UK.; `https://fsl.fmrib.ox.ac.uk/fsl/fslwiki`], retrieve the FA parameter for all test/retest cases, and non-linearly register the FA maps using a normalized correlation cost function to the common template FMRIB58 (a high-resolution FA volume aggregated from 58 subjects) with a voxel resolution of $1 \times 1 \times 1\ \mathrm{mm}^3$ [7.30, 7.31]. Eventually, all the above-mentioned propagator-based measures are non-linearly warped to the common space with trilinear interpolation. Once the measures are warped to the standard space, we calculate their reliability as:

$$\mathrm{Reliability}(\mathbf{x}) = \frac{\mathrm{Separability}(\mathbf{x})}{\mathrm{Repeatability}(\mathbf{x})}, \tag{7.27}$$

with $\mathbf{x}$-dependent $\mathrm{Repeatability}(\mathbf{x})$ averaged from the repeatabilities of each of the m out of M subjects:

$$\mathrm{Repeatability}_m(\mathbf{x}) = \frac{\text{std. dev. across sessions}_s(\mathbf{x})}{\text{mean across sessions}_s(\mathbf{x})} \text{ for } s = \{\text{test}, \text{retest}\}. \tag{7.28}$$

repeatability (in %)	RTOP	RTAP	RTPP	MSD
MAPL	6.31	5.15	1.90	4.38
HYDI-DSI	2.12	1.98	1.67	4.24
HYDI-DSI-AB	8.18	6.85	2.36	3.52
HYDI-DSI-QP	4.78	3.76	1.45	3.04

(a)

reliability	RTOP	RTAP	RTPP	MSD
MAPL	2.79	3.12	3.10	2.45
HYDI-DSI	2.73	3.07	2.23	2.49
HYDI-DSI-AB	2.79	3.05	2.47	2.38
HYDI-DSI-QP	2.73	3.05	3.47	2.84

(b)

Tab. 7.1.: Averaged repeatability (a) and reliability (b) inside the white matter from the test-retest subset of the HCP WuMinn database. The smaller, the better reproducibility, while the higher, the better reliability.

$\text{Separability}(\mathbf{x})$ is conversely given by:

$$\text{Separability}(\mathbf{x}) = \frac{\text{std. dev. across subjects}_m\left(\text{mean across sessions}_s(\mathbf{x})\right)}{\text{mean across subjects}_m\left(\text{mean across sessions}_s(\mathbf{x})\right)} \text{ for } m = \{1, \ldots, M\}. \tag{7.29}$$

Table 7.1 presents the results of the repeatability and reliability studies using ten subjects ($M = 10$) from the HCP WuMinn test-retest subset. In both cases, the numbers were averaged from 20 representative slices in the standard space and the WM area extracted from the John Hopkins University DTI-based atlas [7.39]. Table 7.1 (a) displays the coefficients of variation of the measures expressed as a percentage (i.e. multiplied by 100). This means the smaller the repeatability score, the better the reproducibility achieved. Generally, all measures are characterized by a high level of reproducibility, with the RTPP being the most reproducible measure (the coefficient of variation is at most 2.36%). The HYDI-DSI-QP technique achieves improved results over HYDI-DSI-AB including all measures and is superior to the standard HYDI-DSI technique for RTPP and MSD. However, in the case of RTOP and RTAP, the HYDI-DSI provides better performance over both HYDI-DSI-AB and HYDI-DSI-QP. Noticeably, both HYDI-DSI and HYDI-DSI-QP consistently outperform MAPL for all indices with regard to repeatability. The averaged reliability of the measures, as defined in eq. (7.27), is presented in Table 7.1 (b). In this experiment, the higher the value, the better the reliability. The results show comparable (virtually identical) reliability for RTOP and RTAP among all four methods, despite large discrepancies occur if we pay attention only to the repeatability. For RTPP and MSD, HYDI-DSI-QP is notably superior to all the other methods compared.

7.5.9 Execution times

Quantitative dMRI is often computationally very demanding, entailing processing times that range from several minutes to many hours or even days per subject. Hence, the study of the

computational complexity is undoubtedly interesting in this context. Table 7.2 summarizes the average computation times taken by each method compared in this paper to process one single voxel. We have used subject HCP MGH-1007 for illustration purposes, and tested several sampling schemes with the same fixed configurations described in Section 7.5.7: four shells up to $b = 10,000\,\mathrm{s/mm^2}$, three shells up to $b = 5,000\,\mathrm{s/mm^2}$, two shells up to $b = 3,000\,\mathrm{s/mm^2}$, or one shell at $b = 1,000\,\mathrm{s/mm^2}$. Times are reported for Matlab R2020a implementations (HYDI-DSI-like) or Python 3.6 (MAPL) running on an Intel(R) Xeon(R) E5-2695 CPU with 54 cores at 2.30GHz and 110GB RAM memory under Ubuntu Linux 20.04, all of them multi-threaded. As it could be expected beforehand, MAPL and HYDI-DSI-QP are always faster as the number of q-space samples decreases, since the size of the QP is obviously smaller. This comment does not hold for HYDI-DSI, for which the bottleneck is in the computation of the convex hull and Delaunay's triangulation (linear interpolation will take a negligible time): the computation time is not always monotonically increasing with the number of samples, which makes this method less predictable with regard to their complexity. Though HYDI-DSI-AB takes decreasing times with smaller samplings, it is still prone to the same issue as HYDI-DSI. HYDI-DSI and HYDI-DSI-AB are comparable in all cases, each one being faster for certain configurations and slower for others. In any case, the proposed HYDI-DSI-QP is notably faster than the re-gridding/interpolation methods, with an acceleration factor ranging $3\times$ to $10\times$. Finally, MAPL is dramatically slower than all other methods, nearly $100\times$ to $200\times$ compared to HYDI-DSI-QP: meanwhile a complete volume from the HCP database can be processed with the latter in roughly half an hour, the former will take well over two days.

7.6 Discussion and Conclusions

The proposed HYDI-DSI-QP is able to estimate fully non-parametric, positive, unit-mass constrained EAPs at a regular Cartesian lattice from arbitrary q-space samplings (though we have focused on multi-shells). As opposed to the original HYDI-DSI, the quantitative indices derived from these EAPs are relatively robust to the maximum b-value acquired, since the bandwidth of the signal is estimated from a DTI approximation fitted to the low b-value regimen instead of from the sampling protocol itself. Of course, smoothness constraints impose a reduction of the bandwidth of the estimated EAP as the maximum acquired b-value decreases. The keystone of HYDI-DSI-QP is replacing the re-gridding and linear interpolation of the q-space with a constrained, Laplacian-regularized optimization problem, which indeed makes the algorithm more time-efficient.

	4 shells	3 shells	2 shells	1 shell
MAPL	368.2	303.1	252.1	203.7
HYDI-DSI	17.6	4.8	10.3	2.8
HYDI-DSI-AB	14.3	9.4	4.9	4.7
HYDI-DSI-QP	3.0	1.8	1.1	0.9

Tab. 7.2.: Average per-voxel execution times (milliseconds) depending on the number of shells considered.

Indeed, the computational complexity in the original HYDI-DSI approach becomes unnecessarily increased by its straightforward implementation with a voxel-wise call to Matlab's `griddatan`. Note the slowest part of this method is the computation of the convex hull and Delaunay's triangulation: if the lattice layout is kept constant with respect to the q-space samples (i.e. it is non-adaptive with regard to the DTI approximation), these two computations could be done once for the entire volume, and the only repeated operation would be the (very fast) linear interpolation. Note, however, this would not apply in case we want to accurately compute directional indices (e.g. RTAP and RTPP) or design adaptive bandwidths like in HYDI-DSI-AB. In the former case, the lattice will become rotated with respect to the q-space samples to align its axes with the principal diffusion directions; in the latter, the lattice will be both rotated and stretched. In both cases, the proposed HYDI-DSI-QP will be a faster option.

An additional advantage of the proposed HYDI-DSI-QP is the possibility it grants to impose positivity constraints, which is not feasible with interpolation-based methods. Fig. 7.5 highlights this is certainly a non-negligible issue, as long as the greatest impact of negative-valued EAP samples shows up within relevant white matter structures such as the CC or the CST. Morevoer, this problem worsens for more modest (hence, closer to what may be found in clinical applications) q-space samplings than the outstanding MGH HCP data set. Remarkably, it has been shown that non-negativity constraints unleash their highest potential when the underlying function representing the EAP is enforced to be non-negative in its entire continuous domain [7.19]. With HYDI-DSI-QP, on the contrary, only a discrete subset of the EAP (the lattice nodes) is assured to be non-negative. Note this is inherent to DSI-like, non-parametric approaches, for which the discrete values to be estimated are not parameters to reconstruct a continuous (non-negative) function, but sparse values of the function itself.

The problems of q-space re-gridding have been previously recognized in the Generalized DSI [7.53, GDSI], where the authors work around the problem with a direct discretization of eq. (7.1) in the form of a quadrature rule for Fourier's integral. There, each q-space sample is weighted accounting for the volume it *occupies*, in a way that there is no need for further interpolation. It has the obvious advantage of being computationally very efficient, since it reduces to a (fixed) matrix product at each voxel. Besides, the same scheme easily fits Cartesian or spherical lattices in both the q-space and the EAP domain. However, it is by no means free of certain problems: first, the bandwidth of the signal is directly limited by the maximum b-value acquired, as it is with HYDI-DSI, which in practice means this method will be well suited only for specific data sets like the HCP MGH. Second, the raw discretization of eq. (7.1), as opposed to the DFT computed over a q-space signal forced to evaluate to 1 at $\mathbf{q} = \mathbf{0}$, does not guarantee the EAP to have unit mass, which is indeed the case for all the methods explored in this paper. Of course, the positivity of the EAP is neither assured *per se*. Finally, for more general samplings than Cartesian or spherical, it is not clear how the volume-dependent weights of GDSI would be computed. These samplings would not represent any particular issue for HYDI-DSI-like approaches.

A different approach dealing with q-space interpolation was proposed by [7.66], where the authors drew HARDI data from DSI-like or multi-shell samplings by interpolation. This is based on the linear relation between the so-called Spin Distribution Function (SDF) and the attenuation signal samples. At the very end, the problem is solved as a Tikhonov-regularized, non-constrained least squares problem. The authors claim that non-negativity constraints

become unnecessary resorting to empirical considerations, likely owing to the fact that, being aimed at reducing DSI-like/multi-shell data to HARDI schemes, the problem they address is vastly over-determined. In any case, this approach focuses on HARDI analysis techniques, so that it does not stand a direct comparison with our proposal.

The price to pay when getting rid of q-space interpolation is the introduction of two additional algorithm parameters (besides the lattice size) that were not present in the original HYDI-DSI: the bandwidth selection μ and the Laplacian weighting λ. Fortunately, Figs. 7.3 and 7.4 show they can be fixed in a *one size fits all* fashion, regardless of the actual q-space sampling used. Indeed, their values remain constant in Figs. 7.7–7.10 as the outermost acquired shells are progressively removed, and even so HYDI-DSI-QP exhibits a stable behavior. Moreover, all the results reported throughout the paper used $\mu = 0.05$ and $\lambda = 0.5$ after Figs. 7.3 and 7.4, without any further optimization.

Regarding the actual accuracy of HYDI-DSI-like approaches, Fig. 7.6 shows the three of them provide excellent approximations for the full HCP MGH protocol (with b-values up to $10,000\,\mathrm{s/mm^2}$), unless very poor PSNR values are considered. Though the estimations obtained with either of the three methods strongly correlate with ground-truth values, it remains clear that the proposed HYDI-DSI-QP performs the best at estimating the actual order of magnitude of the RTxP indices, with logarithmic scale-shifts near 0. The actual advantage of our proposal, however, is demonstrated in Figs. 7.7–7.10: HYDI-DSI-QP clearly outperforms the original HYDI-DSI in the estimation of RTxP values as fewer shells are available, hence proving itself more useful with non-dedicated, more clinically-suitable diffusion data sets.

Remarkably, the progressive removal of the outermost shells results in two artifacts: first, since fewer samples are available for the estimation, the variance of the estimation (the width of the points clouds in the joint histograms) increases, as expected. Second, the measures are scale-shifted with respect to their values at $b = 10,000\,\mathrm{s/mm^2}$. This is evident with HYDI-DSI, since the calculated bandwidth is directly provided by the maximum b-value acquired. With HYDI-DSI-QP, the reason may be found in eq. (7.16): since no high-frequency samples are available, this part of the spectrum is governed by the penalty term, which promotes lower-pass solutions, hence decreasing the values of the RTxP. With HYDI-DSI-AB, on the contrary, the non-measured part of the spectrum will be linearly interpolated, so that the bandwidth can even result artificially increased. Note this is a major difference of our approach when compared to CS-based proposals [7.12, 7.37, 7.67]: CS will provide faithful, full-bandwidth approximations to the EAP even if the q-space is sampled below Nyquist's rate (but up to a sufficiently large b-value). This is attained through the use of a *sparsifying* transform and ℓ_1-based optimization procedures. Our HYDI-DSI-QP avoids the need for such transform by directly computing samples of the function of interest (the discrete EAP), which at the same time allows to directly impose positivity constraints in a straightforward manner.

Note the computations of the RTOP (see Fig. 7.7), the RTAP (Fig. 7.8), the RTPP (Fig. 7.9), and the MSD (Fig. 7.10) are quite robust to the elimination of large b-valued shells with HYDI-DSI-QP. In other words, HYDI-DSI-QP, as compared to the original HYDI-DSI, grants the opportunity to accurately estimate non-parametric, DSI-like information from non-specific samplings. Yet, HYDI-DSI-QP provides pretty decent approximations of the bronze standard from even a unique shell at $b = 1,000\,\mathrm{s/mm^2}$, which could allow our proposal to

compete with recent model-based/parametric approaches devised for quantitative dMRI analysis from clinically feasible setups [7.1, 7.3, 7.2].

More interestingly, the experiments presented throughout the paper evidence that our HYDI-DSI-QP attains, at the very least, comparable results to those obtained with MAPL in terms of accuracy, robustness, and reliability. Indeed, we are able to clearly and consistently outperform MAPL in many scenarios (compare top and bottom rows of the Bland and Altman graphs in Figs. 7.7 through 7.10). Though we cannot claim that MAPL is the state of the art in EAP imaging (to our knowledge, there are not systematic and exhaustive comparative studies supporting the better performance of MAPL compared to other techniques), it is undoubtedly the most popular approach for multi-shells, despite being extremely time consuming and resource demanding. In this sense, we have designed an EAP imaging technique that attains a speedup at least $100\times$ over MAPL with a comparable or even better performance.

Compared to its predecessor (HYDI-DSI by [7.62]), HYDI-DSI-QP no longer requires *ad hoc* q-space sampling schemes, but it properly works with those currently available in public databases. Putting all together, HYDI-DSI-QP might constitute a milestone for bringing up the potential of advanced EAP imaging to the analysis of medium-large sized databases.

In this work, we have focused on quantitative dMRI, which is also the main topic covered by [7.62], i.e. we aim at accurately computing certain indices derived from diffusion measurements that can potentially reflect features and processes taking place in the white matter at a micro-structure level. As such, we have not paid attention to the computation of ODF fields or EAP-based tractography, which is in turn an important matter of concern in the related literature [7.5, 7.27, 7.53, 7.55]. The computation of the EAP in a Cartesian lattice, especially when it is oriented following the principal diffusion directions, nicely fits the computation of the usual indices (RTOP, RTAP, RTPP, MSD), but a spherical arrangement is better suited for ODF or directionality description. [7.63], devising HYDI as a put-all-together method, were not concerned about this pitfall because ODF/tractography were supposed to be computed independently with one of the available DTI/HARDI techniques. If this complementary information has to be extracted from the Cartesian EAP itself, some sort of re-gridding/interpolation in the EAP domain is required. This might well be a linear interpolation of the EAP samples themselves, or a more sophisticated approach could be thought of: proceeding as in Appendix 7.A, we could obtain a set of Fourier coefficients of the periodically extended EAP, which is equivalent to a re-gridding of the q-space. Then, the analogous developments as in Section 7.2.3 would allow building a matrix relating the Cartesian sampling of the q-space to the desired spherical grid in the EAP domain, from which computing ODFs would now be trivial. Note that both MAP-MRI and MAPL face similar issues, since they equally rely on functions naturally defined in the Cartesian domain [7.25, 7.45].

Yet, the RTOP, the RTAP, the RTPP and the MSD are not the unique EAP-derived quantities of interest within dMRI: the Non-Gaussianity (NG) and the Propagator Anisotropy (PA), which are naturally derived from the MAP-MRI representation [7.45], have proven themselves certainly valuable for the description of several pathologies [7.6, 7.11, 7.24]. For example, the PA is defined as the *distance* from the EAP to its equivalent isotropic signal, defined as the spherical average of $P(\mathbf{R})$ at each $\|\mathbf{R}\|$. Once again, the Cartesian description of the EAP with HYDI-DSI approaches is a pitfall in the computation of this measurement that needs to be solved via numeric interpolation. Since HYDI-DSI-QP pursues the analytical computation

of quantitative dMRI indices (see Section 7.3), the need for numeric interpolation in all these cases is a clear limitation.

The proposed method is aimed at the non-parametric description of the EAP. The relevance of this particular feature arguably relies on the expectation that a non-parametric representation provides extra DoF over parametric ones, meaning that the derived indices will hopefully exhibit a higher sensitivity to micro-structure changes inside the white matter. Conversely, more DoF are likely to make the EAP representation more prone to random drifts induced by noise and imaging artifacts, i.e. reduced specificity. With regard to the latter issue, we have characterized specificity by means of the inter-session coefficient of variation (hither defined as the reproducibility), which should remain relatively low for the derived dMRI measures to be clinically feasible. This criterion has been met for all measures estimated under HYDI-DSI and HYDI-DSI-QP approaches as stated in Table 7.1 (a), with coefficients of variation always below 5%.

However, the analysis in terms of raw reproducibility, despite being relatively simple, can be misleading: Table 7.1 (a) suggests that the original HYDI-DSI might be clearly preferable for the estimation of RTOP and RTAP, since it is twice as repeatable as HYDI-DSI-QP for these indices. However, the previous experiments highlight the fact that the indices estimated with either technique are not directly comparable due to the very different bandwidths estimated for the EAP in each case. In other words, the heavy scale-shifts HYDI-DSI introduces in RTxP values as a consequence of abruptly cropping the bandwidth of the EAP can be related to sensitivity losses: Table 7.1 (b) measures this effect by normalizing inter-session coefficients of variation with inter-subject differences. With this normalization, it remains clear that all the methods compared are equally reliable for the estimation of RTOP and RTPP, meanwhile HYDI-DSI-QP is clearly preferable for RTPP and MSD. In any case, the reproducibility and reliability studies presented in Table 7.1 demonstrated promising potential of the measures to be further transferred to the clinical domain or to be used in a neurodevelopment research scenario, e.g. brain ageing or longitudinal studies.

Finally, the analysis of dMRI measures in terms of reliability (not just reproducibility) is a novel contribution of this paper, which can pave the way for the selection of an appropriate sample size to preserve a trade-off between a long acquisition time or group size and a high significance of statistical tests [7.70]. Such trade-off will be pursued through the choice for an appropriate EAP reconstruction method, either parametric or non-parametric, and, as we have illustrated here, an appropriate design of the bandwidth of the EAP. Besides, it seems likely that it will strongly depend on the particular characteristics of the database to be analyzed. In this sense, a wider study generalizing the one carried out in Section 7.5.8 would allow the systematic comparison of parametric and non-parametric EAP imaging techniques with regard to their reliability in different situations (i.e. for different imaging protocols). Including HYDI-DSI-like approaches in the pool of compared methods is now possible after the present paper, since we have demonstrated that HYDI-DSI-QP relies notably less on dedicated q-space samplings than the original HYDI-DSI does, so that it can be computed over existing test-retest databases [7.34, 7.58] as-it-is.

Acknowledgments

This work was supported by the Ministerio de Ciencia e Innovación of Spain with research grants PID2021-124407NB-I00 and TED2021-130758B-I00.

Tomasz Pieciak acknowledges the Polish National Agency for Academic Exchange for grant PPN/BEK/ 2019/1/00421 under the Bekker programme and the Ministry of Science and Higher Education (Poland) under the scholarship for outstanding young scientists (692/STYP/13/2018).

Data collection and sharing for this project was partially provided by the *Human Connectome Project*, `https://ida.loni.usc.edu/login.jsp` (HCP; Principal Investigators: Bruce Rosen, M.D., Ph.D., Martinos Center at Massachusetts General Hospital, Arthur W. Toga, Ph.D., University of Southern California, Van J. Weeden, MD, Martinos Center at Massachusetts General Hospital). HCP funding was provided by the National Institute of Dental and Craniofacial Research (NIDCR), the National Institute of Mental Health (NIMH), and the National Institute of Neurological Disorders and Stroke (NINDS). HCP is the result of efforts of co-investigators from the University of Southern California, Martinos Center for Biomedical Imaging at Massachusetts General Hospital (MGH), Washington University, and the University of Minnesota. HCP data are disseminated by the Laboratory of Neuro Imaging at the University of Southern California.

Data were also provided in part by the Human Connectome Project, WU-Minn Consortium (Principal Investigators: David Van Essen and Kamil Ugurbil; 1U54MH091657) funded by the 16 NIH Institutes and Centers that support the NIH Blueprint for Neuroscience Research; and by the McDonnell Center for Systems Neuroscience at Washington University.

Appendices

7.A Description of the Laplacian penalty

The Laplacian of the EAP, as required in eq. (7.16), could be approximated with finite differences computed over $\mathbf{P}$ itself. Instead, we look for an *exact* representation based on the DFT. In order to avoid discontinuities due to the inherent periodic boundary conditions, we extend the original EAP lattice to a new one with size $(2N_x+2)\times(2N_y+2)\times(2N_z+2)$ by zero padding at $N_{e_j}+1$. By rearranging the antipodal symmetric $P_\Theta(k/Q_x, l/Q_y, m/Q_z)$ ($\{k,l,m\}=-N_{e_j}\dots N_{e_j}+1$), we get a column vector $\mathbf{P}_{\text{sym}}$ that relates to the signal in the q-space as:

$$\mathbf{P}_{\text{sym}} = Q\, W_{\text{sym}}\, \mathbf{E}_{\text{sym}}, \tag{7.30}$$

where $\mathbf{E}_{\text{sym}}$ is rearranged from $E_\Theta\left(Q_x u/2(N_x+1), Q_y v/2(N_y+1), Q_z w/2(N_z+1)\right)$ ($\{u,v,w\}=-N_{e_j}\dots N_{e_j}+1$) as a column vector, and W_{sym} is the DFT matrix whose entries have the form [7.43]:

$$[W_{\texttt{sym}}]_{r(u,v,w),c(u,v,w)} = \exp\left(-i\pi\left(k\,u/N_x+1 + l\,v/N_y+1 + m\,w/N_z+1\right)\right). \tag{7.31}$$

Since $W_{\mathtt{sym}}$ has Hermitian symmetry, its inversion becomes trivial. Besides, since both the EAP and the attenuation signal are necessarily real, we get:

$$\mathbf{E}_{\mathrm{sym}} = \frac{1}{Q}\,\Re\{W_{\mathtt{sym}}^{H}\}\,\mathbf{P}_{\mathtt{sym}}. \tag{7.32}$$

The computation of the Laplacian can be done by relating this operator to its dual in the q-space domain, as it has been thoroughly exploited in the literature [7.56, 7.57]. Hence:

$$\mathbf{F}_{\mathtt{sym}} = -4\pi^2 \mathrm{diag}(\mathbf{s}_{\mathrm{sym}})\,\mathbf{E}_{\mathrm{sym}} = \frac{-4\pi^2}{Q}\,\mathrm{diag}(\mathbf{s}_{\mathrm{sym}})\,\Re\{W_{\mathtt{sym}}^{T}\}\,\mathbf{P}_{\mathtt{sym}} = \frac{1}{Q}\,\Re\{W_{f}^{T}\}\,\mathbf{L}_{\mathrm{sym}}, \tag{7.33}$$

where $\mathbf{L}_{\mathrm{sym}}$ stands for the Laplacian of the EAP, sampled at the same lattice points as the EAP itself, and rearranged as a column vector. Vector $\mathbf{s}_{\mathrm{sym}}$ represents the (column-rearranged) squared modules of the lattice nodes in the q-space, i. e.:

$$[\mathbf{s}_{\mathrm{sym}}]_{r(u,v,w)} = \frac{Q_x^2\,u^2}{4(N_x+1)^2} + \frac{Q_y^2\,v^2}{4(N_y+1)^2} + \frac{Q_z^2\,w^2}{4(N_z+1)^2}. \tag{7.34}$$

Therefore, $\mathbf{F}_{\mathtt{sym}}$ is the DFT of the signal corresponding to the Laplacian of the sampled EAP. According to Parsevaal's theorem, the energy of the former equals the energy of the latter. By identifying terms in eqs. (7.16) and (7.33) we can derive:

$$\mathcal{L}_{\mathrm{sym}} = \frac{-4\pi^2}{Q}\,\mathrm{diag}(\mathbf{s}_{\mathrm{sym}})\,\Re\{W_{\mathtt{sym}}^{T}\}. \tag{7.35}$$

It only remains to drop off the rows and columns of $W_{\mathtt{sym}}^{T}$ corresponding to antipodal symmetries (like we did in Section 7.2.3), as well as those columns corresponding to the original zero-padding of the EAP at extra lattice points, to get W^T (and perform analogous operations with the rows of $\mathbf{s}_{\mathrm{sym}}$ to get $\mathbf{s}$). Finally:

$$\mathcal{L} = Q^{-2/3}\frac{-4\pi^2}{Q}\,\mathrm{diag}(\mathbf{s})\,\Re\{W^{T}\} = -4\pi^2 Q^{-5/3}\,\mathrm{diag}(\mathbf{s})\,\Re\{W^{T}\}, \tag{7.36}$$

where the additional normalization factor $Q^{-2/3}$ obeys to the need for dimensional homogeneity between $\mathcal{F}$ and $\mathcal{L}$ in eq. (7.16).

Bibliography

[7.1] Aja-Fernández, S., de Luis-García, R., Afzali, M., Molendowska, M., Pieciak, T., Tristán-Vega, A., 3 2020. Micro-structure diffusion scalar measures from reduced MRI acquisitions. PLOS ONE 15 (3), 1–25.

[7.2] Aja-Fernández, S., Pieciak, T., Martín-Martín, C., Planchuelo-Gómez, Á., de Luis-García, R., Tristán-Vega, A., 2022. Moment-based representation of the diffusion inside the brain from reduced DMRI acquisitions: Generalized AMURA. Medical Image Analysis 77, 102356.

[7.3] Aja-Fernández, S., Tristán-Vega, A., Jones, D. K., 2021. Apparent propagator anisotropy from single-shell diffusion mri acquisitions. Magnetic Resonance in Medicine 85 (5), 2869–2881.

[7.4] Assaf, Y., Basser, P. J., 2005. Composite hindered and restricted model of diffusion (CHARMED) MR imaging of the human brain. NeuroImage 27 (1), 48–58.

[7.5] Assemlal, H.-E., Tschumperlé, D., Brun, L., 2009. Efficient and robust computation of PDF features from diffusion MR signal. Medical Image Analysis 13 (5), 715–729.

[7.6] Avram, A. V., Sarlls, J. E., Barnett, A. S., Özarslan, E., Thomas, C., Irfanoglu, M. O., Hutchinson, E., Pierpaoli, C., Basser, P. J., 2016. Clinical feasibility of using mean apparent propagator (MAP) MRI to characterize brain tissue microstructure. NeuroImage 127, 422–434.

[7.7] Barber, C. B., Dopkin, D. P., Huhdanpaa, H. T., 1996. The quickhull algorithm for convex hulls. ACM Transactions on Mathematical Software 22 (4), 469–483.

[7.8] Basser, P. J., Mattiello, J., Le Bihan, D., 1994. Estimation of the effective self-diffusion tensor from the NMR spin echo. Journal of Magnetic Resonance 103 (3), 247–254.

[7.9] Basser, P. J., Pierpaoli, C., June 1996. Microstructural and physiological features of tissues elucidated by Quantitative–Diffusion–Tensor MRI. Journal of Magnetic Resonance 111 (3), 209–219.

[7.10] Benjamini, D., Basser, P. J., 2019. Water mobility spectral imaging of the spinal cord: Parametrization of model-free Laplace MRI. Magnetic Resonance Imaging 56, 187–193.

[7.11] Bernstein, A. S., 2019. Advanced diffusion MRI techniques: Methodological development and clinical application. Ph.D. thesis, The University of Arizona, Tucson (AZ), United States of America.

[7.12] Bilgic, B., Setsompop, K., Cohen-Adad, J., Yendiki, A., Wald, L. L., Adalsteinsson, E., 2012. Accelerated diffusion spectrum imaging with compressed sensing using adaptive dictionaries. Magnetic Resonance in Medicine 68 (6), 1747–1754.

[7.13] Bland, J. M., Altman, D. G., feb 1986. Statistical methods for assessing agreement between two methods of clinical measurement. Lancet 1, 307–310.

[7.14] Boscolo Galazzo, I., Brusini, L., Obertino, S., Zucchelli, M., Granziera, C., Menegaz, G., 2018. On the viability of diffusion MRI-based microstructural biomarkers in ischemic stroke. Frontiers in neuroscience 12, 92.

[7.15] Brusini, L., Obertino, S., Galazzo, I. B., Zucchelli, M., Krueger, G., Granziera, C., Menegaz, G., 2016. Ensemble average propagator-based detection of microstructural alterations after stroke. International journal of computer assisted radiology and surgery 11 (9), 1585–1597.

[7.16] Callaghan, P., 1991. Principles of Nuclear Magnetic Resonance Microscopy. Clarendon Press, Oxford.

[7.17] Caruyer, E., Deriche, R., 2012. Diffusion MRI signal reconstruction with continuity constraint and optimal regularization. Medical Image Analysis 16 (6), 1113–1120.

[7.18] Daianu, M., Jacobs, R. E., Weitz, T. M., Town, T. C., Thompson, P. M., 2015. Multi-shell hybrid diffusion imaging (HYDI) at 7 Tesla in TgF344-AD transgenic Alzheimer rats. PloS ONE 10 (12), e0145205.

[7.19] Dela Haije, T., Özarslan, E., Feragen, A., 2020. Enforcing necessary non-negativity constraints for common diffusion MRI models using sum of squares programming. NeuroImage 209, 116405.

[7.20] Descoteaux, M., Angelino, E., Fitzgibbons, S., Deriche, R., 2007. Regularized, fast, and robust analytical Q-Ball imaging. Magnetic Resonance in Medicine 58, 497–510.

[7.21] Descoteaux, M., Deriche, R., Le Bihan, D., Mangin, J.-F., Poupon, C., 2011. Multiple q-shell diffusion propagator imaging. Medical image analysis 15 (4), 603–621.

[7.22] Donoho, D. L., 2006. Compressed sensing. IEEE Transactions on Information Theory 52 (4), 1289–1306.

[7.23] Fan, Q., Witzel, T., Nummenmaa, A., Van Dijk, K. R., Van Horn, J. D., Drews, M. K., Somerville, L. H., Sheridan, M. A., Santillana, R. M., Snyder, J., Hedden, T., Shaw, E. E., Hollinshead, M. O., Renvall, V., Zanzonico, R., Keil, B., Cauley, S., Polimeni, J. R., Tisdall, D., Buckner, R. L., Wedeen, V. J., Wald, L. L., Toga, A. W., Rosen, B. R., 2016. MGH–USC Human Connectome Project datasets with ultra-high b-value diffusion MRI. NeuroImage 124, 1108–1114.

[7.24] Fick, R. H., Daianu, M., Pizzolato, M., Wassermann, D., Jacobs, R. E., Thompson, P. M., Town, T., Deriche, R., 2016. Comparison of biomarkers in transgenic Alzheimer rats using multi-shell diffusion MRI. In: International Conference on Medical Image Computing and Computer-Assisted Intervention. Springer, Athens, Greece, pp. 187–199.

[7.25] Fick, R. H., Wassermann, D., Caruyer, E., Deriche, R., 2016. MAPL: Tissue microstructure estimation using Laplacian-regularized MAP-MRI and its application to HCP data. NeuroImage 134, 365–385.

[7.26] Froeling, M., Tax, C. M., Vos, S. B., Luijten, P. R., Leemans, A., 2017. MASSIVE brain dataset: Multiple acquisitions for standardization of structural imaging validation and evaluation. Magnetic Resonance in Medicine 77 (5), 1797–1809.

[7.27] Hosseinbor, A. P., Chung, M. K., Wu, Y.-C., Alexander, A. L., 2013. Bessel Fourier orientation reconstruction (BFOR): An analytical diffusion propagator reconstruction for hybrid diffusion imaging and computation of q-space indices. NeuroImage 64, 650–670.

[7.28] Hosseinbor, A. P., Chung, M. K., Wu, Y.-C., Fleming, J. O., Field, A. S., Alexander, A. L., 2012. Extracting quantitative measures from EAP: A small clinical study using BFOR. In: International Conference on Medical Image Computing and Computer-Assisted Intervention. Springer, Nice, France, pp. 280–287.

[7.29] Jack Jr., C. R., Bernstein, M. A., Fox, N. C., Thompson, P., Alexander, G., Harvey, D., Borowski, B., Britson, P. J., L. Whitwell, J., Ward, C., Dale, A. M., Felmlee, J. P., Gunter, J. L., Hill, D. L., Killiany, R., Schuff, N., Fox-Bosetti, S., Lin, C., Studholme, C., DeCarli, C. S., Krueger, G., Ward, H. A., Metzger, G. J., Scott, K. T., Mallozzi, R., Blezek, D., Levy, J., Debbins, J. P., Fleisher, A. S., Albert, M., Green, R., Bartzokis, G., Glover, G., Mugler, J., Weiner, M. W., 2008. The Alzheimer's disease neuroimaging initiative (ADNI): MRI methods. Journal of Magnetic Resonance Imaging 27 (4), 685–691.

[7.30] Jenkinson, M., Bannister, P., Brady, M., Smith, S., 2002. Improved optimization for the robust and accurate linear registration and motion correction of brain images. Neuroimage 17 (2), 825–841.

[7.31] Jenkinson, M., Smith, S., 2001. A global optimisation method for robust affine registration of brain images. Medical Image Analysis 5 (2), 143–156.

[7.32] Jeurissen, B., Tournier, J.-D., Dhollander, T., Connelly, A., Sijbers, J., 2014. Multi-tissue constrained spherical deconvolution for improved analysis of multi-shell diffusion MRI data. NeuroImage 103, 411–426.

[7.33] Kaden, E., Kelm, N. D., Carson, R. P., Does, M. D., Alexander, D. C., 2016. Multi-compartment microscopic diffusion imaging. NeuroImage 139, 346–359.

[7.34] Koller, K., Rudrapatna, U., Chamberland, M., Raven, E. P., Parker, G. D., Tax, C. M., Drakesmith, M., Fasano, F., Owen, D., Hughes, G., Charron, C., Evans, C. J., Jones, D. K., 2021. MICRA: Microstructural image compilation with repeated acquisitions. NeuroImage 225, 117406.

[7.35] Lampinen, B., Szczepankiewicz, F., Møartensson, J., van Westen, D., Hansson, O., Westin, C.-F., Nilsson, M., 2020. Towards unconstrained compartment modeling in white matter using diffusion-relaxation MRI with tensor-valued diffusion encoding. Magnetic Resonance in Medicine 84 (3), 1605–1623.

[7.36] Luenberger, D. G., Ye, Y., 2008. Linear and Nonlinear Programming, 3rd Edition. International Series on Operations Research & Management Science. Springer.

[7.37] Menzel, M. I., Tan, E. T., Khare, K., Sperl, J. I., King, K. F., Tao, X., Hardy, C. J., Marinelli, L., 2011. Accelerated diffusion spectrum imaging in the human brain using compressed sensing. Magnetic Resonance in Medicine 66 (5), 1226–1233.

[7.38] Merlet, S. L., Deriche, R., 2013. Continuous diffusion signal, EAP and ODF estimation via compressive sensing in diffusion MRI. Medical Image Analysis 17 (5), 556–572.

[7.39] Mori, S., Wakana, S., Van Zijl, P. C., Nagae-Poetscher, L., 2005. MRI atlas of human white matter. Elsevier.

[7.40] Muller, J., Middleton, D., Alizadeh, M., Zabrecky, G., Wintering, N., Bazzan, A. J., Lang, J., Wu, C., Monti, D. A., Wu, Q., Newberg, A. B., Mohamed, F. B., 2021. Hybrid diffusion imaging reveals altered white matter tract integrity and associations with symptoms and cognitive dysfunction in chronic traumatic brain injury. NeuroImage: Clinical 30, 102681.

[7.41] Ning, L., Westin, C.-F., Rathi, Y., 2015. Estimating diffusion propagator and its moments using directional radial basis functions. IEEE Trans Med Imag 34 (10), 2058–2078.

[7.42] Novikov, D. S., Kiselev, V. G., Jespersen, S. N., 2018. On modeling. Magnetic Resonance in Medicine 79 (6), 3172–3193.

[7.43] Oppenheim, A. V., Willsky, A. S., Nawab, S. H., 1997. Signals and Systems, 2nd Edition. Signal Processing Series. Prentice Hall.

[7.44] Özarslan, E., Koay, C. G., Basser, P. J., 2013. Simple harmonic oscillator based reconstruction and estimation for one-dimensional q-space magnetic resonance (1D-SHORE). In: Excursions in Harmonic Analysis. Vol. 2. Springer, pp. 373–399.

[7.45] Özarslan, E., Koay, C. G., Shepherd, T. M., Komlosh, M. E., İrfanoğlu, M. O., Pierpaoli, C., Basser, P. J., 2013. Mean apparent propagator (MAP) MRI: a novel diffusion imaging method for mapping tissue microstructure. NeuroImage 78, 16–32.

[7.46] Pfeuffer, J., Provencher, S. W., Gruetter, R., 1999. Water diffusion in rat brain in vivo as detected at very large b-values is multicompartmental. Magnetic Resonance Materials in Physics, Biology and Medicine 8 (2), 98–108.

[7.47] Planchuelo-Gómez, Á., García-Azorín, D., Guerrero, Á. L., Aja-Fernández, S., Rodríguez, M., de Luis-García, R., 2021. Multimodal fusion analysis of structural connectivity and gray matter morphology in migraine. Human Brain Mapping 42 (4), 908–921.

[7.48] Planchuelo-Gómez, Á., García-Azorín, D., Guerrero, Á. L., de Luis-García, R., Rodríguez, M., Aja-Fernández, S., 2020. Alternative microstructural measures to complement diffusion tensor imaging in migraine studies with standard MRI acquisition. Brain Sciences 10 (10), 711.

[7.49] Salvador, R., Peña, A., Menon, D.-K., Carpenter, T.-A., Pickard, J.-D., Bullmore, E.-T., 2005. Formal characterization and extension of the linearized diffusion tensor model. Human Brain Mapping 24, 144–155.

[7.50] Smith, S. M., Jenkinson, M., Woolrich, M. W., Beckmann, C. F., Behrens, T. E., Johansen-Berg, H., Bannister, P. R., De Luca, M., Drobnjak, I., Flitney, D. E., et al., 2004. Advances in functional and structural MR image analysis and implementation as FSL. Neuroimage 23, S208–S219.

[7.51] Stejskal, E.-O., Tanner, J.-E., 1965. Spin diffusion measurements: Spin echoes in the presence of a time-dependent field gradient. Journal of Chemical Physics 42, 288–292.

[7.52] Tax, C. M., Grussu, F., Kaden, E., Ning, L., Rudrapatna, U., Evans, C. J., St-Jean, S., Leemans, A., Koppers, S., Merhof, D., et al., 2019. Cross-scanner and cross-protocol diffusion MRI data harmonisation: A benchmark database and evaluation of algorithms. NeuroImage 195, 285–299.

[7.53] Tian, Q., Yang, G., Leuze, C., Rokem, A., Edlow, B. L., McNab, J. A., 2019. Generalized diffusion spectrum magnetic resonance imaging (GDSI) for model-free reconstruction of the ensemble average propagator. NeuroImage 189, 497–515.

[7.54] Topgaard, D., 2017. Multidimensional diffusion MRI. Journal of Magnetic Resonance 275, 98–113.

[7.55] Tristán-Vega, A., Aja-Fernández, S., 2021. Efficient and accurate EAP imaging from multi-shell dMRI with micro-structure adaptive convolution kernels and dual Fourier integral transforms (MiSFIT). NeuroImage 227, 117616.

[7.56] Tristán-Vega, A., Westin, C.-F., Aja-Fernández, S., 2009. Estimation of fiber orientation probability density functions in High Angular Resolution Diffusion Imaging. NeuroImage 47 (2), 638–650.

[7.57] Tristán-Vega, A., Westin, C.-F., Aja-Fernández, S., 2010. A new methodology for the estimation of fiber populations in the white matter of the brain with the Funk–Radon transform. NeuroImage 49 (2), 1301–1315.

[7.58] Van Essen, D. C., Smith, S. M., Barch, D. M., Behrens, T. E., Yacoub, E., Ugurbil, K., 2013. The WU-Minn Human Connectome Project: An overview. NeuroImage 80, 62–79.

[7.59] Vemuri, B. C., Sun, J., Banerjee, M., Pan, Z., Turner, S. M., Fuller, D. D., Forder, J. R., Entezari, A., 2019. A geometric framework for ensemble average propagator reconstruction from diffusion MRI. Medical Image Analysis 57, 89–105.

[7.60] Watson, D. F., 1994. Contouring: A guide to the analysis and display of spacial data. Pergamon.

[7.61] Wedeen, V., Hagmann, P., Tseng, W.-Y., Reese, T., Weisskoff, R., 2005. Mapping complex tissue architecture with diffusion spectrum imaging. Magnetic Resonance in Medicine 54, 1377–1386.

[7.62] Wu, Y., Field, A. S., Alexander, A. L., 2008. Computation of diffusion function measures in q-space using magnetic resonance hybrid diffusion imaging. IEEE Transactions on Medical Imaging 27 (6), 858–865.

[7.63] Wu, Y.-C., Alexander, A. L., 2007. Hybrid diffusion imaging. NeuroImage 36 (3), 617–629.

[7.64] Wu, Y.-C., Field, A. S., Whalen, P. J., Alexander, A. L., 2011. Age- and gender-related changes in the normal human brain using hybrid diffusion imaging (HYDI). NeuroImage 54 (3), 1840–1853.

[7.65] Wu, Y.-C., Mustafi, S. M., Harezlak, J., Kodiweera, C., Flashman, L. A., McAllister, T. W., 2018. Hybrid diffusion imaging in mild traumatic brain injury. Journal of Neurotrauma 35 (20), 2377–2390.

[7.66] Yeh, F.-C., Verstynen, T. D., 2016. Converting multi-shell and Diffusion Spectrum Imaging to High Angular Resolution Diffusion Imaging. Frontiers in NeuroScience 10, 418.

[7.67] Young, R. J., Tan, E. T., Peck, K. K., Jenabi, M., Karimi, S., Brennan, N., Rubel, J., Lyo, J., Shi, W., Zhang, Z., Prastawa, M., Liu, X., Sperl, J. I., Fatovic, R., Marinelli, L., Holodny, A. I., 2017. Comparison of compressed sensing diffusion spectrum imaging and diffusion tensor imaging in patients with intracranial masses. Magnetic Resonance Imaging 36, 24–31.

[7.68] Zhang, H., Schneider, T., Wheeler-Kingshott, C. A., Alexander, D. C., 2012. NODDI: Practical in vivo neurite orientation dispersion and density imaging of the human brain. NeuroImage 61 (4), 1000–1016.

[7.69] Ziegler, E., Rouillard, M., André, E., Coolen, T., Stender, J., Balteau, E., Phillips, C., Garraux, G., 2014. Mapping track density changes in nigrostriatal and extranigral pathways in Parkinson's disease. Neuroimage 99, 498–508.

[7.70] Zuo, X.-N., Xu, T., Milham, M. P., 2019. Harnessing reliability for neuroscience research. Nature Human Behaviour 3, 768–771.

Part III

Practical Extensions

8 Anisotropy Measure from Three Diffusion-Encoding Gradient Directions

Santiago Aja-Fernández[1], Guillem París[1], Carmen Martín-Martín[1], Derek K. Jones[2] an Antonio Tristán-Vega[1]

[1] *LPI, ETSI Telecomunicación, Universidad de Valladolid, Castilla y León, Spain*
[2] *Cardiff University Brain Research Imaging Centre (CUBRIC), School of Psychology, Cardiff University, UK*

Abstract: We propose a method that can provide information about the anisotropy and orientation of diffusion in the brain from only 3 orthogonal gradient directions without imposing additional assumptions. The method is based on the Diffusion Anisotropy (DiA) that measures the distance from a diffusion signal to its isotropic equivalent. The original formulation based on a Spherical Harmonics basis allows to go down to only 3 orthogonal directions in order to estimate the measure. In addition, an alternative simplification and a color-coding representation are also proposed. Acquisitions from a publicly available database are used to test the viability of the proposal. The DiA succeeded in providing anisotropy information from the white matter using only 3 diffusion-encoding directions. The price to pay for such reduced acquisition is an increment in the variability of the data and a subestimation of the metric on those tracts not aligned with the acquired directions. Nevertheless, the calculation of anisotropy information from DMRI is feasible using fewer than 6 gradient directions by using DiA. The method is totally compatible with existing acquisition protocols, and it may provide complementary information about orientation in fast diffusion acquisitions.

Originally published as: *Santiago Aja-Fernández, Guillem París, Carmen Martín-Martín, Derek K. Jones and Antonio Tristán-Vega, Anisotropy measure from three diffusion-encoding gradient directions, Magnetic Resonance Imaging 88, 38-43, 2022*

8.1 Introduction

The term Diffusion Magnetic Resonance Imaging (DMRI) refers to a set of diverse imaging techniques that, applied to brain studies, provide useful information about the organization and connectivity of the white matter. The most relevant feature of DMRI is its ability to measure orientational variance in the different tissues, i.e., anisotropy, a feature that is mostly used in research. In the clinical practice, and as a complement to structural studies, there are protocols that incorporate a fast acquisition to obtain a measure of the *amount* of diffusion. A common implementation in commercial scanners, like EPI-DWI, acquires only 3 separate orthogonal diffusion weighted images (DWIs) with diffusion gradients aligned

with directions (x, y, z). These 3 DWIs are averaged into a final combined image [8.1] that resembles measures like the Mean Diffusivity (MD) [8.2] or the Average Sample Diffusion (ASD) [8.3]. Due to the limitation in the number of gradient directions, no extra information is provided. If a measure of anisotropy and orientation of the diffusion wants to be extracted, there is a minimum requirement of 6 acquired DWIs in order to estimate the components of the diffusion tensor (DT) [8.4]. Under the DT approach, it would still be possible to calculate an anisotropy measure with fewer than 6 gradient directions, but we must impose a restricted model that reduces the number of values to estimate, like, for instance, assuming that the diffusion has a cylindrical symmetry. Nevertheless, regardless of the used methodology, it is well known the intrinsic inability of dMRI measures to properly characterize different spatial orientation with fewer than 6 gradient directions.

In this paper we propose a new method that can provide additional information about the anisotropy in the diffusion from only 3 orthogonal gradient directions. This method is totally compatible with existing fast diffusion acquisitions since it only makes use of the same 3 DWIs already acquired. This way, no extra scanning time is needed: the same sequence that provides MD images can also provide anisotropy information.

The method is based on a novel anisotropy metric called Diffusion Anisotropy (DiA) proposed in [8.5]. The metric measures the distance from the actual diffusion signal to its isotropic equivalent. Its original formulation relies on the fitting on the signal using a basis of Spherical Harmonics (SH), but an alternative simpler formulation is here proposed to be exclusively used with 3 orthogonal gradient directions. In addition, we also present a color-coding method, like the one used for the Fractional Anisotropy (FA) in DT imaging. We carry out some examples and tests to show that, although the variability of the anisotropy image is high (compared to the one calculated with more gradient-directions), it succeeds in providing structural information of the white matter with just 3 acquired directions for those tracts aligned with the axis.

Due to the limitations of DMRI, when working with fewer than 6 gradient directions, those tracts not aligned with the axis will be underestimated by the procedure. Thus, we must recall that this method is not initially intended to carry out clinical studies or to obtain detailed anisotropy information, but simply to complement existing acquisition methods with an anisotropy measure. The acquisition remains unchanged, only some extra processing is needed, and new information is then provided.

8.2 Methods

8.2.1 Diffusion Anisotropy

In [8.5], authors proposed a series of advanced anisotropy measures that could be calculated from a single shell acquisition. Among them, the Diffusion Anisotropy (DiA) was presented as a robust alternative to the FA. DiA assumes a mono-exponential diffusion profile for the normalized magnitude signal provided by the MRI scanner, $E(\mathbf{q})$:

$$E(\mathbf{q}) = E(q, \mathbf{u}) = \exp\left(-4\pi^2 \tau q^2 \; D(\mathbf{u})\right) = \exp\left(-b \cdot D(\mathbf{u})\right). \tag{8.1}$$

$D(\mathbf{q}) = D(q, \mathbf{u}) > 0$ is the *diffusivity signal*, also known as the Apparent Diffusion Coefficient (ADC), $b = 4\pi^2\tau\|\mathbf{q}\|^2$ is the b-value, τ is the effective diffusion time, $q = \|\mathbf{q}\|$ and $\mathbf{u} \in \mathcal{S}$ is a unit direction in space where $\|\mathbf{u}\| = 1$ and $\mathbf{q} = q\mathbf{u}$. Note the mono-exponential constraint translates in the diffusivity $D(q, \mathbf{u})$ being independent on the radial direction: $D(q, \mathbf{u}) \equiv D(\mathbf{u})$Under this assumption, the DiA is defined as [8.5]:

$$\text{DiA} = \sqrt{1 - \frac{\left[\int_S D(\mathbf{u})d\mathbf{u}\right]^2}{4\pi \cdot \int_S D^2(\mathbf{u})d\mathbf{u}}}. \tag{8.2}$$

The integration on the surface of the unit sphere, $S = \{\mathbf{u} \in \mathbb{R}^3 : \|\mathbf{u}\| = 1\}$, from a limited number of samples can be performed by fitting corresponding signals in the basis of Spherical Harmonics (SH), whose 0-th order coefficient is defined as:

$$C_{0,0}\left\{H(\mathbf{u})\right\} = \frac{1}{\sqrt{4\pi}} \int_S H(\mathbf{u})d\mathbf{u}. \tag{8.3}$$

This way, a practical implementation of DiA was originally defined as:

$$\text{DiA} = \sqrt{1 - \frac{C_{0,0}^2\{D(\mathbf{u})\}}{\sqrt{4\pi} \cdot C_{0,0}\{D^2(\mathbf{u})\}}}. \tag{8.4}$$

This implementation can be seen as a generalization of the Coefficient of Variation of the Diffusion (CVD), defined in [8.3], and an alternative definition to the Generalized Anisotropy (GA) proposed in [8.6]. Finally, note that, as mentioned in [8.7, 8.8], FA-like measures suffer from confounding factors derived from the MRI resolution being bigger than most of the hydrogen molecules displacement in brain tissues. Therefore, both FA and DiA are the result of an averaged measure of the diffusion contributions over the voxel being studied.

8.2.2 Simplified DiA and Color-by-orientation

The advantage of the definition of DiA using a SH base, like the one proposed in eq. (8.4), is that the integral can be roughly estimated from just 3 orthogonal values. Let $D_x(\mathbf{x})$, $D_y(\mathbf{x})$, and $D_z(\mathbf{x})$ be the diffusion signals acquired for these such directions (that, in principle, we assume aligned with the corresponding axes 'x', 'y', and 'z'). We can calculate the *average diffusivity* by simply drawing:

$$\text{D}_{\text{AV}}(\mathbf{x}) = \frac{D_x(\mathbf{x}) + D_y(\mathbf{x}) + D_z(\mathbf{x})}{3}. \tag{8.5}$$

At the same time, DiA can be calculated using eq. (8.4):

$$\text{DiA}(\mathbf{x}) = \sqrt{1 - \frac{C_{0,0}^2\{D_x(\mathbf{x}), D_y(\mathbf{x}), D_z(\mathbf{x})\}}{\sqrt{4\pi} \cdot C_{0,0}\{D_x^2(\mathbf{x}), D_y^2(\mathbf{x}), D_z^2(\mathbf{x})\}}}. \tag{8.6}$$

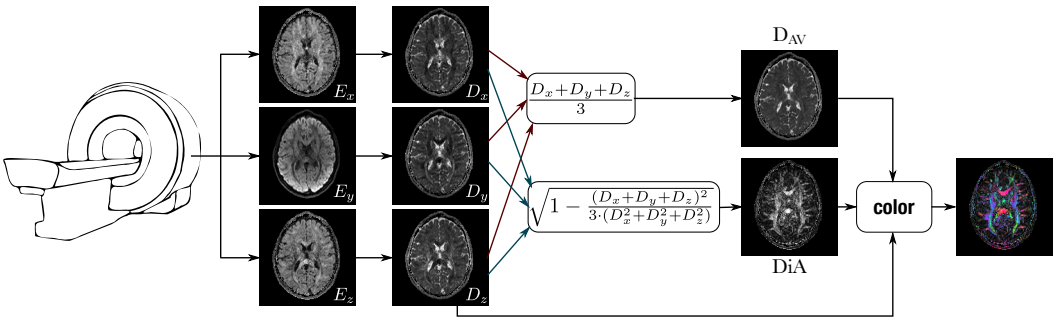

Fig. 8.1.: Scheme of the calculation of the different metrics derived from 3 DWIs acquired with 3 orthogonal gradient directions.

However, since the three acquired DWIs are orthogonal and aligned with the Cartesian axes, the DiA can be alternatively calculated using a simplified formulation [8.3]:

$$\mathrm{DiA}(\mathbf{x}) = \sqrt{1 - \frac{(D_x(\mathbf{x}) + D_y(\mathbf{x}) + D_z(\mathbf{x}))^2}{3 \cdot (D_x^2(\mathbf{x}) + D_y^2(\mathbf{x}) + D_z^2(\mathbf{x}))}}. \tag{8.7}$$

Note that, in this case, since we are assuming three orthogonal vectors, we do not need to use the gradient directions in order to calculate the DiA.

We can also provide color-coded anisotropy information using DiA. In DT imaging, the anisotropy is usually coded using a RGB color system [8.9] in which blue is superior-inferior, red is left-right, and green is anterior-posterior. For visual purposes, the luminance of the color is weighted by the FA. Analogously, we define the RGB components as a function of the three orthogonal directions normalized by the average diffusivity, so that:

$$\mathrm{r}(\mathbf{x}) = \mathrm{DiA}(\mathbf{x}) \times \frac{D_x(\mathbf{x})}{\mathrm{D_{AV}}(\mathbf{x})}; \tag{8.8}$$

$$\mathrm{g}(\mathbf{x}) = \mathrm{DiA}(\mathbf{x}) \times \frac{D_y(\mathbf{x})}{\mathrm{D_{AV}}(\mathbf{x})}; \tag{8.9}$$

$$\mathrm{b}(\mathbf{x}) = \mathrm{DiA}(\mathbf{x}) \times \frac{D_z(\mathbf{x})}{\mathrm{D_{AV}}(\mathbf{x})}. \tag{8.10}$$

Note that this formulation implicitly assumes that the three acquired gradient directions are orthogonal and they are aligned with the axis (x, y, z). Thus, the color coding must be interpreted as orientation of the structures with respect to the axis.

The calculation of the different metrics from the 3 acquired orthogonal measures is surveyed in Fig. 8.1.

8.3 Results

8.3.1 Data used for the experiments

An MRI volume (UVa) from a healthy control was acquired using a Philips Achieva 3T unit (Philips Healthcare, Best, The Netherlands) in the MRI facility at the Universidad de Valladolid (Valladolid, Spain). The acquisition was obtained with these parameters: TR = 9000 ms, TE = 86 ms, flip angle = 90^o, one baseline volume, b-value = 1000 s/mm^2, 128×128 matrix size, $2 \times 2 \times 2$ mm^3 of spatial resolution and 66 axial slices covering the whole brain. 3 different sets were considered: 3, 6 and 61 gradient directions. For the acquisition with 3 directions, the acquired gradients are aligned with the axis. Data were preprocessed using MRtrix software [8.10] for correction of eddy currents, motion, and field inhomogeneities.

In addition, the **Human Connectome Project (HCP)**[1] database was also used, specifically volumes MGH1010 and MGH1016, acquired on a Siemens 3T Connectom scanner with 4 different shells at b =[1000, 3000, 5000, 10000] s/mm^2, with [64, 64, 128, 256] gradient directions each, in-plane resolution 1.5 mm and slice thickness 1.5 mm. We will only make use of the innermost shell ($b = 1000$ s/mm^2 and 64 gradient directions).

8.3.2 Visual Assessment

First, we calculate the proposed metric over 3 slices (31, 40 and 55) from the UVa volume. The D_{AV} and DiA were calculated using only 3 DWIs from the shell at b=1000 s/mm^2 using the simplified expression in eq. (8.7). For the sake of comparison, we have also calculated the FA at b=1000 s/mm^2 with 61 and 6 gradient directions and DiA with 61 (UVa) directions. In the latter case, DiA was calculated using eq. (8.4); the SH are fitted with a Laplace-Beltrami penalty $\lambda = 0.006$. Results are shown in Fig. 8.2.

Although the visual quality of DiA calculated with 3 directions, Fig. 8.2-(e), is clearly poorer than FA and DiA with 61 directions (which is obvious), note that DiA succeeds in estimating information about orientation and anisotropy with just 3 gradient directions. Main structures are visible within the white matter, even clearer in the colored version, Fig. 8.2-(f). Thus, the same fast acquisition that can produce information about the amount of diffusion can also be used to provide rough information about the orientation of such diffusion. Note that the high quality of the images calculated with only 3 gradients is due to the large voxel size used ($2 \times 2 \times 2$ mm^3), which assures a high SNR in the data.

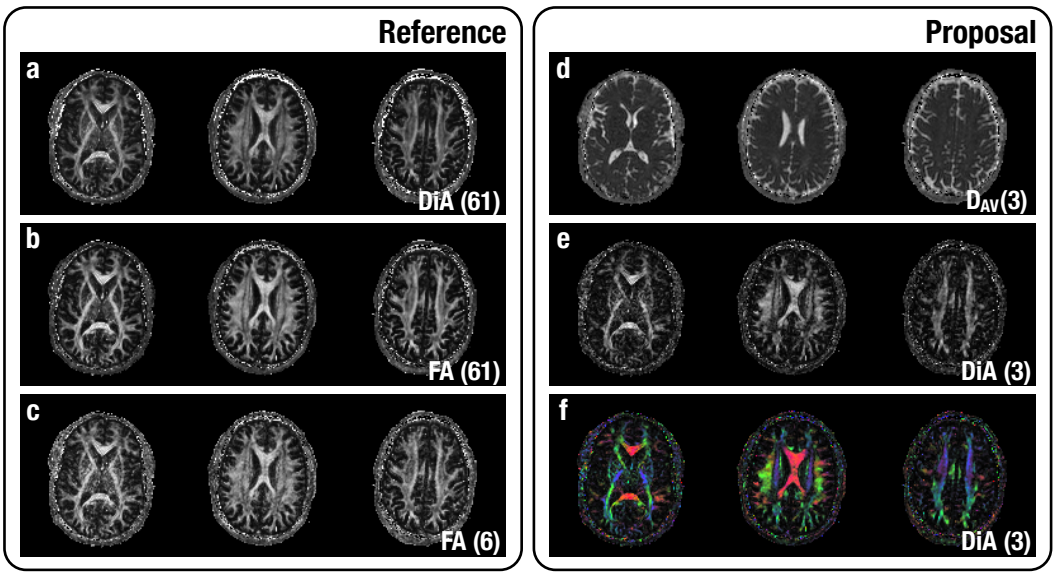

Fig. 8.2.: Visual assessment of proposed methods (2). Slices (31, 40, 55) from the UVa volume are shown. For the sake of comparison, we have added (a) DiA (using 61 gradient directions); (b) FA (using 61 gradient directions; (c) FA (using 6 gradient directions. The proposed metrics are calculated with 3 gradient directions: (d) Average Diffusivity; (e) DiA; (f) DiA with orientation color code.

8.3.3 Numerical assessment

Next, we quantified the loss of information in DiA when calculated using only 3 different orientations. First, we tested the dependency of DiA on the number of diffusion samples taken in a given shell. To that end, we used a whole volume from the HCP data, MGH1016. The volume was divided in 6 different regions according to their diffusion features. The DiA was first calculated at b=1000 s/mm^2 using 64 directions and those voxels with DiA< 0.1 removed. The remaining voxels were clustered in 6 different groups using k-means. Each voxel in the white matter was assigned to one cluster using its DiA value and the minimum distance. The following test was carried out: we began with the 64 samples (gradient directions) and uniformly downsampled this set to obtain either 3, 6, 15, 24, 35 and 48 diffusion directions subsets[2]. The DiA was computed for each considered case, and the median value inside each of the six clusters is depicted in Fig. 8.3. Although DiA shows it is a consistent measure when it is calculated using over 20 different orientations, for fewer gradient directions this measure is underestimated. This effect is much more noticeable when using only 3 directions. However, note that the separation between clusters remains

[1]Data obtained from the Human Connectome Project (HCP) database (`ida.loni.usc.edu/login.jsp`) . The HCP project (Principal Investigators: Bruce Rosen, M.D., Ph.D., Martinos Center at Massachusetts General Hospital; Arthur W. Toga, Ph.D., University of Southern California, Van J. Weeden, MD, Martinos Center at Massachusetts General Hospital) is supported by the National Institute of Dental and Craniofacial Research (NIDCR), the National Institute of Mental Health (NIMH) and the National Institute of Neurological Disorders and Stroke (NINDS). HCP is the result of efforts of co-investigators from the University of Southern California, Martinos Center for Biomedical Imaging at Massachusetts General Hospital (MGH), Washington University, and the University of Minnesota.

[2]A "uniform" downsampling of n gradients among the original 64 is here defined as those n directions that minimize the overall electrostatic repulsion energy among all $\binom{64}{n}$ combinations. The optimization is carried out using heuristic rules.

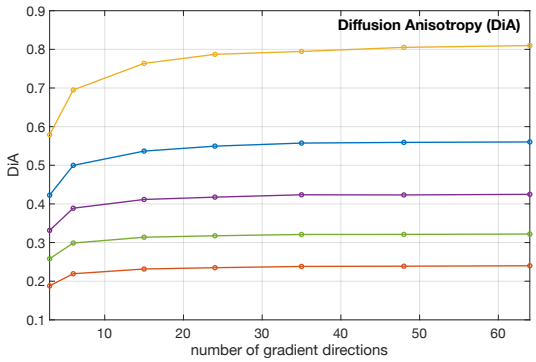

Fig. 8.3.: Evolution of DiA with the angular resolution (number of gradient directions), using data from HCP. The volume has been clustered in 6 different sets (for original DiA with 64 directions) and the median of each set is shown. Centroids of the data $C_L = \{0.24, 0.32, 0.42, 0.57, 0.82\}$.

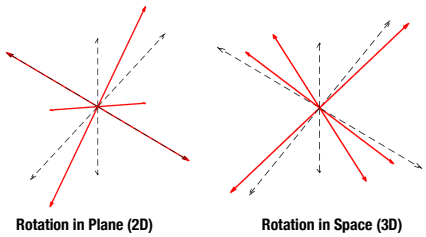

Fig. 8.4.: Directions of the eigenvectors of the synthetic tensor (red) in relation with the axis (black). Two different rotations are applied. LEFT: rotation on a plane. RIGHT: spatial rotation.

constant. This suggest that the differences in the anisotropy detected by these measures can still be seen when using 3 orientations (at least in this example).

8.3.4 Variability of DiA with orientation

One of the issues with anisotropy measures in dMRI is the intrinsic inability to properly characterize fibers in all different spacial orientation when fewer than 6 gradient directions are considered. Thus, in order to quantify the capability of this method to identify fibers that are not aligned with the axis, we will carry out a simple simulation: we generate a synthetic tensor with eigenvalues $[1, 0.3, 0.3] \times 10^{-3}$ mm^2/s totally aligned with axis. This corresponds to FA=0.6444. We rotate the tensor according to two different rotation schemes, see Fig. 8.4:

1. Rotation in plane, so one of the components of the tensor is aligned with one axis. The rotation matrix is:

$$R_M = \begin{bmatrix} \cos(\theta) & 0 & \sin(\theta) \\ 0 & 1 & 0 \\ -\sin(\theta) & 0 & \cos(\theta) \end{bmatrix}$$

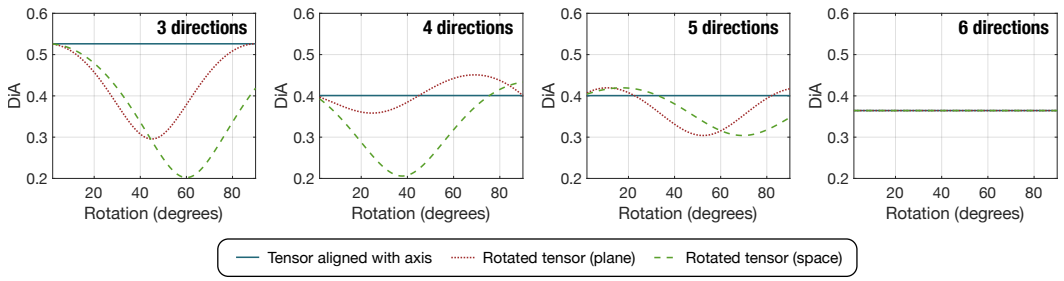

Fig. 8.5.: DiA calculated from 3 acquisitions. The main diffusion direction of the tensor is rotated a certain angle so that the fiber is not aligned with the axis.

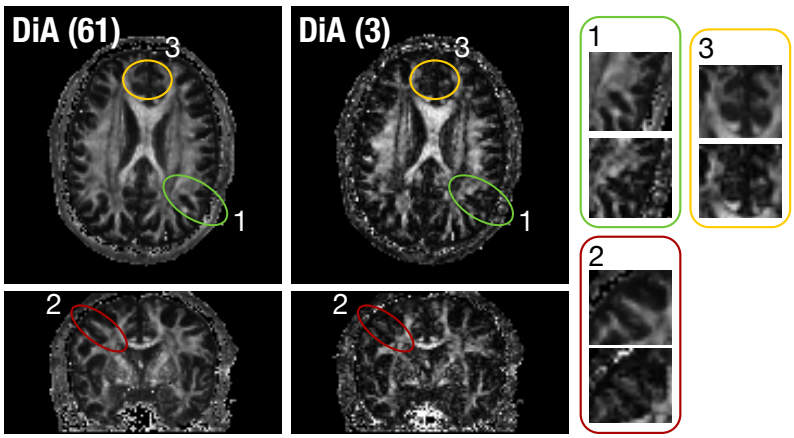

Fig. 8.6.: DiA calculated with 61 and 3 gradient directions: Comparison of the anisotropy in three different areas for bundles not aligned with the axis.

2. Spatial rotation, so none of the components are aligned with any axes. The rotation matrix is:

$$R_M = \begin{bmatrix} \frac{1}{3} + \frac{2}{3}\cos(\theta) & (1-\cos(\theta))\frac{1}{3} - \frac{1}{\sqrt{3}}\sin(\theta) & (1-\cos(\theta))\frac{1}{3} + \frac{1}{\sqrt{3}}\sin(\theta) \\ (1-\cos(\theta))\frac{1}{3} + \frac{1}{\sqrt{3}}\sin(\theta) & \frac{1}{3} + \frac{2}{3}\cos(\theta) & (1-\cos(\theta))\frac{1}{3} - \frac{1}{\sqrt{3}}\sin(\theta) \\ (1-\cos(\theta))\frac{1}{3} - \frac{1}{\sqrt{3}}\sin(\theta) & (1-\cos(\theta))\frac{1}{3} + \frac{1}{\sqrt{3}}\sin(\theta) & \frac{1}{3} + \cos(\theta)\frac{2}{3} \end{bmatrix}.$$

The tensor is sampled using three to six directions. For the case of 3 directions, these correspond to the Cartesian axes. For the sake of simplicity, no noise or simulated artifacts are added to the tensor. The diffusivity $D(\mathbf{x})$ is reconstructed and the DiA is calculated for each case. The values of DiA for the different sampling schemes and for different rotation angles are shown in Fig. 8.5 (plane rotation in red and spatial rotation in green).

Note that, according to the figure, when the DiA is estimated with only 3 directions, there is a clear underestimation of the metric when the main diffusion direction is not aligned with the directions of the acquired gradients. If we focus on the in plane rotation, the maximum error arises precisely for the 45^o angle, when the main direction is diagonal to the axis. This is also the case for 4 and 5 directions, while with 6 directions the same DiA is provided, regardless of the orientation of the tensor.

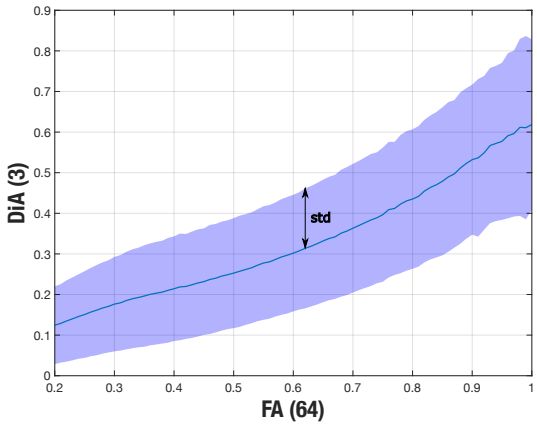

Fig. 8.7.: Variability of the DiA as a function of the orientation of the acquired direction. HCP data have been used. In blue, the median along different gradient configurations.

This experiment raises the main weakness of this method, the underestimation of the anisotropy of those fibers not aligned with the axis. This effect can also be seen on real data. In Fig. 8.6 we show one axial and one coronal slice from the UVa volume. We have calculated DiA for 61 and 3 gradient directions in order to compare the loss of information. We have highlighted some of the fiber bundles that are not aligned with the axis. Let us first focus on the structures circled in green and red (numbers 1 and 2). These structures would correspond to the rotation in plane in Fig. 8.5, with an angle of around 45^o respect to the axis. According to the previous experiment, the anisotropy here would experience its maximum underestimation. This is the case in Fig 8.6: the bundles in DiA with 3 gradient directions show a reduced value, when compared to the 61 case. However, in both cases (1 and 2), although reduced, the bundles are still present. A similar effect can be found on the area number 3. A small structure has almost disappeared due to its orientation.

Finally, we numerically quantified this variability over the HCP data (volume MGH1010). We downsample the 64 acquired directions to sets of 3 directions through an exhaustive search with all possible orientations. This way, we consider sampling schemes not aligned with the axis and in all the possible orientations. DiA is calculated for each acquisition set using eq. (8.4). The median and standard deviation is calculated along the different configuration. Results as a function of the FA are shown in Fig. 8.7.

Despite its great variability with the orientation of the acquired gradients, DiA also shows a great correlation (in median) with the FA, revealing that the differences in the anisotropy detected by FA can still be seen when using DiA 3 orientations, although with a greater variance.

8.4 Discussion and Conclusions

The calculation of anisotropy measures over diffusion data is usually limited by the 6 gradient directions needed to estimate the components of the diffusion tensor. Hence, in those fast acquisitions for which only 3 orientations are acquired, only information about the *amount* of diffusion can be inferred. That is the case of fast diffusion sequences in commercial

scanners (like EPI-DWI) in which the installed software produces an image which is the average of 3 images acquired with 3 orthogonal gradient directions where no information about the orientation of the diffusion is present.

In this work we have proposed a method that is able to calculate a rough anisotropy image that could give complementary information about the anisotropy and orientation of the diffusion with just those 3 orthogonal directions. In addition, we also provide a color-coded version that helps in better understanding the orientation of the different structures. The method is totally compatible with existing fast acquisition sequences, and it does not require extra data: the anisotropy metric is calculated from the same DWIs used for the MD estimation.

On the other hand, the use of 6 gradient directions to better characterize diffusion is not only related with the 6 degrees of freedom of the diffusion tensor. It is well-known that there is an intrinsic limitation in dMRI that hinders the proper estimation of anisotropy measures to characterize fibers in all different spatial directions. This effect also affects the method here proposed, imposing a limitation of use. We have shown that those fibers that are not aligned with the axes will be underestimated, the larger the misalignment the larger the underestimation. Thus, this method is not able to circumvent this intrinsic limitation of dMRI and therefore it must be used with caution. The purpose of the method is not to be used in clinical studies or as a substitute of the FA, but to provide complimentary information in fast diffusion acquisitions. There is a clear loss of information when compared with a complete dMRI acquisition, but there is also a clear additional information when compared with that provided only by the MD. In this sense, the advantage of using DiA is its ability to provide anisotropy information with the smallest possible data set.

Software

The full implementation of DiA is included in the AMURA toolbox and it may be downloaded for Matlab© and Octave, together with use-case examples and test data, from: `http://www.lpi.tel.uva.es/AMURA`.

Acknowledgments

This work was funded in whole, or in part, by Ministerio de Ciencia e Innovación of Spain with research grant RTI2018-094569-B-I00, by a Wellcome Trust Investigator Award (096646/Z/11/Z) and a Wellcome Trust Strategic Award (104943/Z/14/Z). For the purpose of open access, the author has applied a CC BY public copyright license to any Author Accepted Manuscript version arising from this submission. Data collection and sharing for this project was provided by the *Human Connectome Project* (HCP; Principal Investigators: Bruce Rosen, M.D., Ph.D., Arthur W. Toga, Ph.D., Van J. Weeden, MD). HCP funding was provided by the National Institute of Dental and Craniofacial Research (NIDCR), the National Institute of Mental Health (NIMH), and the National Institute of Neurological Disorders and Stroke (NINDS). HCP data are disseminated by the Laboratory of Neuro Imaging at the University of Southern California.

Conflict of interest

The authors declare that there is no conflict of interest.

Bibliography

[8.1] E. H. de Figueiredo, A. Borgonovi, T. M. Doring, Basic concepts of MR imaging, diffusion MR imaging, and diffusion tensor imaging., Magnetic resonance imaging clinics of North America 19 (1) (2011) 1–22.

[8.2] C.-F. Westin, S. E. Maier, H. Mamata, A. Nabavi, F. A. Jolesz, R. Kikinis, Processing and visualization for diffusion tensor MRI, Medical image analysis 6 (2) (2002) 93–108.

[8.3] S. Aja-Fernández, T. Pieciak, A. Tristán-Vega, G. Vegas-Sánchez-Ferrero, V. Molina, R. de Luis-García, Scalar diffusion-MRI measures invariant to acquisition parameters: a first step towards imaging biomarkers, Magnetic Resonance in Medicine 53 (2018) 123–133.

[8.4] P. Basser, C. Pierpaoli, Microstructural features measured using diffusion tensor imaging, Journal of Magnetic Resonance 111 (3) (1996) 209–219.

[8.5] S. Aja-Fernández, A. Tristán-Vega, D. K. Jones, Apparent propagator anisotropy from single-shell diffusion MRI acquisitions, Magnetic Resonance in Medicine 85 (5) (2021) 2869–2881.

[8.6] E. Özarslan, B. C. Vemuri, T. H. Mareci, Generalized scalar measures for diffusion MRI using trace, variance, and entropy, Magnetic Resonance in Medicine 53 (4) (2005) 866–876.

[8.7] I. D. Naranjo, A. Reymbaut, P. Brynolfsson, R. Lo Gullo, K. Bryskhe, D. Topgaard, D. D. Giri, J. S. Reiner, S. B. Thakur, K. Pinker-Domenig, Multidimensional diffusion magnetic resonance imaging for characterization of tissue microstructure in breast cancer patients: A prospective pilot study, Cancers 13 (7).

[8.8] A. Reymbaut, P. Mezzani, J. P. de Almeida Martins, D. Topgaard, Accuracy and precision of statistical descriptors obtained from multidimensional diffusion signal inversion algorithms, NMR in Biomedicine 33 (12) (2020) e4267, e4267 nbm.4267.

[8.9] S. Pajevic, C. Pierpaoli, Color schemes to represent the orientation of anisotropic tissues from diffusion tensor data: application to white matter fiber tract mapping in the human brain, Magnetic Resonance in Medicine 42 (3) (1999) 526–540.

[8.10] J.-D. Tournier, R. Smith, D. Raffelt, R. Tabbara, T. Dhollander, M. Pietsch, D. Christiaens, B. Jeurissen, C.-H. Yeh, A. Connelly, MRtrix3: A fast, flexible and open software framework for medical image processing and visualisation, NeuroImage 202 (2019) 116137.

9

Accurate free-water estimation in white matter from fast diffusion MRI acquisitions using the spherical means technique

Antonio Tristán-Vega, Guillem París, Rodrigo de Luis-García, Santiago Aja-Fernández

Laboratorio de Procesado de Imagen (LPI), Universidad de Valladolid, Spain

Abstract:

Purpose: To accurately estimate the partial volume fraction of free-water in the white matter from diffusion MRI acquisitions not demanding strong sensitizing gradients and/or large collections of different b-values. Data sets considered comprise ∼32–64 gradients near $b = 1,000\,\mathrm{s/mm^2}$ plus ∼6 gradients near $b = 500\,\mathrm{s/mm^2}$.

Theory and Methods: The spherical means of each diffusion MRI set with the same b-value are computed. These means are related to the inherent diffusion parameters within the voxel (free- and cellular-water fractions; cellular water diffusivity), which are solved by constrained Nonlinear Least Squares regression.

Results: The proposed method outperforms those based on mixtures of two Gaussians for the kind of data sets considered. W.r.t. the accuracy, the former does not introduce significant biases in the scenarios of interest, while the latter can reach a bias of 5%–7% if fiber crossings are present. W.r.t. the precision, a variance near 10%, compared to 15%, can be attained for usual configurations.

Conclusion: It is possible to compute reliable estimates of the free-water fraction inside the white matter by complementing typical DTI acquisitions with few gradients at a *low* b-value. It can be done voxel-by-voxel, without imposing spatial regularity constraints.

Originally published as: *Antonio Tristán-Vega, Guillem París, Rodrigo de Luis-García, Santiago Aja-Fernández, Accurate free-water estimation in white matter from fast diffusion MRI acquisitions using the spherical means technique, Magnetic Resonance in Medicine 87 (2), 1028-1035, 2022*

9.1 Introduction

The estimation of the partial volume fraction (PVF) of free-water (FW) inside brain tissues, and specifically inside the white matter (WM), serves two purposes in diffusion MRI: first, eliminating a confounding factor within Diffusion Tensor Imaging (DTI) [9.1], which

emanates from the limited resolution of Diffusion Weighted Images (DWI) [9.2]. Second, the FW-PVF itself can be a biological marker for the description of tumorous edema, neuro-inflammation, and others [9.3, 9.4].

Several techniques for FW-PVF estimation have been proposed that can be classified depending on the kind of DWI collections they employ: micro-structure oriented methods like NODDI [9.5], spherical means [9.6], or MiSFIT [9.7] consider multi-shells, i.e. few medium-high b-values (∼2–4, up to $10,000\,\mathrm{s/mm^2}$) with ∼64–128 gradient directions each; spectral methods [9.8, 9.9] manage large sets (∼15) of low-medium b-values (up to $2,500\,\mathrm{s/mm^2}$) with few gradients each (<15); finally, DTI-based methods use either single-shell acquisitions near $1,000\,\mathrm{s/mm^2}$ [9.2, 9.3] or they complement this *standard* DTI acquisition with few gradients at a smaller b-value ($\sim 500\,\mathrm{s/mm^2}$) [9.10].

We are interested here in little demanding acquisitions. Even when single-shell estimates can be reliable if a proper regularization is embedded [9.3], it has been shown that these results must be interpreted with care [9.11]. Since both regularized [9.10] and unregularized [9.12] schemes benefit from using a complementary b-value, we will focus on samplings like those in [9.10], with ∼32–64 gradient directions at $b \sim 1,000\,\mathrm{s/mm^2}$ plus ∼6 gradients at $b \sim 500\,\mathrm{s/mm^2}$. With a 3T, multi-coil device, acquisition times can thus be reduced from 40 to 15 minutes compared to the protocol suggested in [9.12].

We propose a method to estimate the FW-PVF voxel-wise, without any spatial regularization. It models the DWI as the convolution of a non-parametric fiber Orientation Distribution Function (fODF) with an impulse response that depends on the cellular-water (CW) PVF. This has the additional advantage of releasing our approach of the Gaussian assumption for CW diffusion, which inside the WM is strictly valid only if a unique dominant direction exists [9.3]. CW-PVF estimation then reduces to a Least Squares (LS) fitting of two parameters, so that it can be attained from the spherical means of two acquired shells.

9.2 Theory

According to the two-component model in [9.2], the signal $S(\mathbf{g}_i, b_i)$ obtained when a diffusion gradient $\mathbf{g}_i$ with b-value b_i is applied becomes the mixture of a CW-PVF, f, plus a FW-PVF, $1-f$:

$$\frac{S(\mathbf{g}_i, b_i)}{S_0} = f \cdot \overbrace{\exp\left(-b_i\, \mathbf{g}_i^T \mathbf{D} \mathbf{g}_i\right)}^{\text{CW}} + (1-f) \cdot \overbrace{\exp\left(-b_i\, D_0\right)}^{\text{FW}}, \tag{9.1}$$

where S_0 is the unweighted T2 baseline, $\mathbf{D}$ is the 3×3 symmetric Diffusion Tensor (DT), and D_0 is the diffusivity of FW at body temperature (nearly $3.0 \cdot 10^{-3}\,\mathrm{mm^2/s}$). Provided a collection $\{\mathbf{g}_i, b_i\}_{i=1}^{N}$, $N \gg 7$ is available, eq. (9.1) can be solved for seven unknowns: the six free components of $\mathbf{D}$ and f itself. In [9.3], a unique b is used for all $\mathbf{g}_i$, which turns the problem ill posed. On the contrary, it is shown in [9.12] that a robust estimation of f is feasible voxel-by-voxel by acquiring two shells, i. e. two collections of evenly spaced gradients with two different b-values: $\{\mathbf{g}_{i_1}, b_1\}_{i_1=1}^{N/2} \bigcup \{\mathbf{g}_{i_2}, b_2\}_{i_2=1}^{N/2}$.

Eq. (9.1) models either the GM or single-bundled WM [9.3]. To get rid of the latter limitation, we make use of the representation proposed in [9.7], which entails a continuous mixture of tensors in the space of orientations, $\Omega \equiv \{\mathbf{v} \in \mathbb{R}^3 : \|\mathbf{v}\| = 1\}$:

$$\frac{S(\mathbf{g},b)}{S_0} = f \cdot \overbrace{\iint_{\Omega} \Phi(\mathbf{v}) \exp\left(-b\left(\left(\mathbf{v}^T\mathbf{g}\right)^2\left(\lambda_{\parallel}-\lambda_{\perp}\right)+\lambda_{\perp}\right)\right) d\mathbf{v}}^{\text{CW}} + (1-f)\cdot \overbrace{\exp\left(-b\,D_0\right)}^{\text{FW}}, \tag{9.2}$$

where $\Phi(\mathbf{v}) \geq 0$, which sums up to 1 in Ω, is an fODF that accounts for the PVFs of the continuous mixture of WM bundles. The two parameters $0 \leq \lambda_{\perp} \leq \lambda_{\parallel} \leq D_0$ describe the (distinct) eigenvalues of a prolate DT whose main eigenvector is aligned with $\mathbf{v}$, which can be seen as the impulse response of each WM bundle [9.7, 9.13]. The key point in [9.7] is that, for shells-like samplings, eq. (9.2) can be averaged over Ω to obtain one spherical mean per measured shell that no longer depends on the fODF:

$$\widehat{s}_j \triangleq \frac{1}{4\pi}\iint_{\Omega} \frac{S(\mathbf{g},b_j)}{S_0}\, d\mathbf{g} = f\cdot\frac{\sqrt{\pi}}{2}\exp\left(-b_j\lambda_{\perp}\right)\frac{\operatorname{erf}\left(\sqrt{b_j\left(\lambda_{\parallel}-\lambda_{\perp}\right)}\right)}{\sqrt{b_j\left(\lambda_{\parallel}-\lambda_{\perp}\right)}} + (1-f)\cdot\exp\left(-b_j\,D_0\right), \tag{9.3}$$

which depends on three unknowns, f, $\lambda_{\parallel}$, and $\lambda_{\perp}$, that need to be solved from $M \geq 3$ equations corresponding to each acquired shell with b-value $\{b_j\}_{j=1}^{M}$. Provided we aim at estimating f from dual b-valued data sets, we first modify the method in [9.7] by fixing $\lambda_{\parallel}$ and solving eq. (9.3) for f and $\lambda_{\perp}$ from the spherical averages $\{\widehat{s}_j\}_{j=1}^{M}$ of $M \geq 2$ shells. The rationale behind this is the low sensitivity observed for $\lambda_{\parallel}$ within the WM in [9.7, Fig. 2] and [9.13, Fig. 5].

9.3 Methods

9.3.1 Numerical resolution of equation (9.3)

Let $\mathcal{M} = \bigcup_{j=1}^{M}\{\mathbf{g}_{i_j}, b_j\}_{i_j=1}^{N_j}$ be a multi-shell sampling with M shells and N_j gradient directions each. The j-th spherical mean, $\widehat{s}_j$, is obtained by fitting the samples $\{S(\mathbf{g}_{i_j},b_j)/S_0\}_{i_j=1}^{N_j}$ in the basis of Spherical Harmonics (SH), following the numerical approach described in [9.14]: if C_0^0 is the DC component of the SH expansion, then $\widehat{s}_j = C_0^0/\sqrt{4\pi}$. Like in [9.7], we develop on eq. (9.3) to isolate f in one term and take logarithms. The problem reduces to a LS minimization over $M \geq 2$ shells:

$$\min_{f,\lambda_{\perp}} \frac{1}{2}\sum_{j=1}^{M}\left(\log\left(\frac{\widehat{s}_j-(1-f)e^{-b_j D_0}}{f}\right)+b_j\lambda_{\perp}+\log\left(\frac{2\sqrt{b_j(\lambda_{\parallel}-\lambda_{\perp})}}{\sqrt{\pi}\operatorname{erf}\left(\sqrt{b_j(\lambda_{\parallel}-\lambda_{\perp})}\right)}\right)\right)^2 + \nu\,\frac{\lambda_{\perp}}{\lambda_{\parallel}-\lambda_{\perp}}, \tag{9.4}$$

where we fix $\lambda_{\parallel} = 2.1\cdot 10^{-3}\,\text{mm}^2/\text{s}$ throughout, after the results in [9.7, Fig. 2]. The penalty term weighted by the constant $\nu \geq 0$ is a second necessary modification to [9.7], and promotes prolate convolution kernels when $\mathcal{M}$ is restricted to small b-values. Finally,

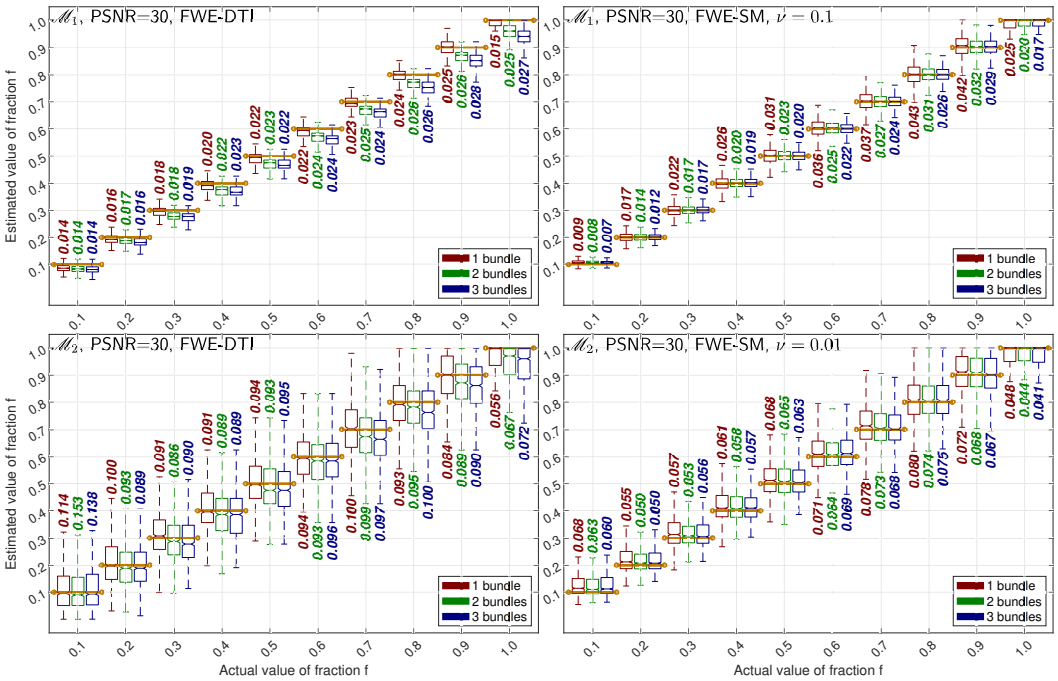

Fig. 9.1.: Numeric comparison of the accuracy of FWE-DTI (left) vs. the proposed FWE-SM (right) based on the model in eq. (9.7) (for either 1, 2, or 3 simulated fiber bundles). The sampling schemes $\mathcal{M}_1$ (top) and $\mathcal{M}_2$ (bottom) are taken from the Dryad volume, with a typical PSNR=30. Boxes represent the 25% and 75% quantiles of the estimated f; whiskers represent the extreme values; notches represent the median value; the quantity next to each boxlplot represents the standard deviation of the corresponding data. All the boxplots are computed over 1,000 random samples.

for the problem to be physically consistent, we need to impose additional constraints to the objective function in eq. (9.4):

$$f_0 \leq f \leq 1, \text{ for } f_0 = \max_{j=1\ldots M} \max\left\{1 - \frac{\widehat{s}_j}{e^{-b_j D_0}}, 1 - \frac{1-\widehat{s}_j}{1-e^{-b_j D_0}}\right\}; \tag{9.5}$$

$$0 \leq \lambda_\perp \leq \lambda_\parallel. \tag{9.6}$$

Eq. (9.5) ensures the CW-PVF remains in the allowed range $[0, 1]$, meanwhile eq. (9.6) ensures the convolution kernel is actually prolate. The LS problem described by the objective function (9.4) and the constraints (9.5) and (9.6) is solved by means of a gradient-projection algorithm derived from [9.7, Appendix A].

9.3.2 Generation of synthetic data

The validation of our proposal is partially based on numeric comparisons over synthetically generated voxels. For each sample $\{\mathbf{g}_{i_j}, b_j\} \in \mathcal{M}$, the synthetic signal will fit this compound multi-tensor model:

$$S(\mathbf{g}_{i_j}, b_j) = f \cdot S_0 \sum_{k=1}^{3} \alpha_k \exp\left(-b_j \mathbf{g}_{i_j}^T \mathbf{D}_k \mathbf{g}_{i_j}\right) + (1-f) \cdot S_0 \exp\left(-b_j D_0\right), \ \sum_{k=1}^{3} \alpha_k = 1, \tag{9.7}$$

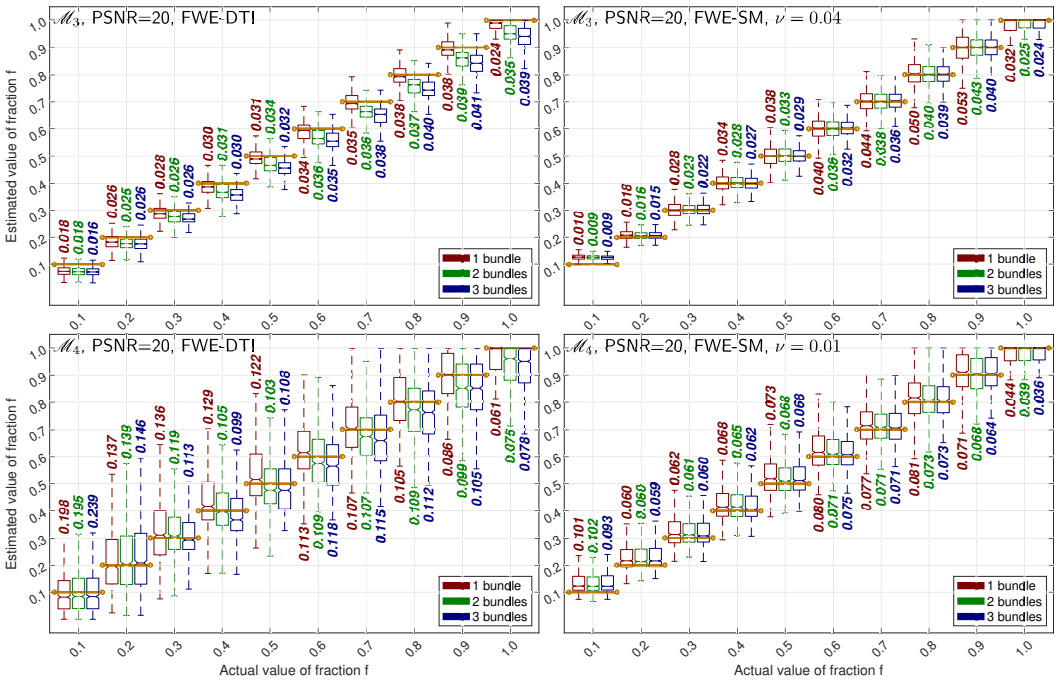

Fig. 9.2.: Numeric comparison of the accuracy of FWE-DTI (left) vs. the proposed FWE-SM (right) based on the model in eq. (9.7) (for either 1, 2, or 3 simulated fiber bundles). The sampling schemes $\mathcal{M}_3$ (top) and $\mathcal{M}_4$ (bottom) are taken from the UVa volume, with a typical PSNR=20. The notation is as in Fig. 9.1. All the boxplots are computed over 1,000 random samples.

which allows simulating WM configurations with either a unique dominant fiber bundle, $\{\alpha_1 \neq 0, 0, 0\}$, two bundles, $\{\alpha_1 \neq 0, \alpha_2 \neq 0, 0\}$, or three bundles $\{\alpha_1 \neq 0, \alpha_2 \neq 0, \alpha_3 \neq 0\}$. In all cases, the non-null α_k are generated as uniform random numbers in $[0.4, 0.6]$, and then normalized to sum to 1. The eigenvalues of each DT, $\mathbf{D}_k$, are designed as Gaussian random variables with mean and standard deviation retrospectively chosen based on the experiment in Fig. 9.3: $\lambda_1 \sim N(1.3, 0.3)$; $\lambda_2 \sim N(0.4, 0.1)$; $\lambda_3 \sim N(0.25, 0.08)$ ($\times 10^{-3}$ mm^2/s). The eigenvectors of $\mathbf{D}_1$ are respectively aligned with axes 'x', 'y', and 'z'; those of $\mathbf{D}_2$ are aligned with axes 'y', 'z', and 'x'; those of $\mathbf{D}_3$, with 'z', 'x', and 'y'. The whole ensemble is randomly rotated, and both the diffusion signal and the unweighted T2 baseline are contaminated with Rician noise with known PSNR (defined as S_0/σ, with σ^2 the noise power in the complex domain).

9.3.3 Materials

Two different data sets have been used for testing:

- From the Dryad data repository[1], the human data set described in [9.15]. It was acquired with a Siemens Trio 3T with resolution $2.5\,\text{mm}^3$ and matrix size $96 \times 96 \times 19$ covering the central part of the brain. Imaging parameters are TR= $7,200$ ms, TE= 116 ms, with a typical PSNR of 30 inside the WM. Among the available b-values, we use a multi shell scheme $\mathcal{M}_1$ with $M = 8$ shells and $N_j = 33, \forall j$ gradient directions

[1] Available: `https://datadryad.org/stash/dataset/doi:10.5061/dryad.9bc43`.

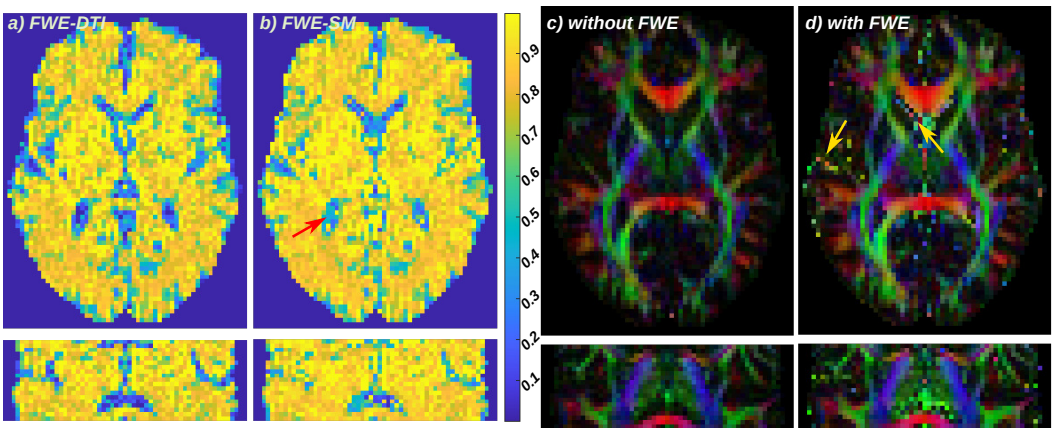

Fig. 9.3.: CW-PVF in the Dryad volume, f, as estimated with either FWE-DTI (a) or the proposed FWE-SM with $\nu = 0.1$ (b). For the latter, standard color-coded maps based on the first eigenvector of the DTI are shown before (c) and after (d) FW elimination. The central axial and coronal slices are shown in all cases. The red arrow points to CSF voxels for which FWE-SM overestimates f. The yellow arrows point to DTI outliers after FWE in these same regions.

each. The b-values $\{b_j\}_{j=1}^{8}$ are evenly spaced from $b_1 = 200$ to $b_8 = 1,600$ in steps of 200 (in s/mm^2). A sub-sampled multi-shell scheme $\mathcal{M}_2$ is obtained from $\mathcal{M}_1$ with just $M = 2$ shells: the first one, with all $\{\mathbf{g}_{i_5}\}_{i_5=1}^{33}$ at $b_5 = 1,000\,\text{s/mm}^2$ directly taken from $\mathcal{M}_1$; the second one, by decimating the set $\{\mathbf{g}_{i_2}\}_{i_2=1}^{33}$ at $b_2 = 400\,\text{s/mm}^2$ from $\mathcal{M}_1$ to 6 gradient directions minimizing the electrostatic repulsion energy (by greedy search). Hence, in $\mathcal{M}_2$, $M = 2$, $N_1 = 33, b_1 = 1,000\,\text{s/mm}^2$, $N_2 = 6, b_2 = 400\,\text{s/mm}^2$.

- A volume acquired with a 3T Philips Achieva at the Universidad de Valladolid (UVa), with a multi-shell scheme $\mathcal{M}_3$ defined by $M = 3$ shells with $N_j = 64, \forall j$ gradient directions each. The respective b-values (in s/mm^2) are $b_1 = 500$, $b_2 = 1,000$, and $b_3 = 1,500$. The spatial resolution is $1.875^2 \times 2.5\,\text{mm}^3$, with matrix size $128 \times 128 \times 52$ for full-brain coverage. The TE and TR are, respectively, 83 ms and 9,000 ms, granting a typical PSNR nearly 20 inside the WM. We obtain an additional multi-shell scheme $\mathcal{M}_4$ with $M = 2$, $N_1 = 64, b_1 = 1,000\,\text{s/mm}^2$, $N_2 = 6, b_2 = 500\,\text{s/mm}^2$ by keeping the original shell at $b = 1,000\,\text{s/mm}^2$ from $\mathcal{M}_3$ and decimating the shell at $b = 500\,\text{s/mm}^2$.

The WM was roughly segmented by thresholding the Fractional Anisotropy (FA) at a value of 0.35. The FA was computed in all cases from a DTI fitted to the DWI with regular LS [9.16]. Besides, the WM was classified in three groups based on Westin's coefficients [9.16]: linear (C_l), planar (C_p), and spherical (C_s). After initializing three clusters with centroids $[C_l, C_p, C_s] = \{[1,0,0],[0,1,0],[0,0,1]\}$, the C-means algorithm was run until convergence. We can reasonably hypothesize the first cluster corresponds to WM configurations with a unique dominant direction ($\alpha_2 = \alpha_3 = 0$ in eq. (9.7)), the second one to configurations with two dominant bundles ($\alpha_3 = 0$ in eq. (9.7)), and the third one to more complex configurations ($\alpha_k \neq 0,\ \forall k$).

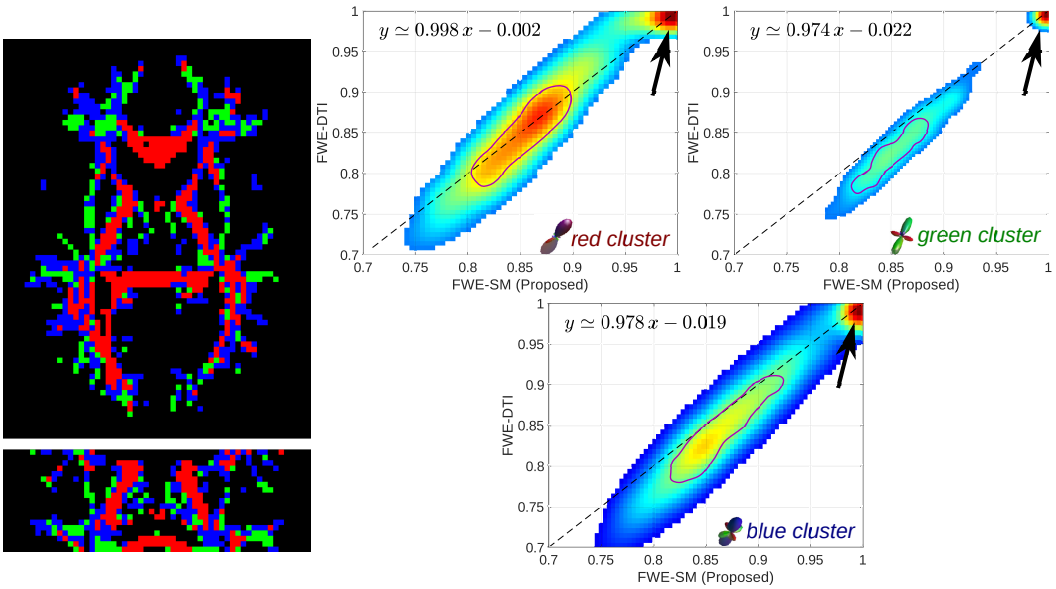

Fig. 9.4.: WM clustering of the Dryad volume. The 2-D histograms compare the CW-PVF, f, computed with either FWE-DTI or the proposed FWE-SM ($\nu = 0.1$) with the *full* sampling $\mathcal{M}_1$, inside each WM cluster. The black arrows point to histogram values coming from the saturation of f to its maximum value of 1. The equations $y = a\,x + b$ are obtained from linear regression, so that b stands for the relative bias of FWE-DTI w. r. t. FWE-SM.

9.4 Results

The proposed method (hereafter FWE-SM, standing for Free-Water Elimination–Spherical Means) will be compared to [9.12] (hereafter FWE-DTI), as long as it is also aimed at voxel-by-voxel estimation, without spatial regularization, with b-values typical of DTI. According to Section 9.3.2, we can simulate synthetic voxels for the multi-shell schemes $\mathcal{M}_{1,2,3,4}$ with ground truth values of f, so that we can evaluate the performance of each method at scenarios reasonably similar to those expected within the WM of the subjects described in Section 9.3.3. The respective results are shown in Figs. 9.1 and 9.2 (the parameter ν in eq. (9.4) has been empirically fixed in all cases): with the *whole* samplings $\mathcal{M}_1$ and $\mathcal{M}_3$, both methods are precise, with small variances in all cases. In terms of precision, FWE-DTI provides smaller variances for 1-bundle configurations, but similar or greater variances for 2- or 3-bundles. In terms of accuracy, while FWE-SM remains unbiased for almost all configurations (except for very small f), FWE-DTI presents noticeable negative biases for 2-bundles and 3-bundles, reaching values near 5%–7% for CW-PVF in the range $[0.7, 0.8]$. Yet, the main purpose of the present paper is the accurate estimation of f from acquisitions more alike $\mathcal{M}_2$ and $\mathcal{M}_4$. In these cases, FWE-SM remains accurate (no noticeable biases appear), with a more subtle effect on the precision than FWE-DTI suffers: note, both in Figs. 9.1 and 9.2, the heavy increase of boxes and whiskers sizes (i. e. $25\%\,/\,75\%$ quantiles and extreme values), as well as variances, from the top line to the bottom for FWE-DTI, which is not equally dramatic for FWE-SM.

The consistency of FWE-SM for a real data set is checked in Fig. 9.3, where f is calculated for the Dryad volume with the *full* sampling $\mathcal{M}_1$. As it could be predicted from Fig. 9.1, the results from both FWE-DTI and FWE-SM look quite similar throughout the WM. This

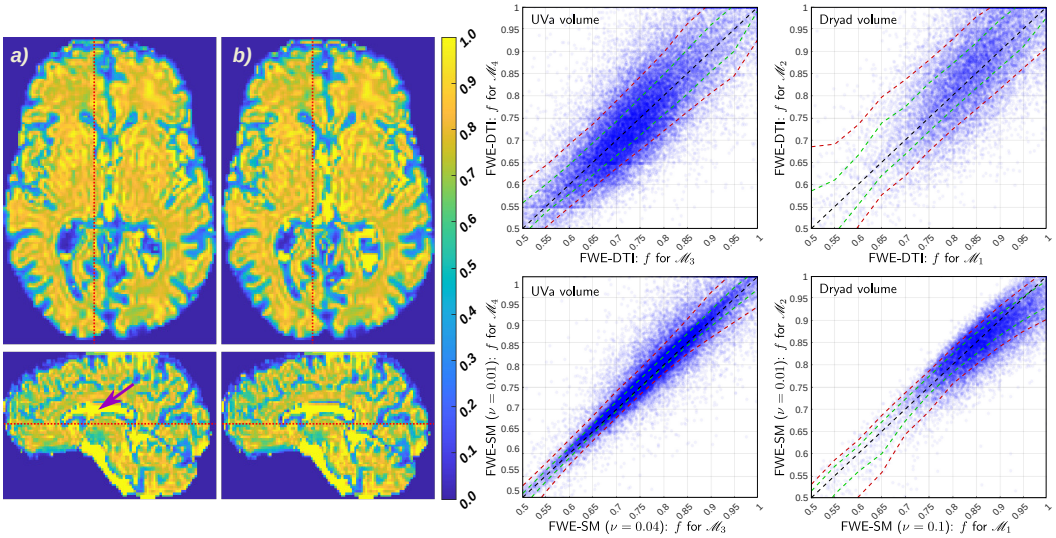

Fig. 9.5.: Comparison of the estimates of the CW-PVF, f, obtained with either *ad hoc* samplings ($\mathcal{M}_1$, $\mathcal{M}_3$) or DTI-like samplings ($\mathcal{M}_2$, $\mathcal{M}_4$): axial and sagittal slices are shown for the UVa volume, estimated with FWE-SM from a) $\mathcal{M}_3$ ($\nu = 0.04$), b) $\mathcal{M}_4$ ($\nu = 0.01$). The scatter plots depict the comparison of the *full* sampled data sets with the sub-sampled data sets, for both test volumes, and for either FWE-DTI or FWE-SM, inside the WM. Green dashed lines represent the 25% / 75% quantiles, and red dashed lines represent the 10% / 90% quantiles. The purple arrow points to pure CSF voxels, for which the FWE-SM model becomes ambiguous.

statement holds also for the GM, the main difference between the two approaches being at the CSF (red arrow): in these pure FW regions, our FWE-SM tends to overestimate f, which is also visible in Fig. 9.2 (top, right) for the sampling scheme $\mathcal{M}_3$ (but not really evident in Fig. 9.1 for $\mathcal{M}_1$). Moreover, we can refer to eq. (9.1), then use standard LS [9.16], to compare the DTI estimation either with or without FW elimination as shown in Fig. 9.3 (c) and (d). As expected, eliminating the FW compartment does not alter the structure or directionality of the WM bundles, but it notably increases their observed anisotropy (which translates in *brighter colors*). On the other hand, FW elimination is likely to introduce outliers at the CSF (yellow arrows).

To further investigate the behavior observed in Figs.9.1 and 9.2, Fig. 9.4 compares FWE-DTI and FWE-SM inside three WM clusters obtained as described in Section 9.3.3, roughly corresponding to prolate, oblate, or spherical configurations. In all cases, a prominent histogram mode at $[1.0, 1.0]$ is present, likely corresponding to the saturation of f to its maximum value. Obviating this artifact, the histograms demonstrate a strong correlation between both methods with slope approximately 1. While the principal mode for the red cluster (purple contour) is completely over the identity line, the principal modes of the other clusters demonstrate a negative bias of FWE-DTI one order of magnitude above that found inside the red cluster, which is consistent with Figs.9.1 and 9.2. The computation of the eigenvalues of the DTI inside the red cluster yields respective values (mean$\pm$standard deviation, $\times 10^{-3}$ mm^2/s): 1.3 ± 0.3; 0.4 ± 0.1; 0.25 ± 0.08.

The final experiment, summarized in Fig. 9.5, is aimed at checking to what extent the performance in the estimation of f worsens when a nearly standard DTI acquisition, like $\mathcal{M}_2$ or $\mathcal{M}_4$, is used instead of an *ad hoc* one, like $\mathcal{M}_1$ or $\mathcal{M}_3$. The estimates obtained for either the Dryad volume with $\mathcal{M}_1$ or the UVa with $\mathcal{M}_3$ are used as a silver standard, and the respective

estimates for $\mathcal{M}_2$ and $\mathcal{M}_4$ are compared against it: for the UVa volume, the appearance of the f maps are almost identical with both $\mathcal{M}_3$ and $\mathcal{M}_4$ (the results for the Dryad volume, not shown, are analogous), which translates in a tight fit of the 25% / 75% quantiles of the sub-sampled estimates compared to the silver standard. Though these quantiles spread more for the Dryad volume, probably due to the smaller number of gradients in the shell at $b = 1,000\,\mathrm{s/mm^2}$, they still show a much better performance compared to the FWE-DTI approach, whose 10% / 90% quantiles show a great dispersion for the extreme values. Noticeably, the miss-estimation at CSF voxels becomes accentuated for the UVa volume, see the purple arrow in Fig. 9.5 (a).

9.5 Discussion and Conclusions

The proposed FWE-SM is able to compute accurate estimates of the CW-PVF f from acquisitions comparable to those in DTI studies, at the only expense of acquiring as few as six additional gradients at a lower b-value. This allows to complement, or even improve, such DTI studies with little additional effort. With acquisitions specifically designed for FW elimination, it is as precise as DTI-based methods [9.3, 9.10, 9.12], but it remains unbiased in almost all situations. Though the bias for FWE-DTI is predictable in terms of f itself, it directly depends on the number of crossing fibers, which is unknown beforehand. FWE-SM gets rid of this confounding factor by averaging all fiber bundles.

For the fast acquisitions object of study in this paper, the errors committed by FWE-SM may increase to 10% for typical CW-PVF values (in the range of $[0.7, 1.0]$), or up to 70% for CSF voxels. Though these errors are still below those achievable with FWE-DTI, it is arguable if this accuracy might suffice to describe FW voxel-wise. As opposed to [9.3, 9.10], we do not rely on any spatial regularization to provide consistent results, but such techniques could be used by either applying a corresponding penalty to eq. (9.4) or pre-processing the DWI with some sort of denoising technique. Since using reduced samplings increases the variance of the results without notably biasing them, both approaches should help improving the voxel-wise accuracy.

On the other hand, our proposal reduces the number of degrees of freedom by fixing $\lambda_\parallel$ in eq. (9.2), which compels using a regularization parameter ν we need to fix. Fortunately, we have empirically checked that this parameter is much less sensitive to the PSNR than it is to the sampling scheme, so that it can be fixed, based on synthetic experiments like those in Figs. 9.1 and 9.2, for the entire volume (like we did throughout the paper). Moreover, since we are focusing on acquisitions like $\mathcal{M}_2$ and $\mathcal{M}_4$, we can recommend a standard value $\nu = 0.01$.

Finally, the proposed method fails at estimating f inside voxels with large CSF contamination, for which the convolution model in eq. (9.2) becomes ambiguous [9.7]. This illness compromises its validity for the study of pathological conditions like edema or WM hyperintensities, though *ad hoc* corrections like those in [9.12] could be thought of in the presence of abnormally large $\lambda_\perp$ and small f.

Acknowledgments

This work was supported by Ministerio de Ciencia e Innovación (Spain) through research grant RTI2018-094569-B-I00.

Software

All methods tested in this paper, including a clone of the FWE-DTI [9.12], have been coded using Matlab© as a part of the dMRI-Lab toolbox (the FWE-DTI is implemented as `atti2freewaterTensor.m`, and the FWE-SM as `atti2micro.m`; the greedy search algorithm for gradients decimation is coded as `decimateGradients.m`). It can be freely downloaded from: `http://www.lpi.tel.uva.es/dmrilab`.

Conflict of interest

The authors declare there is no conflict of interest.

Bibliography

[9.1] M. Bergamino, O. Pasternak, M. Farmer, M. Shenton, and J.P. Hamilton. Applying a free-water correction to diffusion imaging data uncovers stress-related neural pathology in depression. *NeuroImage Clinical*, 10:336–342, 2015.

[9.2] Carlo Pierpaoli and Derek K. Jones. Removing CSF contamination in brain DT-MRIs by using a two-compartment tensor model. In *11th Conference of the International Society of Magnetic Resonance in Medicine (ISMRM)*, page 1215, Melbourne, Australia, 2004.

[9.3] Ofer Pasternak, Nir Sochen, Yaniv Gur, Nathan Intrator, and Yaniv Assaf. Free water elimination and mapping from diffusion MRI. *Magnetic Resonance in Medicine*, 62(3):717–730, 2009.

[9.4] Ofer Pasternak, Carl-Fredrik Westin, Sylvain Bouix, Larry J Seidman, Jill M Goldstein, Tsung-Ung W Woo, Tracey L Petryshen, Raquelle I Mesholam-Gately, Robert W McCarley, Ron Kikinis, Martha E Shenton, and Marek Kubicki. Excessive extracellular volume reveals a neurodegenerative pattern in schizophrenia onset. *Journal of NeuroScience*, 32(48):17365–17372, 2012.

[9.5] Hui Zhang, Torben Schneider, Claudia A. Wheeler-Kingshott, and Daniel C. Alexander. NODDI: Practical in vivo neurite orientation dispersion and density imaging of the human brain. *NeuroImage*, 61(4):1000–1016, 2012.

[9.6] Enrico Kaden, Nathaniel D. Kelm, Robert P. Carson, Mark D. Does, and Daniel C. Alexander. Multi-compartment microscopic diffusion imaging. *NeuroImage*, 139:346–359, 2016.

[9.7] Antonio Tristán-Vega and Santiago Aja-Fernández. Efficient and accurate EAP imaging from multi-shell dMRI with micro-structure adaptive convolution kernels and dual Fourier integral transforms (MiSFIT). *NeuroImage*, 227:117616, 2021.

[9.8] Alberto De Luca, Alexander Leemans, Alessandra Bertoldo, Filippo Arrigoni, and Martijn Froeling. A robust deconvolution method to disentangle multiple water pools in diffusion MRI. *NMR in Biomedicine*, 31(11):e3965, 2018.

[9.9] Sau May Wong, Walter H. Backes, Gerhard S. Drenthen, C. Eleana Zhang, Paulien H.M. Voorter, Julie Staals, Robert J. van Oostenbrugge, and Jacobus F.A. Jansen. Spectral diffusion analysis of intravoxel incoherent motion MRI in cerebral small vessel disease. *Journal of Magnetic Resonance Imaging*, 51(4):1170–1180, 2020.

[9.10] Ofer Pasternak, Martha E Shenton, and Carl-Fredrik Westin. Estimation of extracellular volume from regularized multi-shell diffusion mri. In *15th International Conference on Medical Image Computing and Computer-Assisted Intervention (MICCAI)*, volume 7512-2 of *Lecture Notes in Computer Science*, pages 305–312, Nice, France, 2012.

[9.11] Marc Golub, Rafael Neto Henriques, and Rita Gouveia Nunes. Free-water DTI estimates from single b-value data might seem plausible but must be interpreted with care. *Magnetic Resonance in Medicine*, 85(5):2537–2551, 2021.

[9.12] Andrew R. Hoy, Cheng Guan Koay, Steven R. Kecskemeti, and Andrew L. Alexander. Optimization of a free water elimination two-compartment model for diffusion tensor imaging. *NeuroImage*, 103:323–333, 2014.

[9.13] Enrico Kaden, Frithjof Kruggel, and Daniel C. Alexander. Quantitative mapping of the per-axon diffusion coefficients in brain white matter. *Magnetic Resonance in Medicine*, 75(4):1752–1763, 2016.

[9.14] M. Descoteaux, E. Angelino, S. Fitzgibbons, and R. Deriche. Regularized, fast, and robust analytical Q-Ball imaging. *Magnetic Resonance in Medicine*, 58:497–510, 2007.

[9.15] Brian Hansen and Sune Nørhøj Jespersen. Data for evaluation of fast kurtosis strategies, b-value optimization and exploration of diffusion mri contrast. *Scientific Data*, 3(1):160072, 2016.

[9.16] C.-F. Westin, S.E. Maier, H. Mamata, A. Nabavi, F.A. Jolesz, and R. Kikinis. Processing and visualization for diffusion tensor MRI. *Medical Image Analysis*, 6:93–108, 2001.